

**ABSOLUTE PHOTOABSORPTION AND PHOTOIONIZATION  
STUDIES OF LARGE POLYATOMIC MOLECULES BY HIGH  
ENERGY ELECTRON IMPACT AND MASS SPECTROMETRY**

By

Jennifer W. Au

B.Sc. (Hons.), University of British Columbia, 1992

A THESIS SUBMITTED IN PARTIAL FULFILLMENT OF  
THE REQUIREMENTS FOR THE DEGREE OF  
DOCTOR OF PHILOSOPHY

in

THE FACULTY OF GRADUATE STUDIES  
DEPARTMENT OF CHEMISTRY

We accept this thesis as conforming  
to the required standard

THE UNIVERSITY OF BRITISH COLUMBIA

January 1997

© Jennifer W. Au, 1997

In presenting this thesis in partial fulfilment of the requirements for an advanced degree at the University of British Columbia, I agree that the Library shall make it freely available for reference and study. I further agree that permission for extensive copying of this thesis for scholarly purposes may be granted by the head of my department or by his or her representatives. It is understood that copying or publication of this thesis for financial gain shall not be allowed without my written permission.

Department of CHEMISTRY

The University of British Columbia  
Vancouver, Canada

Date MARCH 10, 1997.

## Abstract

Electronic excitation spectra and absolute differential oscillator strengths (cross sections) have been measured from the visible up to the soft X-ray energy regions (2–200 eV) for the valence-shell photoabsorption of a series of normal alkanes ( $C_5H_{12}$ ,  $C_6H_{14}$ ,  $C_7H_{16}$ , and  $C_8H_{18}$ ), single carbon Freons ( $CFCl_3$ ,  $CF_2Cl_2$ ,  $CF_3Cl$ , and  $CF_4$ ), nitrogen dioxide ( $NO_2$ ), and phosphorus halides ( $PF_3$ ,  $PCl_3$ , and  $PF_5$ ) at 1 eV resolution using dipole ( $e,e$ ) spectroscopy. The absolute differential oscillator strength data for  $PF_3$ ,  $PCl_3$ , and  $PF_5$  have also been extended through the P  $2p,2s$  and Cl  $2p,2s$  inner shells up to 300 eV. In addition, the discrete structures in the valence region and in the vicinity of the P  $2p$  and Cl  $2p$  ( $PCl_3$ ) inner shells of these molecules have been studied at higher resolution (0.05–0.1 eV fwhm). Comparisons have been made to previously reported optical measurements in those limited energy regions where such data exist. The accuracy of the absolute differential oscillator strength scales have been critically evaluated by comparison of the static electric-dipole polarizabilities of the normal alkanes, single carbon Freons,  $NO_2$ ,  $PCl_3$ , and  $PF_5$  derived from the present data using the  $S(-2)$  sum rule with those determined from refractivity and dielectric constant measurements in the literature. The  $S(-2)$  sum rule has also been used with the differential oscillator strength data to determine the experimental dipole polarizability of  $PF_3$  for the first time.

The feasibility of using atomic and molecular mixture rules as well as group additivity concepts for predicting differential oscillator strengths for the valence-shell photoabsorption of long-chained alkane molecules has been investigated over a wide energy range from 20 to 200 eV. The predictions are discussed with reference to the experimental measurements for the normal alkanes obtained in the present work ( $C_nH_{2n+2}$ ,  $n = 5-8$ ) as well as for the smaller alkanes ( $n = 1-4$ ) previously

reported in my B.Sc. undergraduate thesis project.

Dipole ( $e, e^+ion$ ) coincidence spectroscopy has been used to obtain the photoion branching ratios and absolute photoionization efficiencies of the valence shells of  $C_3H_8$ ,  $n-C_4H_{10}$ , and  $NO_2$ , and the valence and inner (P  $2p, 2s$ ; Cl  $2p, 2s$ ) shells of  $PF_3$ ,  $PCl_3$ , and  $PF_5$ . These data are used together with the absolute photoabsorption differential oscillator strengths to determine the absolute partial differential oscillator strengths for the molecular and dissociative photoionization channels of these molecules. A consideration of the photoabsorption and photoionization measurements of  $PF_3$  together with thermodynamic data and results from previously published photoelectron branching ratios and photoelectron-photoion coincidence (PEPICO) studies provides quantitative information on the valence-shell dipole-induced breakdown pathways of  $PF_3$  in the photon energy region below 100 eV. Some qualitative deductions have also been made concerning the dipole-induced breakdown pathways of  $C_3H_8$ ,  $n-C_4H_{10}$ ,  $PCl_3$ ,  $PF_5$ , and  $NO_2$  under UV and vacuum UV radiation.

# Table of Contents

<b>Abstract</b>	<b>ii</b>
<b>Table of Contents</b>	<b>iv</b>
<b>List of Tables</b>	<b>vii</b>
<b>List of Figures</b>	<b>xi</b>
<b>List of Abbreviations</b>	<b>xvi</b>
<b>Acknowledgements</b>	<b>xviii</b>
<b>1 Introduction</b>	<b>1</b>
<b>2 Theoretical Background</b>	<b>8</b>
2.1 Photoabsorption by Dipole ( $e,e$ ) Spectroscopy .....	8
2.1.1 Bethe-Born theory .....	10
2.1.2 Sum rules.....	14
2.2 Photoionization by Dipole ( $e,e+ion$ ) Coincidence Spectroscopy .....	16
2.3 Photoabsorption and Photoionization Processes .....	19
2.3.1 Spectral features.....	20
2.3.2 Decay processes.....	25
<b>3 Experimental Methods</b>	<b>27</b>
3.1 The Low Resolution Spectrometer .....	27
3.1.1 The dipole ( $e,e$ ) mode .....	29
3.1.2 The dipole ( $e,e+ion$ ) coincidence mode.....	33
3.2 The High Resolution Dipole ( $e,e$ ) Spectrometer .....	36
3.3 Sample Handling .....	39
<b>4 Photoabsorption and Photoionization Studies of Normal Alkanes</b>	<b>42</b>
4.1 Introduction.....	42
4.2 Results and Discussion.....	44
4.2.1 Electronic structures .....	44
4.2.2 Molecular and dissociative photoionization of propane .....	45
4.3.3 Molecular and dissociative photoionization of $n$ -butane.....	52
4.3.4 Photoabsorption of $n$ -pentane, $n$ -hexane, $n$ -heptane, and $n$ -octane...58	
4.3 Atomic and Molecular Mixture Rules and Group Additivity Concepts.....	66
4.3.1 Measured absolute photoabsorption differential oscillator strengths for the normal alkanes .....	70
4.3.2 Atomic mixture rules.....	73
4.3.3 Molecular mixture rules.....	76
4.3.4 Group additivity.....	83
4.3.5 Conclusions.....	90

<b>5</b>	<b>Photoabsorption Studies of Phosphorus Halides</b>	<b>92</b>
5.1	Introduction.....	92
5.2	Results and Discussion.....	94
5.2.1	Electronic structures .....	95
5.2.2	Phosphorus trifluoride.....	98
5.2.2.1	Long range photoabsorption spectrum .....	98
5.2.2.2	Valence-shell spectrum .....	101
5.2.2.3	P $2p,2s$ inner-shell spectra .....	108
5.2.3	Phosphorus trichloride .....	113
5.2.3.1	Long range photoabsorption spectrum .....	113
5.2.3.2	Valence-shell spectrum .....	116
5.2.3.3	P $2p,2s$ inner-shell spectra .....	120
5.2.3.4	Cl $2p,2s$ inner-shell spectra .....	125
5.2.4	Phosphorus pentafluoride .....	129
5.2.4.1	Long range photoabsorption spectrum .....	129
5.2.4.2	Valence-shell spectrum .....	131
5.2.4.3	P $2p,2s$ inner-shell spectra .....	134
<b>6</b>	<b>Photoionization Studies of Phosphorus Halides</b>	<b>139</b>
6.1	Introduction.....	139
6.2	Results and Discussion.....	141
6.2.1	Phosphorus trifluoride.....	142
6.2.1.1	Valence-shell photoionization.....	142
6.2.1.2	Dipole-induced breakdown.....	148
6.2.1.3	P $2p,2s$ inner-shell photoionization.....	155
6.2.2	Phosphorus trichloride .....	161
6.2.2.1	Valence-shell photoionization.....	161
6.2.2.2	P $2p,2s$ and Cl $2p,2s$ inner-shell photoionization.....	170
6.2.3	Phosphorus pentafluoride .....	176
6.2.3.1	Valence-shell photoionization.....	176
6.2.3.2	P $2p,2s$ inner-shell photoionization.....	184
<b>7</b>	<b>Photoabsorption and Photoionization Studies of Nitrogen Dioxide</b>	<b>190</b>
7.1	Introduction.....	190
7.2	Results and Discussion.....	192
7.2.1	Electronic structure .....	192
7.2.2	Long range photoabsorption spectrum .....	193
7.2.3	Valence-shell spectrum in the discrete region .....	196
7.2.4	Molecular and dissociative photoionization .....	202
7.2.5	Dipole-induced breakdown.....	209

<b>8 Photoabsorption Studies of Freons</b>	<b>212</b>
8.1 Introduction.....	212
8.2 Results and Discussion.....	214
8.2.1 Electronic structures .....	214
8.2.2 Long range photoabsorption spectra.....	215
8.2.3 Discrete photoabsorption spectra.....	220
8.2.3.1 CFC1 <sub>3</sub> .....	220
8.2.3.2 CF <sub>2</sub> Cl <sub>2</sub> .....	225
8.2.3.3 CF <sub>3</sub> Cl .....	229
8.2.3.4 CF <sub>4</sub> .....	233
<b>9 Conclusions</b>	<b>239</b>
<b>Bibliography</b>	<b>242</b>
<b>Appendix Absolute Differential Oscillator Strength Data Tables</b>	<b>256</b>

## List of Tables

Table 3.1	Valence-shell oscillator strength estimates used to establish the absolute photoabsorption differential oscillator strength scales of molecules reported in this thesis via the VTRK sum rule .....	33
Table 3.2	Sources and purities of samples used in the present work .....	40
Table 4.1	Experimental appearance potentials for the production of positive ions from propane .....	51
Table 4.2	Experimental appearance potentials for the production of positive ions from <i>n</i> -butane .....	57
Table 4.3	Experimental static electric-dipole polarizability values of <i>n</i> -pentane, <i>n</i> -hexane, <i>n</i> -heptane, <i>n</i> -octane .....	64
Table 4.4	Types of molecular mixture rules (MMR) employed in the estimation of the absolute photoabsorption differential oscillator strengths for the normal alkanes, C <sub><i>n</i></sub> H <sub>2<i>n</i>+2</sub> .....	78
Table 4.5	Best fit parameters determined by least squares fits of the average differential oscillator strengths for the methylene (CH <sub>2</sub> ) and methyl (CH <sub>3</sub> ) alkane group fragments using the polynomial function given by equation (3.1) .....	87
Table 5.1	Best fit parameters determined by fitting equation (3.1) to the valence-shell differential oscillator strengths at high energy for PF <sub>3</sub> , PCl <sub>3</sub> , and PF <sub>5</sub> .....	95
Table 5.2	Absolute photoabsorption oscillator strengths for regions of the valence-shell spectrum of PF <sub>3</sub> .....	104
Table 5.3	Absolute oscillator strengths for the 4 <i>s</i> ← 8 <i>a</i> <sub>1</sub> <sup>-1</sup> vibronic bands of the valence-shell photoabsorption spectrum of PF <sub>3</sub> .....	106
Table 5.4	Absolute photoabsorption oscillator strengths for regions of the P 2 <i>p</i> inner-shell spectrum of PF <sub>3</sub> .....	112
Table 5.5	Absolute photoabsorption oscillator strengths for regions of the valence-shell spectrum of PCl <sub>3</sub> .....	120
Table 5.6	Absolute photoabsorption oscillator strengths for regions of the P 2 <i>p</i> spectrum of PCl <sub>3</sub> .....	123

Table 5.7	Absolute photoabsorption oscillator strengths for regions of the Cl $2p$ spectrum of $\text{PCl}_3$ .....	127
Table 5.8	Absolute photoabsorption oscillator strengths for regions of the valence-shell spectrum of $\text{PF}_5$ .....	134
Table 5.9	Absolute photoabsorption oscillator strengths for regions of the P $2p$ spectrum of $\text{PF}_5$ .....	136
Table 6.1	Calculated and measured appearance potentials for the production of positive ions from $\text{PF}_3$ .....	146
Table 6.2	Calculated and measured appearance potentials for the production of positive ions from $\text{PCl}_3$ .....	166
Table 6.3	Appearance potentials for the production of positive ions from $\text{PF}_5$ .....	183
Table 7.1	Absolute photoabsorption oscillator strengths for the discrete regions of the valence-shell spectrum of nitrogen dioxide.....	199
Table 7.2	Calculated and measured appearance potentials for the production of positive ions from nitrogen dioxide.....	204
Table 8.1	Static electric-dipole polarizability values of $\text{CFCl}_3$ , $\text{CF}_2\text{Cl}_2$ , $\text{CF}_3\text{Cl}$ , and $\text{CF}_4$ .....	219
Table 8.2	Absolute photoabsorption oscillator strengths for regions of the valence-shell spectrum of $\text{CFCl}_3$ .....	224
Table 8.3	Absolute photoabsorption oscillator strengths for regions of the valence-shell spectrum of $\text{CF}_2\text{Cl}_2$ .....	227
Table 8.4	Absolute photoabsorption oscillator strengths for regions of the valence-shell spectrum of $\text{CF}_3\text{Cl}$ .....	231
Table 8.5	Absolute photoabsorption oscillator strengths for regions of the valence-shell spectrum of $\text{CF}_4$ .....	235
Table A.1	Absolute partial differential oscillator strengths for the molecular and dissociative photoionization of propane.....	257
Table A.2	Absolute partial differential oscillator strengths for the molecular and dissociative photoionization of $n$ -butane.....	260
Table A.3	Absolute photoabsorption differential oscillator strengths for $n$ -pentane from 7.5 to 220 eV.....	262

Table A.4	Absolute photoabsorption differential oscillator strengths for <i>n</i> -hexane from 7 to 220 eV .....	264
Table A.5	Absolute photoabsorption differential oscillator strengths for <i>n</i> -heptane from 7 to 220 eV.....	266
Table A.6	Absolute photoabsorption differential oscillator strengths for <i>n</i> -octane from 7.5 to 220 eV .....	268
Table A.7	Absolute differential oscillator strengths for the total photoabsorption and the dissociative photoionization of PF <sub>3</sub> up to 130 eV .....	270
Table A.8	Absolute differential oscillator strengths for the total photoabsorption of PF <sub>3</sub> in the P 2 <i>p</i> ,2 <i>s</i> inner-shell region from 125 to 300 eV .....	272
Table A.9	Absolute differential oscillator strengths for the total photoabsorption and the dissociative photoionization of PCl <sub>3</sub> up to 125 eV .....	274
Table A.10	Absolute differential oscillator strengths for the total photoabsorption of PCl <sub>3</sub> in the P 2 <i>p</i> ,2 <i>s</i> and Cl 2 <i>p</i> ,2 <i>s</i> inner-shell regions from 124 to 350 eV.....	276
Table A.11	Absolute differential oscillator strengths for the total photoabsorption and the dissociative photoionization of PF <sub>5</sub> up to 130 eV.....	278
Table A.12	Absolute differential oscillator strengths for the total photoabsorption of PF <sub>5</sub> in the P 2 <i>p</i> ,2 <i>s</i> inner-shell region from 126 to 300 eV .....	281
Table A.13	Absolute differential oscillator strengths for the total photoabsorption and the molecular and dissociative photoionization of PF <sub>3</sub> in the valence and the P 2 <i>p</i> ,2 <i>s</i> inner-shell regions from 130 to 192.5 eV.....	283
Table A.14	Absolute differential oscillator strengths for the total photoabsorption and the molecular and dissociative photoionization of PCl <sub>3</sub> in the valence and the P 2 <i>p</i> ,2 <i>s</i> and Cl 2 <i>p</i> ,2 <i>s</i> inner-shell regions from 125 to 271 eV .....	284
Table A.15	Absolute differential oscillator strengths for the total photoabsorption and the dissociative photoionization of PF <sub>5</sub> in the P 2 <i>p</i> ,2 <i>s</i> inner-shell region.....	285

Table A.16	Absolute differential oscillator strengths for the total photoabsorption and the molecular and dissociative photoionization of nitrogen dioxide up to 80 eV.....	286
Table A.17	Absolute differential oscillator strengths for the valence-shell photoabsorption of nitrogen dioxide from 80 to 200 eV.....	288
Table A.18	Absolute differential oscillator strengths for the valence-shell photoabsorption of $\text{CFCl}_3$ from 5.5 to 200 eV.....	289
Table A.19	Absolute differential oscillator strengths for the valence-shell photoabsorption of $\text{CF}_2\text{Cl}_2$ from 6 to 200 eV.....	291
Table A.20	Absolute differential oscillator strengths for the valence-shell photoabsorption of $\text{CF}_3\text{Cl}$ from 7 to 200 eV.....	293
Table A.21	Absolute differential oscillator strengths for the valence-shell photoabsorption of $\text{CF}_4$ from 10 to 200 eV.....	295

## List of Figures

Figure 2.1	Schematic of various photoabsorption and photoionization processes .....	21
Figure 3.1	Schematic of the low resolution dipole ( $e,e$ ) and dipole ( $e,e+ion$ ) coincidence spectrometer .....	28
Figure 3.2	Schematic of the high resolution dipole ( $e,e$ ) spectrometer .....	37
Figure 4.1	TOF mass spectrum of propane obtained at 70 eV .....	46
Figure 4.2	Photoionization efficiencies for propane (11–80 eV) .....	46
Figure 4.3	Branching ratios for the molecular and dissociative photoionization of propane .....	48
Figure 4.4	Absolute partial photoionization differential oscillator strengths for the molecular and dissociative photoionization of propane .....	50
Figure 4.5	TOF mass spectrum of $n$ -butane obtained at 50 eV .....	53
Figure 4.6	Photoionization efficiencies for $n$ -butane (10–50 eV) .....	53
Figure 4.7	Branching ratios for the molecular and dissociative photoionization of $n$ -butane .....	55
Figure 4.8	Absolute partial photoionization differential oscillator strengths for the molecular and dissociative photoionization of $n$ -butane .....	56
Figure 4.9	Absolute differential oscillator strengths for the valence-shell photoabsorption of $n$ -pentane (7–220 eV) .....	59
Figure 4.10	Absolute differential oscillator strengths for the valence-shell photoabsorption of $n$ -hexane (7–220 eV) .....	60
Figure 4.11	Absolute differential oscillator strengths for the valence-shell photoabsorption of $n$ -heptane (7–220 eV) .....	61
Figure 4.12	Absolute differential oscillator strengths for the valence-shell photoabsorption of $n$ -octane (7–220 eV) .....	62
Figure 4.13	Systematic comparison of the absolute differential oscillator strengths for the valence-shell photoabsorption of the normal alkanes, $C_nH_{2n+2}$ ( $n = 1-8$ ). .....	71

Figure 4.14	Comparison of atomic mixture rules with experimental photoabsorption differential oscillator strengths.....	75
Figure 4.15	Comparison of molecular mixture rules with experimental photoabsorption differential oscillator strengths .....	80
Figure 4.16	Average differential oscillator strengths for the methylene ( $\text{CH}_2$ ) group fragment .....	85
Figure 4.17	Average differential oscillator strengths for the methyl ( $\text{CH}_3$ ) group fragment .....	86
Figure 4.18	Comparison of differential oscillator strength sums obtained using group additivity with experimental measurements of <i>n</i> -octane .....	89
Figure 5.1	Absolute long range photoabsorption spectrum of $\text{PF}_3$ (5–300 eV) .....	99
Figure 5.2	Absolute high resolution photoabsorption spectrum of the valence-shell region of $\text{PF}_3$ .....	102
Figure 5.3	Features observed in the discrete valence-shell absolute photoabsorption spectrum of $\text{PF}_3$ (7–23 eV) .....	103
Figure 5.4	Absolute photoabsorption differential oscillator strengths of the P $2p, 2s$ inner-shell region of $\text{PF}_3$ (134–250 eV) .....	109
Figure 5.5	Absolute long range photoabsorption spectrum of $\text{PCl}_3$ (5–350 eV) .....	114
Figure 5.6	Absolute high resolution photoabsorption spectra of the valence, P $2p$ , and Cl $2p$ regions of $\text{PCl}_3$ .....	117
Figure 5.7	Features observed in the discrete valence-shell absolute photoabsorption spectrum of $\text{PCl}_3$ (5–21.5 eV) .....	119
Figure 5.8	Absolute photoabsorption differential oscillator strengths of the P $2p, 2s$ inner-shell region of $\text{PCl}_3$ (132–200 eV) .....	122
Figure 5.9	Absolute photoabsorption differential oscillator strengths of the Cl $2p, 2s$ inner-shell region of $\text{PCl}_3$ (198–340 eV) .....	126
Figure 5.10	Absolute long range photoabsorption spectrum of $\text{PF}_5$ (10–300 eV) .....	130

Figure 5.11	Absolute high resolution photoabsorption spectra of the valence and P 2 <i>p</i> regions of PF <sub>5</sub> .....	132
Figure 5.12	Features observed in the discrete valence-shell absolute photoabsorption spectrum of PF <sub>5</sub> (10–23 eV).....	133
Figure 5.13	Absolute photoabsorption differential oscillator strengths of the P 2 <i>p</i> ,2 <i>s</i> inner-shell region of PF <sub>5</sub> (137–260 eV).....	135
Figure 6.1	TOF mass spectrum of PF <sub>3</sub> at 70 eV.....	143
Figure 6.2	Photoionization efficiencies for PF <sub>3</sub> (11–130 eV).....	143
Figure 6.3	Branching ratios for the molecular and dissociative photoionization of PF <sub>3</sub> .....	144
Figure 6.4	Absolute partial photoionization differential oscillator strengths for the valence-shell molecular and dissociative photoionization of PF <sub>3</sub> (11–130 eV).....	147
Figure 6.5	Absolute electronic ion state partial photoionization differential oscillator strengths for PF <sub>3</sub> (10–100 eV).....	150
Figure 6.6	Differential oscillator strength sums determined for the proposed dipole-induced breakdown scheme for PF <sub>3</sub> below 130 eV.....	151
Figure 6.7	Dipole-induced breakdown pathways following valence-shell photoionization of PF <sub>3</sub> below 130 eV.....	154
Figure 6.8	TOF mass spectra of PF <sub>3</sub> at selected energies in the P 2 <i>p</i> ,2 <i>s</i> inner-shell region.....	156
Figure 6.9	Absolute partial photoionization differential oscillator strengths for the molecular and dissociative photoionization of PF <sub>3</sub> in the P 2 <i>p</i> ,2 <i>s</i> inner-shell region (130–193 eV).....	159
Figure 6.10	TOF mass spectrum of PCl <sub>3</sub> at 40 eV.....	162
Figure 6.11	Photoionization efficiencies for PCl <sub>3</sub> (10–36 eV).....	162
Figure 6.12	Branching ratios for the molecular and dissociative photoionization of PCl <sub>3</sub> .....	164

Figure 6.13	Absolute partial photoionization differential oscillator strengths for the valence-shell molecular and dissociative photoionization of $\text{PCl}_3$ (10–125 eV) .....	165
Figure 6.14	TOF mass spectra of $\text{PCl}_3$ at selected energies in the P $2p$ inner-shell region .....	171
Figure 6.15	TOF mass spectra of $\text{PCl}_3$ at selected energies in the P $2s$ and Cl $2p,2s$ inner-shell regions .....	172
Figure 6.16	Absolute partial photoionization differential oscillator strengths for the molecular and dissociative photoionization of $\text{PCl}_3$ in the P $2p,2s$ and Cl $2p,2s$ inner-shell regions (120–271 eV) .....	174
Figure 6.17	TOF mass spectrum of $\text{PF}_5$ at 80 eV .....	177
Figure 6.18	Photoionization efficiencies for $\text{PF}_5$ (15–75 eV) .....	177
Figure 6.19	Branching ratios for the dissociative photoionization of $\text{PF}_5$ .....	179
Figure 6.20	Absolute partial photoionization differential oscillator strengths for the valence-shell dissociative photoionization of $\text{PF}_5$ (15–130 eV) ...	180
Figure 6.21	Comparison of the summed ( $\text{P}^+ + \text{F}^+$ ) differential oscillator strengths with five times the F $2s$ photoionization differential oscillator strengths for atomic fluorine .....	182
Figure 6.22	TOF mass spectra of $\text{PF}_5$ at selected energies in the P $2p$ inner-shell region .....	185
Figure 6.23	TOF mass spectra of $\text{PF}_5$ at selected energies in the P $2p,2s$ inner-shell region .....	186
Figure 6.24	Absolute PPOS for the dissociative photoionization of $\text{PF}_5$ in the P $2p,2s$ inner-shell region (130–197.5 eV) .....	188
Figure 7.1	Absolute differential oscillator strengths for the valence-shell photoabsorption of nitrogen dioxide (2–200 eV) .....	194
Figure 7.2	Absolute high resolution differential oscillator strengths for the valence-shell photoabsorption of nitrogen dioxide (1.6–30 eV) .....	197
Figure 7.3	Rydberg profiles observed in the valence-shell discrete region of the nitrogen dioxide photoabsorption spectrum .....	198

Figure 7.4	TOF mass spectrum of nitrogen dioxide at 50 eV.....	203
Figure 7.5	Branching ratios for the molecular and dissociative photoionization of nitrogen dioxide.....	206
Figure 7.6	Absolute partial photoionization differential oscillator strengths for the valence-shell molecular and dissociative photoionization of nitrogen dioxide .....	208
Figure 8.1	Absolute long range differential oscillator strengths for the valence-shell photoabsorption of $\text{CFCl}_3$ , $\text{CF}_2\text{Cl}_2$ , $\text{CF}_3\text{Cl}$ , and $\text{CF}_4$ (5–200 eV).....	216
Figure 8.2	Absolute high-resolution oscillator strengths for the valence-shell photoabsorption of $\text{CFCl}_3$ (5–60 eV) .....	221
Figure 8.3	Absolute high-resolution oscillator strengths for the valence-shell photoabsorption of $\text{CF}_2\text{Cl}_2$ (6–60 eV) .....	226
Figure 8.4	Absolute high-resolution oscillator strengths for the valence-shell photoabsorption of $\text{CF}_3\text{Cl}$ (8–60 eV) .....	230
Figure 8.5	Absolute high-resolution oscillator strengths for the valence-shell photoabsorption of $\text{CF}_4$ (10–60 eV).....	234
Figure 8.6	Absolute photoabsorption differential oscillator strengths of $\text{CF}_4$ at the vicinity of the $(3t_2)^{-1}$ autoionization region.....	237

## List of Abbreviations

AMR	atomic mixture rule
AP	appearance potential
Calc.	calculated
CI	configuration interaction
DOSD	dipole oscillator strength distribution
EEL	electron energy-loss
EELS	electron energy-loss spectroscopy
EMS	electron momentum spectroscopy
fwhm	full width at half maximum
GOS	generalized oscillator strength
HOMO	highest occupied molecular orbital
HR	high resolution
HV	high voltage
IP	ionization potential
LCAO	linear combination of atomic orbitals
LR	low resolution
MMR	molecular mixture rule
MO	molecular orbital
MS	multiple scattering
PE	photoelectron
PEPICO	photoelectron-photoion coincidence
PEPIPICO	photoelectron-photoion-photoion coincidence
PES	photoelectron spectroscopy
PIMS	photoionization mass spectrometry

PIPICO	photoion-photoion coincidence
PPOS	partial photoionization differential oscillator strength
SCF	self consistent field
SW	scattered waves
TAC	time-to-amplitude converter
TOF	time-of-flight
TPEPICO	threshold-photoelectron-photoion coincidence
TRK	Thomas-Reiche-Kuhn
UV	ultraviolet
VIP	vertical ionization potential
VTRK	valence-shell Thomas-Reiche-Kuhn
VUV	vacuum ultraviolet
XPS	X-ray photoelectron spectroscopy

## Acknowledgements

I would like to express my sincere thanks to my research supervisor, Professor C.E. Brion, for his support, invaluable comments, and persistent encouragements throughout the course of this work. Special thanks should also go to Dr. G. Cooper, Dr. G. Burton, and Dr. T. Olney for teaching me the operation of the dipole ( $e,e$ ) and dipole ( $e,e+ion$ ) spectrometers and for their help and assistance in problematic times. I am additionally indebted to Professor W.J. Meath and Professor A.P. Hitchcock for helpful discussions concerning the normal alkane additivity assessments and the inner-shell phosphorus halide studies, respectively. I would also like to thank J. Rolke for his friendship and help during the course of my graduate studies.

The measurements of the high resolution valence-shell photoabsorption spectra of  $CF_4$  and  $CF_3Cl$  provided by Dr. G. Burton are gratefully acknowledged. Moreover, I am indebted to Professor S. Withers and Dr. B. Clifford for supplying the liquid samples of  $CFCl_3$  and the normal alkanes ( $C_nH_{2n+2}$ ,  $n = 5-8$ ) for the present measurements.

Finally, I would like to thank B. Greene of the electronic engineering shop as well as E. Gomm, B. Henderson, and R. Marwick of the mechanical engineering shop for their assistance in maintaining the spectrometers. In particular, B. Henderson is acknowledged for his expertise in constructing special adapters and fittings required to mount my samples to the machines.

Funding for this research was provided by the Natural Sciences and Engineering Research Council of Canada and by the Canadian National Networks of Centres of Excellence (Centre of Excellence in Molecular and Interfacial Dynamics). The receipt of a F.J. Nicholson scholarship is also gratefully acknowledged.

# Chapter 1

## Introduction

Absolute oscillator strengths (cross sections) for photoabsorption and photoionization processes in the visible through to the X-ray regions of the electromagnetic spectrum provide useful information for the quantitative study of radiation chemistry, physics, and biology, as well as for aeronomy, astrophysics, laser development, and electron microscopy [1,2]. Such information is also required for the quantitative evaluation of quantum mechanical calculations. However, most of the photoabsorption spectra and photoionization yield curves available in the literature only provide *relative* intensities and not absolute cross sections. For example, in the case of nitrogen dioxide, only two [3,4] of the ~30 experimental studies of valence-shell excitation and ionization reported absolute data in the near ultraviolet (UV) region above 5 eV, and the overlap between these two data sets is very small (< 0.5 eV).

The scarcity of absolute oscillator strengths in the UV, vacuum UV, and soft X-ray regions can be attributed to the many difficulties involved in making absolute measurements using conventional optical techniques. In the discrete excitation region, the resonant characteristic of photon absorption can cause serious errors in absolute cross sections determined by Beer-Lambert law photoabsorption. These "line saturation" effects [5,6] occur when the instrumental bandwidth is greater than the natural linewidth of the discrete transitions, resulting in serious perturbations in the cross sections subsequently determined from the logarithmic transformation of intensity ratios using the Beer-Lambert law [5-8]. These errors are largest for transitions of high cross section and very narrow linewidth. At higher

excitation energies, optical spectroscopic techniques are further limited by the lithium fluoride (LiF) cut-off above 11.7 eV and by the availability of continuum photon sources above 20 eV. It is well known that LiF windows completely absorb all photons above 11.7 eV, and therefore, spectrometer design and light handling techniques become very challenging. Specifically, this requires the use of reflection instead of transmission optics, and the use of a windowless vacuum spectrometer [9]. Secondly, while the need for continuum photon sources above 20 eV has been met by synchrotron radiation, its use is affected by monochromator problems such as low reflectivity at higher energies and contamination from higher order radiation and stray light. In particular, the presence of higher order radiation can cause experimental errors in both the shape and magnitude of the photoabsorption cross sections by up to  $\pm 20\%$  between 22–40 eV [10]. In addition, synchrotron radiation facilities are expensive and remotely located. It should also be noted that the measurement of wide-ranging photoabsorption spectra spanning the visible to the X-ray regions using optical methods is furthermore complicated by the need to use many different monochromators over selected energy regions, thereby making it impossible to study the photoabsorption spectrum of a target species from the first excitation threshold up to several hundred electron volts using one spectrometer.

Alternatively, high energy electron impact spectroscopy can provide an inexpensive and effective method for the measurement of absolute photoabsorption and photoionization oscillator strengths of free atoms and molecules. The general theoretical background of the inelastic collision of fast charged particles with matter was first established in 1930 by Bethe [11] based on the Born approximation and was later reviewed in greater detail by Inokuki [12,13]. Bethe [11] showed that under certain inelastic electron scattering conditions (i.e., high impact energy and small scattering angles) such that the momentum transfer ( $\mathbf{K}$ ) is negligibly small, the electronic transitions of the target atom or molecule obey the same dipole

selection rules as in optical spectroscopy. In this process the fast, high energy incident electron imparts a small amount of energy (with respect to its initial energy) to the target species in order to cause a dipole transition to occur, and this "energy-loss" by the scattered electron is comparable to the excitation or photon energy in optical experiments. The resulting electron scattering cross section has been shown [11] to be related to the optical (photoabsorption) cross section<sup>1</sup> by factors which depend only on the excitation energy and the geometry and kinematics of the experimental apparatus. These Bethe-Born factors can be determined for any particular electron impact spectrometer and subsequently be used to mathematically convert electron scattering differential cross sections for any given free atom or molecule to the corresponding photoabsorption cross sections [2,5,14-16], and the "energy-loss" of the electron impact process becomes equivalent to the photon energy.

Three experimental techniques have been developed to achieve the negligibly small momentum transfer (i.e.,  $\mathbf{K}^2 \rightarrow 0$ ) required by the Bethe-Born theory for obtaining photoabsorption differential oscillator strengths by electron impact. In order for  $\mathbf{K}^2$  to be zero, the scattering event must occur with a high impact energy ( $E_0$ ) and a zero degree scattering angle ( $\theta$ ). One method involves the measurement of electron scattering cross sections over a range of  $E_0$  (40-100 eV) at  $\theta \approx 0^\circ$  [17]. This produces a series of electron energy-loss (EEL) spectra, each having a different momentum transfer. The squares of the momentum transfers are then plotted against  $df(\mathbf{K},E)/dE$ , and the optical limit is obtained by extrapolation to  $\mathbf{K}^2 = 0$ . Alternatively, Lassetre [18,19] fixed the impact energy (~500 eV) and measured

---

<sup>1</sup> The optical (photoabsorption) cross section,  $\sigma_p$ , is directly proportional to the photoabsorption differential oscillator strength,  $df/dE$  (a special case of the generalized differential oscillator strength,  $df(\mathbf{K},E)/dE$ , when  $\mathbf{K}^2 = 0$ ), by a constant factor. See section 2.1.1 for details.

EEL spectra at different scattering angles. Extrapolation of the resulting  $df(\mathbf{K},E)/dE$  data as a function of  $\mathbf{K}^2$  to zero momentum transfer similarly gives the optical limit. Unfortunately, the extrapolations required for both of these techniques can result in large uncertainties [18]. In addition, the experimental procedures are tedious in that transitions must be studied individually, and as such no wide range photoabsorption spectra were obtained. A third method developed by Van der Wiel [20,21] measures the photoabsorption differential oscillator strength for discrete and continuum transitions at low resolution (1 eV fwhm) *directly* by setting the impact energy to a sufficiently high value (typically several thousand electron volts) and the scattering angle to a very small cone subtended around zero degrees so that negligible momentum transfer conditions exist. The latter so called dipole ( $e,e$ ) technique has been further developed and used by Brion and co-workers [2,5,14,22–24] to extend the measurements of absolute photoabsorption data to high resolution studies (0.05–0.1 eV fwhm) of the valence and inner-shell regions of atoms and molecules.

Fast electron scattering techniques at negligible momentum transfer have continued to provide reliable alternatives to direct optical photoabsorption and photoionization experiments for the measurement of absolute total photoabsorption and partial photoionization differential oscillator strengths (cross sections) of atoms and molecules [2,5,7,8,22–26]. The results obtainable using dipole ( $e,e$ ) and dipole ( $e,e+\text{ion}$ ) coincidence spectroscopies have been shown to be quantitatively equivalent to measurements obtained from photoabsorption and photoionization mass spectrometry, respectively [2]. In addition to being easily tunable over a wide energy range (1–1000 eV energy-loss or equivalent photon energy), the technique of dipole ( $e,e$ ) spectroscopy can be used to obtain absolute measurements via the  $S(0)$  and  $S(-2)$  sum rules [27,28] (see sections 2.1.2 and 3.1.1 below for details) and therefore does not require determinations of absolute target particle densities

involved in the Beer-Lambert law. Since electron impact excitation experiments are non-resonant and do not require logarithmic transforms to obtain the cross sections, errors due to "line saturation" (bandwidth / linewidth) effects [5-8] cannot occur. Furthermore, use of the dipole ( $e,e$ ) method does not involve corrections for higher order radiation and stray light which are usually required when using monochromated synchrotron radiation for photoabsorption measurements.

In the present work, dipole ( $e,e$ ) and dipole ( $e,e+ion$ ) coincidence spectroscopies have been used to obtain absolute valence-shell photoabsorption and/or partial photoionization differential oscillator strengths for a series of atmospheric-related molecules ( $CFCl_3$ ,  $CF_2Cl_2$ ,  $CF_3Cl$ ,  $CF_4$ ,  $NO_2$ ,  $C_3H_8$ , and  $n-C_4H_{10}$ ), large normal alkanes ( $C_5H_{12}$ ,  $C_6H_{14}$ ,  $C_7H_{16}$ , and  $C_8H_{18}$ ), and phosphorus halides ( $PF_3$ ,  $PCl_3$ , and  $PF_5$ ) from the visible up to the soft X-ray energy regions (2-200 eV). The absolute photoabsorption and partial photoionization data for the phosphorus halides have been additionally extended through the P  $2p,2s$  and Cl  $2p,2s$  inner shells up to 300 eV. The atmospheric-related molecules were selected for the present study because of their fundamental interest and because of the importance of their interaction with UV, VUV, and soft X-ray radiation in a number of applications. In particular, absolute photoabsorption data for the Freons are of considerable interest due to their role in the catalytic decomposition of atmospheric ozone in the stratosphere [29,30]. The release of chlorine atoms through dissociation by solar UV radiation sets off a chain reaction that results in the net conversion of ozone into oxygen. Similarly, nitrogen dioxide ( $NO_2$ ) is also involved in the decomposition of stratospheric ozone via a cyclic catalytic pathway with nitric oxide [30-32]. Moreover,  $NO_2$  is also responsible for the formation of photochemical smog as a result of its production from the combustion of fuels used for heat, power, and transportation [33]. Propane is also of some interest in aeronomy due to its ability to scavenge chlorine atoms [34], thereby interrupting the chain reactions that can

lead to ozone depletion. Butane, on the other hand, is used in Britain as an aerosol propellant substitute for Freons [35]. In addition to the atmospheric-related molecules, absolute photoabsorption spectra for the large normal alkanes ( $C_nH_{2n+2}$ ,  $n = 5-8$ ) have been recorded in order to make available the wide-ranging data required for the evaluation of mixture rules and additivity concepts. These data have been used together with those obtained for the smaller alkanes ( $n = 1-4$ ) in my B.Sc. undergraduate thesis project [36] in order to estimate differential oscillator strength distributions from contributing molecular group "fragments" or "chromophores" for alkanes (i.e.,  $CH_2$  and  $CH_3$  groups), which can subsequently be summed to provide oscillator strength predictions for radiation absorption by larger alkanes as well as for estimating contributions from hydrocarbon groupings in more complex systems (e.g., organic molecules such as carbohydrates and triglycerides). Finally, the phosphorus halides were selected for the present work because the high symmetry of these large inorganic molecules makes them a good test-bed for theoretical calculations. The absolute differential oscillator strengths for the photoabsorption and photoionization processes of these molecules in both the valence and inner-shells are also of fundamental scientific interest.

The remainder of this thesis has been organized as follows. Chapter 2 presents the theoretical background behind the use of high energy electron impact in obtaining absolute photoabsorption and partial photoionization differential oscillator strengths. A review of some spectral features and processes characteristic of valence and inner shell excitation and ionization are also given. Chapter 3 describes the dipole ( $e,e$ ) and dipole ( $e,e+ion$ ) coincidence spectrometers and the corresponding procedures used in the determination of absolute "optical" data. Chapters 4 to 8 present the experimental results and discussions for the normal alkanes (chapter 4), phosphorus halides (chapters 5 and 6), nitrogen dioxide (chapter 7), and the single carbon Freons (chapter 8). Some general conclusions and

suggestions for further work are given in chapter 9. Finally, the appendix at the end of this thesis contains a numerical compilation of the absolute differential oscillator strength data and photoionization efficiencies measured in the present work.

Note that all the results presented in this thesis can be found in the following publications:

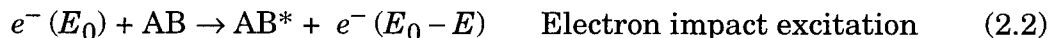
- (1) J.W. Au, G. Cooper, G.R. Burton, T.N. Olney, and C.E. Brion, "The valence shell photoabsorption of the linear alkanes,  $C_nH_{2n+2}$  ( $n = 1-8$ ): absolute oscillator strengths (7–220 eV)," *Chemical Physics*, **173** (1993) 209.
- (2) J.W. Au, G. Cooper, and C.E. Brion, "The molecular and dissociative photoionization of ethane, propane, and  $n$ -butane: absolute oscillator strengths (10–80 eV) and breakdown pathways," *Chemical Physics*, **173** (1993) 241.
- (3) J.W. Au, G. Cooper, G.R. Burton, and C.E. Brion, "An evaluation of additivity concepts for the estimation of radiation absorption by long-chained hydrocarbons at vacuum UV and soft X-ray energies," *Chemical physics*, **187** (1994) 305.
- (4) J.W. Au, G. Cooper, and C.E. Brion, "Photoabsorption and photoionization of the valence and inner (P  $2p,2s$ ) shells of  $PF_3$ : absolute oscillator strengths and dipole-induced breakdown pathways," *Chemical Physics*, **215** (1997) 397.
- (5) J.W. Au and C.E. Brion, "Quantitative studies of the photoabsorption and photoionization of  $PCl_3$  in the valence and inner (P  $2p,2s$ ; Cl  $2p,2s$ ) shell regions," *Chemical Physics* (1997). In press.
- (6) J.W. Au and C.E. Brion, "Absolute oscillator strengths for the valence-shell photoabsorption (2–200 eV) and photoionization (11–80 eV) of nitrogen dioxide," *Chemical Physics* (1997). In press.
- (7) J.W. Au and C.E. Brion, "Absolute oscillator strengths for the valence and inner (P  $2p,2s$ ) shell photoabsorption, photoionization, and ionic photofragmentation of  $PF_5$ ," *Chemical Physics* (1997). Submitted.
- (8) J.W. Au, G.R. Burton, and C.E. Brion, "Quantitative spectroscopic studies of the valence-shell electronic excitation of Freons ( $CFCl_3$ ,  $CF_2Cl_2$ ,  $CF_3Cl$ , and  $CF_4$ ) in the VUV and soft X-ray regions," *Chemical Physics* (1997). Submitted.

## Chapter 2

### Theoretical Background

#### 2.1 Photoabsorption by Dipole ( $e,e$ ) Spectroscopy

The technique of dipole ( $e,e$ ) spectroscopy involves the inelastic scattering of high-energy electrons off gaseous target molecules at negligible momentum transfer such that dipole selection rules are obeyed. The excitation of a molecule AB in the ground state to an excited state AB\* induced by this process can be compared to that obtained by the absorption of a photon ( $h\nu$ ) in optical spectroscopy,



where  $E$  is the energy required to produce the molecule AB\* in its excited state and  $E_0$  is the impact energy of the excitation. The electron ( $e^-$ ) involved in the electron impact process has an initial ( $\mathbf{k}$ ) and a final ( $\mathbf{k}'$ ) momentum, and it is the momentum transfer ( $\mathbf{K} = \mathbf{k} - \mathbf{k}'$ ) for the electron impact process that determines the selection rules for the excitation. It will be shown in section 2.1.1 that under the conditions of negligibly small momentum transfer, dipole selection rules predominate, and the "energy-loss" ( $E$ ) of the inelastically scattered electron is equivalent to the resonant photon energy ( $h\nu$ ) in the optical process. Moreover, the transition probability of the electron impact process will be shown to be quantitatively related to that for the optical (photoabsorption) process. From equation (2.2) it can also be seen that the dipole scattering of one incident electron followed by the detection of one scattered electron reflects the term "dipole ( $e,e$ )

spectroscopy”.

The transition probability can be represented by a number of different (but related) quantities such as cross section, differential oscillator strength, molar absorption coefficient, et cetera. The Beer-Lambert law is usually used in optical experiments to determine the transition probability or photoabsorption cross section ( $\sigma_p$ ),

$$\ln \frac{I_0}{I} = \sigma_p n l. \quad (2.3)$$

In this relationship,  $I_0$  and  $I$  are the incident and transmitted light intensities, respectively,  $n$  is the target density, and  $l$  is the path length. The determination of absolute data using the Beer-Lambert law requires accurate measurements of the target density and path length which are often quite difficult, especially in the windowless VUV region and beyond. In contrast, the dipole ( $e,e$ ) method establishes the absolute cross section scale using a simple  $S(0)$  or  $S(-2)$  sum-rule normalization procedure without the need to determine the target density and path length (see section 2.1.2 for details).

In this thesis, the optical (photoabsorption) differential oscillator strength ( $df/dE$ ) will be used to describe the dipole transition probabilities, and this quantity is directly related to the photoabsorption cross section by a constant factor,

$$\sigma_p = \left( \frac{e^2 \pi \hbar}{mc} \right) \frac{df}{dE}. \quad (2.4)$$

The (total) dipole or optical oscillator strength ( $f$ ) for an excitation process is a dimensionless quantity defined [12] in atomic units as

$$f = 2E_n \left| \left\langle n \left| \sum_{j=1}^Z \mathbf{r}_j \right| 0 \right\rangle \right|^2, \quad (2.5)$$

where  $E_n$  is the energy required to excite the target species from the ground state

$|0\rangle$  to the excited state  $\langle n|$ ,  $Z$  is the number of electrons in the target, and  $\mathbf{r}_j$  are the electron coordinates.

In practice, measured oscillator strengths are differential (i.e.,  $df/dE$ ) in both the discrete and ionization continuum regions. In the case of discrete transitions, this is due to finite linewidth and spectrometer bandwidth, whereas in the ionization region, it is due to the continuous nature of the final states (i.e., the states  $n$  consist of an ion plus a photoelectron). Therefore, the oscillator strength ( $f$ ) for any discrete transition or continuum region is obtained by integration according to

$$f = \int_{E_1}^{E_2} \left( \frac{df}{dE} \right) dE \quad (2.6)$$

where  $E_1$  and  $E_2$  are the lower and upper bounds of the absorption band or continuum region. The differential oscillator strength is given by [12]

$$\frac{df}{dE} = \sum_n 2E_n \left| \left\langle n \left| \sum_{j=1}^Z \mathbf{r}_j \right| 0 \right\rangle \right|^2 \delta(E_n - E) \quad (2.7)$$

and has units of  $(\text{energy})^{-1}$ . The values of  $\sigma_p$  and  $df/dE$  are commonly expressed in units of megabarns ( $1 \text{ Mb} = 10^{-18} \text{ cm}^2$ ) and  $\text{eV}^{-1}$ , respectively, and are related in these units by

$$\sigma_p [\text{Mb}] = 109.75 \frac{df}{dE} [\text{eV}^{-1}]. \quad (2.8)$$

### 2.1.1 Bethe-Born theory

The Bethe-Born theory was first proposed by Bethe [11] to describe the inelastic scattering of fast electrons off matter using the first Born approximation, which states that for sufficiently fast collisions:

- (1) The incident and scattered electron waves are undistorted by the interaction with the target species and thus can be represented by plane waves, and

- (2) Excitation to the final state result from a direct transition from the initial state and does not involve any intermediate states. Therefore, energy and momentum are transferred directly from the incident electron to the target.

Within the first Born approximation, Bethe defined the transition probability for the electron impact induced excitation process from the ground state to the  $n^{\text{th}}$  excited state as the generalized oscillator strength (GOS) [12]

$$f_{0n}(\mathbf{K}, E) = \frac{2E_n}{|\mathbf{K}|^2} |\epsilon_{0n}(\mathbf{K})|^2 \quad (2.9)$$

(given in atomic units), where  $\epsilon_{0n}(\mathbf{K})$  is the matrix element,

$$\epsilon_{0n}(\mathbf{K}) = \left\langle n \left| \sum_{j=1}^Z \exp(i\mathbf{K} \cdot \mathbf{r}_j) \right| 0 \right\rangle. \quad (2.10)$$

The generalized oscillator strength is a dimensionless quantity defined for discrete excitations, but for ionization processes in the continuum, the (differential) GOS becomes a continuous function of energy,

$$\frac{df_{0n}(\mathbf{K}, E)}{dE} = \sum_n \frac{2E_n}{|\mathbf{K}|^2} |\epsilon_{0n}(\mathbf{K})|^2 \delta(E_n - E). \quad (2.11)$$

In an electron impact experiment, where the incident electrons are scattered inelastically into a cone of solid acceptance angle ( $d\Omega$ ), the electron scattering differential cross section is given by [12]

$$\frac{d^2\sigma_e(\mathbf{K}, E)}{dEd\Omega} = \sum_n \frac{4 |\mathbf{k}'|}{|\mathbf{k}| |\mathbf{K}|^4} |\epsilon_{0n}(\mathbf{K})|^2 \delta(E_n - E). \quad (2.12)$$

Comparing equations (2.11) and (2.12), it can be seen that the electron scattering differential cross section is quantitatively related to the differential GOS by

$$\frac{d^2\sigma_e(\mathbf{K}, E)}{dEd\Omega} = \left( \frac{2 |\mathbf{k}'|}{|\mathbf{k}| |\mathbf{K}|^2 E_n} \right) \frac{df_{0n}(\mathbf{K}, E)}{dE}. \quad (2.13)$$

The differential GOS can in turn be related to the optical (photoabsorption) differential oscillator strength ( $df/dE$ ) as follows. The exponential term in the transition probability matrix element can be expanded in a Taylor series,

$$\exp(i\mathbf{K} \cdot \mathbf{r}_j) = 1 + i\mathbf{K} \cdot \mathbf{r}_j + \left(\frac{i\mathbf{K} \cdot \mathbf{r}_j}{2!}\right)^2 + \left(\frac{i\mathbf{K} \cdot \mathbf{r}_j}{3!}\right)^3 + \dots \quad (2.14)$$

From the orthogonality requirement,  $\langle n|0\rangle = 0$ , equation (2.10) becomes

$$\varepsilon_{0n}(\mathbf{K}) = 0 + \alpha_1(i\mathbf{K}) + \alpha_2(i\mathbf{K})^2 + \alpha_3(i\mathbf{K})^3 + \dots \quad (2.15)$$

where  $\alpha_x$  is the  $x^{\text{th}}$  order multipole matrix element,

$$\alpha_x = \frac{1}{x!} \left\langle n \left| \sum_j \mathbf{r}_j^x \right| 0 \right\rangle. \quad (2.16)$$

Therefore, the differential generalized oscillator strength can be written as a power series of momentum transfer by substitution of equation (2.15) into equation (2.11):

$$\begin{aligned} \frac{df_{0n}(\mathbf{K}, E)}{dE} &= \sum_n 2E_n \left[ \alpha_1^2 + (\alpha_2^2 - 2\alpha_1\alpha_3)\mathbf{K}^2 + (\alpha_3^2 + 2\alpha_1\alpha_5 - 2\alpha_2\alpha_4)\mathbf{K}^4 + \dots \right] \delta(E_n - E) \\ &= \frac{df_{0n}^0(E)}{dE} + \frac{df_{0n}^1(\mathbf{K}, E)}{dE} \mathbf{K}^2 + \frac{df_{0n}^2(\mathbf{K}, E)}{dE} \mathbf{K}^4 + \dots \end{aligned} \quad (2.17)$$

The first term of the differential GOS,  $df_{0n}^0(E)/dE$ , is the dipole (or photoabsorption) differential oscillator strength<sup>1</sup> as defined earlier by equation (2.7), and the higher terms,  $df_{0n}^x(\mathbf{K}, E)/dE$ , represent the  $x^{\text{th}}$  order multipole (e.g., quadrupole, octapole, etc.) differential oscillator strengths. Clearly, at the limit of zero momentum transfer (i.e.,  $\mathbf{K}^2 \rightarrow 0$ ), the differential GOS becomes equivalent to the optical value,

---

<sup>1</sup> Note that for simplicity, the indexes in the dipole differential oscillator strength ( $df_{0n}^0(E)/dE$ ) will be dropped after section 2.1.1 and will simply be written as  $df/dE$ .

$$\lim_{\mathbf{K}^2 \rightarrow 0} \frac{df_{0n}(\mathbf{K}, E)}{dE} = \frac{df_{0n}^0(E)}{dE}, \quad (2.18)$$

and the electron scattering differential cross section in equation (2.13) is therefore related to  $df_{0n}^0(E)/dE$  by

$$\lim_{\mathbf{K}^2 \rightarrow 0} \frac{d^2\sigma_e(\mathbf{K}, E)}{dEd\Omega} = \left( \frac{2|\mathbf{k}'|}{|\mathbf{k}||\mathbf{K}|^2 E_n} \right) \frac{df_{0n}^0(E)}{dE} \quad (2.19)$$

or

$$\frac{df_{0n}^0(E)}{dE} = \left( \frac{|\mathbf{k}||\mathbf{K}|^2 E_n}{2|\mathbf{k}'|} \right) \frac{d^2\sigma_e(\mathbf{K}, E)}{dEd\Omega}. \quad (2.20)$$

In practice,  $d^2\sigma_e(\mathbf{K}, E)/dEd\Omega$  is integrated over the acceptance angles ( $\Omega$ ) of the spectrometer, and this gives a simplified form of equation (2.20):

$$\frac{df_{0n}^0(E)}{dE} = B(E) \frac{d\sigma_e(E)}{dE} \quad (2.21)$$

where  $B(E)$  is the Bethe-Born factor, which is proportional to  $E^3$  in the hypothetical case of zero angular resolution. Since the Bethe-Born factor is a function of the experimental scattering geometry and the energy loss ( $E_n$ ) of the scattered electron, it can be determined for any particular electron impact spectrometer from the scattering geometry [15,16] or by scaling to a known continuum differential oscillator strength spectrum [5,14], and subsequently be used to convert the measured electron scattering differential cross sections for any target species to optical (photoabsorption) differential oscillator strengths.

The conditions required for a negligibly small momentum transfer such that the limit  $\mathbf{K}^2 \rightarrow 0$  is experimentally achieved can be seen by considering the conservation of momentum,

$$|\mathbf{K}|^2 = |\mathbf{k} - \mathbf{k}'|^2 = |\mathbf{k}|^2 + |\mathbf{k}'|^2 - 2|\mathbf{k}||\mathbf{k}'|\cos\theta, \quad (2.22)$$

where  $\theta$  is the polar scattering angle, and the conservation of energy,

$$E_0 = \frac{1}{2}|\mathbf{k}|^2 \quad (2.23)$$

and

$$E_n = \frac{1}{2}(|\mathbf{k}|^2 - |\mathbf{k}'|^2), \quad (2.24)$$

for the electron impact event where  $\mathbf{k}$  and  $\mathbf{k}'$  are the initial and final momenta of the incident electron. Substituting equations (2.23) and (2.24) into equation (2.22) gives

$$\begin{aligned} |\mathbf{K}|^2 &= 2E_0 + (2E_0 - 2E_n) - 2\sqrt{2E_0}\sqrt{2E_0 - 2E_n}(\cos\theta) \\ &= 2E_0 \left[ 2 - \frac{E_n}{E_0} - 2\sqrt{1 - \frac{E_n}{E_0}}(\cos\theta) \right]. \end{aligned} \quad (2.25)$$

Hence, for the optical limit  $\mathbf{K}^2 \rightarrow 0$  to be approached,

- (1) The incident electron energy ( $E_0$ ) must be much higher in energy than the energy-loss ( $E_n$ ) of the scattered electron, i.e.,  $E_0 \gg E_n$ , and
- (2) The scattering angle ( $\theta$ ) must be  $\sim 0^\circ$ .

### 2.1.2 Sum rules

Integral sums of photoabsorption differential oscillator strength distributions ( $df/dE$ ) can be related to important physical properties of the target species in the ground state. These “sum rules” are defined by [37,38]

$$S(u) = \int_{E'}^{\infty} \left( \frac{E}{E_H} \right)^u \left( \frac{df}{dE} \right) dE, \quad (2.26)$$

where  $E'$  is the electronic excitation threshold and  $E_H$  is the Hartree energy constant (27.217 eV). Different values of the exponent,  $u$ , correspond to different

molecular properties. Of particular interest to the present work are the  $S(0)$  and  $S(-2)$  sums.

The  $S(0)$  or Thomas-Reiche-Kuhn (TRK) sum rule,

$$S(0) = Z_T = \int_{E'}^{\infty} \left( \frac{df}{dE} \right) dE, \quad (2.27)$$

is equal to the total number of electrons ( $Z_T$ ) in the target atom or molecule and can be used to normalize relative photoabsorption differential oscillator strength measurements onto an absolute scale. However, this procedure is not always experimentally feasible because use of the  $S(0)$  sum rule requires a complete knowledge of the differential oscillator strength distribution from the first excitation threshold up to infinite energy, encompassing the valence-shell and all the inner-shell regions. In practice, a valence-shell modification of the  $S(0)$  sum rule is used, such that the resulting  $S_{val}(0)$  sum is equal to the total number of valence-shell electrons ( $Z_{val}$ ) plus a small correction ( $Z_p$ ) for Pauli-excluded transitions from the inner-shells to the occupied valence-shell orbitals [27]:

$$S_{val}(0) = Z_{val} + Z_p = \int_{E'}^{\infty} \left( \frac{df}{dE} \right) dE. \quad (2.28)$$

This relationship is also known as the valence-shell Thomas-Reiche-Kuhn (VTRK) sum rule. Equation (2.28) can be applied by combining relative valence-shell  $df/dE$  measurements obtained up to high energy (~200 eV) with an accurate estimate of the valence-shell differential oscillator strength from 200 eV to infinite energy via a curve-fitting and extrapolation procedure outlined in section 3.1.1.

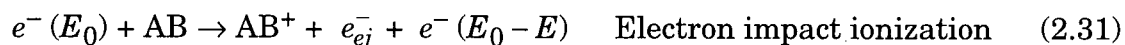
The  $S(-2)$  sum is equivalent to the static electric-dipole polarizability ( $\alpha_N$ ) of the target species,

$$S(-2) = \alpha_N = \int_{E'}^{\infty} \left( \frac{E}{E_H} \right)^{-2} \left( \frac{df}{dE} \right) dE, \quad (2.29)$$

and can also be used to normalize relative spectral intensities to absolute differential oscillator strengths if the electric-dipole polarizability of the target atom or molecule is known [28]. The  $S(-2)$  sum (equation (2.29)) differs from the  $S_{val}(0)$  sum rule in that the former is weighted heavily in the low energy region ( $< 100$  eV) due to the  $E^{-2}$  term, whereas the latter is uniformly weighted over all energies. In this regard, application of the  $S(-2)$  sum rule does not necessarily require differential oscillator strength data to be available up to infinite energy, since anything above  $\sim 100$  eV would not make a significant contribution to the  $S(-2)$  sum. Therefore, the  $S(-2)$  sum rule provides a good normalization alternative to the  $S_{val}(0)$  sum rule, especially when the latter technique cannot be employed because of complications in the photoabsorption spectrum from low energy inner-shell thresholds, Cooper minima, and shape resonances. In cases where the absolute differential oscillator strength scale has been established using the VTRK sum rule, equation (2.29) can additionally be used to critically evaluate the accuracy of the absolute data. Moreover, the  $S(-2)$  sum rule can provide an experimental value for the static electric-dipole polarizability of a given target species in the absence of such data in the literature.

## 2.2 Photoionization by Dipole ( $e, e+\text{ion}$ ) Coincidence Spectroscopy

The dipole ionization of a molecule AB to form an ion  $AB^+$  can be studied both by photons ( $h\nu$ ) and by high-energy electrons ( $e^-$ ):



where  $e_{ej}^-$  is the ejected photoelectron and  $(E)$  is the energy loss of the scattered electron, which is equivalent to the photon energy ( $h\nu$ ) in the photoionization process. In both situations, the energy  $E$  is transferred to form  $AB^+$  and  $e_{ej}^-$ . The transition probability or partial photoionization differential oscillator strength (PPOS) for the production of the molecular ( $AB^+$ ) and dissociative ( $A^+$ ,  $B^+$ ) ion fragments can be obtained by photoionization mass spectrometry (PIMS) or by the complementary technique of dipole ( $e, e+ion$ ) coincidence spectroscopy. Similar to dipole ( $e, e$ ) spectroscopy, under the condition of negligibly small momentum transfer, ionization processes induced by the latter method would be governed by dipole selection rules, and the energy-loss ( $E$ ) would be analogous to the photon energy ( $h\nu$ ). From equation (2.31) it can be seen that the term “dipole ( $e, e+ion$ ) coincidence spectroscopy” describes the dipole scattering of one incident electron, followed by the coincident detection of one scattered electron and the associated ion.

The total photoabsorption differential oscillator strength,  $(df/dE)_T^{abs}$ , discussed earlier in section 2.1, can be represented at each energy by the sum of the differential oscillator strengths for all neutral species,  $(df/dE)_T^{neu}$ , and ions,  $(df/dE)_T^{ion}$ :

$$\left(\frac{df}{dE}\right)_T^{abs} = \left(\frac{df}{dE}\right)_T^{neu} + \left(\frac{df}{dE}\right)_T^{ion} \quad (2.32)$$

The energy-dependent photoionization efficiency ( $\eta_i$ ) is defined to be the ratio of the total number of ionization events to the total number of photons absorbed,

$$\eta_i = \frac{\text{Total number of ionization events}}{\text{Total number of photons absorbed}} \quad (2.33)$$

and gives a measure of the degree of ionization per photon absorbed as a function of

energy. It is related to the total photoabsorption and photoionization differential oscillator strengths by

$$\left(\frac{df}{dE}\right)_T^{ion} = \eta_i \left(\frac{df}{dE}\right)_T^{abs}. \quad (2.34)$$

The total photoionization differential oscillator strength can be partitioned into PPOS of molecular and dissociative ion fragments,  $(df/dE)_F^{ion}$ ,

$$\left(\frac{df}{dE}\right)_T^{ion} = \sum_F \left(\frac{df}{dE}\right)_F^{ion} \quad (2.35)$$

or into PPOS of electronic ion states,  $(df/dE)_S^{ion}$ ,

$$\left(\frac{df}{dE}\right)_T^{ion} = \sum_S \left(\frac{df}{dE}\right)_S^{ion}. \quad (2.36)$$

The PPOS of ion fragments and electronic ion states are generally obtained from photoionization mass spectrometry and from tunable energy photoelectron spectroscopy, respectively, as a function of photon energy. Photoion branching ratios ( $BR_F$ ) for the various ionic species ( $F$ ) can be determined from the integrals ( $N_F$ ) under the appropriate ion peaks in the mass spectra and represent the fraction of the total number of ions formed:

$$BR_F = \frac{N_F}{\sum_F N_F}. \quad (2.37)$$

The PPOS for the production of molecular and dissociative ions are then given by the triple product of the photoion branching ratio, photoionization efficiency, and total photoabsorption differential oscillator strength, as a function of photon energy,

$$\left(\frac{df}{dE}\right)_F^{ion} = BR_F \eta_i \left(\frac{df}{dE}\right)_T^{abs} = BR_F \left(\frac{df}{dE}\right)_T^{ion}. \quad (2.38)$$

Similarly, electronic ion state branching ratios for the various ion states,  $S$ , can be determined from the integrals ( $N_S$ ) under the appropriate electronic state peaks in the photoelectron spectra and represent the fraction of the total number of electronic states formed:

$$BR_S = \frac{N_S}{\sum_S N_S}. \quad (2.39)$$

At each photon energy, multiplication of the electronic state branching ratio with the photoionization efficiency and total photoabsorption differential oscillator strength gives the PPOS for the production of that electronic state,

$$\left(\frac{df}{dE}\right)_S^{ion} = BR_S \eta_i \left(\frac{df}{dE}\right)_T^{abs} = BR_S \left(\frac{df}{dE}\right)_T^{ion}. \quad (2.40)$$

Since the total photoionization differential oscillator strength can be represented as sums of ion fragments or sums of electronic ion states, detailed quantitative information on the dipole-induced breakdown pathways for a molecule can be obtained. Above the upper energy limit of the Franck-Condon region for production of a given electronic ion state, fragmentation ratios for dissociative photoionization from that electronic ion state should be constant, except in local regions where autoionization effects are significant or where multiple photoionization is appreciable [39]. Therefore, the PPOS for a given ion may be expressed as a linear combination of electronic ion state PPOS and vice versa.

## 2.3 Photoabsorption and Photoionization Processes

In the molecular orbital (MO) model, molecular orbitals are formed by linear combination of atomic orbitals (LCAO). In a given molecule, the molecular orbitals

consist of (1) occupied valence-shell and inner-shell (bonding and non-bonding) orbitals, and (2) unoccupied virtual valence (anti-bonding) and Rydberg (largely non-bonding) orbitals. The two types of occupied orbitals differ in that the valence-shell orbitals are generally delocalized over the molecule and thus are mainly responsible for all molecular properties including bonding, while inner-shell orbitals (which have higher binding energies) are largely localized near the corresponding atomic centers and therefore have a dominant atomic character. Given sufficient energy, electrons from any of the occupied orbitals can be excited to various virtual valence and Rydberg orbitals, or be directly ionized into the continuum. Other processes that result in the formation of an ion include autoionization, Auger processes, and resonant Auger processes. These non-radiative processes are shown schematically in figure 2.1. Such electronic transitions are manifested by the many different features observed in the photoabsorption spectrum. Some of the features which are relevant to the present work will be reviewed in section 2.3.1. In addition, various decay processes associated with the dissipation of energy from a high-energy hole state formed from the excitation or ionization of an electron from an occupied orbital will be discussed in section 2.3.2.

### **2.3.1 Spectral features**

In the discrete portion of the photoabsorption spectrum, the observed absorption bands typically arise from a combination of Rydberg and virtual valence transitions. Additional spectral features such as window resonances, shape resonances, and Cooper minima can also appear in the ionization continuum. Rydberg orbitals are large, diffuse, atomic-like orbitals which are located well beyond the occupied valence orbitals of ground state molecules. Within this model, a Rydberg transition from the ground state corresponding to an excitation energy  $E$

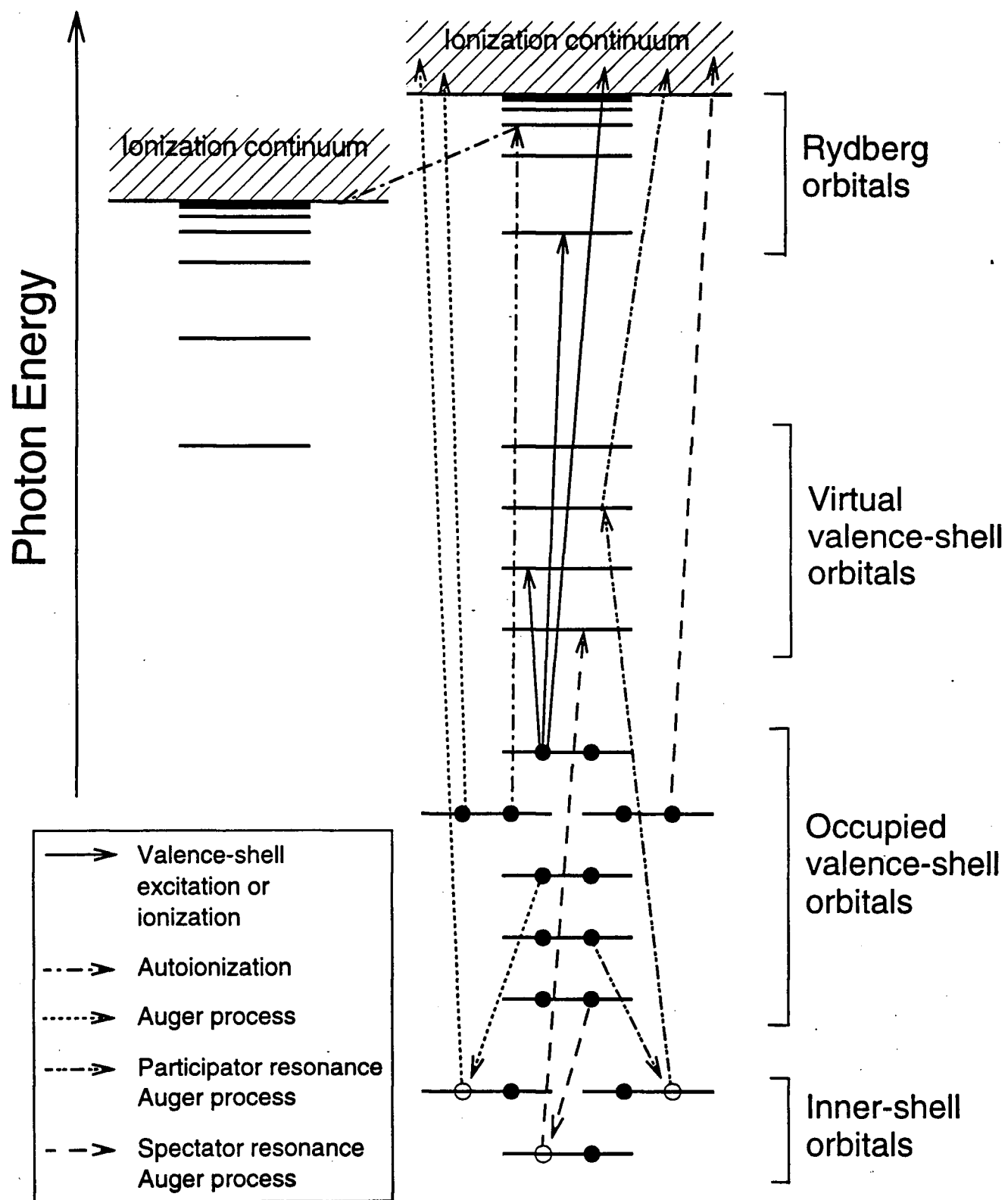


**Figure 2.1:** Schematic of various photoabsorption and photoionization processes.

is characterized by an angular momentum ( $l$ ) dependent quantum defect ( $\delta_l$ ) and a term value ( $T$ ),

$$T = E_{\text{VIP}} - E = \frac{E_{\text{R}}}{(n - \delta_l)^2}, \quad (2.41)$$

where  $n$  is the principal quantum number of the final orbital,  $E_{\text{VIP}}$  is the vertical ionization potential to which the Rydberg series converges as  $n$  approaches infinity, and  $E_{\text{R}}$  is the Rydberg energy constant (13.606 eV). The close similarity of equation (2.41) to the Rydberg formula for the hydrogen atom, where  $\delta_l$  is zero, is due to the fact that Rydberg transitions are characteristic of a one-electron system in which the excited electron is located so far away from the positively charged molecular core that it "sees" the core as a point charge (+1). Therefore, Rydberg term values are independent of the originating molecular orbital and thus can be transferred between different transitions to the same final orbital. In multi-electron systems, the quantum defect reflects the penetrability of the final orbital and takes on different values depending on the subshell of the Rydberg orbital. When the excited electron is situated far away from the molecular core (e.g., the  $3d$  orbital of  $\text{CF}_4$ ), there is no penetration of the core, so  $\delta_d$  is zero. In contrast, an electron in the  $3s$  orbital of  $\text{CF}_4$  can penetrate the core and become more tightly bound; in this case the quantum defect ( $\delta_s$ ) is approximately one. According to Robin [40], the quantum defects for first and second row atoms take on values in the ranges of 0.8–1.3, 0.5–0.9, and 0–0.3 for the  $ns$ ,  $np$ , and  $nd$  Rydberg series, respectively. For molecules containing third or higher row atoms, the  $\delta_l$  values increase by a integral number with respect to the principal quantum number of the lowest unoccupied  $s$ ,  $p$ , or  $d$  type orbitals of second row atoms (i.e.,  $3s$ ,  $3p$ , and  $3d$ ). For example, in the case of  $\text{PF}_3$ , which has lowest unoccupied Rydberg orbitals of  $4s$ ,  $4p$ , and  $3d$ , the quantum defects fall within the ranges of 1.8–2.3 ( $\delta_s$ ), 1.5–1.9 ( $\delta_p$ ), and 0–0.3 ( $\delta_d$ ).

Rydberg profiles are generally characterized by sharp peaks in the discrete region of the photoabsorption spectrum. Beyond the first ionization potential, they may be lifetime broadened by autoionization, resulting in either broad bands superimposed on the continuum (constructive interference) or in window resonances (destructive interference). In the latter case, the Rydberg profiles appear as dips in the continuum (e.g., see the  $\text{NO}_2$  valence-shell spectrum in chapter 6). Absorption bands should ideally be assigned based on oscillator strength and excitation energy *ab initio* calculations. However, in practice such calculations may not exist or are inaccurate due to difficulties in modeling the excited state wavefunction. In these circumstances, equation (2.41) can sometimes be used as an empirical alternative in assigning observed Rydberg spectral profiles.

In contrast to Rydberg orbitals, virtual valence orbitals are localized and are of similar size to the occupied valence orbitals. Consequently, term values for transitions to virtual valence states are not transferable from one ionization manifold to another, since the excited electron now "sees" the details of the remaining localized valence-shell electronic structure instead of a point charge. Transitions to virtual valence orbitals can be identified by their term values, which are often larger than those of the lowest Rydberg transitions, as well as the generally broad nature of these profiles in the photoabsorption spectrum.

In addition to Rydberg and virtual valence transitions, sometimes the close proximity of the lowest Rydberg orbital to a localized virtual valence orbital can cause Rydberg-valence mixing to occur. This results in a higher term value than predicted by equation (2.41) for the corresponding Rydberg transition, and therefore, it can no longer be transferred from one ionization manifold to another. For example, Rydberg-valence mixing is observed in the phosphorus  $2p$  inner-shell spectrum of  $\text{PF}_3$  (chapter 5) where the broad  $9a_1$  absorption band is situated beneath the sharp  $4s$  Rydberg band. Consequently, the  $4s \leftarrow 2p_{3/2}^{-1}$  transition has a

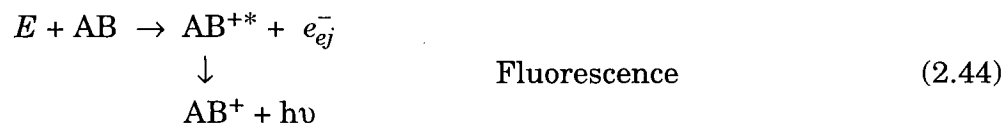
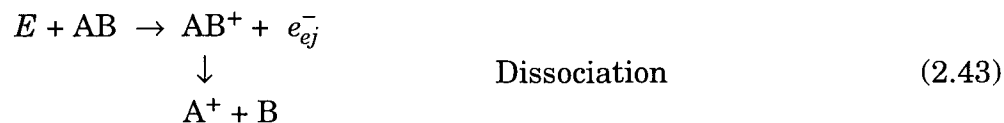
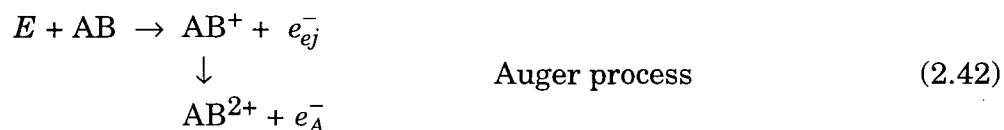
term value of 3.17 eV, which is higher than that of 2.75 eV for the  $4s \leftarrow 8a_1^{-1}$  transition in the  $\text{PF}_3$  valence-shell spectrum.

Although transitions to virtual valence orbitals usually arise at lower energy than the corresponding Rydberg transitions from the same initial molecular orbital, sometimes intense virtual valence type transitions (shape resonances) can also be observed to higher lying neutral states above the ionization threshold in the inner-shell region (e.g., see  $\text{PF}_3$  and  $\text{PF}_5$  in chapter 5). On the basis of multiple scattering calculations, Dehmer and Dill [41,42] rationalized that this redistribution in oscillator strength intensity from the weak Rydberg pre-edge bands to the strong post-edge shape resonances can be attributed to the interaction of the excited electron with the anisotropy of the molecular field, causing it to be trapped temporarily behind the centrifugal barrier until it has sufficient kinetic energy to tunnel out by reaching an outgoing channel (dominated by high angular momentum partial waves), which penetrates the barrier. Such rapid penetration of the centrifugal barrier results in a resonant enhancement of selected outgoing electron partial wave channels. For example, recent continuum MS-X $\alpha$  calculations [43] predicted the two strong shape resonances observed in the phosphorus  $2p$  ionization continuum of  $\text{PF}_3$  at 146 and 159 eV arise, respectively, from the  $a_1$  channel associated with the  $p$ -wave ( $l = 1$ ) of the fluorine ligands, and from both the  $a_1$  and  $e$  channels of the atomic-like phosphorus  $3d$  orbitals ( $l = 2$ ).

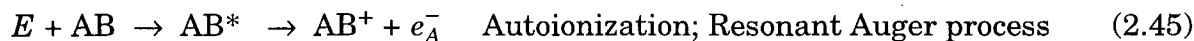
Another spectral feature commonly present in the ionization continua of molecules containing atoms that have subshells with radial nodes (e.g.,  $\text{PCl}_3$ ) are Cooper minima (i.e., local minima in the differential oscillator strength curve). This phenomenon arises from the zero net overlap in the dipole matrix element of the initial and final state wavefunctions in the vicinity of the radial node. In the case of  $\text{PCl}_3$ , one radial node is present in the chlorine  $3p$  wavefunction, and as such a Cooper minimum is observed in the valence-shell photoabsorption spectrum.

### 2.3.2 Decay processes

High energy hole states created by photoexcitation and photoionization of an electron from a valence-shell or inner-shell orbital at an energy  $E$  can undergo a number of competing decay processes in order to dissipate the excess energy. An ion ( $AB^+$ ) produced from the initial photoionization of a molecule ( $AB$ ) in the ground state can decay by Auger processes, dissociation, or fluorescence:



where  $e_{ej}^-$  is the ejected photoelectron and  $e_A^-$  is the Auger electron. In the fluorescence process,  $AB^{+*}$  denotes the  $AB^+$  ion in an excited ion state. Similarly, a molecule in an excited state ( $AB^*$ ) can decay by autoionization, resonant Auger processes (a special case of autoionization), predissociation, or fluorescence:



Auger emission (dotted arrows in figure 2.1) is a two-step process involving three electrons that result in the formation of a doubly-charged cation. In the first step, an electron ( $e_{ej}^-$ ) from a valence-shell or inner-shell orbital is ionized to form a hole state (represented by an open circle in figure 2.1). This is followed by the

simultaneous relaxation of a less tightly bound electron to fill the hole and ionization of a third electron ( $e_A^-$ ) from the energy released in the relaxation of the second electron. An Auger process is denoted by three letters corresponding to the type of subshell from which the electrons originate in the initial ionization, relaxation, and final ionization pathways. For example, a KLL Auger process involves ionization of a K-shell electron, followed by relaxation and ionization of two L-shell electrons. In contrast, a VVV Auger process begins with the ionization of an inner-valence electron, followed by the subsequent relaxation and ionization of two outer-valence electrons.

A resonant Auger process is similar to the Auger process described above except that the initial formation of a hole state results from excitation rather than ionization of an electron. Figure 2.1 shows two types of resonance Auger processes. A participator resonance Auger emission (dash-dot-dot arrows) occurs when the electron from the initial excitation becomes ionized in the second step. Alternatively, if a different electron is ionized, the process is termed a spectator resonance Auger emission (dashed arrows), since the excited electron from the first step acts as a spectator in the second step. As indicated by equation (2.45), a resonance Auger process produces a singly-charged cation. In fact, resonant Auger is a special case of autoionization (dash-dot arrows in figure 2.1) in which an excited state of a more tightly bound electron is first formed above a lower ionization continuum. The excited state then decays into the lower ion state continuum, thereby forming a singly-charged ion.

Alternatively, hole states can decay by direct dissociation or by predissociation. This involves the transfer of excess energy to bond breaking and to the kinetic energies of the resulting fragments. Finally, fluorescence can also release excess energy via the emission of a radiative photon (in contrast to Auger emission, resonant Auger emission, and autoionization which are all non-radiative processes).

## Chapter 3

### Experimental Methods

The measurements reported in this thesis have been obtained using two high energy electron impact spectrometers, operating at a mean scattering angle of zero degrees, so that negligible momentum transfer conditions exist. The low resolution spectrometer [15,16,39,44,45] utilizes an 8000 eV incident electron beam and has a resolution of 1 eV fwhm. It can operate in two different modes: Measurements obtained in the dipole ( $e,e$ ) mode are used for photoabsorption studies, while those obtained in the dipole ( $e,e+\text{ion}$ ) coincidence mode are used for photoionization studies. In addition, a high resolution dipole ( $e,e$ ) spectrometer [5,46] operating at 3000 eV incident electron energy has been employed to determine absolute oscillator strengths in the discrete excitation region in both the valence-shell (0.05 eV fwhm) and selected inner-shell (0.1 eV fwhm) regions of the photoabsorption spectra presented in chapters 4–8. Since details of the construction and operation of these two spectrometers have been fully described in refs. [5,14–16,39,44–46], only brief accounts of the instruments will be presented in this chapter. The experimental procedures used in the determination of absolute photoabsorption and partial photoionization differential oscillator strengths from electron energy-loss (EEL) and time-of-flight (TOF) measurements obtained directly from the two spectrometers will also be outlined in the corresponding sections below.

### 3.1 The Low Resolution Spectrometer

The low resolution, high energy electron impact spectrometer (1 eV fwhm) [15,16,39,44,45] is shown in figure 3.1. The various electrostatic deflectors used to

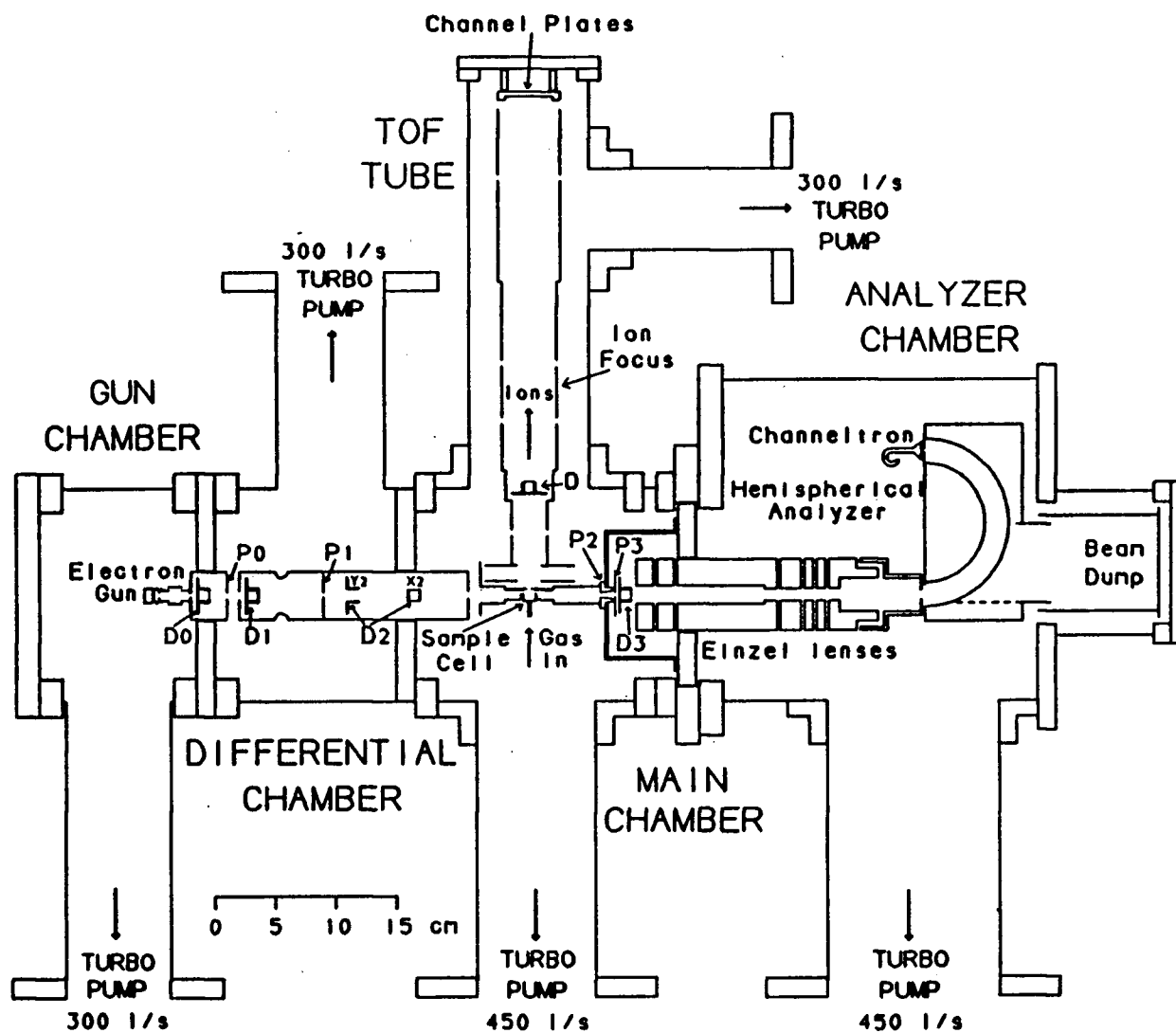


**Figure 3.1:** Schematic of the low resolution dipole ( $e,e$ ) and dipole ( $e,e+\text{ion}$ ) coincidence spectrometer

guide the electron beam are labeled by D0 to D3, while the apertures through which the electron beam passes are represented by P0 to P3. Note that the TOF tube is actually positioned at  $90^\circ$  to the focal plane of the electron analyzer (i.e., pointing outwards from the face of the page). This spectrometer can be used to study the photoabsorption or photoionization of a given target species by operating in either the dipole ( $e,e$ ) or dipole ( $e,e+\text{ion}$ ) coincidence mode. In the dipole ( $e,e$ ) mode (see section 3.1.1), electron energy-loss spectroscopy is used to obtain long range absolute photoabsorption spectra from the first excitation threshold up to several hundred electron volts, while the dipole ( $e,e+\text{ion}$ ) coincidence mode (section 3.1.2) employs time-of-flight mass spectroscopy to determine absolute partial differential oscillator strengths for molecular and dissociative photoionization.

### 3.1.1 The dipole ( $e,e$ ) mode

In the dipole ( $e,e$ ) mode [15,16,39,44,45], an electron energy-loss spectrum is measured as follows. A narrow beam of electrons is produced by a barium oxide cathode in a black and white television tube gun (Phillips 6AW59), which is floated at a potential of  $-4000$  V. The electron beam is accelerated to  $8000$  eV and electrostatically deflected into the collision chamber (floated at  $+4000$  V) where it scatters off the gaseous target sample. Only those electrons scattered in the forward direction within a small cone of  $1.4 \times 10^{-4}$  steradians subtended about a zero degree scattering angle are allowed to pass through an angular selection aperture (P3 in figure 3.1). In the electron scattering process, each of these scattered electrons loses a small amount of energy ( $E$  in equation (2.2)) in the collision with the target, and it is this "energy loss" that is transferred to the target to produce a dipole-allowed electronic excitation. After entering the forward scattering angular selection aperture, the (scattered and main beam) electrons are refocussed, selected for a

particular energy loss ( $E$ ), and decelerated to  $(50+E)$  eV before entering the hemispherical analyzer (floated at  $-3950$  V). In the deceleration step, the 50 eV energy represents the analyzer pass energy. The electrons then pass through the analyzer and are detected in the saturated pulse counting mode by a channeltron electron multiplier (Mullard B419AL). The resulting electron signal (i.e., relative electron scattering differential cross section) is processed by an IBM compatible computer (Intel 80286) using data acquisition software written by Dr. G. Cooper of this laboratory. The computer also serves to control the energy loss to be selected by the decelerating lens and the analyzer/detection system in a tunable fashion during the data acquisition process in order for an EEL spectrum to be obtained, as a function of energy loss. Note that most of the remaining electrons that were not selected to pass through the analyzer are collected at the beam dump at the back of the analyzer. The spectrometer is also designed with mumetal shields and Helmholtz coils to shield the electron trajectories from external magnetic fields.

As a first step in obtaining a long range, absolute photoabsorption spectrum, electron energy-loss spectra are measured in several overlapping energy loss regions (e.g., 4.5–40, 30–80, 60–134, 120–155, 145–195, 185–220, 210–280, and 260–350 eV in the case of  $\text{PCl}_3$ ). This procedure is necessary because the electron scattering differential cross section decreases very rapidly with increasing energy loss (in the order of  $E^{-3}$ ). Therefore, in order to maintain good signal-to-noise ratios at increasing energy loss, the electron current is increased with each higher energy region measured. For each EEL spectrum measured at full pressure ( $\sim 8$   $\mu\text{Torr}$ ), a background EEL spectrum is obtained immediately afterwards at one-quarter the pressure ( $\sim 2$   $\mu\text{Torr}$ ) which is then subtracted from the full pressure spectrum. This background-subtraction procedure serves to remove any contributions from non-spectral electrons and background residual gases in the spectrometer. The resulting background subtracted EEL spectra are normalized to one another to form a long

range spectrum (e.g., 4.5–350 eV in the example of  $\text{PCl}_3$  above), which is subsequently converted to a relative photoabsorption differential oscillator strength spectrum using the known Bethe-Born factor for the spectrometer [15,16] according to equation (2.21). As a result of this transformation, the energy loss becomes equivalent to the photon energy. Finally, the relative photoabsorption spectrum is normalized onto an absolute differential oscillator strength scale using the valence-shell Thomas-Reiche-Kuhn (VTRK) or  $S_{val}(0)$  sum rule given by equation (2.28). In the present work, the  $S(-2)$  sum rule has not been used for absolute scale determination. Instead, the  $S(-2)$  sum rule has been employed to critically evaluate the absolute data obtained via the VTRK sum rule by comparing the resulting static electric-dipole polarizability ( $\alpha_N$ ) with published values. In the case of  $\text{PF}_3$ , no experimental  $\alpha_N$  data are available in the literature; therefore, differential oscillator strength measurements obtained in the present work have been used to provide the first such value.

The use of the VTRK sum rule with the dipole ( $e,e$ ) method provides a simpler and often more accurate alternative to the direct optical method involving the Beer-Lambert law for obtaining absolute photoabsorption cross sections (oscillator strengths), since neither path length or particle density determinations are required. In the VTRK sum rule normalization procedure, the contribution of the target molecule to the valence-shell photoabsorption above the upper limit of the measured valence-shell spectrum is estimated by fitting a polynomial of the form

$$\frac{df}{dE} = AE^{-2} + BE^{-3} + CE^{-4} \quad (3.1)$$

to the high energy, smooth continuum region of the relative photoabsorption data and extrapolating to infinite energy. The relative valence-shell photoabsorption spectrum is then integrated from the first excitation threshold to infinite energy, and the total area is set to an oscillator strength value corresponding to the number

of valence electrons ( $Z_{val}$ ) in the target molecule, plus a small estimated contribution ( $Z_p$ ) for Pauli excluded transitions from the inner-shells to the occupied valence-shell orbitals [47,48].

The total valence-shell oscillator strength estimates ( $Z_{val} + Z_p$ ) used in the present work (see equation (2.28)) have been obtained using atomic calculations of oscillator strength contributions for excitations from each of the individual shells of atoms [48]. These calculations have been used to estimate the valence-shell oscillator strengths for different molecules as follows. For one-center hydrides such as  $\text{CH}_4$ , the valence-shell contribution is modeled using that for an atom with which the molecule is isoelectronic. For example, since  $\text{CH}_4$  is isoelectronic with neon, the valence-shell oscillator strength estimate for  $\text{CH}_4$  (8.33) is determined by summing the oscillator strength calculations for the  $np \leftarrow 2s$ ,  $nd \leftarrow 2p$ , and  $ns \leftarrow 2p$  excitations of neon [48]. For molecules with more than one central heavy atom such as *n*-pentane, the normalization factor for the  $S_{val}(0)$  sum rule is determined by first breaking the molecule down into components that can be represented by isoelectronic atoms, followed by summing the corresponding atomic valence-shell oscillator strength contributions. In the present work, the valence-shell oscillator strength estimates ( $Z_{val} + Z_p$ ) used to establish the absolute oscillator strength scales for the photoabsorption spectra reported in chapters 4–8 via the VTRK sum rule are listed in table 3.1.

The low resolution photoabsorption data obtained in the present work have been energy calibrated by adjusting the electron analyzer pass energy in the spectrometer such that the positions of the observed spectral profiles match those obtained in the high resolution spectrum (see section 3.2 below) after it has been convoluted with a 1 eV fwhm gaussian function (in order to mathematically degrade the resolution of the high resolution spectrum to the 1 eV fwhm of the low resolution spectrum).

**Table 3.1**

Valence-shell oscillator strength estimates used to establish the absolute photoabsorption differential oscillator strength scales of molecules reported in this thesis via the VTRK sum rule

Molecule	Number of valence-shell electrons ( $Z_{val}$ )	Isoelectronic atoms	Total valence-shell oscillator strength estimate ( $Z_{val} + Z_p$ )
<i>n</i> -pentane: $\text{CH}_3(\text{CH}_2)_3\text{CH}_3$	32	F + 3(O) + F	33.17
<i>n</i> -hexane: $\text{CH}_3(\text{CH}_2)_4\text{CH}_3$	38	F + 4(O) + F	39.38
<i>n</i> -heptane: $\text{CH}_3(\text{CH}_2)_5\text{CH}_3$	44	F + 5(O) + F	45.59
<i>n</i> -octane: $\text{CH}_3(\text{CH}_2)_6\text{CH}_3$	50	F + 6(O) + F	51.80
$\text{CFCl}_3$	32	C + F + 3(Cl)	33.15
$\text{CF}_2\text{Cl}_2$	32	C + 2(F) + 2(Cl)	33.16
$\text{CF}_3\text{Cl}$	32	C + 3(F) + Cl	33.17
$\text{CF}_4$	32	C + 4(F)	33.18
$\text{NO}_2$	17	N + 2(O)	17.57
$\text{PF}_3$	26	P + 3(F)	27.00
$\text{PCl}_3$	26	P + 3(Cl)	26.98
$\text{PF}_5$	40	P + 5(F)	41.55

### 3.1.2 The dipole ( $e,e+\text{ion}$ ) coincidence mode

The dipole ( $e,e+\text{ion}$ ) coincidence mode of operation [15,16,39,44,45] involves the detection of a forward scattered electron subtended in a small cone of  $1.4 \times 10^{-4}$  steradians about a zero degree scattering angle in coincidence with a positive ion produced in the electron scattering process. A dipole ( $e,e+\text{ion}$ ) experiment therefore requires the use of all components of the spectrometer in the dipole ( $e,e$ ) mode for the detection of the scattered electron at a particular energy loss, plus an additional time-of-flight tube for extracting the positive ions (see figure 3.1). In this procedure, as the scattered electron travels through the angular selection aperture (and is

eventually detected as described earlier in section 3.1.1), the positive ion produced in the collision chamber is simultaneously extracted at  $90^\circ$  to the incident electron beam into a TOF tube by a  $400 \text{ V}\cdot\text{cm}^{-1}$  electrostatic field that is applied across the collision region. The ion travels down the 10 cm TOF tube and is detected in the saturated pulse counting mode by a double microchannel plate ion detector (Electro-Optical Sensors, model VUW-8920ES). The design of the ion extraction voltages and TOF analyzer lens system [15,16] ensures uniform collection of ions with up to 20 eV excess kinetic energy of fragmentation. This is essential if accurate branching ratios and absolute partial differential oscillator strengths are to be obtained for molecular and dissociative photoionization. In determining the flight time, which is proportional to the square root of the  $m/e$  ratio for a particular ion, a single-stop time-to-amplitude converter (TAC) is used. The TAC is started by a pulse signal from the ion channel and stopped by a pulse from the (delayed) electron of a given energy loss. The time between the start and stop pulses (typically in the range of 5–10  $\mu\text{sec}$ ) is then converted to a DC amplitude and processed by an IBM compatible computer (Intel 80286) via an analog-to-digital converter. The computer keeps track of the number of electron-ion coincidences as a function of flight time at a particular energy loss over a selected time period and converts the resulting data into a TOF mass spectrum.

As a first step in studying the molecular and dissociative photoionization of the molecules reported in this thesis, TOF mass spectra for each molecule have been collected as a function of energy loss (i.e., equivalent photon energy) at an ambient sample pressure of  $\sim 4 \mu\text{Torr}$  in several overlapping energy regions and analyzed individually. Photoion branching ratios are determined by integrating the ion peaks in each of the baseline-subtracted TOF mass spectra and then correcting the peak areas for the mass ( $m/e$ ) sensitivity of the microchannel plate ion detector using the response function reported in ref. [45]. For each fragment ion formed, the branching

ratio, representing the fraction of the total number of ions produced, is obtained as given by equation (2.37).

In the dipole ( $e,e+ion$ ) experiment, the relative photoionization efficiency is defined to be the ratio of the total coincidence ion signals to the total number of forward scattered electrons as a function of energy loss in the given time period. When these values for a target molecule become effectively constant within experimental uncertainty (e.g., above 17.5 eV in the case of  $PF_3$ ), it is reasonable to assume that the photoionization efficiency ( $\eta_i$ ) has reached a magnitude value of unity. This usually occurs at energy losses above 14–25 eV, depending on the target molecule. The absolute photoionization efficiencies can therefore be obtained by normalizing these values that have leveled off to a value of one (e.g., the  $\eta_i$  values above 17.5 eV in  $PF_3$  have been normalized to unity). It should be noted that the detection efficiency of the ion extraction and transportation system of the TOF mass spectrometer is ~10 % using the microchannel plate ion detector [45]. Therefore, both ions formed in Coulomb explosions in dissociative double ionization processes (i.e.,  $AB^{2+} \rightarrow A^+ + B^+$ ) will be detected in approximately equal proportions (i.e., 10% for the fastest, lower  $m/e$  ion and 9% (10% of 90%) for the slower, higher  $m/e$  ion).

Finally, absolute partial photoionization differential oscillator strengths (PPOS) for the production of molecular and dissociative fragment ions from the target molecule at 1 eV fwhm resolution can be determined from the triple product of the absolute total photoabsorption differential oscillator strength (obtained as detailed in section 3.1.1), the photoionization efficiency, and the photoion branching ratio for each ion, as a function of photon energy (equation (2.38)).

The energy loss (equivalent photon energy) scales for the photoionization data reported in the present work have been calibrated by measuring an EEL spectrum under the experimental conditions of the dipole ( $e,e+ion$ ) coincidence experiment and referencing the spectral features to those of the energy-calibrated

EEL spectrum obtained earlier either in the low resolution dipole ( $e,e$ ) mode (see section 3.1.1) or in the high resolution spectrum (see below) after it has been convoluted with a 1 eV fwhm gaussian function.

## 3.2 The High Resolution Dipole ( $e,e$ ) Spectrometer

The dipole ( $e,e$ ) spectrometer [5,14,46] used to obtain high resolution electronic spectra and absolute differential oscillator strengths for the molecular species reported in this thesis in the valence-shell (0.05 eV fwhm) and inner-shell (0.1 eV fwhm) discrete regions is shown in figure 3.2. This spectrometer operates at an incident electron impact energy of 3000 eV and a mean scattering degree of zero degrees such that the momentum transfer is negligible and electric-dipole transitions dominate the electron energy-loss spectra. The high resolution is achieved primarily by the addition of a large (19 cm mean radius) electrostatic, hemispherical electron monochromator, which selects out a small section of the broad Maxwell-Boltzmann energy distribution of the incident electron beam, and the use of an identical hemispherical electron analyzer. This is furthermore aided by the presence of high precision electron optics in the form of seven electron lens elements ( $L_1-L_7$ ), which serve to focus, accelerate, and decelerate the electron beam, and nine sets of quadrupole deflectors ( $Q_1-Q_9$ ) that guide the beam of electrons through eight apertures ( $P_1-P_8$ ).

The spectrometer resolution is largely governed by the pass energies of the monochromator and analyzer. In the valence-shell region (1–60 eV) where the electron scattering cross section is high, the pass energies of both the monochromator and analyzer can be set to 10 eV. This setting produces an incident electron beam with an overall energy spread of  $0.035 \pm 0.003$  eV fwhm as measured by recording the main beam passing through both the monochromator and the

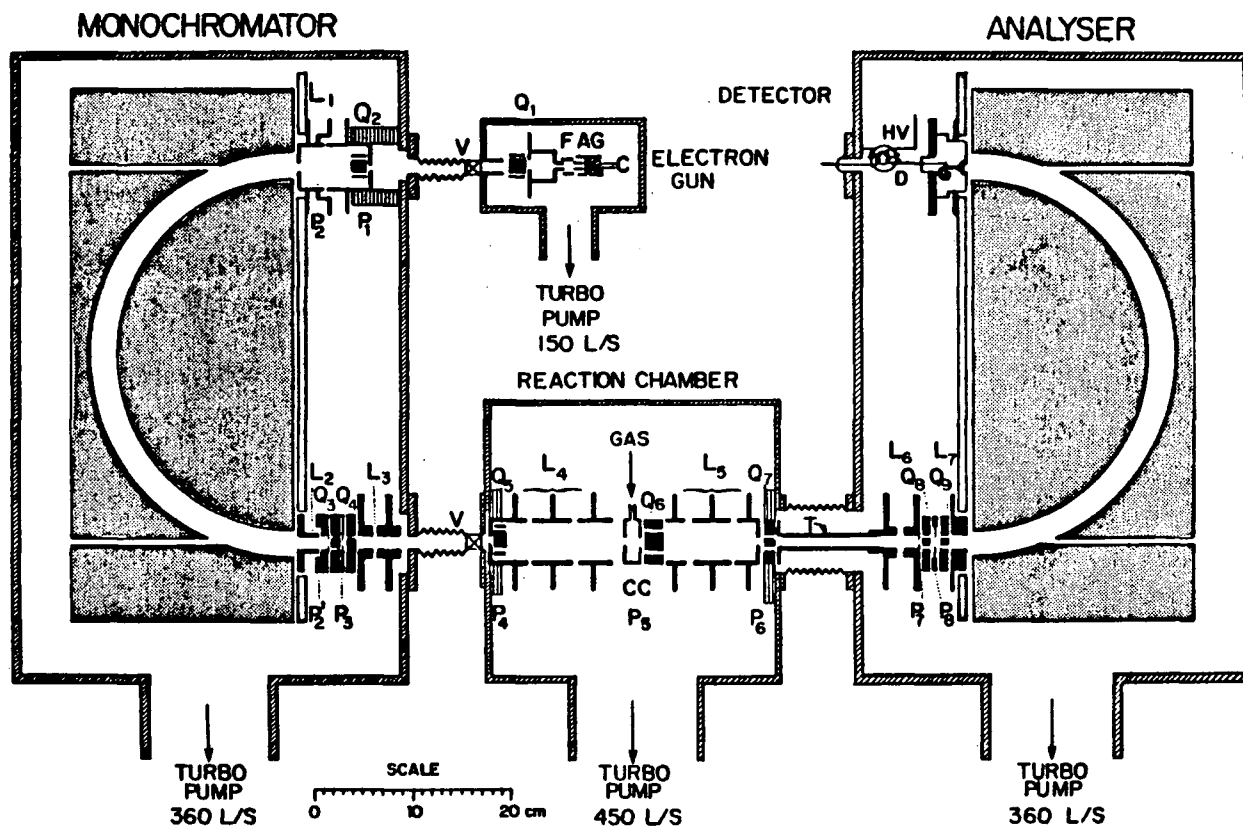


Figure 3.2: Schematic of the high resolution dipole  $(e,e)$  spectrometer [5,14,46].

analyzer. This translates to a  $\sim 0.05$  eV fwhm resolution for the inelastically scattered beam when measured on the  $2^1P \leftarrow 1^1S$  transition of helium [5]. In the inner-shell region (e.g., between 128–150 eV in the vicinity of the P  $2p$  discrete spectrum of  $PF_3$ ), the inelastic electron scattering cross sections become very small. Therefore, in order to obtain a reasonable signal-to-noise ratio, the pass energies of the monochromator and analyzers must be increased to 30 eV, at the expense of lower resolution ( $\sim 0.1$  eV fwhm in the inelastically scattered electron beam).

A high resolution electron energy-loss spectrum is measured as follows. Within the electron gun chamber, electrons are produced by a heated thoriated tungsten cathode (C) in a Cliftronic CE5AH gun body, accelerated into a 3000 eV electron beam by the grid (G) and anode (A), and focused by a lens element (F). At  $L_1$  the electron beam is decelerated to the pass energy of the monochromator, which serves to reduce the energy spread of the 0.8 eV fwhm incident electron beam. The monochromated beam is again accelerated to 3000 eV and focused by  $L_2$  and  $L_3$  into the collision chamber (CC) where it scatters off the target gaseous sample. Only those electrons scattered in the forward direction into a very small cone of  $3.0 \times 10^{-5}$  steradians about a zero degree scattering angle are allowed to pass through the angular selection aperture ( $P_5$ ). These inelastically scattered electrons are then refocused and decelerated before being admitted into the hemispherical analyzer. At the other end of the analyzer, the electrons are detected in the saturated pulse counting mode by a channeltron multiplier (Mullard B419AL), and the resulting signal is processed by an IBM compatible computer (Intel 80386). The computer also controls the energy-loss selection by the decelerating lenses ( $L_6$  and  $L_7$ ) so that a tunable energy EEL spectrum can be obtained. Note that the monochromator and electron gun chambers are floated at a potential of  $-3000$  V, and the analyzer is floated at  $(-3000 + E)$  eV, but the collision chamber is held at ground. The design of this spectrometer also incorporates hydrogen annealed mumetal shielding, which is

used to shield the electron trajectories from external magnetic fields.

For each of the valence-shell and inner-shell high resolution photoabsorption spectra reported in the present work, EEL spectra are measured at an ambient sample pressure of  $\sim 20$   $\mu$ Torr in two overlapping regions (e.g., 7–30 and 20–60 eV in the case of  $\text{CF}_2\text{Cl}_2$ ), corresponding to the discrete portion where sharp structures are observed and a higher energy continuum portion. These spectra are background subtracted at one-quarter of full pressure ( $\sim 5$   $\mu$ Torr) and normalized to one another. The resulting EEL spectrum is converted to relative photoabsorption differential oscillator strengths using the Bethe-Born conversion factor for the high resolution spectrometer [5,14]. Finally, the absolute differential oscillator strength scale is established by single-point normalization of the relative data to the absolute low resolution photoabsorption spectrum (obtained as described in section 3.1.1) in the smooth continuum region where no sharp structures are present. The absolute oscillator strength data determined in this way are estimated to have an accuracy of better than  $\pm 5\%$ . The reliability and accuracy of the dipole ( $e,e$ ) method has been confirmed by the excellent agreement of the experimental oscillator strengths for helium [5] and molecular hydrogen [7] with highly accurate *ab initio* calculations.

The absolute energy scale for the high resolution data have been calibrated by simultaneous admission of the target sample and helium and referencing the spectral features of the target to the  $2^1\text{P} \leftarrow 1^1\text{S}$  transition of helium at 21.218 eV [49].

### 3.3 Sample Handling

The stated purity and commercial supply company for each of the samples used in the present work are listed in table 3.2. The gaseous samples of  $\text{C}_3\text{H}_8$ ,  $n\text{-C}_4\text{H}_{10}$ ,  $\text{CF}_2\text{Cl}_2$ ,  $\text{CF}_3\text{Cl}$ ,  $\text{CF}_4$ ,  $\text{NO}_2$ , and  $\text{PF}_3$  were used without further purification.

**Table 3.2**

Sources and purities of samples used in the present work

Sample	Supply company	Stated purity (%)
$C_3H_8$	Matheson Chemical Inc.	99.5
$n-C_4H_{10}$	Matheson Chemical Inc.	99.0
$n-C_5H_{12}$	BDH	99.0
$n-C_6H_{14}$	Aldrich Chemical Company	99.0
$n-C_7H_{16}$	BDH	99.5
$n-C_8H_{18}$	BDH	99.0
$CFCl_3$	Aldrich Chemical Company	99.0
$CF_2Cl_2$	Matheson Chemical Inc.	99.0
$CF_3Cl$	Matheson Chemical Inc.	99.0
$CF_4$	Matheson Chemical Inc.	99.0
$NO_2$	Matheson Chemical Inc.	99.5
$PF_3$	Ozark-Mahoning	99.0
$PCl_3$	Aldrich Chemical Company	98
$PF_5$	Strem Chemicals Inc.	99

Appropriate gas regulators were placed on the  $C_3H_8$ ,  $CF_3Cl$ ,  $CF_4$ , and  $PF_3$  cylinders before they were introduced into the spectrometer inlet systems. The liquid samples of  $n-C_5H_{12}$ ,  $n-C_6H_{14}$ ,  $n-C_7H_{16}$ ,  $n-C_8H_{18}$ ,  $CFCl_3$ , and  $PCl_3$  were transferred into glass-based sample holders in a nitrogen atmosphere, mounted onto the spectrometer manifold via a swage lock connection, and degassed by repeated freeze-pump-thaw cycles before being admitted into the spectrometers. The  $PF_5$  liquid sample was supplied in a lecture bottle and was thus used directly without the need for degassing. Except for small amounts of impurities detected in the TOF spectra of  $PF_5$ ,  $NO_2$ ,  $C_3H_8$ ,  $n-C_4H_{10}$  (see below), there is no evidence of impurities in

the TOF mass spectra of the remaining samples.

Small amounts of  $\text{POF}_3$  were detected in the TOF mass spectra of  $\text{PF}_5$ , and corrections in the branching ratios were made to account for this. In this procedure TOF mass spectra were obtained for  $\text{POF}_3$ . The peak areas of the  $\text{POF}_2^+$  ion peak (the dominant ion in the  $\text{POF}_3$  mass spectra) were matched up with those observed in the  $\text{PF}_5$  spectra so that the corresponding ratios of the peak areas for  $\text{PF}_x^+$  ( $x = 0-3$ ) and  $\text{F}^+$  in the  $\text{PF}_5$  TOF spectra can be subtracted. While extremely small impurity peaks in the sample are also observed at 10.99, 11.05, 11.39, and 12.92 eV in the valence-shell photoabsorption spectrum, their intensities are negligible compared to the  $\text{PF}_5$  excitations and therefore should not affect the presently reported absolute oscillator strength values.

In the cases of  $\text{C}_3\text{H}_8$  and  $n\text{-C}_4\text{H}_{10}$ , very small impurity peaks (likely due to an air leak) at  $m/e$  values of 32 ( $\text{O}_2^+$ ), 28 ( $\text{N}_2^+$ ), 16 ( $\text{O}^+$ ), and 14 ( $\text{N}^+$ ) were detected, and corrections for these contributions to the corresponding dissociative ions produced from  $\text{C}_3\text{H}_8$  and  $n\text{-C}_4\text{H}_{10}$  (having the same  $m/e$  values) were made in the determination of branching ratios and PPOS using the photoion branching ratios of  $\text{O}_2^+$ ,  $\text{N}_2^+$ ,  $\text{O}^+$ , and  $\text{N}^+$  derived from ref. [2].

In the case of  $\text{NO}_2$ , a very small impurity ( $\leq 1\%$ ) from oxygen in the sample was detected in the TOF mass spectra, and corrections have been made to the branching ratios and PPOS for the production of  $\text{O}_2^+$  and  $\text{O}^+$  from nitrogen dioxide using the absolute PPOS data for the production of  $\text{O}_2^+$  and  $\text{O}^+$  from oxygen [2].

## Chapter 4

# Photoabsorption and Photoionization Studies of Normal Alkanes

### 4.1 Introduction

The photoabsorption and photoionization of the normal alkanes are of considerable fundamental as well as applied interest. The saturated hydrocarbons have been chosen for the present study since hydrocarbon structures are a major constituent of larger organic molecules, including those of biochemical and radiological significance. Moreover, hydrocarbons are important in a number of applications involving interaction with energetic electromagnetic radiation. Propane ( $C_3H_8$ ), for example, is of interest in aeronomy due to its ability to scavenge chlorine atoms [34], thereby interrupting the chain reactions that can lead to ozone depletion. Butane ( $n-C_4H_{10}$ ), on the other hand, is used in Britain as an aerosol propellant substitute for Freons [35]. In view of this, it is therefore surprising to note that no absolute photoionization data exist for the molecular and dissociative photoionization of propane and  $n$ -butane other than the limited measurements below 25 eV reported by Schoen [50] in 1962. However, the accuracy of these data [50] is questionable since they were obtained using a sector-type mass spectrometer, and it is well known that such instruments suffer from serious fragment ion kinetic energy and mass discrimination effects. In other work, a few measurements of *relative* photoionization yield curves [51–53] and appearance potentials [54–56] have also been reported.

In photoabsorption work, relatively little absolute differential oscillator

strength information exists for the photoabsorption of the larger normal alkanes ( $C_nH_{2n+2}$ ,  $n = 5-8$ ). In fact, other than the previously reported measurements made using conventional optical methods below 12 eV for  $n$ -pentane to  $n$ -octane [57,58], between 10–41 eV for  $n$ -hexane [59], and in the region 7–25 eV for  $n$ -pentane [50], to date no other absolute experimental data or *ab initio* calculations are available for the absolute oscillator strengths of these larger alkanes in the VUV and soft X-ray regions. Moreover, the previously published absolute differential oscillator strength data show significant differences in both shape and magnitude, and comprehensive data are unavailable for the valence-shell spectra over wide energy ranges.

In the present work, photoion branching ratios and photoionization efficiencies for the molecular and dissociative photoionization of propane and  $n$ -butane are reported from the first ionization potential up to 80 and 50 eV, respectively. These data are used together with the earlier reported photoabsorption data [36] to derive the absolute partial photoionization differential oscillator strengths (PPOS) for molecular and dissociative photoionization and to investigate the dipole induced breakdown pathways of these molecules following the absorption of energetic radiation in the VUV and soft X-ray regions.

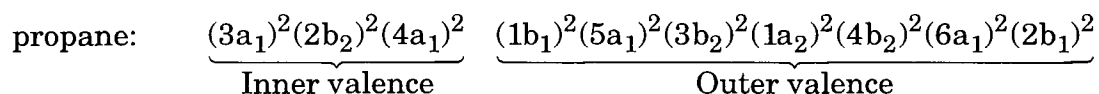
In addition, the photoabsorption spectra of the larger normal alkanes,  $C_nH_{2n+2}$  ( $n = 5-8$ ), have also been measured in the present work for two main reasons. Firstly, the absolute photoabsorption differential oscillator strength data available for these molecules is very limited. The present work therefore provides the widest ranging oscillator strength distribution data yet available and the only data above 41 eV for any of these molecules. Secondly, such wide-ranging data for a homologous series of molecules, such as the normal alkanes ( $n = 1-8$  from previous [36] and present studies in this laboratory), are important for the quantitative assessment of atomic and molecular mixture rule calculations. These mixture rules can be used to (1) provide estimates of absolute oscillator strengths for larger

molecules, including those of biochemical and radiological significance, where direct measurement may be difficult, and (2) predict absolute oscillator strengths in energy regions where measured experimental data are unavailable. It should be noted in the latter context that molecular mixture rules have been used by Meath and co-workers for constructing dipole oscillator strength distributions (DOSD's) for a variety of molecules including the normal alkane series [60]. Indeed, since DOSD's are constructed from the electronic absorption threshold to infinite energy, and since experimental photoabsorption data for these molecules are limited, mixture rules and other empirical concepts played a crucial role in the DOSD construction. The present study thus provides the first experimental test of these procedures for the normal alkanes, at least up to 220 eV. In section 4.3, the presently reported absolute differential oscillator strength data will be used together with earlier measurements for the smaller alkanes ( $n = 1-4$ ) [36] to provide a detailed quantitative assessment of the use of atomic and molecular mixture rules and also group additivity concepts for the estimation of photoabsorption differential oscillator strengths in hydrocarbon based systems.

## 4.2 Results and Discussion

### 4.2.1 Electronic Structures

The point group symmetries of propane and  $n$ -butane are  $C_{2v}$  and  $C_{2h}$ , respectively. The breakdown pathways of these molecules under energetic radiation will be discussed in sections 4.2.2 and 4.2.3 with reference to the following ground state valence-shell electronic configurations in the independent particle model:



$$n\text{-butane: } \underbrace{(3a_g)^2(3b_u)^2(4a_g)^2(4b_u)^2}_{\text{Inner valence}}$$

$$\underbrace{(1a_u)^2(5a_g)^2(1b_g)^2(5b_u)^2(6b_u)^2(6a_g)^2(2a_u)^2(2b_g)^2(7a_g)^2}_{\text{Outer valence}}$$

The outer and inner valence shell vertical ionization potentials (VIP's) as determined by photoelectron spectroscopy [61,62] for propane are: 11.51 (2b<sub>1</sub>), 12.14 (6a<sub>1</sub>), 12.6 (4b<sub>2</sub>), 13.53 (1a<sub>2</sub>), 14.2 (3b<sub>2</sub>), 15.33 (5a<sub>1</sub>), 15.85 (1b<sub>1</sub>), 19.15 (4a<sub>1</sub>), 22.1 (2b<sub>2</sub>), and 24.5 eV (3a<sub>1</sub>). For *n*-butane the VIP's are [61,62]: 11.09 (7a<sub>g</sub>), 11.66 (2b<sub>g</sub>), 12.3 (2a<sub>u</sub>), 12.74 (6a<sub>g</sub>), 13.2 (6b<sub>u</sub>), 14.2 (5b<sub>u</sub>), 15.0 (1b<sub>g</sub>), 15.59 (5a<sub>g</sub>), 15.99 (1a<sub>u</sub>), 18.80 (4b<sub>u</sub>), 20.7 (4a<sub>g</sub>), 23.0 (3b<sub>u</sub>), and 24.7 eV (3a<sub>g</sub>). To date no measurements or calculations of electronic state partial photoionization differential oscillator strengths have been reported.

## 4.2.2 Molecular and dissociative photoionization of propane

TOF mass spectra of propane were obtained at equivalent photon energies from the first ionization potential up to 80 eV. In the TOF mass spectrum obtained at 70 eV (figure 4.1), eighteen positive ions were detected: C<sub>3</sub>H<sub>*x*</sub><sup>+</sup> (*x* = 1–8), C<sub>2</sub>H<sub>*x*</sub><sup>+</sup> (*x* = 1–5), CH<sub>*x*</sub><sup>+</sup> (*x* = 1–3), and H<sub>*x*</sub><sup>+</sup> (*x* = 1–2). It is not possible to unambiguously identify stable doubly charged species due to the (*m/e*) degeneracy with singly charged ions of half the mass. However, electron impact studies of isotopically substituted molecules [63] have indicated that the amount of stable double ionization occurring in hydrocarbon molecules is extremely small. The role of multiple ionization in alkanes has been further discussed by Field and Franklin [64], and individual doubly charged ion peaks were found to have intensities of less than 0.1% of the most intense peak in the mass spectrum. It was suggested [64] that the small amount of stable double ionization observed in hydrocarbons may be

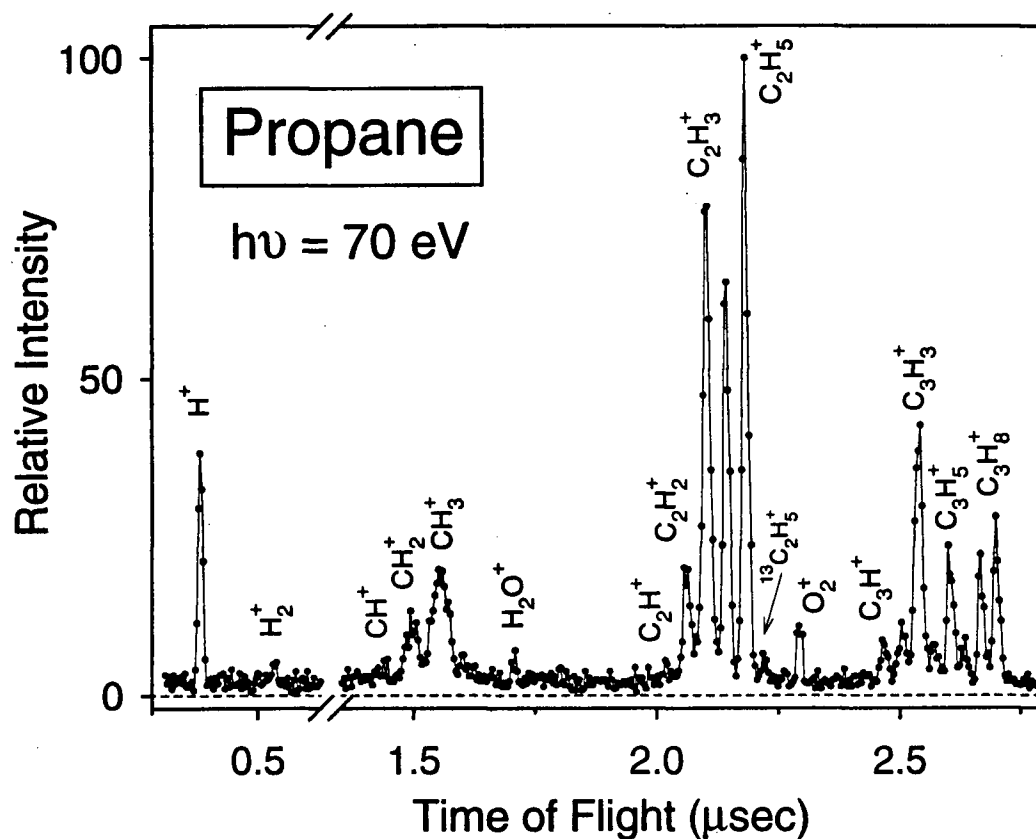


Figure 4.1: TOF mass spectrum of propane obtained at 70 eV.

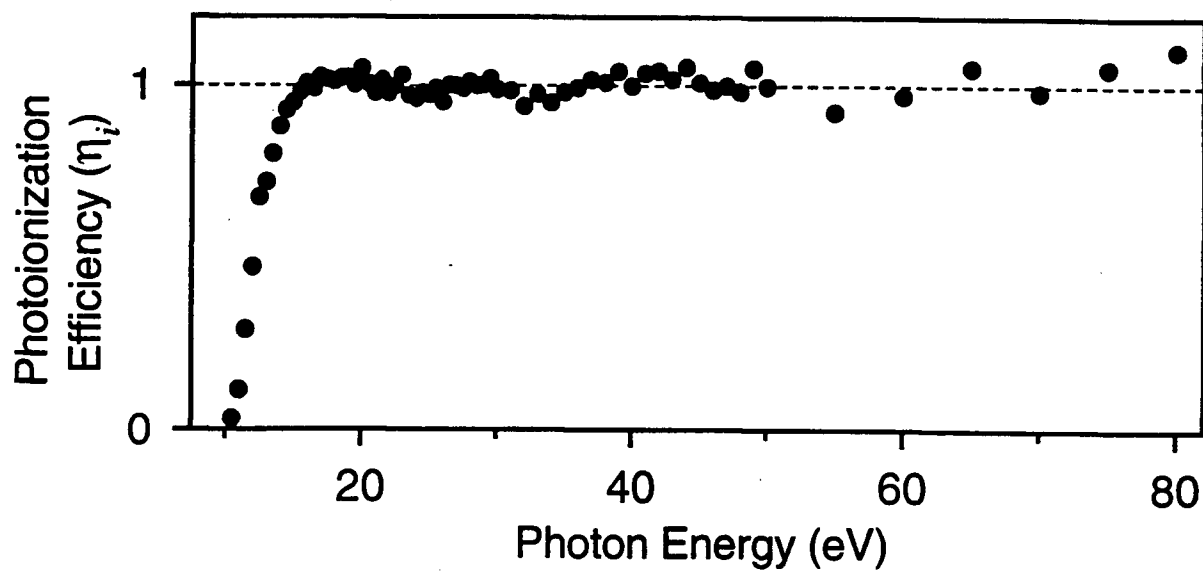
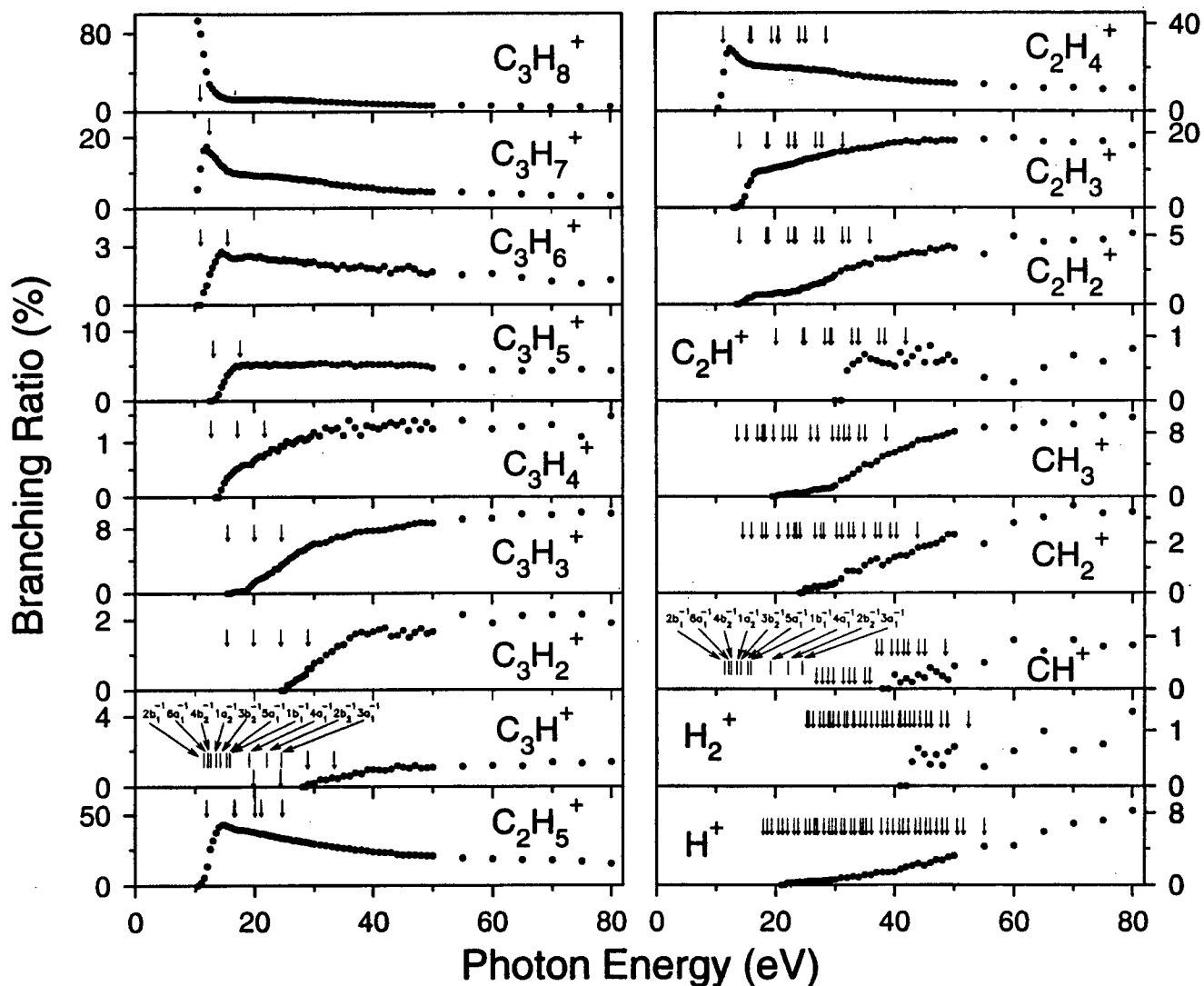


Figure 4.2: Photoionization efficiencies for propane (11–80 eV).

due to the rapid decomposition (Coulomb explosion) of doubly charged ions into two energetic, singly charged ions. The fact that the  $\text{CH}_3^+$  and  $\text{CH}_2^+$  ion peaks in the presently determined TOF mass spectrum at 70 eV (figure 4.1) are relatively broad indicates that they are formed with considerable kinetic energies of fragmentation at this photon energy. The  $\text{CH}_3^+$  peak becomes significantly broader above ~34 eV, which is in the expected region for the onset of double ionization [64]. However, the presence of double dissociative photoionization can only be confirmed by photoion-photoion coincidence (PIPICO) (e.g., see ref. [65]) or photoelectron-photoion-photoion coincidence (PEPIPICO) [66] studies. In recently published PEPIPICO measurements (without photoelectron energy analysis) using He (II) radiation (40.8 eV), Hagan and Eland [66] have studied the stable and dissociative double photoionization of propane and *n*-butane, and have reported the yields to be very small (< 1 % and 5–10 % of singly charged yields for stable doubly charged ions and dissociated doubly charged ions, respectively).

In a dipole ( $e, e+\text{ion}$ ) experiment, the ratio of the total coincident ion signal to the forward scattered electron energy-loss signal at each energy loss yields the *relative* photoionization efficiency, which has been normalized to a value of unity above 15.5 eV where the values become effectively constant. These are shown in figure 4.2 and given numerically in the last column of table A.1 in the appendix.

From the photoion branching ratios for propane shown in figure 4.3, it is clear that  $\text{C}_2\text{H}_5^+$ ,  $\text{C}_2\text{H}_4^+$ , and  $\text{C}_2\text{H}_3^+$  are the dominant ions produced from propane above ~30 eV photon energy. The branching ratios for the molecular ion and the other ions having three carbon atoms are noticeably lower than those for the fragment ions of ethane [36] having two carbon atoms. Moreover, when comparing the measured intensities of cations with the same number of carbon atoms from  $\text{C}_3\text{H}_7^+$  to  $\text{C}_2\text{H}^+$ , the dissociative ions containing an odd number of hydrogen atoms tend to have higher intensities than those with an even number of hydrogens. Field and Franklin [64]



**Figure 4.3:** Branching ratios for the molecular and dissociative photoionization of propane. The vertical arrows indicate calculated thermodynamic appearance potentials (calculated using heats of formation of neutral and positively charged ion data from ref. [67]), while the vertical lines represent vertical ionization potentials [61,62] for the production of electronic states of  $C_3H_8^+$ .

have suggested that this tendency may be due to the entropy of activation for processes leading to products with an odd number of hydrogens being lower than for the processes leading to products with an even number of hydrogens. The former processes involve only simple bond fission reactions, whereas the latter require higher entropy transition states where several atoms come together to form neutral molecular products plus the fragment ion.

The shapes of the presently obtained absolute partial photoionization differential oscillator strengths (figure 4.4 and table A.1) for production of the molecular and dissociative ions of propane are in reasonable agreement with the *relative* photoionization yield spectra reported by Chupka and Berkowitz [52] over the limited energy range from 10.7 to 14.0 eV. However, the absolute cross sections reported earlier by Schoen [50] below 25 eV show appreciable differences in both shape and magnitude from the values in this work for some of the ions.

The appearance potentials for the production of the positive ions from propane measured in the present work are summarized in table 4.1, where they are compared with previously published experimental data [50–52,55,56]. The presently obtained values are seen to be within the ranges previously reported in the literature [50–52,55,56], except in the cases of  $\text{CH}_3^+$  and  $\text{CH}^+$ , for which the values measured in the present work and those compiled by Rosenstock *et al.* [56] from electron impact based experiments show substantial disagreement. Thermodynamic thresholds, calculated using heats of formation of neutral and positively charged ions [67], and assuming zero kinetic energy of fragmentation, are denoted by vertical arrows in figures 4.3 and 4.4. The vertical ionization potentials [61,62] for production of the electronic ion states of the respective molecular ions, also shown on figures 4.3 and 4.4, provide some indication of the possible dipole induced breakdown pathways following the initial absorption of a photon.

From a consideration of the measured (table 4.1) and calculated appearance

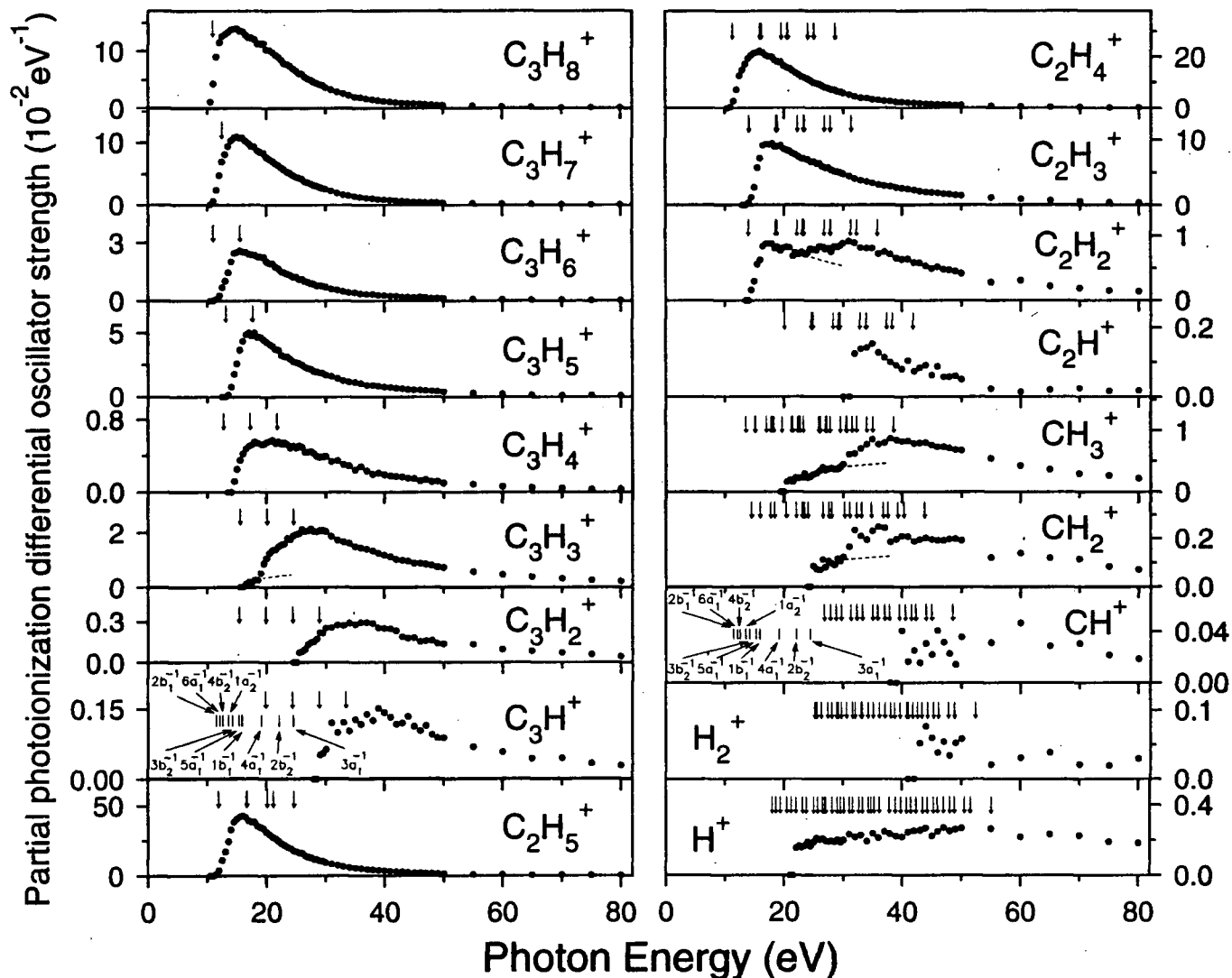


**Figure 4.4:** Absolute partial photoionization differential oscillator strengths for the molecular and dissociative photoionization of propane. The vertical arrows indicate calculated thermodynamic appearance potentials (calculated using heats of formation of neutral and positively charged ion data from ref. [67]), while the vertical lines represent vertical ionization potentials [61,62] for the production of electronic states of  $C_3H_8^+$ . The dashed lines correspond to estimated contributions from higher energy processes.

Table 4.1

Experimental appearance potentials for the production of positive ions from propane

Ion	Appearance potential (eV)					
	This work ( $\pm 1$ eV)	Photoionization			Electron impact	
		ref. [51]	ref. [52]	ref. [50]	ref. [55]	ref. [56]
$C_3H_8^+$	10.5	10.95	11.1	11.05	11.1	11.09
$C_3H_7^+$	10.5	11.00	11.5	11.53	11.3	11.52
$C_3H_6^+$	11.5	11.75	12.2	11.15		
$C_3H_5^+$	13.5		14.1			14.76
$C_3H_4^+$	14.5		14.7			
$C_3H_3^+$	16.5		16.8			
$C_3H_2^+$	25.5					
$C_3H^+$	29.0					
$C_2H_5^+$	11.0	11.90			12.2	12.02
$C_2H_4^+$	10.5	11.72			11.7	
$C_2H_3^+$	14.0					14.5
$C_2H_2^+$	14.5					14.1
$C_2H^+$	32.0					30.4
$CH_3^+$	20.5					25.0
$CH_2^+$	25.0					
$CH^+$	40.0					26.0
$H_2^+$	43.0					
$H^+$	22.0					

potentials (AP's) and VIP's of propane, together with the shapes of the branching ratio curves (figure 4.3) and of the partial differential oscillator strengths (figure 4.4), the following details of the dipole induced breakdown of propane may be inferred. The ions  $C_3H_x^+$  ( $x = 4-8$ ) and  $C_2H_x^+$  ( $x = 3-5$ ), as well as parts of  $C_3H_3^+$  and  $C_2H_2^+$  arise from a combination of the outer valence states of  $C_3H_8^+$  (see section 4.2.1). The higher photon energy parts of the  $C_3H_3^+$  and  $C_2H_2^+$  ion yields, and all remaining smaller fragment ions, must therefore come from dissociative photoionization of the  $4a_1^{-1}$ ,  $2b_2^{-1}$ , and  $3a_1^{-1}$  inner valence states of  $C_3H_8^+$ . It is clear from the high values of the measured appearance potentials for these smaller fragment ions that many of these inner valence contributions come from higher energy many-body ion states of  $C_3H_8^+$  at  $\sim 30$  eV and  $\sim 40$  eV, similar to the situation for ethane [36]. A more detailed analysis of the breakdown pathways of propane must await photoelectron energy resolved PEPIPICO studies and electronic ion state partial differential oscillator strength measurements using variable energy PES, as well as EMS or PES studies of the inner valence regions.

### 4.2.3 Molecular and dissociative photoionization of *n*-butane

TOF mass spectra of *n*-butane were measured in the equivalent photon energy range 10–50 eV. At 50 eV the TOF mass spectrum (figure 4.5) shows the presence of 22 positively charged ions:  $C_4H_x^+$  ( $x = 1,2,4,5,7-10$ ),  $C_3H_x^+$  ( $x = 1-7$ ),  $C_2H_x^+$  ( $x = 2-5$ ),  $CH_x^+$  ( $x = 2-3$ ), and  $H^+$ . Similar to the situation for propane, no stable doubly charged ionic species were observed. Field and Franklin have reported that in electron impact mass spectra the amount of double ionization is very small and decreases as the molecular weight of the alkane increases [64]. As in the case of propane, the widths of the  $CH_3^+$  peak (above  $\sim 30$  eV) and also the  $CH_2^+$  ion peak indicate that these ions are produced with considerable kinetic energies of

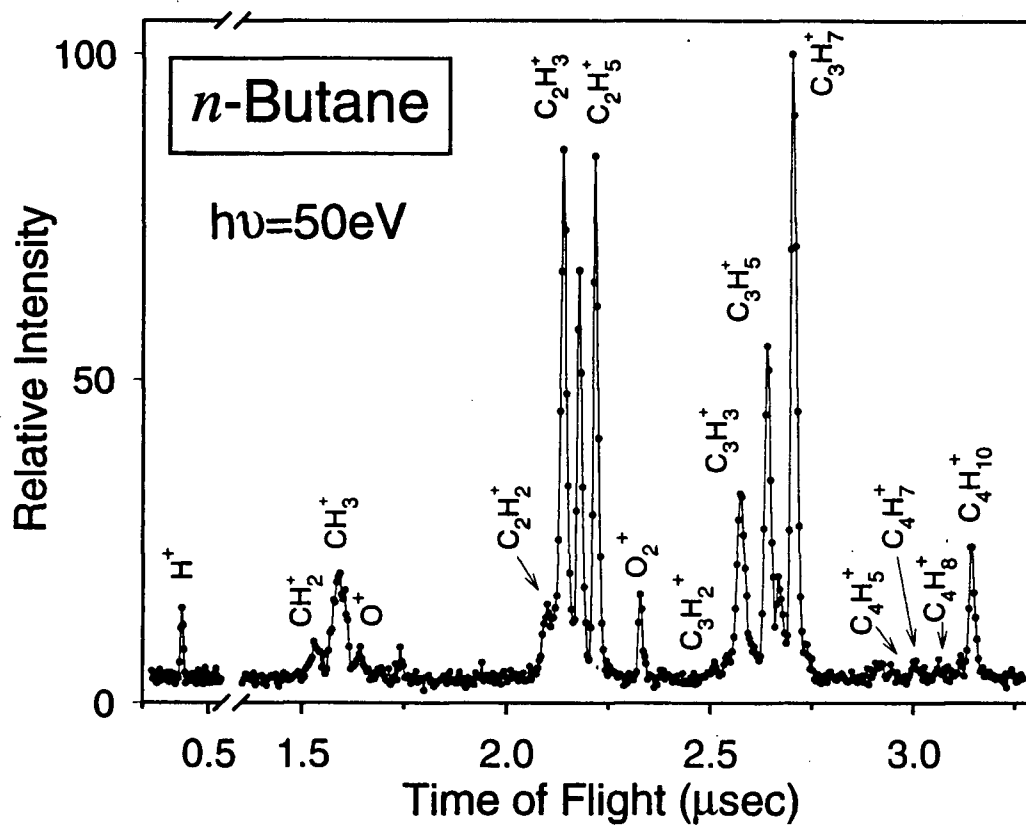


Figure 4.5: TOF mass spectrum of *n*-butane obtained at 50 eV.

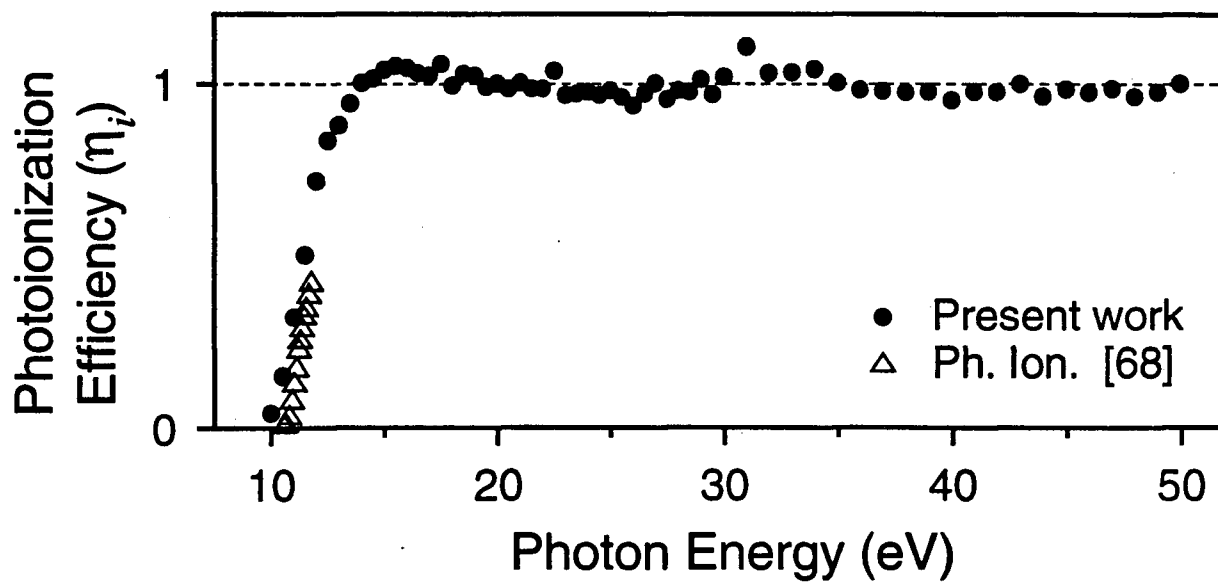
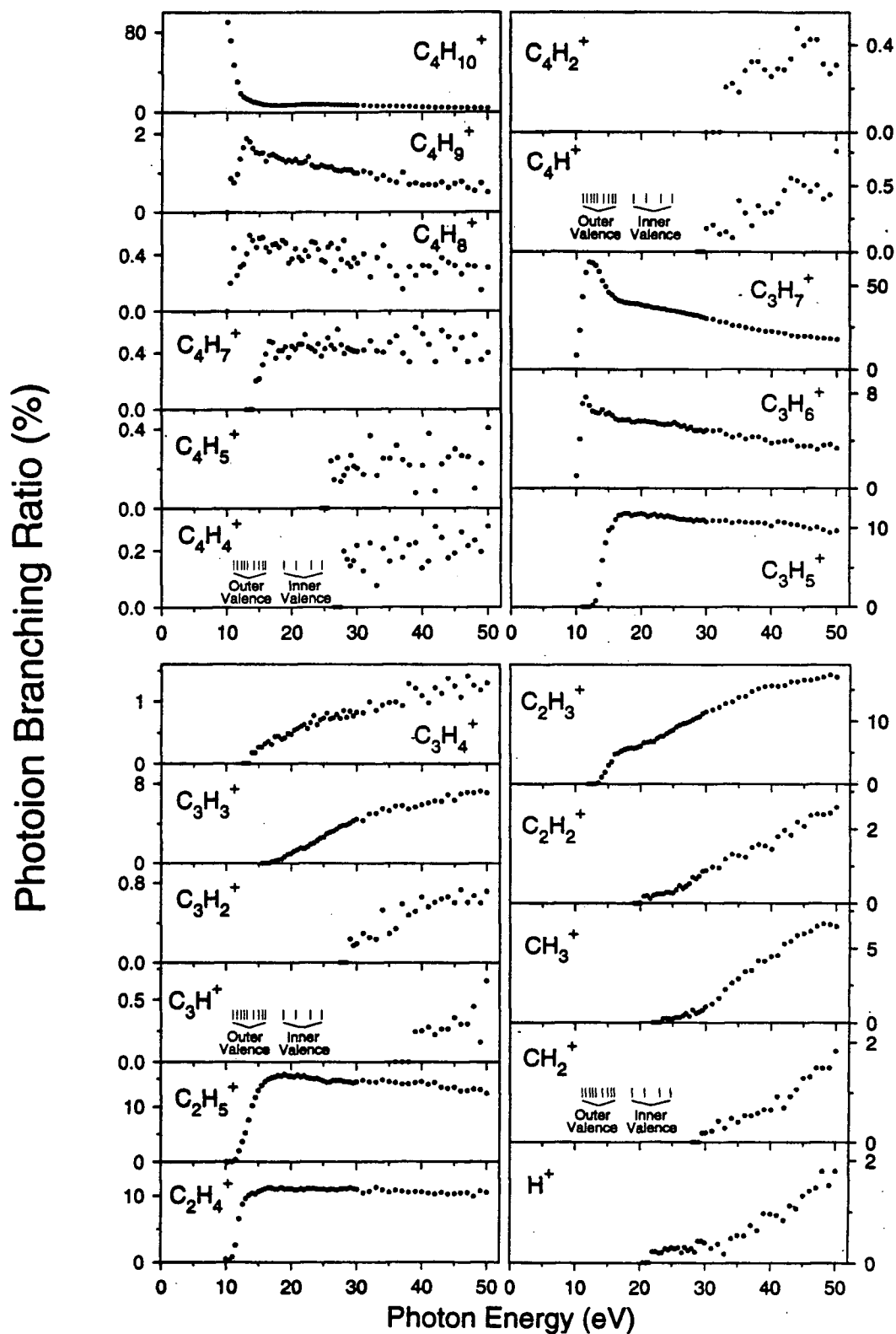


Figure 4.6: Photoionization efficiencies for *n*-butane (10–50 eV).

fragmentation, which is consistent with the observations of Steiner *et al.* [53] (see also above comments for propane concerning stable double photoionization and double dissociative photoionization). For *n*-butane only a small amount of  $\text{H}^+$  was detected in the TOF mass spectra, and no  $\text{H}_2^+$  ion was observed, in contrast to the results for propane.

The absolute photoionization efficiencies for *n*-butane shown in figure 4.6 (table A.2) have been normalized to a value of unity above 13.5 eV where the values become effectively constant. It can be seen that the presently measured photoionization efficiencies for *n*-butane are in reasonable agreement with those reported by Person and Nicole [68], given that the uncertainty of the energy scale in the present low resolution work is  $\pm 1$  eV and the resolution is  $\sim 1$  eV fwhm.

The photoion branching ratios for the molecular and dissociative photoionization of *n*-butane (figure 4.7) show  $\text{C}_3\text{H}_7^+$ ,  $\text{C}_3\text{H}_5^+$ ,  $\text{C}_2\text{H}_5^+$ ,  $\text{C}_2\text{H}_4^+$ , and  $\text{C}_2\text{H}_3^+$  to be the dominant ions produced at photon energies above  $\sim 30$  eV. The molecular ion  $\text{C}_4\text{H}_{10}^+$  and the other ions having four carbon atoms are produced in very small quantities, which is similar to the situation for propane, where those fragment ions having three carbon atoms showed relatively low intensities compared with the lower mass fragment ions. In fact, at 40 eV, only 4 % of the total ion signal is due to  $\text{C}_4\text{H}_{10}^+$  and the photoion branching ratios for  $\text{C}_4\text{H}_x^+$  ( $x = 1-9$ ) range from 0-0.7 %. The dissociative ions produced from *n*-butane which have an odd number of hydrogens have higher partial differential oscillator strengths than those with an even number (see figures 4.5 and 4.7), and this has been attributed to the loss of neutral  $\text{CH}_3$  from the molecular ion followed by subsequent losses of  $\text{CH}_4$  and  $\text{H}_2$  [69]. Moreover, it can be seen in figure 4.5 that the production of ionic fragments tends to favor the breaking of C-C bonds rather than C-H bonds. These observations are consistent with those reported for electron impact mass spectra by Field and Franklin [64], as discussed in section 4.2.2 above.



**Figure 4.7:** Branching ratios for the molecular and dissociative photoionization of *n*-butane. The vertical lines represent the outer and inner valence VIP's [61,62] for the production of electronic states of  $C_4H_{10}^+$  (see section 3.2.1).

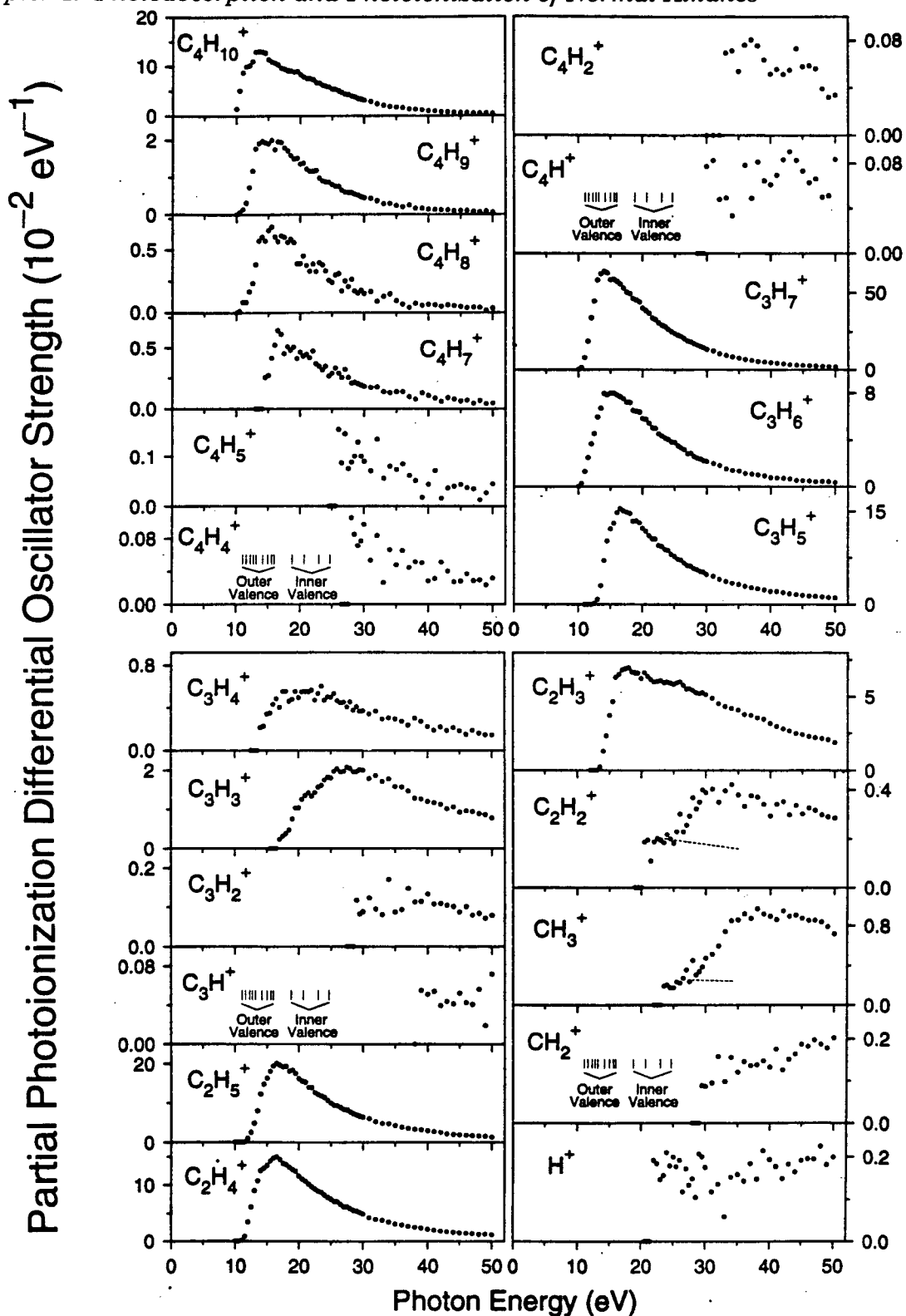


**Figure 4.8:** Absolute partial differential oscillator strengths for the molecular and dissociative photoionization of *n*-butane. The vertical lines represent outer and inner valence VIP's [61,62] for the production of electronic states of  $\text{C}_4\text{H}_{10}^+$  (see section 3.2.1). The dashed lines correspond to estimated contributions from higher energy processes.

Table 4.2

Experimental appearance potentials for the production of positive ions from *n*-butane

Ion	Appearance potential (eV)			
	This work ( $\pm 1$ eV)	Photoionization ref. [51]	Photoionization ref. [52]	Electron impact ref. [55]      ref. [56]
$C_4H_{10}^+$	10.0	10.55	10.56	10.7
$C_4H_9^+$	10.5	10.9		11.0
$C_4H_8^+$	10.5			
$C_4H_7^+$	14.5			
$C_4H_5^+$	26.0			
$C_4H_4^+$	28.0			
$C_4H_2^+$	33.0			
$C_4H^+$	30.0			
$C_3H_7^+$	10.0	11.18	11.10	11.10
$C_3H_6^+$	10.0	11.18	11.09	13.40
$C_3H_5^+$	12.5			
$C_3H_4^+$	14.0			
$C_3H_3^+$	17.0			
$C_3H_2^+$	34.0			
$C_3H^+$	39.0			
$C_2H_5^+$	11.5	11.94		12.55
$C_2H_4^+$	10.0	11.65		
$C_2H_3^+$	13.5			
$C_2H_2^+$	20.5			
$CH_3^+$	23.5			29.7
$CH_2^+$	29.5			
$H^+$	22.0			

The shapes of the presently obtained absolute PPOS for the production of the molecular and fragment ions of *n*-butane (figure 4.8 and table A.2) are in good agreement with those for the *relative* spectra obtained by Chupka and Berkowitz [52] in the rather limited energy region from 10.3 to 14.0 eV. The experimental appearance potentials for the production of positive ions from *n*-butane obtained in the present work (table 4.2) are seen to be in reasonable agreement with those obtained from photoionization experiments [51,52] and electron impact based methods [55,56]. The only disagreement is found between the present value for  $\text{CH}_3^+$  and that reported by Rosenstock *et al.* [56].

From similar considerations to those used above for propane, the following qualitative deductions can be made concerning the dipole induced breakdown of *n*-butane. The ions  $\text{C}_4\text{H}_x^+$  ( $x = 7-10$ ),  $\text{C}_3\text{H}_x^+$  ( $x = 3-7$ ), and  $\text{C}_2\text{H}_x^+$  ( $x = 3-5$ ) arise from dissociation of the outer valence electronic states of  $\text{C}_4\text{H}_{10}^+$ . In contrast, all smaller ions plus  $\text{C}_4\text{H}_x^+$  ( $x = 1,2,4,5$ ) and  $\text{C}_3\text{H}_x^+$  ( $x = 1,2$ ) must come from the inner valence ion states [62] of  $\text{C}_4\text{H}_{10}^+$ .

#### 4.2.4 Photoabsorption of *n*-pentane, *n*-hexane, *n*-heptane, and *n*-octane

The absolute differential oscillator strengths for the valence-shell photoabsorption of *n*-pentane, *n*-hexane, *n*-heptane, and *n*-octane measured in the present work at low and high resolution are plotted as a function of photon energy in figures 4.9–4.12, respectively. In each of figures 4.9–4.12, part (a) shows the differential oscillator strength spectrum over the whole energy range measured (the insert shows the fitted valence-shell extrapolation curve), part (b) presents the data between 7–60 eV in more detail, and part (c) shows the data between 7–13 eV. Parts (b) and (c) of each of figures 4.9–4.12 also provide a critical comparison of the

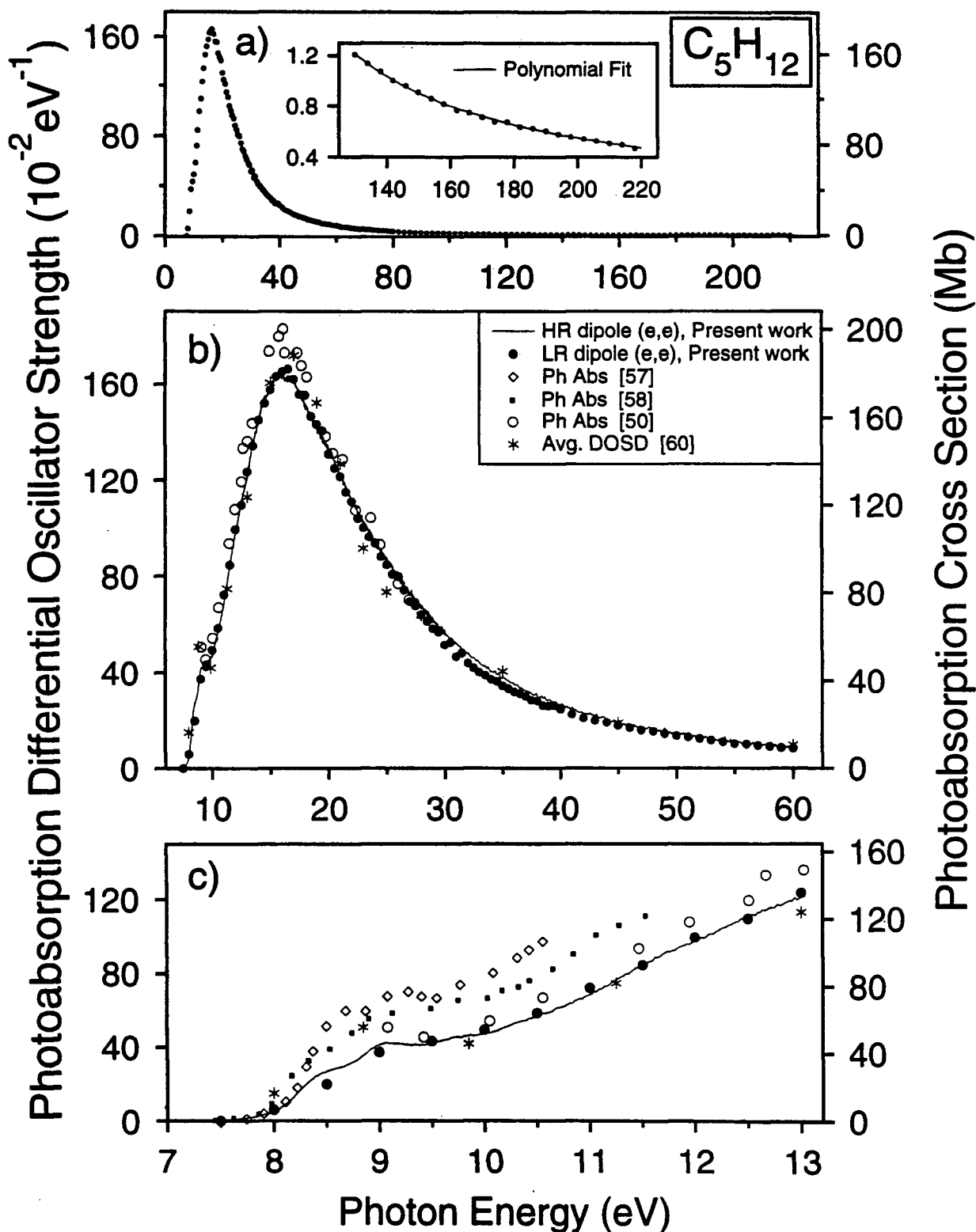


**Figure 4.9:** Absolute differential oscillator strengths for the valence-shell photoabsorption of  $n$ -pentane: a) 7–220 eV (inset shows the polynomial fit to the 130–220 eV region; note offset vertical scale); b) 7–60 eV; c) 7–13 eV.

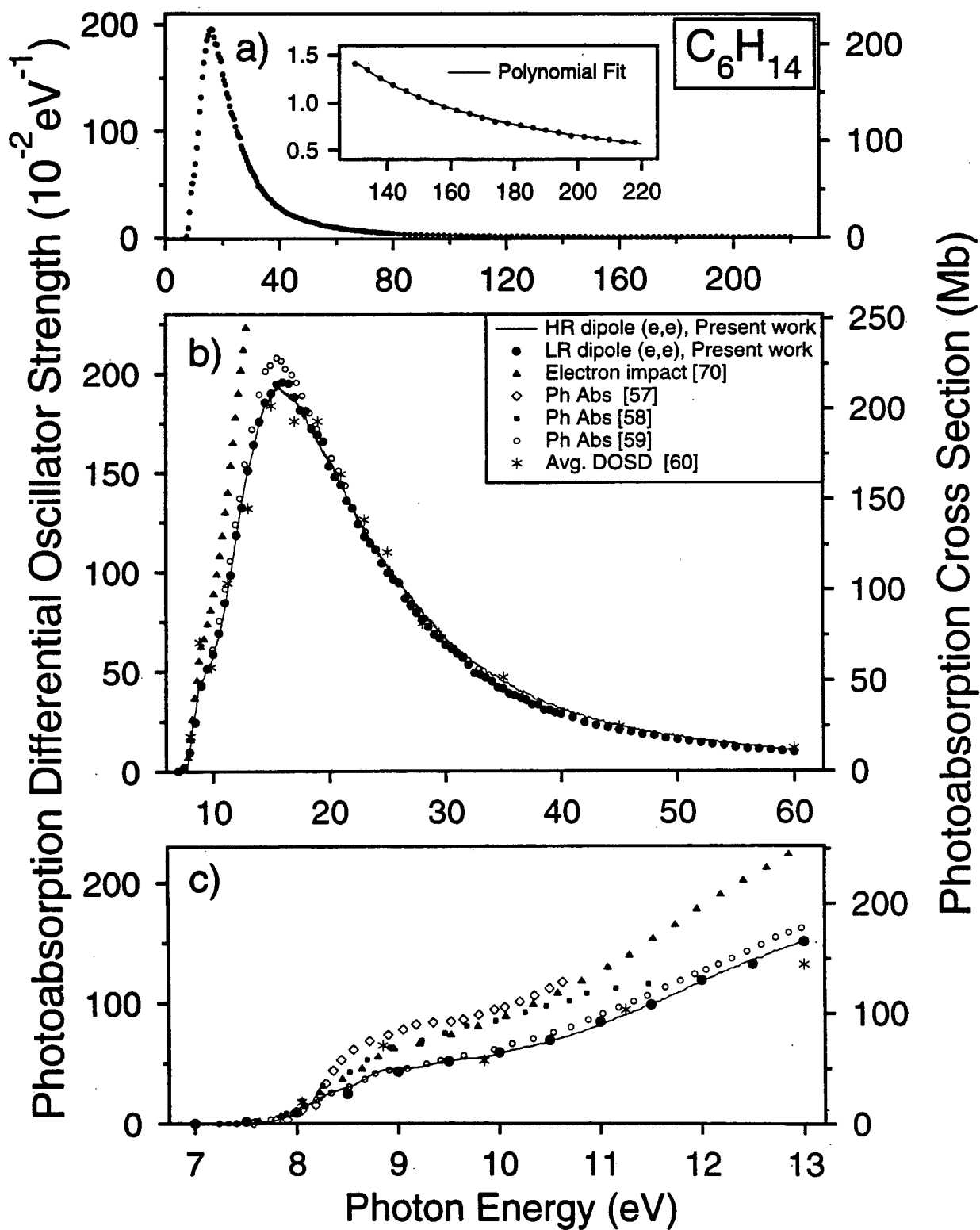


**Figure 4.10:** Absolute differential oscillator strengths for the valence-shell photoabsorption of  $n$ -hexane: a) 7–220 eV (inset shows the polynomial fit to the 130–220 eV region; note offset vertical scale); b) 7–60 eV; c) 7–13 eV.

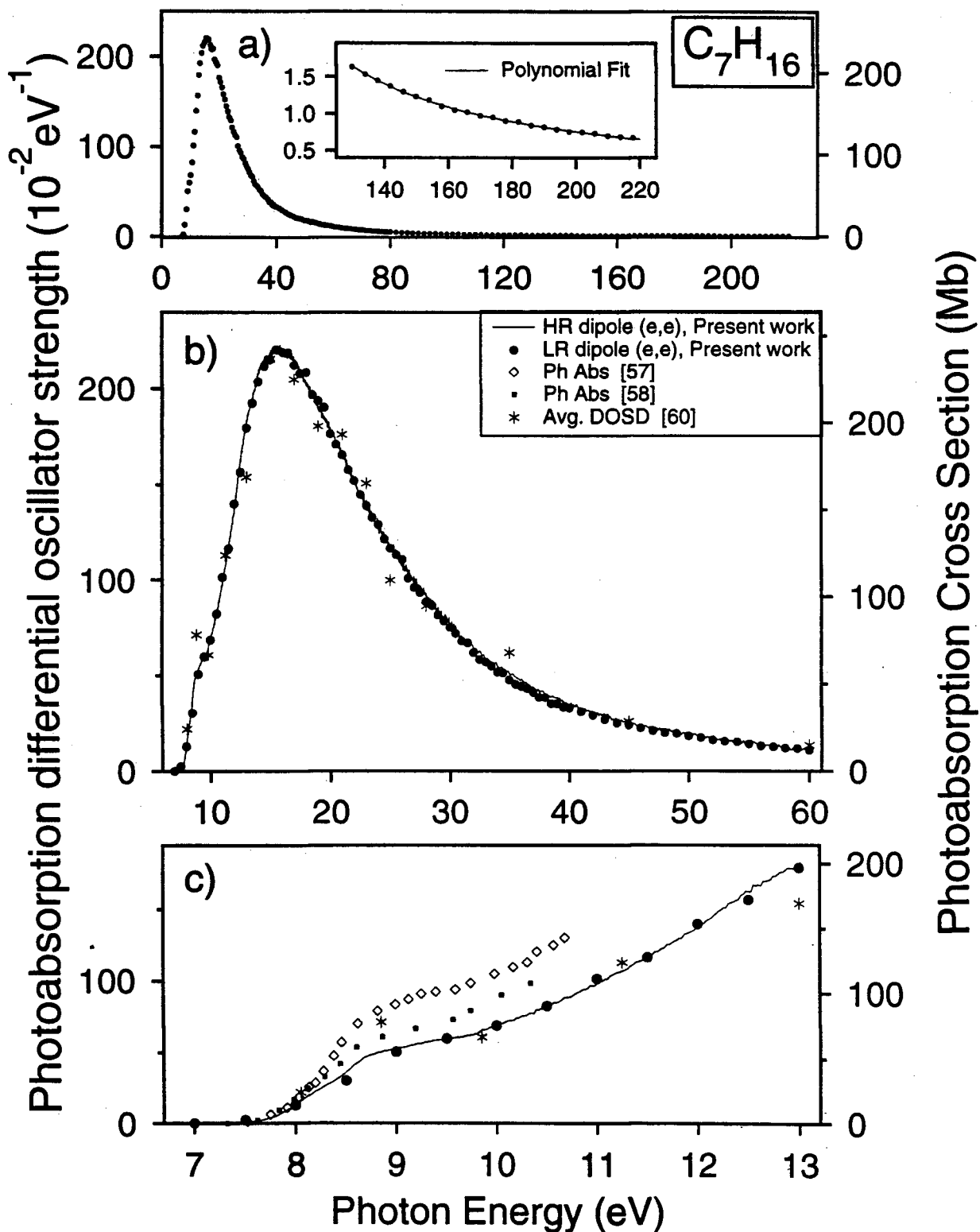


**Figure 4.11:** Absolute differential oscillator strengths for the valence-shell photoabsorption of  $n$ -heptane: a) 7–220 eV (inset shows the polynomial fit to the 130–220 eV region; note offset vertical scale); b) 7–60 eV; c) 7–13 eV.

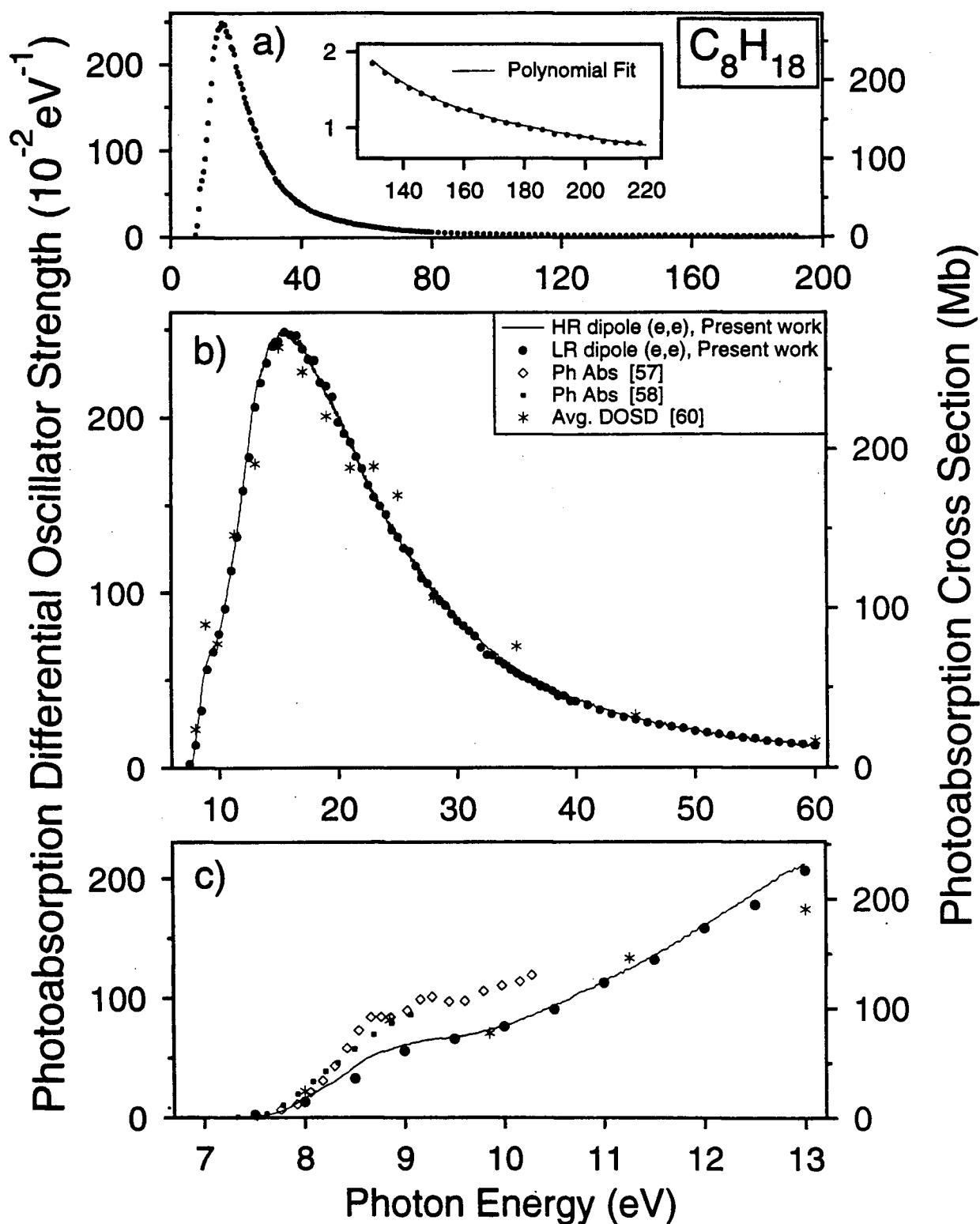


**Figure 4.12:** Absolute differential oscillator strengths for the valence-shell photoabsorption of  $n$ -octane: a) 7–220 eV (inset shows the polynomial fit to the 130–220 eV region; note offset vertical scale); b) 7–60 eV; c) 7–13 eV.

present measurements for the normal alkanes, with such previously reported absolute photoabsorption data as is available from measurements obtained using tunable light sources [57–59], electron energy loss spectroscopy [70], as well as recommended average dipole oscillator strength distribution (DOSD) values [60] estimated from previously published experimental data [50,57,59,70] and mixture rules. The numerical values of the oscillator strengths measured in the present work at 1 eV fwhm resolution for *n*-pentane to *n*-octane are listed in tables A.3–A.6, respectively, in the appendix.

The absolute scales of the photoabsorption differential oscillator strengths for *n*-pentane, *n*-hexane, *n*-heptane, and *n*-octane were established by VTRK sum-rule normalization [27] of the low resolution, Bethe-Born converted, EEL spectra to total valence-shell oscillator strengths of 33.17, 39.38, 45.59, and 51.80, respectively, as discussed in section 3.1.1. Each value corresponds to the total number of valence electrons in the molecule plus small estimated contributions (~5%) for Pauli excluded transitions from the inner shells to the already-occupied valence orbitals [47,48]. In the curvefitting and extrapolation procedure using equation (3.1), the percent area from 220 eV (the upper limit of the present measurements) to infinite energy for each of the alkanes,  $C_nH_{2n+2}$  ( $n = 5-8$ ), was found to be ~4.5 % with respect to the total integrated area from the first excitation threshold.

A method by which the accuracy of the absolute photoabsorption differential oscillator strengths can be critically evaluated is by comparing the experimental static electric-dipole polarizability ( $\alpha_N$ ) for the molecule of interest with that derived from the oscillator strength data using the S(-2) sum-rule [28], given by equation (2.29). The S(-2) sum is heavily weighted at low energies due to the  $E^{-2}$  term and therefore can be used to determine the electric-dipole polarizability with good accuracy of a given molecule when absolute differential photoabsorption oscillator strengths up to ~100 eV are available [28]. Using the absolute data presently

obtained for the normal alkanes and equation (2.29), electric-dipole polarizabilities of  $95.79 \times 10^{-25}$ ,  $114.47 \times 10^{-25}$ ,  $132.88 \times 10^{-25}$ , and  $149.22 \times 10^{-25} \text{ cm}^3$  have been derived for *n*-pentane, *n*-hexane, *n*-heptane, and *n*-octane, respectively. From table 4.3 it can be seen that these values are in very good agreement (within 1–3 %) with the experimental polarizabilities directly determined from dielectric constant [71,72] and refractivity [71] measurements. This good agreement supports the accuracy of the presently determined absolute oscillator strength scales. It should be noted that the  $\alpha_N$  values presently derived from the  $df/dE$  data are in closer agreement with those obtained from dielectric constant and refractivity measurements as compiled by Stuart [71] than with those reported in the Maryott and Buckley compilation [72].

**Table 4.3**

Experimental static electric-dipole polarizability values of  
*n*-pentane, *n*-hexane, *n*-heptane, and *n*-octane

Normal alkane	Static electric-dipole polarizability ( $10^{-25} \text{ cm}^3$ )			
	From $df/dE$ This work	From dielectric constants		From refractivity
		ref. [71]	ref. [72]	ref. [71]
<i>n</i> -pentane	95.79	96.32	99.88	99.43
<i>n</i> -hexane	114.47	116.18	118.70	117.79
<i>n</i> -heptane	132.88	133.51	136.92	135.50
<i>n</i> -octane	149.22	152.63	158.56	154.41

The shapes of the presently obtained absolute photoabsorption differential oscillator strength spectra for *n*-pentane, *n*-hexane, *n*-heptane, and *n*-octane (figures

4.9–4.12, respectively) are in reasonable agreement with those reported by Lombos *et al.* [57] and Raymonda and Simpson [58] below  $\sim 10$  eV. However, although the overall *shapes* of the differential oscillator strength distributions reported in refs. [57,58] are generally quite similar to those in the present work, the magnitudes are 30–40 % higher. In the cases of the *n*-pentane and *n*-octane spectra, the work of Lombos *et al.* [57], show additional broad structures not seen in the present work. For *n*-pentane (figure 4.9), the data reported by Schoen [50] are consistently 10–15 % higher than the present results. Similarly, while the measurements obtained by Person and Nicole [59] for *n*-hexane are in excellent agreement with the present high resolution data at lower energies (figure 4.10(c)), the data become progressively higher beyond 9.6 eV, again showing the largest absolute difference with the present work at the spectral maximum (figure 4.10(c)). However, beyond 25 eV the data of ref. [59] are in reasonable agreement with the present results. The differential oscillator strengths for *n*-hexane obtained from relative EEL measurements by Huebner *et al.* [70] clearly have a similar overall shape to the presently reported spectrum. The differences in the magnitudes (with respect to the present work) of the differential oscillator strengths are due to the fact that Huebner *et al.* [70] normalized their results to the measurements of Raymonda and Simpson [58] at 10.067 eV.

The average DOSD values recommended by Jhanwar *et al.* [60] (constructed empirically by applying TRK sum rule and molar refractory constraints to the very limited available experimental data [50,57,59,70] in the region 7.5–9.2 eV and using mixture rules beyond 9.2 eV) are in reasonable agreement with the present results for all four normal alkanes. While there is clearly some scatter in the DOSD values, from figures 4.9–4.12 it can be seen that the average DOSD results of Jhanwar *et al.* [60] are generally in close agreement with the present differential oscillator strength data over the entire energy range shown (up to 60 eV). In fact, of all the previously

published data sets shown in figures 4.9–4.12, the (semi-empirical) average DOSD results agree best with the present differential oscillator strength values, even though assessments and, in some cases, rescaling of the other data sets [50,57,59,70] were involved in constructing the initial DOSD's. This can be clearly seen in the 10–12 eV energy region of figures 4.9(c)–4.12(c), where the DOSD technique predicts values which are in excellent agreement with the present data, yet are lower than those reported by Lombos *et al.* [57]. Moreover, it is interesting to note that while molecular mixture rules were used to predict the oscillator strengths above ~9 eV for *n*-pentane to *n*-octane, these estimates [60] follow the present results very closely.

The two prominent discrete spectral features observed in the high resolution spectra of *n*-pentane (figure 4.9(c), 8.4 eV, 9.0 eV), *n*-hexane (figure 4.10(c), 8.2 eV, 8.8 eV), *n*-heptane (figure 4.11(c), 8.1 eV, 8.7 eV), and *n*-octane (figure 4.12(c), 8.0 eV, 8.6 eV) clearly correspond to similar features identified as Rydberg transitions in propane and *n*-butane [36]. Therefore, it is probable that these bands contain significant contributions from electronic transitions from the two outermost valence molecular orbitals to  $3p$  Rydberg states.

### 4.3 Atomic and Molecular Mixture Rules and Group Additivity Concepts

Absolute photoabsorption and photoionization differential oscillator strengths for large molecules in the vacuum UV and soft X-ray regions are required for a quantitative understanding of the interaction of highly energetic radiation with matter in a wide range of chemical, physical, biological, and medical applications [1,2]. Therefore, probabilities for radiation absorption and for the subsequent decomposition of these molecules by ionic photofragmentation [2] are of significant interest. In most cases, measured absolute differential oscillator strengths are not

available for large molecules, and furthermore, the complexity of such targets precludes accurate *ab initio* quantum mechanical calculations of the transition probabilities from the ground electronic state to either discrete or continuum final states. In such circumstances empirical estimates of the oscillator strengths are the only recourse, and both atomic and molecular mixture rules involving linear combinations of oscillator strengths for "component" atoms and molecules have been used for these purposes (for example, see refs. [60,73-77]).

Over the past few years Meath and co-workers have employed various types of mixture rules to estimate oscillator strength data over selected energy ranges for the construction of dipole oscillator strength distributions (DOSD's) for a variety of molecules including the normal alkane series from methane to *n*-octane [60,73-77]. Mixture rules were used in the initial construction of the DOSD's [60,73-77] to supplement the limited experimental data (of varying accuracy) available in the literature. With the further application of constraints based on molar refractivity and sum rule considerations, improved (integrated) DOSD's are obtained and have then been used by Meath and co-workers as input data for calculating a wide range of other molecular dipole properties [60,73-77] and for investigating their additivity [38,78-80]. However, it is important to note that, while the constraint procedures result in a generally improved *global* accuracy of the overall integrated DOSD's which is sufficient for calculating reasonably accurate values of the dipole properties, such results do not necessarily provide a sensitive test of the accuracy of the differential oscillator strengths predicted (by mixture rules) or measured at specific energies. The important fact that *global* accuracy in the constrained DOSD does not necessarily imply high *local* accuracy in the (measured or predicted) oscillator strength values has been emphasized earlier by Meath and co-workers [74,75].

Until recently it has not, in general, been possible to test the accuracy and

reliability of mixture rule procedures for predicting dipole differential oscillator strengths at specific local energies, since sufficiently high quality experimental data have not been available for large molecules over wide energy ranges. While the availability of monochromatized synchrotron radiation and, in particular, dipole electron scattering techniques have in the past decade dramatically increased the amount and scope of accurate *absolute* differential oscillator strength data for small molecules [2,5,8,14,22–25], no comprehensive wide energy range measurements have been available for a sufficient range of any homologous series of molecules, which includes larger homologues. In view of this, such wide ranging photoabsorption measurements have been reported in this thesis (section 4.2.4) for the larger normal alkanes,  $C_nH_{2n+2}$  ( $n = 5-8$ ), which supplement those obtained earlier in this laboratory for the smaller alkanes in the series ( $n = 1-4$ ) [36], from 7 to 220 eV using dipole ( $e,e$ ) spectroscopy. In addition to providing a consistent “test-bed” for atomic and molecular mixture rule differential oscillator strength estimates, such data for an homologous series also afford the possibility of an alternative group (fragment) additivity approach to the empirical prediction of oscillator strengths for large molecules of related type. In particular, the absolute photoabsorption data in section 4.2.4 and in ref. [36] for a homologous series can be used to estimate differential oscillator strength contributions from contributing molecular group “fragments” or “chromophores”, which would be the methylene ( $CH_2$ ) and methyl ( $CH_3$ ) groups in the case of the alkanes. These component differential oscillator strength distributions could then be summed to provide oscillator strength predictions not only for radiation absorption by larger alkanes, but also to estimate contributions from hydrocarbon groupings in larger and more complex molecular systems. For example, long hydrocarbon chains are major structural components of bio-organic molecules such as carbohydrates and triglycerides.

Additivity concepts in the total electron impact ionization cross sections of

series of organic molecules, including alkanes, have been discussed earlier by Grosse and Bothe [81] and Schram *et al.* [82], and have been reviewed by de Heer and Inokuti [83]. Using photoabsorption differential oscillator strengths for  $C_nH_{2n+2}$  ( $n = 1-9$ ) in the limited photon energy range of 6.2–11.7 eV, Raymonda and Simpson [58] found a linear dependence of the oscillator strengths on the number of C–C bonds in the molecule. It should also be noted that while the concept of group additivity has not previously been used to predict or test dipole differential oscillator strengths at specific energies for large molecules, “molecularized” additivity concepts have been used and extensively discussed by Meath *et al.* [38,78–80] to predict a range of other molecular properties based on sum rules. Since these other properties depend only on the accuracy of the integrated DOSD’s in a *global* sense, it is of interest to investigate the applicability of group additivity concepts to the predictions of differential oscillator strengths at specific (i.e., *local*) energies.

The applicability of mixture rules or additivity concepts for the estimation of dipole differential oscillator strengths for large species from those measured or calculated for smaller ones is based on the isolated species approximation [73], which treats a large molecule as an assembly of non-interacting atoms, molecules, and/or groups. Using this type of model, the dipole oscillator strength ( $df/dE$ ) of a molecule having the general form,  $A_mB_n$ , can be approximated at any given photon energy,  $E$ , by

$$\frac{df}{dE}(A_mB_n) = \sum_i x_i \frac{df}{dE}(C_i) \quad (4.1)$$

where the  $C_i$  can be atoms, molecules, and/or functional groups, whose linear combination (with coefficient  $x_i$ ) comprises  $A_mB_n$ . Such an equation is often known as a mixture rule [73].

In the present work, previously published absolute photoabsorption and

photoionization data for atoms [84–86] have been used to assess the effectiveness of atomic mixture rules for estimating the differential oscillator strengths for the alkanes ( $C_nH_{2n+2}$ ,  $n = 1-8$ ). In addition, the differential oscillator strengths for larger alkanes have been predicted using published experimental data for  $H_2$  [2] and measurements for the lower alkanes [36] in a variety of molecular mixture rules. The possibility of using a group additivity approach have also been investigated using the absolute photoabsorption data in section 4.2.4 and those in ref. [36] for the alkane series,  $C_nH_{2n+2}$  ( $n = 2-7$ ), to assess systematically the differential oscillator strength contributions for the methylene ( $CH_2$ ) and methyl ( $CH_3$ ) groups in the long-chained alkane environment. The estimation of the photoabsorption spectrum for *n*-octane ( $C_8H_{18}$ ) using these  $CH_2$  and  $CH_3$  group differential oscillator strengths is then compared with the experimental measurements presented earlier in section 4.2.4.

### 4.3.1 Measured absolute photoabsorption differential oscillator strengths for the normal alkanes

The absolute photoabsorption spectra (1 eV fwhm) of the normal alkanes,  $C_nH_{2n+2}$ , reported in section 4.2.4 ( $n = 5-8$ ) and in ref. [36] ( $n = 1-4$ ), are plotted together as a function of photon energy in figure 4.13. The structured, low energy pre-edge regions have also been investigated (section 4.2.4 and ref. [36]) at much higher resolution (0.05 eV fwhm). The absolute differential oscillator strength scales for these measurements are estimated to have an uncertainty of less than  $\pm 5\%$ , which is confirmed by the  $\alpha_N$  values obtained by using the  $S(-2)$  sum rule (see section 4.2.4). Figure 4.13(a) shows the photoabsorption spectra over the entire energy range studied (7–220 eV), while figure 4.13(b) presents the data between 7–50 eV on an expanded scale. The spectra are generally characterized by a broad

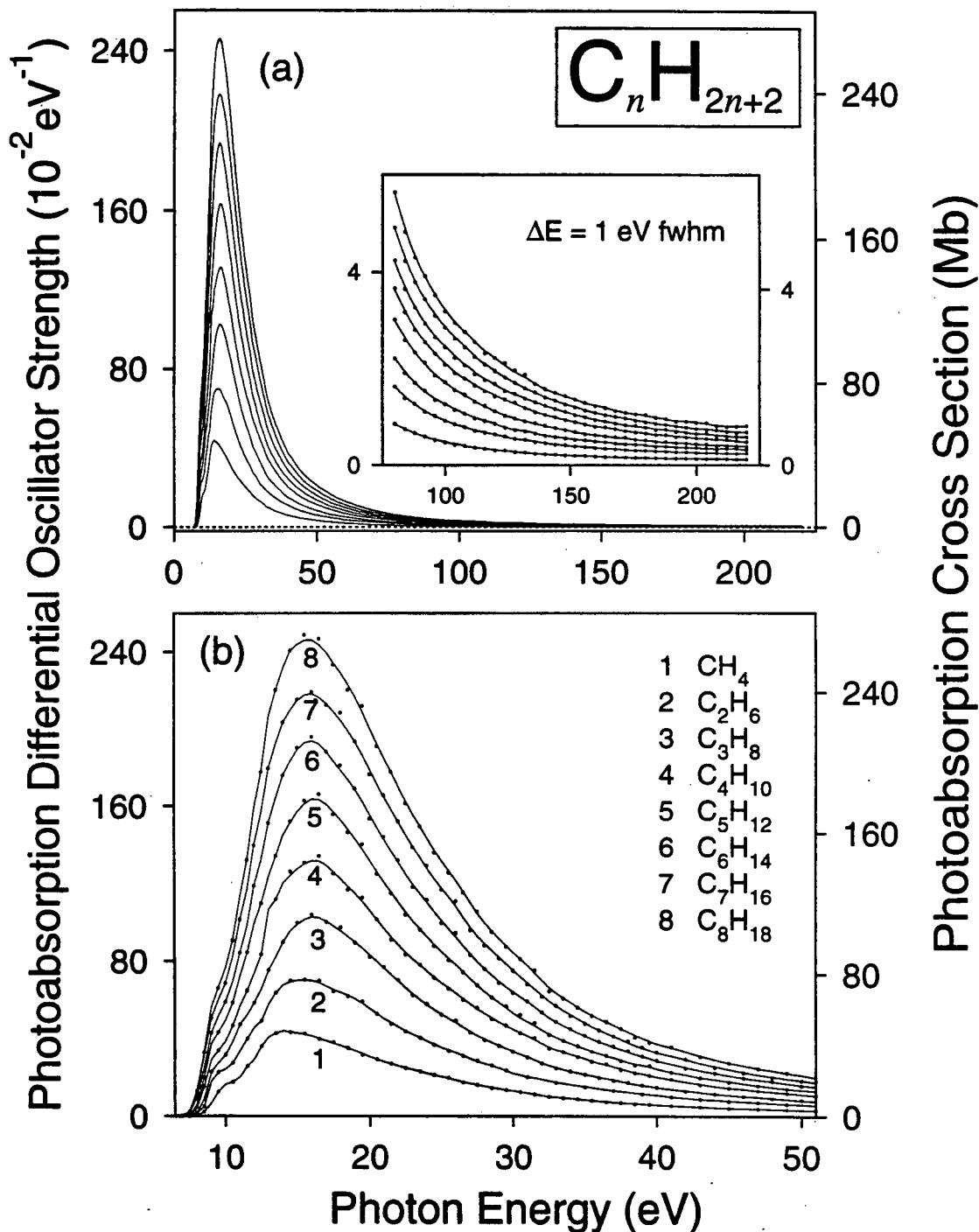


**Figure 4.13:** Systematic comparison of the absolute differential oscillator strengths measured at a resolution of 1 eV fwhm for the valence-shell photoabsorption of the normal alkanes,  $C_nH_{2n+2}$ , reported in section 4.2.4 ( $n=5-8$ ) and in ref. [36] ( $n=1-4$ ): (a) 7–220 eV (inset shows the region 80–220 eV on an expanded scale); (b) 7–50 eV. The dots represent the experimentally measured data, while the lines represent the result of a smoothing procedure applied to the data in order to remove non-spectral fluctuations due to random noise in the experimental measurements.

absorption region between ~12 to 25 eV, with the spectral maximum converging to ~16 eV as the size of the alkane molecule increases. A notable feature in these spectra is the essentially linear increase in the magnitude of the differential oscillator strength at a given photon energy with increasing length of the carbon chain in the molecule. This trend can be attributed to the fact that the overall spectral shapes are similar and that the area under each spectrum (i.e., the oscillator strength from the first excitation threshold to infinity) must reflect the total number of valence electrons (plus a small correction due to Pauli-excluded transitions from the inner shells) according to the valence shell Thomas-Reiche-Kuhn (VTRK) sum rule [2,27]. Thus, as the hydrocarbon chain is lengthened by an increase in the number of CH<sub>2</sub> units, the oscillator strength is expected to increase proportionally. These observations and considerations suggest that mixture rules and group additivity concepts utilizing the differential oscillator strength data for small "component" atoms, such as for normal alkane molecules and H<sub>2</sub>, may be suitable for estimating the continuum differential oscillator strengths for much larger alkane molecules. No attempt has been made to assess additivity relations below 18 eV, since the detailed spectrum of each molecule in this energy region is characterized by different discrete transitions and as such is unsuitable for the present type of investigation.

It is important to note that the use of an experimental data set for a range of molecules obtained from the same laboratory, as in the present work, is likely to provide a much more objective evaluation of the effectiveness of mixture rules and additivity concepts than previous work. Earlier mixture rule studies [60,73-79] have typically employed a variety of data sets, originating from different laboratories and obtained using various techniques, over different energy ranges. Variations in both the shapes and magnitudes of differential oscillator strengths from different sources can often be quite large due to systematic errors. In contrast, the more

unified approach employed in the present work largely avoids any effects of systematic experimental errors in either the input or the test data. Furthermore, the accuracy of the dipole ( $e,e$ ) method used for obtaining the absolute differential oscillator strength data for the normal alkanes in section 4.2.4 and ref. [36] has been demonstrated in earlier work by comparison of the measured oscillator strengths for helium [5] with highly accurate *ab initio* calculations and the results of other measurements [87].

In order to facilitate a comparison of the various molecular mixture rules over wide energy ranges, the calculated differential oscillator strength data for each mixture rule (see sections 4.3.3 and 4.3.4 below) have been least squares fitted with polynomial functions which largely reduces any local short term (non-spectral) fluctuations due to random noise.

### 4.3.2 Atomic mixture rules

The simplest mixture rule for predicting the oscillator strength distribution of a saturated hydrocarbon of the form  $C_nH_{2n+2}$ , which also satisfies equation (4.1), is the atomic mixture rule (AMR) defined as

$$\frac{df}{dE}(C_nH_{2n+2}) = n \frac{df}{dE}(C) + (2n + 2) \frac{df}{dE}(H), \quad (4.2)$$

where the differential oscillator strength distribution of the species of interest ( $C_nH_{2n+2}$ ) is assumed to be a linear combination of those of its constituent atoms. Such a simple approach clearly ignores any chemical bonding or molecular resonance effects. Experimental [84] and calculated [85,86] atomic differential oscillator strength data have been employed separately in equation (4.2) for alkanes with  $n = 1-8$ . Absolute differential oscillator strength values for the hydrogen atom,

derived from the exact formula for the differential oscillator strength distribution for transitions from the ground electronic state to the continuum as given by Inokuti [12], were used to supplement the calculated data for the carbon atom in ref. [85]. In general, while the experimentally and theoretically based AMR estimates agree reasonably well with one another, they provide a poor estimate of the experimentally measured oscillator strengths for each of the normal alkanes. For example, in figure 4.14, comparison of the photoabsorption spectrum of  $C_8H_{18}$  obtained experimentally (in section 4.2.4) with that derived from atomic mixture rule sums shows that such sums have an overall different shape. A similar disagreement in shape between the AMR's and the measured differential oscillator strength data is likewise observed for the other alkanes ( $n = 1-7$ ). In the typical case of  $C_8H_{18}$  (figure 4.14), it is clear that "cross overs" of the AMR and experimental differential oscillator strengths occur. The low AMR values at lower energies reflect the fact that atomic differential oscillator strength data neglect the contributions from near-edge molecular effects which are present in the experimental data. The consistency between the theoretically and experimentally based AMR estimates suggests that these atomic data [84-86] are reasonably accurate and that any uncertainties in these values [84-86] are not responsible for the observed deviation from the experimental measurements for  $C_8H_{18}$ . The observed "cross overs" in the AMR and experimental data are expected to occur because the VTRK sum rule must apply to both atomic and molecular systems. From these results it is clear that atomic mixture rules are unsatisfactory for accurately predicting differential oscillator strengths for valence-shell photoabsorption of alkane molecules throughout the vacuum UV and soft X-ray regions.

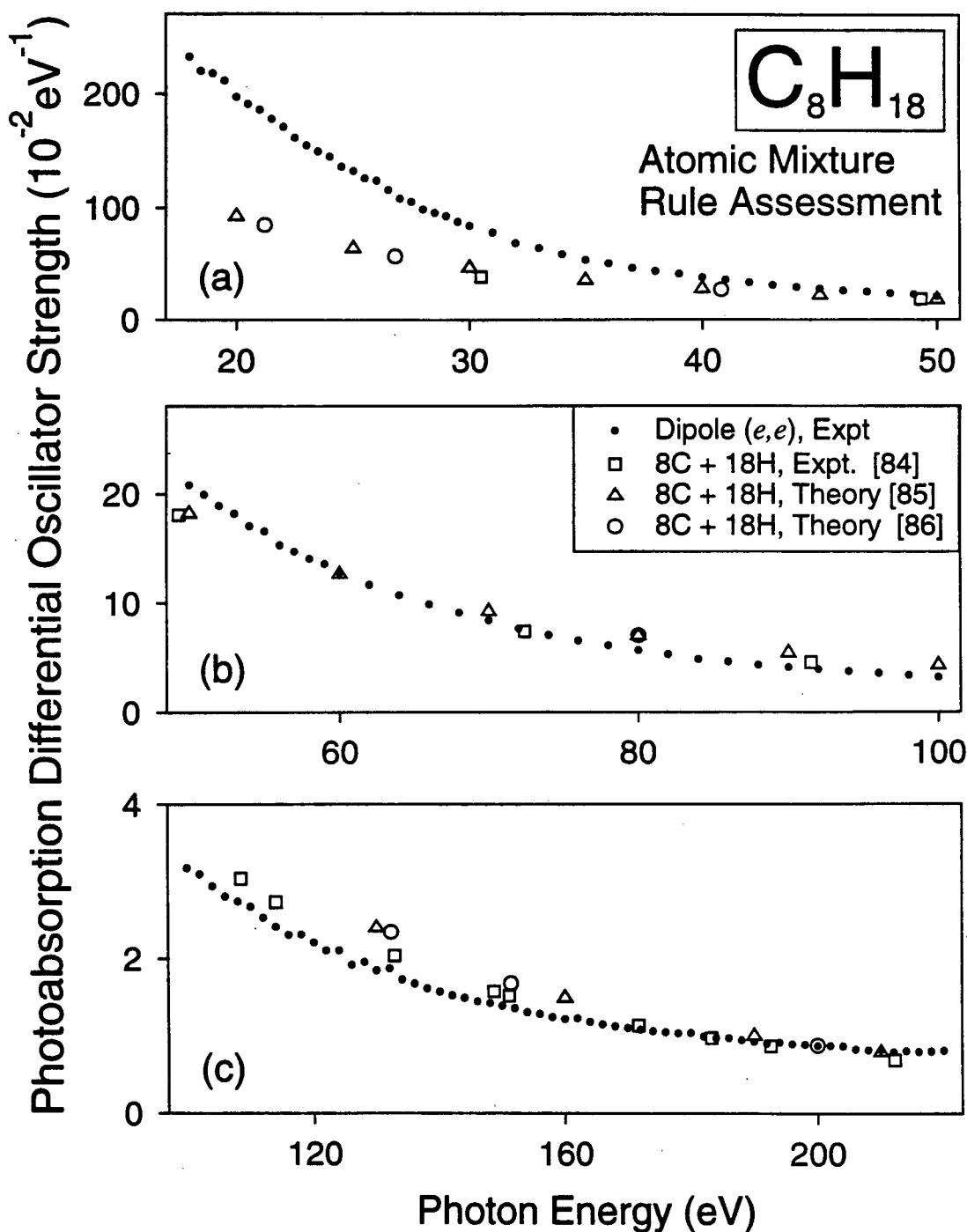


**Figure 4.14:** Comparison of atomic mixture rules (AMR's) determined using both experimentally [84] and theoretically [85,86] based data with directly measured photoabsorption differential oscillator strengths (1 eV fwhm) in the continuum energy region for normal octane: (a) 18–50 eV; (b) 50–100 eV; (c) 100–220 eV. The theoretical values for atomic hydrogen used to obtain the AMR represented by the triangles were derived from the exact formula for the differential oscillator strength distribution of the hydrogen atom for transitions from the ground electronic state to the continuum as given by Inokuti [12].

### 4.3.3 Molecular mixture rules

In addition to atomic mixture rules, equation (4.1) also permits molecular mixture rules (MMR's) to be constructed from linear combinations of data for smaller component molecules ( $C_i$ ). Using the experimentally measured photoabsorption differential oscillator strengths for the lower alkanes,  $C_nH_{2n+2}$  ( $n = 1-5$ ), (section 4.2.4, ref. [36]) and for molecular hydrogen [2] in place of  $C_i$ , a range of MMR's can be constructed. These mixture rules have been employed to estimate the differential oscillator strengths for  $C_5H_{12}$ ,  $C_6H_{14}$ ,  $C_7H_{16}$ , and  $C_8H_{18}$ . Since the data reported for  $H_2$  [2] only extend to 124 eV, they have been estimated at higher energies up to 220 eV by extrapolating a curve of the form

$$\frac{df}{dE} = AE^{-B}, \quad (4.3)$$

which was fitted in the 60 to 124 eV region to the measured data ( $A$  and  $B$  are best fit parameters). Such fitting procedures and extrapolation to higher energies have been found to provide reliable oscillator strength scales in previous work [5,8,14] and therefore can be expected to provide reasonably accurate predictions for  $H_2$  over the 124–220 eV energy range.

The various molecular mixture rules have been conveniently categorized into general classes of types I to IV (and labeled as equations (4.4) to (4.13)), as shown in table 4.4. These can in turn be further classified as being either  $H_2$ -dependent (types I to III) or  $H_2$ -independent (type IV). In the present work for alkanes, the coefficients (e.g.,  $q$ ,  $[(n/2)-1]$ , and  $[(n-1)/2]$  in table 4.4) have been limited to integral values. MMR's of type I comprise integral multiples of differential oscillator strengths for individual normal alkanes, ranging from  $CH_4$  to  $C_4H_{10}$  in equations (4.4) to (4.7), respectively<sup>1</sup>. An appropriate amount of differential oscillator strength contribution from  $H_2$  must also be subtracted from the total in order for the

number of hydrogen atoms in the mixture rule to be consistent with that required for the alkanes. Type II MMR's are constructed from the differential oscillator strength sum of two alkanes, less the differential oscillator strength value for one  $H_2$  molecule. In the present work, the first of the two alkane molecules is chosen from either  $CH_4$ ,  $C_2H_6$ , or  $C_3H_8$  (i.e., equations (4.8) to (4.10), respectively)<sup>1</sup>. Since the coefficient is one for the second alkane species, its size must be dependent on  $n$ , the carbon chain length for the alkane whose differential oscillator strength distribution is being predicted. While MMR's of type III appear similar to those of type II in the kinds of component molecules employed in the mixture rule, type III differs in that the differential oscillator strengths for  $CH_4$  are present in both equations (4.11) and (4.12), and that there is no dependence on  $n$  for the number of carbon atoms present in the second alkane species. Instead, type III MMR's estimate the differential oscillator strengths for larger alkane molecules by taking multiple sums of oscillator strengths for  $C_2H_6$  or  $C_3H_8$ <sup>1</sup> together with the corresponding values for  $CH_4$ . It is clear that type III cannot be applied in the case of even values of  $n$  (e.g.,  $C_8H_{18}$ ) if the coefficients in the mixture rule are integral. In contrast to the other three types of MMR, type IV (equation (4.13) in table 4.4) is independent of any differential oscillator strength data for molecular hydrogen. As such, formulations of type IV depend, as in the case of group additivity (see section 4.3.4 which follows), only on measurements for the alkanes reported in this laboratory (section 4.2.4 and ref. [36]). This type IV mixture rule can be used for estimating the differential oscillator strength distribution for  $C_nH_{2n+2}$  by adding the differential oscillator strength data for a small alkane molecule ( $C_nH_{2n+2}$ ) to those for a chain of  $CH_2$  fragments, obtained from the difference between the differential oscillator strengths for any two

---

<sup>1</sup> It should be noted that equations (4.4) to (4.12) in table 4.4 can be extended to involve higher homologues as appropriate.

Table 4.4

Types of molecular mixture rule (MMR) employed in the estimation of the absolute photoabsorption differential oscillator strengths for the normal alkanes,  $C_nH_{2n+2}$

Type	Molecular Mixture Rule (MMR) <sup>1</sup>	
	General formulation for $C_nH_{2n+2}$ <sup>2</sup>	Explicit formulation for $C_8H_{18}$
I	$n \, df/dE (CH_4) - (n-1) \, df/dE (H_2)$ (4.4) $(n/2) \, df/dE (C_2H_6) - [(n/2)-1] \, df/dE (H_2)$ (4.5) $(n/3) \, df/dE (C_3H_8) - [(n/3)-1] \, df/dE (H_2)$ (4.6) $(n/4) \, df/dE (C_4H_{10}) - [(n/4)-1] \, df/dE (H_2)$ (4.7) <i>etc.</i>	$8 \, df/dE (CH_4) - 7 \, df/dE (H_2)$ $4 \, df/dE (C_2H_6) - 3 \, df/dE (H_2)$ not applicable <sup>2</sup> $2 \, df/dE (C_4H_{10}) - df/dE (H_2)$
II	$df/dE (CH_4) + df/dE (C_{n-1}H_{2n}) - df/dE (H_2)$ (4.8) $df/dE (C_2H_6) + df/dE (C_{n-2}H_{2n-2}) - df/dE (H_2)$ (4.9) $df/dE (C_3H_8) + df/dE (C_{n-3}H_{2n-4}) - df/dE (H_2)$ (4.10) <i>etc.</i>	$df/dE (CH_4) + df/dE (C_7H_{16}) - df/dE (H_2)$ $df/dE (C_2H_6) + df/dE (C_6H_{14}) - df/dE (H_2)$ $df/dE (C_3H_8) + df/dE (C_5H_{12}) - df/dE (H_2)$
III	$df/dE (CH_4) + [(n-1)/2] \, df/dE (C_2H_6) - [(n-1)/2] \, df/dE (H_2)$ (4.11) $df/dE (CH_4) + [(n-1)/3] \, df/dE (C_3H_8) - [(n-1)/3] \, df/dE (H_2)$ (4.12) <i>etc.</i>	not applicable <sup>2</sup> not applicable <sup>2</sup>
IV	$df/dE (C_nH_{2n+2}) + q [df/dE (C_rH_{2r+2}) - df/dE (C_sH_{2s+2})];$ $n = p + q (r - s)$ (4.13)	see text for details

<sup>1</sup> Absolute oscillator strength data ( $df/dE$ ) estimated for  $C_nH_{2n+2}$ .

<sup>2</sup> All coefficients (e.g.,  $q$ ,  $[(n/2)-1]$ , and  $[(n-1)/2]$ ) are integral.

alkanes, i.e.,  $q [df/dE (C_rH_{2r+2}) - df/dE (C_sH_{2s+2})]$ , such that  $n = p + q (r - s)$ . Since the values for each of  $p$ ,  $r$ , and  $s$  can vary between one to five (as the data for  $CH_4$  up to  $C_5H_{12}$  are used in the present work), many possible MMR combinations can result from this equation.

In the present work, the MMR's described above have been evaluated by comparison with experimentally measured data for the higher normal alkanes,  $C_nH_{2n+2}$  ( $n = 5-8$ ) reported in section 4.2.4. It should be noted that only MMR's independent of any particular  $C_nH_{2n+2}$  data have been utilized for estimating the dipole differential oscillator strengths for that alkane. In total, 15, 25, 31, and 30 MMR's involving all four types (see table 4.4) have been evaluated for  $C_5H_{12}$ ,  $C_6H_{14}$ ,  $C_7H_{16}$ , and  $C_8H_{18}$ , respectively. Of these mixture rules, approximately 80% are of type IV (equation (4.13)). In all instances where linear combinations of integral multiples of component molecules (i.e., small alkane molecules and/or  $H_2$ ) can be obtained for equations (4.4) to (4.13), relative departures from experiment are found to be typical for a given MMR for each of  $C_5H_{12}$ ,  $C_6H_{14}$ ,  $C_7H_{16}$ , and  $C_8H_{18}$ . Therefore, a representative range of MMR's for  $C_8H_{18}$  are shown in figure 4.15, and the explicit formulations of types I-IV in the case of  $C_8H_{18}$  are shown in the right hand panel of table 4.4. Although as noted above no applicable MMR's of type III can be derived for  $C_8H_{18}$ , it has been found that in those alkanes (e.g.,  $C_5H_{12}$  and  $C_7H_{16}$ ) where type III MMR's are applicable, agreement of this type of molecular mixture rule with experiment falls in between types I and II.

Curves *a* and *b* in figure 4.15 represent MMR's involving  $H_2$  (i.e., selected from types II and I in table 4.4), which show the best and worst agreement, respectively, with the experimentally measured data. Note that the experimental oscillator strengths for  $C_6H_{14}$  and  $C_7H_{16}$  were also used in the second term of equations (4.9) and (4.8), respectively, for the construction of molecular mixture rules for estimating the differential oscillator strengths of  $C_8H_{18}$ . Curves *c* and *d*

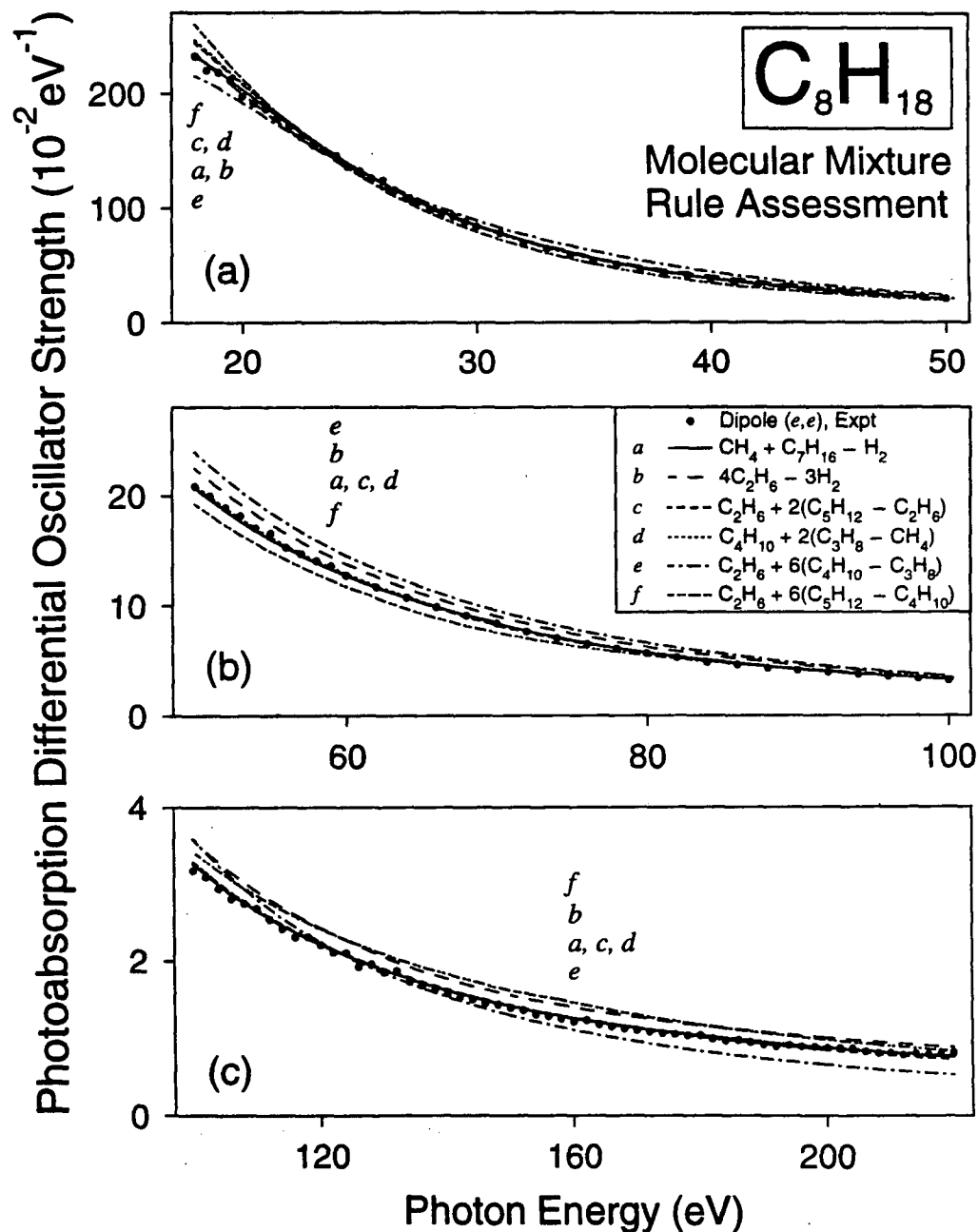


**Figure 4.15:** Comparison of selected molecular mixture rules (MMR's) with experimentally measured photoabsorption differential oscillator strengths (1 eV fwhm) in the continuum energy region for normal octane: (a) 18–50 eV; (b) 50–100 eV; (c) 100–220 eV. Curves *a* and *b* represent MMR's involving H<sub>2</sub> (i.e., selected from types II and I in table 4.4), which show the best and worst agreement, respectively, with the experimentally measured data. Curves *c* and *d* represent two of the H<sub>2</sub>-independent MMR's assessed in the present work (i.e., derived from type IV in table 4.4) showing the best agreement with experiment, while curves *e* and *f* depict two extreme cases where there is poor agreement with the experimental data. The sets of values,  $\{p, q, r, s\}$ , for curves *c*, *d*, *e*, and *f* are  $\{2, 2, 5, 2\}$ ,  $\{2, 4, 3, 1\}$ ,  $\{7, 2, 4, 3\}$ , and  $\{7, 2, 5, 4\}$ , respectively (see text for details).

represent two of the 24  $H_2$ -independent MMR's assessed in the present work (i.e., derived from type IV in table 4.4) which show the best agreement with experiment. The two sets of values,  $\{p, q, r, s\}$ , for curves  $c$  and  $d$  are  $\{2, 2, 5, 2\}$  and  $\{2, 4, 3, 1\}$ , respectively. In contrast, curves  $e$  and  $f$  depict two extreme cases of type IV where very poor agreement with experiment is found. The  $\{p, q, r, s\}$  values for these two curves are  $\{7, 2, 4, 3\}$  and  $\{7, 2, 5, 4\}$ , respectively. In order to facilitate comparison of the various molecular mixture rules, the curves ( $a$  to  $f$ ) shown in fig. 4.15 are the result of a least squares fit procedure involving polynomial functions, which has been applied to the final MMR sums. This procedure reduces any non-spectral fluctuations due to random noise in the experimental data [36].

In general, the present evaluation of the various types of molecular mixture rules shows that MMR's provide very variable estimates of the photoabsorption oscillator strengths for  $C_5H_{12}$ ,  $C_6H_{14}$ ,  $C_7H_{16}$ , and  $C_8H_{18}$ . Of the molecular mixture rules involving  $H_2$  in the linear combination (types I to III in table 4.4), those of type II (e.g. curve  $a$  in figure 4.15) provide the best estimates of the experimentally measured differential oscillator strengths for the normal alkanes, especially when the largest possible alkane subcomponent is used. In contrast, MMR's belonging to types I (see for example curve  $b$ ) and III show fair to poor agreement with experiment. Within each type of MMR, in some cases agreement with experiment tends to become progressively better as the alkane component molecule in the mixture rule increases in size. For example, equation (4.7) provides a better estimate of the oscillator strengths for  $C_8H_{18}$  than do equations (4.4) and (4.5); however, equation (4.5) actually departs from the experimental data more than equation (4.4). In view of these considerations, curves  $a$  and  $b$  in figure 4.15 illustrate the best and worst photoabsorption differential oscillator strength estimates for  $C_8H_{18}$  selected from MMR's of types I to III. All remaining molecular mixture rules of these types (I to III) predict values which fall within the range

between curves *a* and *b* in the case of  $C_8H_{18}$ . Analogous results are found for  $C_5H_{12}$ ,  $C_6H_{14}$ , and  $C_7H_{16}$ .

Molecular mixture rules of type IV (equation (4.13) in table 4.4) afford by far the largest number of MMR's to be constructed, since many different combinations of *p*, *q*, *r*, and *s* can result when differential oscillator strengths for  $C_nH_{2n+2}$  ( $n = 1-5$ ) [36] are used as input data. In the present work, all 24 possible MMR's of this type were constructed and assessed for  $C_8H_{18}$ . Similar to the situation for types I to III, MMR's derived from type IV result in very variable estimates of the photoabsorption differential oscillator strengths for the higher alkanes ( $n = 5-8$ ). Although good agreement with experiment is obtained with some linear combinations, many others result in substantial errors ( $\sim 10-30\%$  over the 18-220 eV range). For example, in figure 4.15 curves *c* and *d* illustrate two MMR's which show good agreement with the experimentally measured data above 25 eV for  $C_8H_{18}$ , while curves *e* and *f* illustrate two extreme cases where very poor agreement with experiment for both magnitude and shape is observed. In general, these MMR's provide progressively better estimates of the oscillator strengths for  $C_5H_{12}$ ,  $C_6H_{14}$ ,  $C_7H_{16}$ , and  $C_8H_{18}$  as the following two conditions for the *p*, *q*, *r*, and *s* values in equation (4.13) are met in order:

- (1) Firstly, the difference ( $r - s$ ) should be as large as possible, i.e., the values for *r* and *s* must result in differential oscillator strengths for as long a chain of  $CH_2$  fragments as is possible, when differences between the differential oscillator strengths for  $C_rH_{2r+2}$  and  $C_sH_{2s+2}$  are taken.
- (2) Secondly, *p* should also be as large as possible. As a result, *q* will be small, in keeping with the values of *r* and *s*.

The validity of these conditions can simply be attributed to the fact that differential oscillator strengths for long chains of  $CH_2$  fragments, and for large alkane species, contain more molecular effects characteristic of long-chained hydrocarbon molecules.

In view of these considerations, it can be seen from figure 4.15 that the two sets of values,  $\{p, q, r, s\}$ , for curves  $c$  and  $d$  which show good agreement with the experimental data for  $C_8H_{18}$  are  $\{2, 2, 5, 2\}$  and  $\{2, 4, 3, 1\}$ , respectively. Likewise, it is found that the MMR (not shown in figure 4.15) having the set of values,  $\{1, 5, 4, 1\}$ , for  $\{p, q, r, s\}$  provide similarly good estimates of the dipole differential oscillator strengths for octane. In contrast, the  $\{p, q, r, s\}$  values for curves  $e$  and  $f$ , which depict two extreme cases where very poor agreement with experiment occurs, are  $\{7, 2, 4, 3\}$  and  $\{7, 2, 5, 4\}$ , respectively. All remaining MMR's for  $C_8H_{18}$  derived from equation (4.13) provide photoabsorption oscillator strength estimates that fall in between curves  $e$  and  $f$  in figure 4.15.

From the present assessment of the feasibility of using molecular mixture rules for predicting dipole differential oscillator strengths for the higher alkanes ( $n = 5-8$ ), it is found that while MMR's constructed using differential oscillator strengths for larger alkanes tend to give better estimates of the experimentally measured data, no other *a priori* physical or chemical reasons can be advanced for any particular choice of MMR. Therefore, the molecular mixture rule procedure can be considered unsatisfactory for general application, particularly for the prediction of differential oscillator strengths for much larger alkane homologues unless data for nearby homologues are available.

#### 4.3.4 Group Additivity

As mentioned previously in section 4.3.1 and illustrated in figure 4.13, continuum photoabsorption differential oscillator strengths at any given photon energy for  $CH_4$  to  $C_8H_{18}$  increase essentially linearly with increasing number of carbon atoms in the molecule. Since the linear alkane chain elongates by addition of  $CH_2$  units, it seems likely that such an addition is directly related to the increase in

oscillator strength between any two consecutive hydrocarbon molecules. Therefore, taking equation (4.1) with  $C_i$  as the functional group entities,  $\text{CH}_2$  and  $\text{CH}_3$ , we can obtain a mixture rule using group additivity,

$$\overline{\frac{df}{dE}}(\text{C}_n\text{H}_{2n+2}) = 2 \overline{\frac{df}{dE}}(\text{CH}_3) + (n-2) \overline{\frac{df}{dE}}(\text{CH}_2), \quad (4.14)$$

where  $\overline{df/dE}(\text{CH}_3)$  and  $\overline{df/dE}(\text{CH}_2)$  are "average" oscillator strengths for the methyl ( $\text{CH}_3$ ) and methylene ( $\text{CH}_2$ ) groups, respectively, in the alkane environment. The value for  $\text{CH}_2$  has been obtained in the present work by averaging the results obtained from all fifteen possible combinations within the summation,

$$\overline{\frac{df}{dE}}(\text{CH}_2) = \frac{1}{15} \sum_{l=2}^7 \sum_{\substack{k=2 \\ k < l}}^7 \frac{1}{l-k} \left[ \overline{\frac{df}{dE}}(\text{C}_l\text{H}_{2l+2}) - \overline{\frac{df}{dE}}(\text{C}_k\text{H}_{2k+2}) \right], \quad (4.15)$$

using the complete experimental data for  $\text{C}_n\text{H}_{2n+2}$  ( $n = 2-7$ ) reported in section 4.2.4 and in ref. [36]; thus, all data have been used and no *a priori* choice of any particular molecular data set is involved. The differential oscillator strength values for  $\text{CH}_4$  have been excluded since the chemical environment for the  $\text{CH}_2$  and  $\text{CH}_3$  components in the  $\text{CH}_4$  molecule differs appreciably from that in the higher alkanes. The importance of incorporating the considerations of a relevant chemical environment in additivity schemes has been stressed earlier by Meath and co-workers in the context of other dipole properties [80]. The average (dots in figure 4.16) of the complete range of results from 18 to 220 eV, evaluated according to equation (4.15) for all possible combinations of  $n = 2-7$ , was least squares fitted with (overlapping) polynomial functions of the form given earlier by equation (3.1) to remove the effects of random noise on the originally measured data (see figure 4.13). The best fit parameters,  $A$ ,  $B$ , and  $C$ , for the polynomial functions are given in table 4.5, and the resulting average values for  $\overline{df/dE}(\text{CH}_2)$  as a function of photon energy are shown

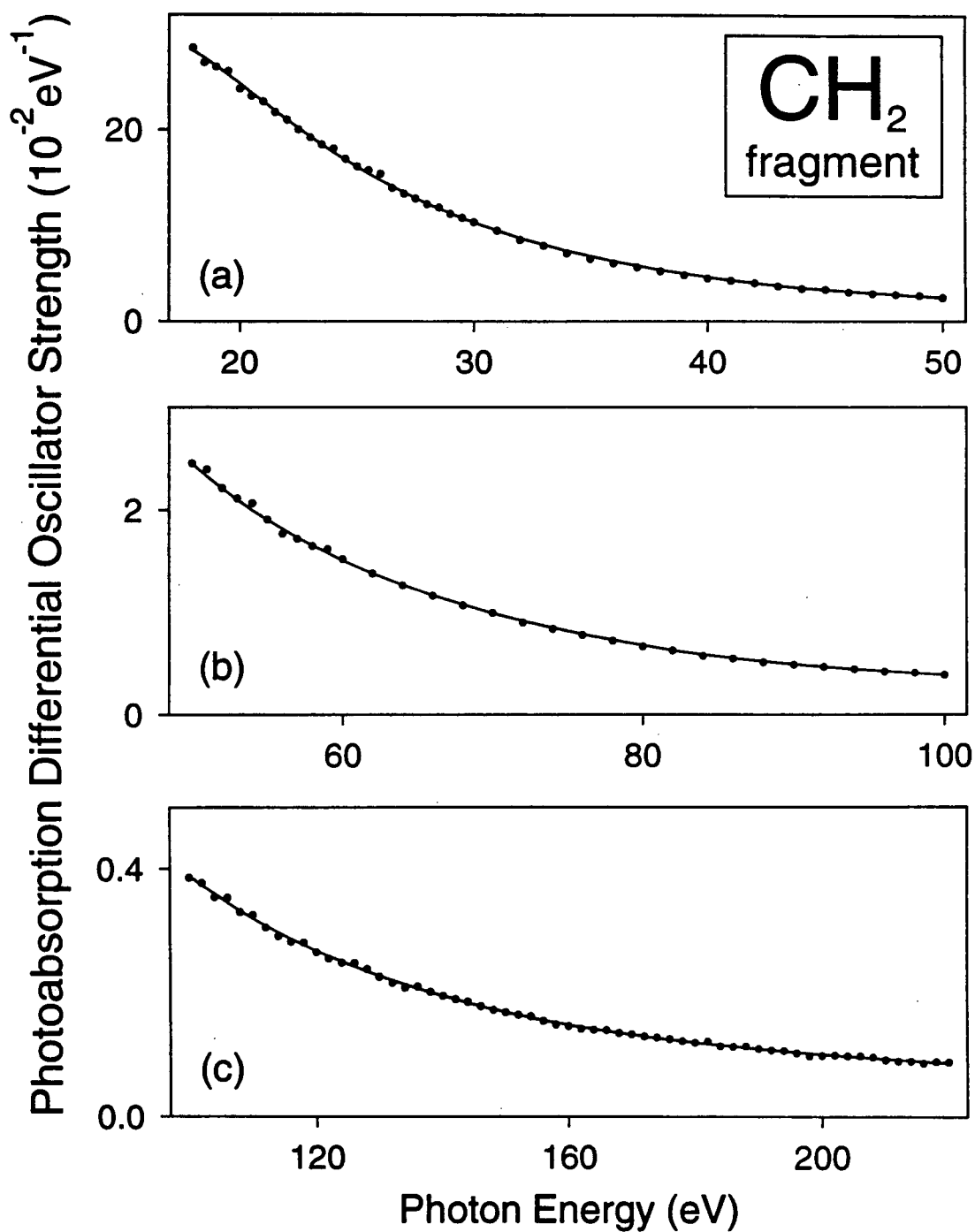


**Figure 4.16:** Average dipole differential oscillator strengths for the methylene ( $\text{CH}_2$ ) group fragment, derived from photoabsorption measurements in section 4.2.4 and in ref. [36] for the homologous series,  $\text{C}_n\text{H}_{2n+2}$  ( $n = 2-7$ ), using equation (4.15): (a) 18–50 eV; (b) 50–100 eV; (c) 100–220 eV. The line represents the result of a least squares fit procedure involving polynomial functions (see table 4.5 for details) applied to the averaged data (shown as dots).

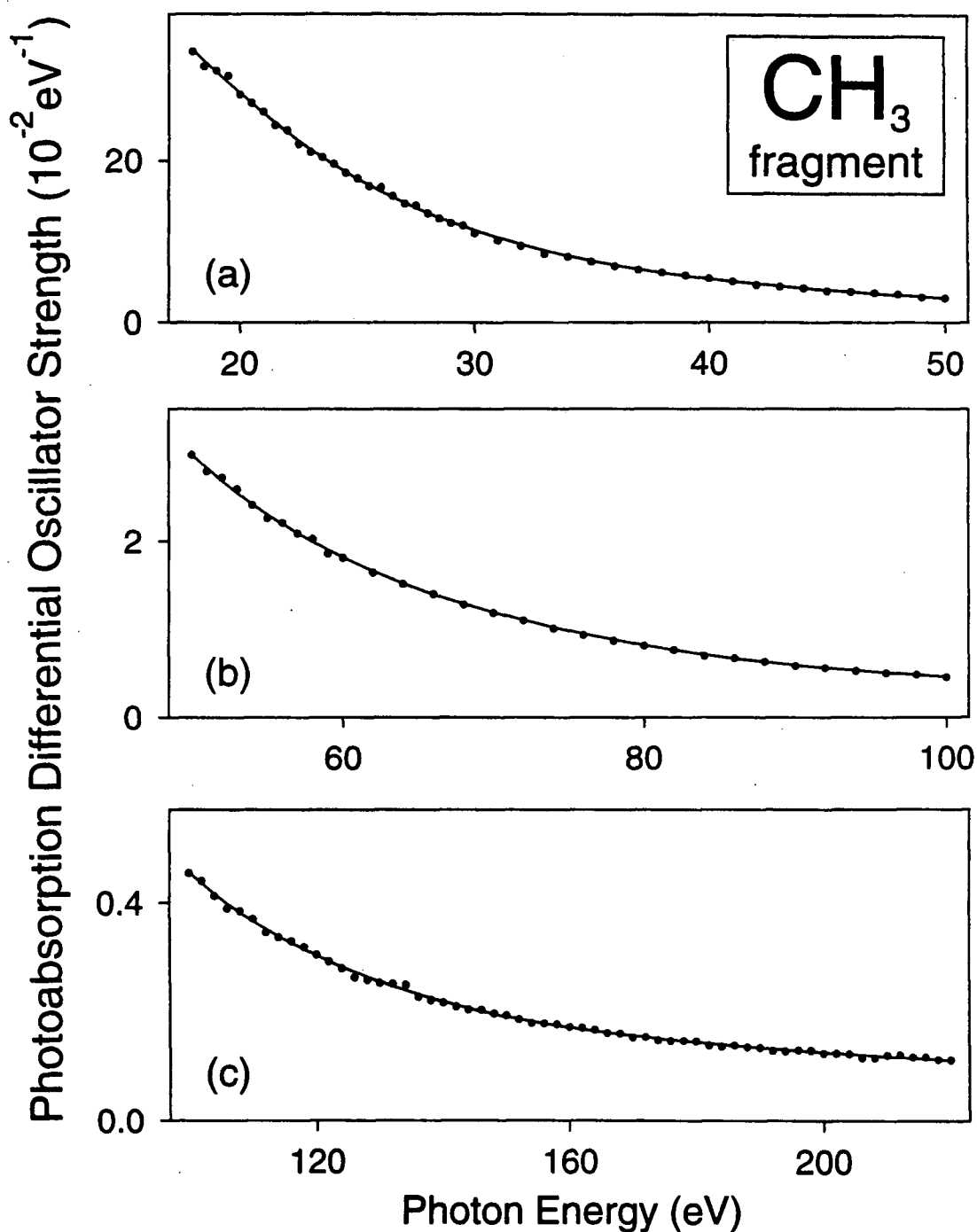


**Figure 4.17:** Average dipole differential oscillator strengths for the methyl ( $\text{CH}_3$ ) group fragment, derived from photoabsorption measurements in section 4.2.4 and in ref. [36] for the homologous series,  $\text{C}_n\text{H}_{2n+2}$  ( $n = 2-7$ ), using equation (4.16): (a) 18–50 eV; (b) 50–100 eV; (c) 100–220 eV. The line represents the result of a least squares fit procedure involving polynomial functions (see table 4.5 for details) applied to the average data (shown as dots).

**Table 4.5**

Best fit parameters determined by least squares fits of the average differential oscillator strengths for the methylene ( $\text{CH}_2$ ) and methyl ( $\text{CH}_3$ ) alkane group fragments using the polynomial function given by equation (3.1)

The methylene ( $\text{CH}_2$ ) group fragment <sup>1</sup>				The methyl ( $\text{CH}_3$ ) group fragment <sup>1</sup>			
Energy region (eV)	A (eV)	B ( $\text{eV}^2$ )	C ( $\text{eV}^3$ )	Energy region (eV)	A (eV)	B ( $\text{eV}^2$ )	C ( $\text{eV}^3$ )
18 – 43	$-4.9674 \times 10^1$	$6.8878 \times 10^3$	$-7.8171 \times 10^4$	18 – 40	$-1.6300 \times 10^1$	$5.5842 \times 10^3$	$-5.9895 \times 10^4$
43 – 59	$2.4133 \times 10^1$	$1.5822 \times 10^3$	$1.4097 \times 10^4$	40 – 64	$6.3181 \times 10^{-1}$	$4.7683 \times 10^3$	$-5.3315 \times 10^4$
59 – 82	$-1.7901 \times 10^1$	$6.5162 \times 10^3$	$-1.3178 \times 10^5$	64 – 82	$-2.7251 \times 10^1$	$8.9675 \times 10^3$	$-2.0928 \times 10^5$
82 – 102	$1.0040 \times 10^2$	$-1.2332 \times 10^4$	$6.1696 \times 10^5$	82 – 100	$7.1467 \times 10^1$	$-6.7404 \times 10^3$	$4.1416 \times 10^5$
102 – 142	$3.6355 \times 10^1$	$1.9431 \times 10^2$	$7.4152 \times 10^3$	100 – 144	$5.5180 \times 10^1$	$-3.5570 \times 10^3$	$2.6000 \times 10^5$
142 – 220	$8.1266 \times 10^1$	$-1.3450 \times 10^4$	$1.0409 \times 10^6$	144 – 220	$1.3134 \times 10^2$	$-2.5411 \times 10^4$	$1.8268 \times 10^6$

<sup>1</sup> The differential oscillator strengths ( $df/dE$ ), obtained by substitution of these parameters into equation (3.1), may be converted to absolute photoabsorption cross sections using the relation,  $\sigma [\text{Mb}] = 1.0975 \times 10^2 (df/dE) [\text{eV}^{-1}]$ .

by the line through the data points in figure 4.16.

Using the  $\overline{df/dE}(\text{CH}_2)$  data derived from equation (4.15),  $\overline{df/dE}(\text{CH}_3)$  has been determined by averaging the results obtained from all possible combinations within the summation,

$$\overline{\frac{df}{dE}}(\text{CH}_3) = \frac{1}{12} \sum_{n=2}^7 \left[ \frac{df}{dE}(\text{C}_n\text{H}_{2n+2}) - (n-2) \overline{\frac{df}{dE}}(\text{CH}_2) \right]. \quad (4.16)$$

The average differential oscillator strengths for the  $\text{CH}_3$  group were then smoothed with a similar polynomial fitting procedure as employed in the case of  $\text{CH}_2$ . The best fit parameters,  $A$ ,  $B$ , and  $C$ , obtained for the  $\text{CH}_3$  group fragment are also given in table 4.5, and the resulting average values for  $\overline{df/dE}(\text{CH}_3)$  as a function of photon energy are shown in figure 4.17.

Using the values derived for  $\overline{df/dE}(\text{CH}_2)$  and  $\overline{df/dE}(\text{CH}_3)$  in the formulation of equation (4.14), it can be seen from figure 4.18 that excellent agreement ( $\leq 2\%$  difference at any given photon energy) is obtained between the group additivity sum (solid line) and the presently measured differential oscillator strengths (dots) for  $\text{C}_8\text{H}_{18}$  over the entire energy region studied (18–220 eV). In order to provide a more direct comparison with the molecular mixture rules, which were constructed using only certain selections of the differential oscillator strengths for  $\text{CH}_4$  to  $\text{C}_5\text{H}_{12}$  [36] in section 4.3.3, modified sets of average differential oscillator strengths for the methylene and methyl groups,  $\overline{df/dE}(\text{CH}_2)$  and  $\overline{df/dE}(\text{CH}_3)$ , have also been derived using only the data for  $\text{C}_2\text{H}_6$  to  $\text{C}_5\text{H}_{12}$  in equations (4.15) and (4.16). The resulting photoabsorption differential oscillator strength estimate for  $\text{C}_8\text{H}_{18}$  is plotted as a function of photon energy in figure 4.18 in the form of a dashed line. It can be seen that the dashed line shows as good agreement with the experimentally measured data as that given by the solid line derived using data for  $\text{C}_2\text{H}_6$  to  $\text{C}_7\text{H}_{16}$ . Equally excellent agreement with experiment is also obtained for  $\text{C}_6\text{H}_{14}$  and  $\text{C}_7\text{H}_{16}$ .

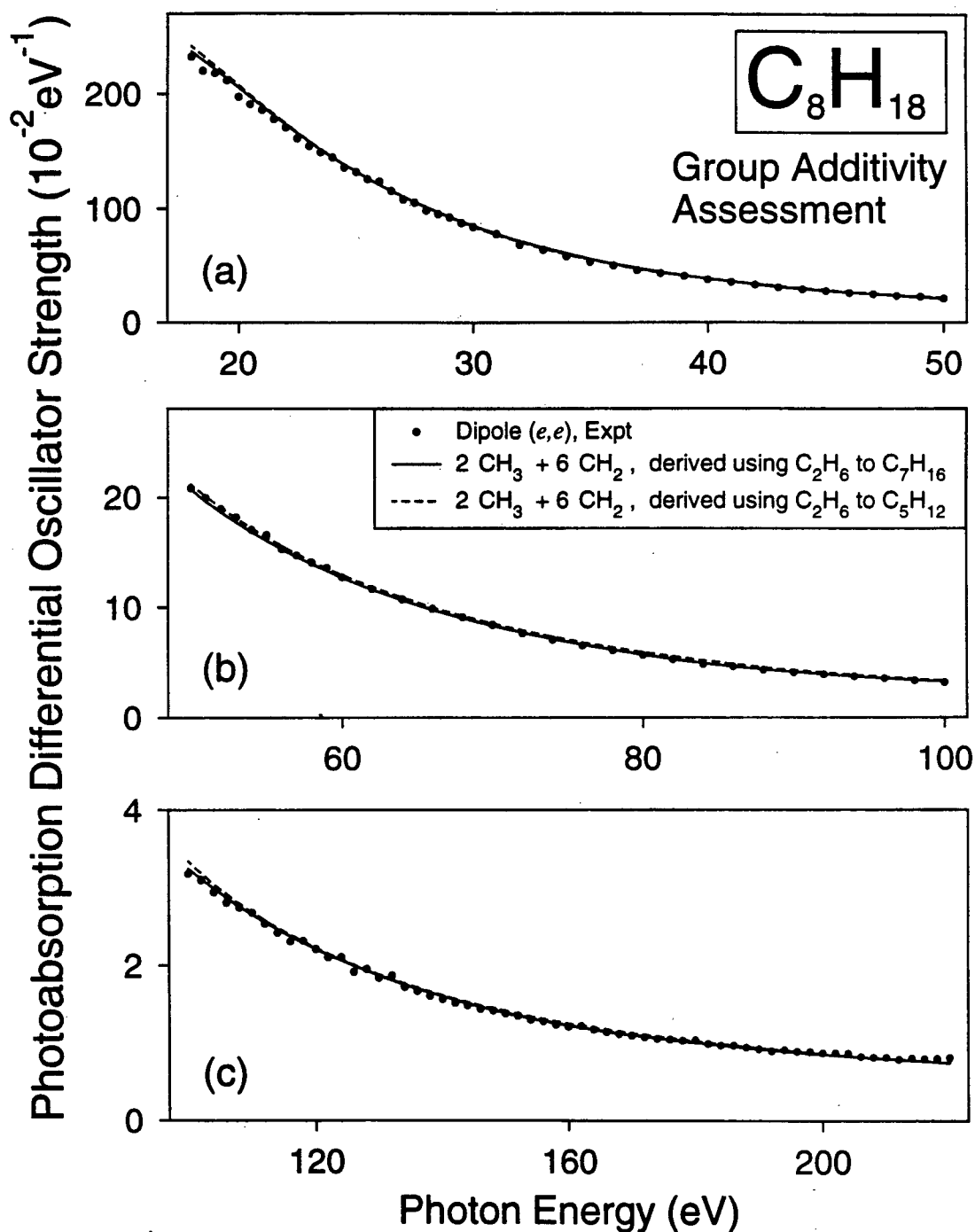


**Figure 4.18:** Comparison of  $(2 \text{ CH}_3 + 6 \text{ CH}_2)$  differential oscillator strength sums, obtained using group additivity involving the values in figures 4.16 and 4.17, with directly measured photoabsorption differential oscillator strengths (1 eV fwhm) in the continuum energy region for normal octane: (a) 18–50 eV; (b) 50–100 eV; (c) 100–220 eV. The differential oscillator strengths for  $\text{C}_2\text{H}_6$  to  $\text{C}_7\text{H}_{16}$  and for  $\text{C}_2\text{H}_6$  to  $\text{C}_5\text{H}_{12}$  were used in the group additivity estimate for  $\text{C}_8\text{H}_{18}$ , and these are represented by the solid and dashed lines, respectively. See text for details.

when the appropriately modified data sets (i.e., using the data from  $C_2H_6$  to  $C_5H_{12}$ ) for  $\overline{df/dE}(CH_2)$  and  $\overline{df/dE}(CH_3)$  are employed in equation (4.14). The good agreement between the present group additivity investigations for  $C_8H_{18}$  using data for  $C_2H_6$  to  $C_5H_{12}$ , or alternatively for  $C_2H_6$  to  $C_7H_{16}$ , suggests that "convergence" of the  $\overline{df/dE}(CH_2)$  and  $\overline{df/dE}(CH_3)$  group differential oscillator strengths has essentially been reached, and thus lends further support to the accuracy of these procedures. Therefore, in the case of group additivity, good predictions for higher members of an homologous series can be expected using data for a limited but sufficient number of lower homologues. The requirement found earlier for MMR's (see section 4.3.3), that the best results are obtained using data for a similarly large member of a series, is not essential in the case of group additivity. These findings suggest that group additivity using data for the first four to six homologues in the series (excluding  $CH_4$ ) is a far more reliable and generally applicable technique than MMR's for the estimation of photoabsorption differential oscillator strength distributions for long-chained alkane molecules.

### 4.3.5 Conclusions

The feasibility of using atomic and molecular mixture rules as well as group additivity concepts for predicting differential oscillator strengths (cross sections) for the valence-shell photoabsorption of long-chained alkane molecules has been investigated over a wide energy range from 18 to 220 eV. It has been found that atomic mixture rules (AMR's) based on both theoretical and experimental atomic oscillator strength data are unsatisfactory, giving very large errors at most photon energies. Such departures from experiment are to be expected due to the intrinsic neglect of contributions from molecular effects in the AMR values. In the case of molecular mixture rules (MMR's), although good agreement with experiment is

obtained with some linear combinations, many others result in substantial errors. While it is found that MMR's constructed using differential oscillator strengths for larger component alkanes tend to give somewhat better estimates of the experimentally measured data, no other *a priori* physical or chemical reasons can be advanced as general criteria for choosing reliable MMR's for predictions for much larger species. In contrast, a group additivity procedure based on estimates of the oscillator strengths for CH<sub>2</sub> and CH<sub>3</sub> functional group fragments, derived from photoabsorption measurements for lower members of the homologous series [36], C<sub>n</sub>H<sub>2n+2</sub>, provides excellent agreement with the measured differential oscillator strengths for C<sub>8</sub>H<sub>18</sub> over the entire energy range studied (18–220 eV).

The results of the present assessment suggest that the isolated species approximation [73], given by equation (1), provides the best differential oscillator strength estimates when the component species, C<sub>i</sub>, are molecules or functional groups closely related in terms of chemical environment to the species of interest (in this case the long-chained, saturated hydrocarbons). These conclusions are consistent with the findings of Meath *et al.* [38,80] for prediction of other dipole properties and also with the concept of bond transferability within the alkane series [88]. The applicability of group additivity clearly reflects the preservation of alkane-like molecular effects in the differential oscillator strength estimates for the CH<sub>2</sub> and CH<sub>3</sub> components. The present group additivity work furthermore suggests that accurate differential oscillator strength measurements for the first four to six members of an homologous series will, in general, provide an adequate input database for the accurate prediction of radiation absorption by larger homologues and corresponding hydrocarbon groupings involved in other large molecules in the vacuum UV and soft X-ray region above 20 eV.

## Chapter 5

# Photoabsorption Studies of Phosphorus Halides

### 5.1 Introduction

The phosphorus halides,  $\text{PF}_3$ ,  $\text{PCl}_3$ , and  $\text{PF}_5$ , have been chosen for the present valence and inner shell photoabsorption study because the absolute oscillator strengths for third row molecules are of fundamental scientific interest, given that very few experimental studies have been made for such species compared to second row molecules. In particular, phosphorus is interesting among the third row atoms in that it can form stable neutral molecules having either three or five ligands. Although the large number of electrons in  $\text{PF}_3$ ,  $\text{PCl}_3$ , and  $\text{PF}_5$  present a challenge to theoretical studies, the high symmetry of these molecules make them a good test-bed for theory.

In the case of phosphorus trichloride ( $\text{PCl}_3$ ), there is also considerable industrial interest in quantitative photoabsorption data, since  $\text{PCl}_3$  is a widely used chemical reagent in the synthesis of organic and inorganic molecules. For example, photochemical reactions involving  $\text{PCl}_3$  [e.g., 89–92] have been documented over the past decade.  $\text{PCl}_3$  also finds applications in surface science as a dopant of silicon surfaces [93], in photo-assisted chemical vapor deposition, in gas phase etching of indium phosphide [94] and in dry plasma etching of semiconductors [95].

The valence shell spectral data available in the literature for electronic excitation of phosphorus trifluoride ( $\text{PF}_3$ ) is very limited, with few measurements of absolute differential oscillator strengths. Following the relative photographic work of Humphries *et al.* [96] in the limited valence-shell region, 6.9–11.8 eV, McAdams

and Russell [97] reported absolute optical density measurements from 5 to 10 eV. Inner-shell excitation in  $\text{PF}_3$  has been examined by synchrotron radiation [98,99,100], but only the work of Ishiguro *et al.* [98] reported absolute photoabsorption spectra for the P  $2p$  and  $2s$  inner-shell regions. In other related work, Sodhi and Brion [101,102] obtained relative intensities for valence and inner shell (P  $2p,2s$  and F  $1s$ ) excitation of  $\text{PF}_3$  using electron energy-loss spectroscopy at 2.5 keV impact energy.

The spectroscopic information available in the literature for photoabsorption of  $\text{PCl}_3$  is similarly very limited. Following the photographic work of Humphries *et al.* [96] between 6.2–9.5 eV, Halmann [103] and McAdams and Russell [97] recorded the absolute valence-shell photoabsorption spectrum of  $\text{PCl}_3$  over the energy ranges of 5.0–6.7 and 5–10 eV, respectively. In the phosphorus and chlorine  $2p$  and  $2s$  inner shell regions, relative [104] and absolute [98] cross sections have been measured using monochromated synchrotron radiation. X-ray emission spectra for the valence and  $2p$  (phosphorus and chlorine) shells of  $\text{PCl}_3$  have been obtained and assigned, based on SCF-X $\alpha$ -SW calculations, by Topol *et al.* [105]. In other work, Sodhi and Brion [101,102] obtained the valence (5–25 eV) and inner (P  $2p,2s$ ; Cl  $2p,2s$ ) shell EEL spectra of  $\text{PCl}_3$  using high impact energy and small scattering angles, but no absolute measurements were made. In this latter work [102], the phosphorus  $2p$  spectrum unexpectedly showed a prominent transition at 135.11 eV, which was not observed in either of the photon-based studies [98,104]. Impurities were seemingly ruled out as the cause of this transition from a careful consideration of the high resolution valence shell EEL spectrum. Since this peak was found to increase in intensity with increase in momentum transfer (achieved by measuring the spectrum over a small range of scattering angles), the authors [102] attributed it to a dipole-forbidden transition even though such a possibility was surprising in view of the low momentum transfer conditions.

In the case of phosphorus pentafluoride ( $\text{PF}_5$ ), the valence [101] and inner (P  $2p,2s$ ; F  $1s$ ) [106] shell electronic spectra have been previously investigated by electron energy-loss spectroscopy in 1985, and tentative spectral assignments were then made based on term values and quantum defects. More recently, two optical studies [107,108] have been reported over a very limited energy region (135–180 eV) of the phosphorus  $2p$  shell spectrum, but to date no absolute photoabsorption data have been reported for either of the valence or core regions of  $\text{PF}_5$ .

In the present work, the absolute photoabsorption spectra of  $\text{PF}_3$ ,  $\text{PCl}_3$ , and  $\text{PF}_5$  have been measured by low resolution (1 eV fwhm) dipole ( $e,e$ ) spectroscopy over wide energy ranges spanning the valence and inner (P  $2p,2s$ ; Cl  $2p,2s$ ) shells from 5 to 300 eV. High resolution dipole ( $e,e$ ) spectroscopy has also been used to obtain absolute oscillator strengths for the discrete profiles observed in the valence and inner (P  $2p$ , Cl  $2p$ ) shell regions at 0.05–0.1 eV fwhm.

## 5.2 Results and Discussions

The VTRK sum-rule [27] has been used to normalize the long-range, relative photoabsorption spectra (1 eV fwhm) of  $\text{PF}_3$ ,  $\text{PCl}_3$ , and  $\text{PF}_5$  obtained in the present work to absolute values. In this procedure the contribution of each of the phosphorus halides to the valence-shell photoabsorption above 130 eV (the onset of the P  $2p$  spectrum) was estimated by fitting a polynomial of the form given by equation (3.1) to the relative valence-shell photoabsorption data ( $df/dE$ ) over the energy range, 85–130 eV, and extrapolating to infinite energy. Each of the relative valence-shell photoabsorption spectra was then integrated from the first excitation threshold to infinite energy, and the total area were normalized to total valence-shell oscillator strengths ( $Z_{val} + Z_p$ ) of 27.00, 26.98, and 41.55 for  $\text{PF}_3$ ,  $\text{PCl}_3$ , and  $\text{PF}_5$ , respectively (see section 3.1.1 and table 3.1 for details). The parameters, A, B,

and C given in table 5.1 have been normalized such that the absolute valence-shell contribution to the total photoabsorption of  $\text{PF}_3$ ,  $\text{PCl}_3$ , and  $\text{PF}_5$  can be estimated in the inner-shell regions above 130 eV by direct substitution into equation (3.1). This permits estimates of the inner shell (P  $2p,2s$ ; Cl  $2p,2s$ ) oscillator strengths to be obtained from the total differential oscillator strength values in tables A8, A10, and A12, respectively, by subtracting the corresponding valence-shell contributions determined from equation (3.1).

**Table 5.1**

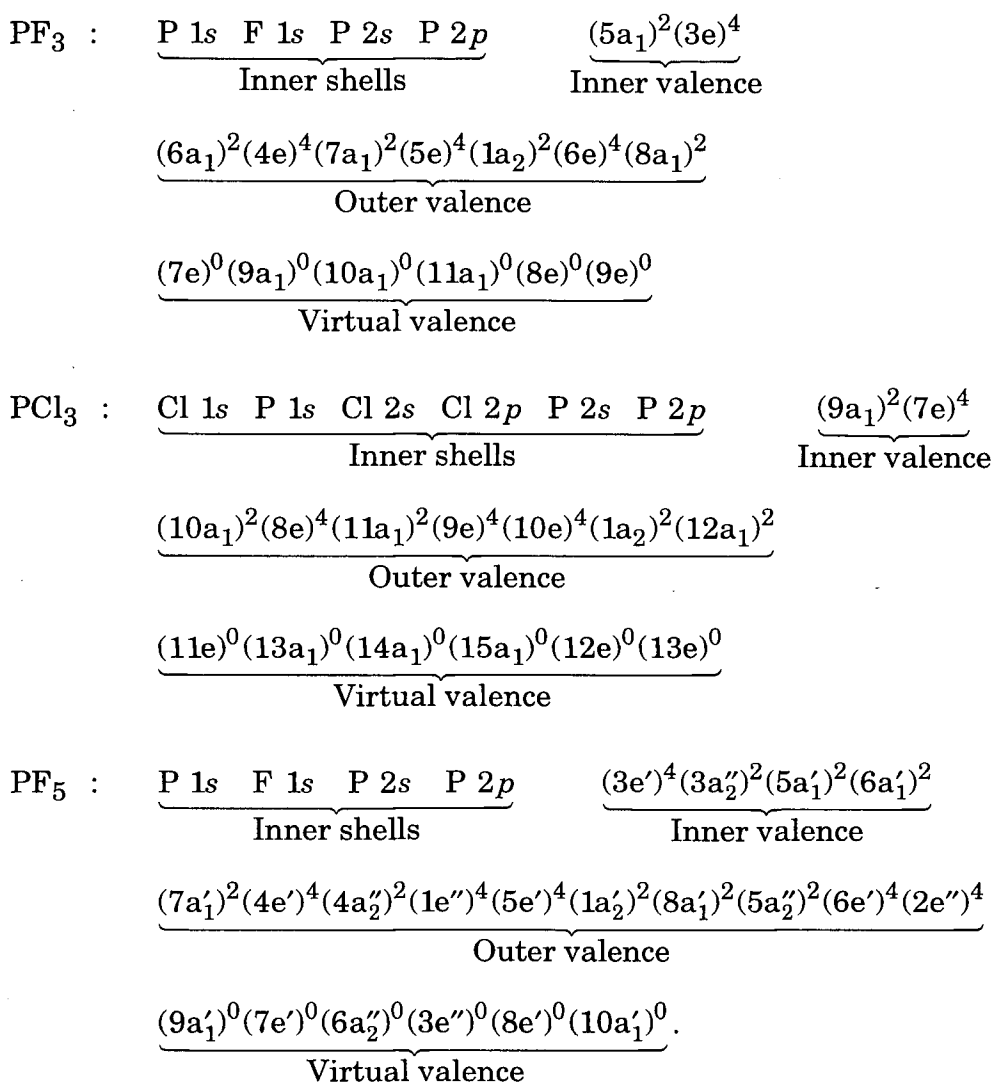
Best fit parameters determined by fitting equation (3.1) to the valence-shell differential oscillator strengths at high energy for  $\text{PF}_3$ ,  $\text{PCl}_3$ , and  $\text{PF}_5$

Phosphorus halide	Best fit parameters <sup>1</sup>		
	A (eV)	B (eV <sup>2</sup> )	C (eV <sup>3</sup> )
$\text{PF}_3$	$-2.3274 \times 10^4$	$2.2561 \times 10^7$	$-1.1931 \times 10^9$
$\text{PCl}_3$	$3.9361 \times 10^4$	$-5.1302 \times 10^5$	$-8.3066 \times 10^7$
$\text{PF}_5$	$3.9311 \times 10^4$	$2.1274 \times 10^7$	$-1.2251 \times 10^9$

<sup>1</sup> Coefficients in equation (3.1)

## 5.2.1 Electronic structures

Both phosphorus trifluoride ( $\text{PF}_3$ ) and phosphorus trichloride ( $\text{PCl}_3$ ) have trigonal pyramidal geometry and belong to the  $C_{3v}$  symmetry group. Phosphorus pentafluoride ( $\text{PF}_5$ ) has  $D_{3h}$  symmetry and trigonal bipyramidal geometry. The photoabsorption spectra of these molecules will be discussed with reference to the electronic ground state, molecular orbital configuration in the independent particle model:



In the case of  $\text{PF}_3$ , the  $11a_1$ ,  $8e$ , and  $9e$  virtual valence orbitals involve P  $3d$  character [43,108]. The vertical ionization potentials (VIP's) for the seven outer-valence ion states have been determined to be 12.27 ( $8a_1^{-1}$ ), 15.88 ( $6e^{-1}$ ), 16.30 ( $1a_2^{-1}$ ), 17.46 ( $5e^{-1}$ ), 18.60 ( $7a_1^{-1}$ ), 19.50 ( $4e^{-1}$ ), and 22.55 eV ( $6a_1^{-1}$ ) using He (I) and He (II) photoelectron spectroscopy [109]. No experimental data or many-body Greens' Function calculations are available for the two inner-valence ionization processes ( $3e^{-1}$  and  $5a_1^{-1}$ ), which are each expected to be split into a range of final ion states (poles) by electron correlation effects [110]. Therefore, in the present work the independent particle orbital energies of 35.48 and 36.47 eV, respectively, from

the continuum MS-X $\alpha$  calculations of Powis [43] have been used as average estimates of the VIP's for these ionization processes. The ordering of the virtual valence orbitals is that determined from *ab initio* [98] and MS-X $\alpha$  [43,108] calculations. The mean binding energy for the P 2*p* edge, as measured by XPS [111], is 142.07 eV, and values of 0.86 eV [99] and 0.90 eV [102] have been reported for the spin-orbit splitting between the  $2p_{3/2}^{-1}$  and  $2p_{1/2}^{-1}$  components. Based on a statistical weighting of 2:1, the  $2p_{3/2}$  and  $2p_{1/2}$  edges have been estimated to be at 141.77 and 142.67 eV [102]. The value for the P 2*s* VIP, as measured by XPS [111], is 199.49 eV.

The vertical ionization potentials for the seven outermost orbitals of PCl<sub>3</sub>, as measured using He (I) resonance radiation [112], are 10.52 ( $12a_1^{-1}$ ), 11.69 ( $1a_2^{-1}$ ), 11.97 ( $10e^{-1}$ ), 12.94 ( $9e^{-1}$ ), 14.23 ( $11a_1^{-1}$ ), 15.19 ( $8e^{-1}$ ), and 18.81 eV ( $10a_1^{-1}$ ). Since no experimental data or many-body Greens' Function calculations are available for the two inner-valence ionization processes ( $7e^{-1}$  and  $9a_1^{-1}$ ), the average independent particle orbital energies of 24.70 and 26.62 eV, respectively, from the SCF-X $\alpha$ -SW calculations of Xin *et al.* [113], have been used in the present work as estimates of the average ionization energies for the inner-valence orbitals. The ordering of the virtual valence orbitals given above for PCl<sub>3</sub> is that determined from *ab initio* [98] and MS-X $\alpha$  [108] calculations. X-ray photoelectron spectroscopy has been used to obtain the mean binding energies for the P 2*p* (140.14 eV) [111] and for the Cl 2*p* (206.6 eV) thresholds [114]. The positions of the  $2p_{3/2}$  and  $2p_{1/2}$  spin-orbit components at 139.84 (P  $2p_{3/2}$ ), 140.74 (P  $2p_{1/2}$ ), 206.1 (Cl  $2p_{3/2}$ ), and 207.7 eV (Cl  $2p_{1/2}$ ) were previously determined [102] based on a statistical weighting of 2:1 and spin-orbit separation estimates of 0.90 [115] and 1.6 eV [116] for the P 2*p* and Cl 2*p* edges, respectively. The P 2*s* (197.47 eV) and Cl 2*s* (278.2 eV) VIP's were taken from refs. [102,114].

In the final case of PF<sub>5</sub>, the vertical ionization potentials for the first nine

outer-valence orbitals have been determined by PES [112,117] to be 15.54 ( $2e''$ ), 16.46 ( $6e'$ ), 16.75 ( $5a_2''$ ), 17.13 ( $8a_1'$ ), 17.79 ( $1a_2'$ ), 18.43 ( $5e'$ ), 19.1 ( $1e''$ ), 19.5 ( $4a_2''$ ), and  $\sim 21$  eV ( $4e'$ ). The VIP for the  $7a_1'$  molecular orbital has been calculated by Berry *et al.* [118] to be  $\sim 23$  eV. No experimental data or many-body Greens' function calculations are available in the literature for the four inner-valence ionization processes. The ordering of the virtual valence orbitals given above is that determined from MS-X $\alpha$  calculations [108]. X-ray photoelectron spectroscopy studies have reported a mean binding energy of 144.68 eV [111] for the P  $2p$  ionization threshold, and the positions of the  $2p_{3/2}$  and  $2p_{1/2}$  components were determined [106] to be 144.38 and 145.28 eV based on a statistical weighting of 2:1 and a spin-orbit splitting estimate of 0.90 eV [115]. The ionization potential for the P  $2s$  ionization threshold (201.87 eV) was taken from ref. [111].

## 5.2.2 Phosphorus trifluoride

### 5.2.2.1 Long range photoabsorption spectrum

The low resolution (1 eV fwhm) absolute photoabsorption spectrum of PF<sub>3</sub> spanning the valence, P  $2p$ , and P  $2s$  regions (5–300 eV) is shown in figure 5.1(a). Panels (b) and (c) show the valence (5–130 eV) and inner (P  $2p, 2s$ ) shell regions, respectively, in greater detail on expanded scales, and the corresponding data are given numerically in tables A.7 and A.8 in the appendix. Also shown for comparison in figure 5.1(c) is the synchrotron radiation data above 142 eV reported by Ishiguro *et al.* [98], which are in excellent agreement with the present work except in the vicinity of the second continuum shape resonance (159 eV) where their data lower than the present measurements by  $\sim 6\%$ . The dashed curves in (a) and (c) represent the estimated contribution from the valence-shell spectrum (determined from the

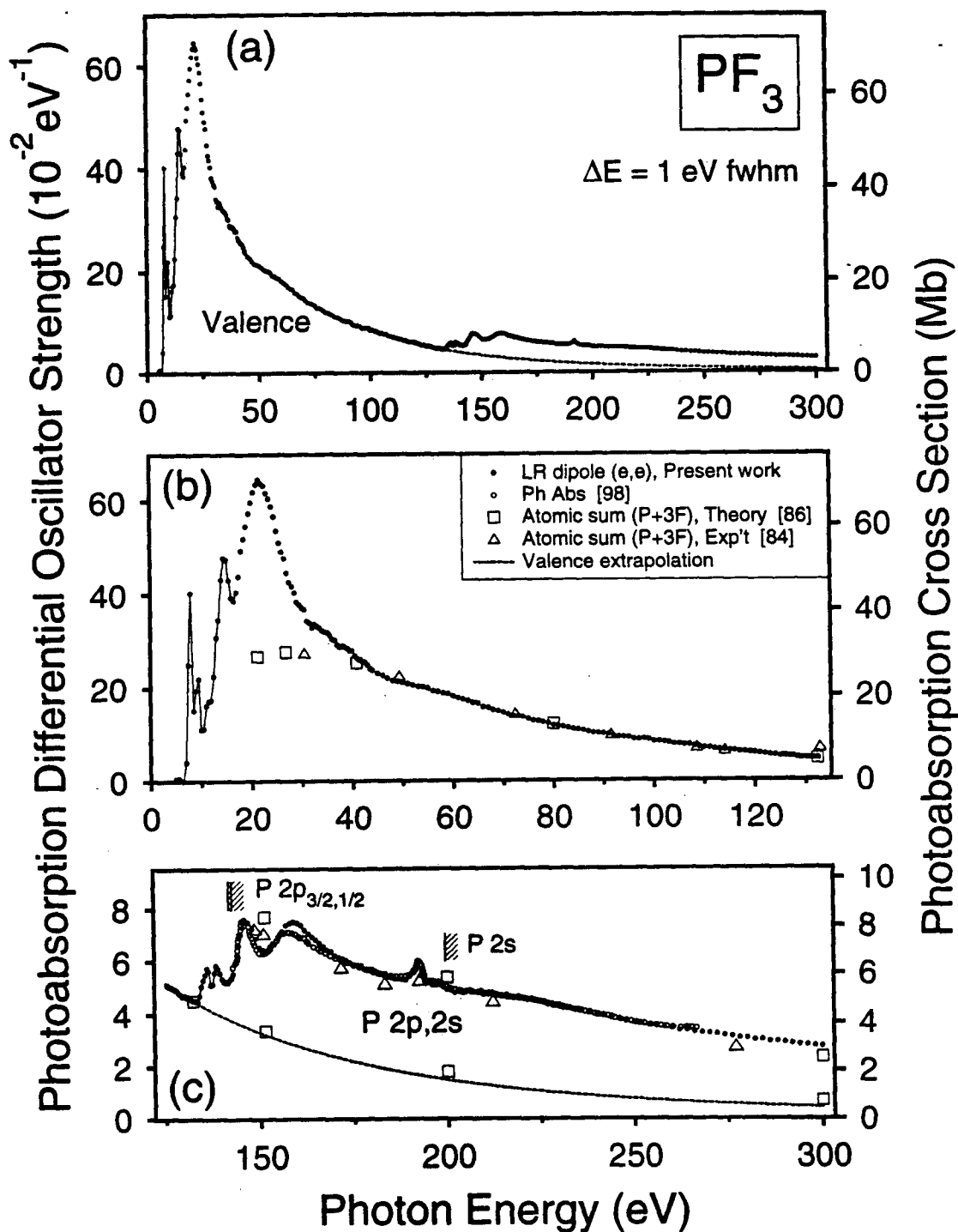


**Figure 5.1:** Absolute photoabsorption differential oscillator strengths for  $\text{PF}_3$  obtained at a resolution of 1 eV fwhm: (a) Long-range spectrum measured from 5 to 300 eV; (b) the valence region (5–130 eV); and (c) the P 2p and 2s inner-shell regions (125–300 eV) shown on an expanded scale. The dashed lines represent the valence-shell extrapolation curve obtained by fitting equation (3.1) to the high-energy portion of the valence spectrum from 85 to 130 eV (see sections 3.1.1 and 5.2 for details).

VTRK sum-rule normalization and extrapolation procedure discussed earlier in sections 3.1.1 and 5.2) to the total photoabsorption above 130 eV.

Experimental [84] and theoretical [86] atomic differential oscillator strength sums (or atomic mixture rules (AMR's)) for the constituent atoms (P+3F) are plotted together with the present photoabsorption results in figure 5.1(b) and (c). The theoretical [86] valence-shell atomic data have also been used to model the underlying valence contribution (figure 5.1(c)) in the P  $2p,2s$  photoabsorption region above 130 eV, and are in good agreement with the extrapolation based on the curve fit to 300 eV. It can also be seen in figure 5.1(b) and (c) that such atomic sums provide good estimates of the oscillator strengths in the valence continuum above 40 eV and in the core continuum above ~170 eV (i.e., in regions, away from the ionization edges, where any molecular effects become negligible).

The static electric-dipole polarizability ( $\alpha_N$ ) of a molecule can be determined from the S(-2) sum rule (equation (2.29)) if a sufficiently accurate absolute photoabsorption spectrum is available up to ~100 eV [28] (data above 100 eV in general contribute less than 1% to the summation). Alternatively, equation (2.29) may be used to establish the absolute oscillator strength scale if a sufficiently accurate value of the static dipole polarizability is available [28]. Since the low energy region of the oscillator strength is heavily weighted by the  $E^{-2}$  factor in the S(-2) sum rule, the absolute photoabsorption data (5–300 eV) obtained in the present work are more than sufficient for deriving the electric-dipole polarizability for  $\text{PF}_3$ . This is of some interest since no experimental values of  $\alpha_N$  for  $\text{PF}_3$  have been published thus far. In sections 5.2.3.1 and 5.2.4.1 below, equation (2.29) has been used to obtain  $\alpha_N$  values from the VTRK sum-rule normalized spectra for other phosphorus halides,  $\text{PCl}_3$  and  $\text{PF}_5$ , which are in good agreement with experimental and theoretical estimates reported in the literature [119–122] for these molecules. In the present work, the electric-dipole polarizability of  $\text{PF}_3$  has been determined to be  $44.32 \times 10^{-25} \text{ cm}^3$

using the photoabsorption data in tables A.7 and A.8 in equation (2.29). This value differs significantly from the theoretical estimates performed by Lippincott *et al.* ( $29.02 \times 10^{-25} \text{ cm}^3$ ) [123] and Pandey *et al.* ( $29.154 \times 10^{-25} \text{ cm}^3$ ) [124] obtained using the delta-function potential model. However, it should be noted that difficulties in computing the dipole polarizabilities for group 15 trifluorides have been reported by these authors [123,124] since the experimental data upon which the necessary polarity corrections can be based are not available. Therefore at best the theoretical values of  $\alpha_N$  reported for  $\text{PF}_3$  [123,124] are questionable. Furthermore, the reliability of the presently reported oscillator strength scale is supported by the good agreement with the data of Ishiguro *et al.* [98] in the P  $2p,2s$  region and with the atomic sums [84,86] over a wide range in both the valence and inner shell continuum regions.

### 5.2.2.2 Valence-shell spectrum

The valence-shell absolute photoabsorption spectrum of  $\text{PF}_3$  from 5 to 50 eV obtained at 0.05 eV fwhm resolution in the present work is presented in figure 5.2(a) together with the positions of the vertical ionization potentials of the seven outer-valence ion states as given in section 5.2.1. Figure 5.3 shows an expanded view of the discrete region (7–23 eV) of the spectrum; the assignments given on the manifolds have been taken from ref. [101] with the exception of feature 3 which was attributed [101] to both the  $4s$  Rydberg and  $9a_1$  virtual valence transitions. In reference [101], transferability of both virtual valence and Rydberg term values was assumed in assigning the valence shell spectrum. Therefore, the positions shown for the virtual valence transitions will be, at best, very approximate.

The Jahn-Teller split band (see features 1 and 2 in figure 5.3) centered at a mean energy of 8.06 eV were previously assigned to  $7e \leftarrow 8a_1^{-1}$  [97,101]. The

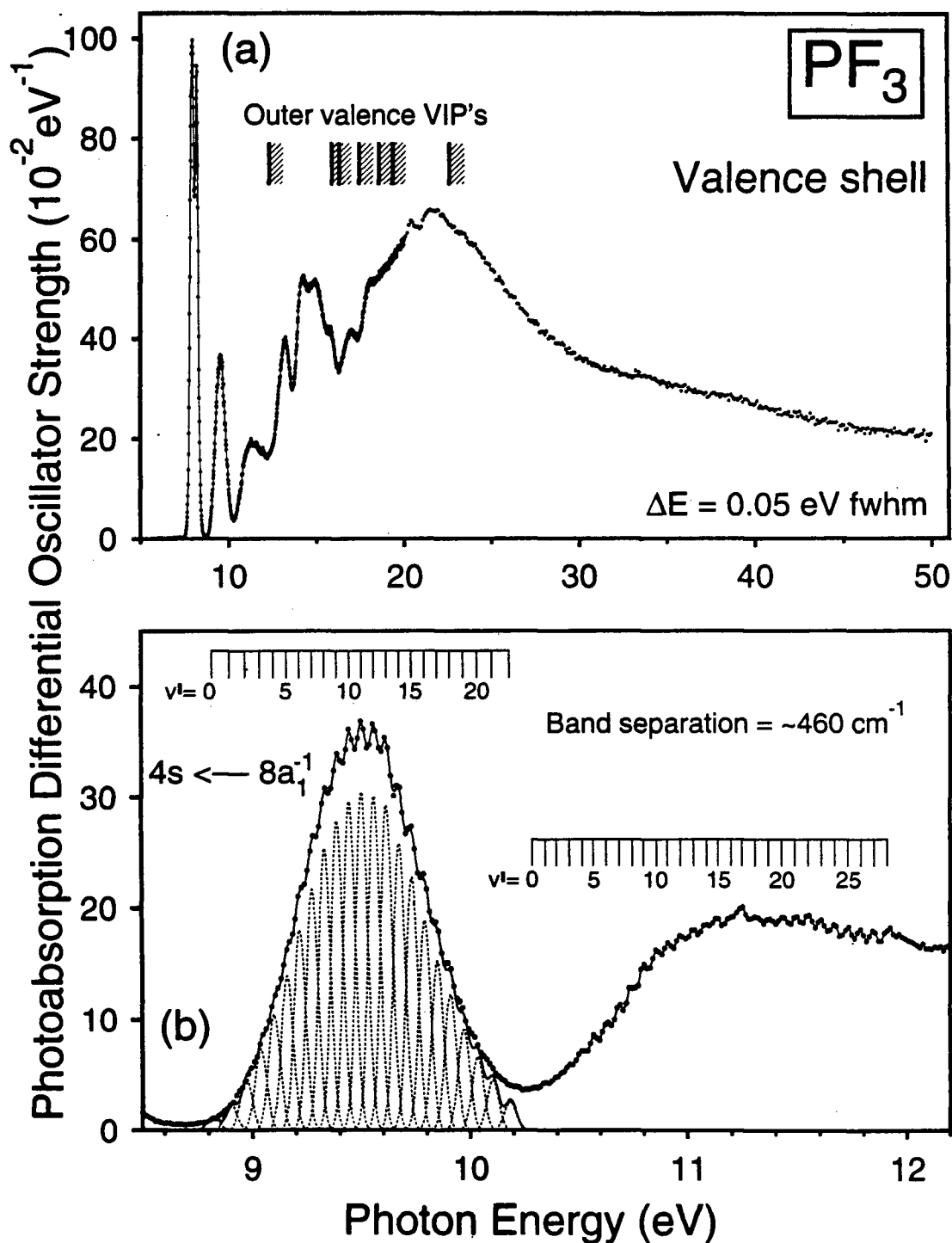


**Figure 5.2:** (a) Absolute high resolution (0.05 eV fwhm) photoabsorption spectra of the valence-shell region of  $\text{PF}_3$  from 5 to 50 eV. The hatched lines indicate positions of the outer valence VIP's as determined by high resolution PES [109]. Panel (b) shows the two vibronic progressions in the bands at 9.52 and 11.08 eV. Note that the photoabsorption differential oscillator strengths can be converted to absolute photoabsorption cross sections using the relation,  $\sigma \text{ (Mb)} = 109.75 \times (df/dE) \text{ (eV}^{-1}\text{)}$ .

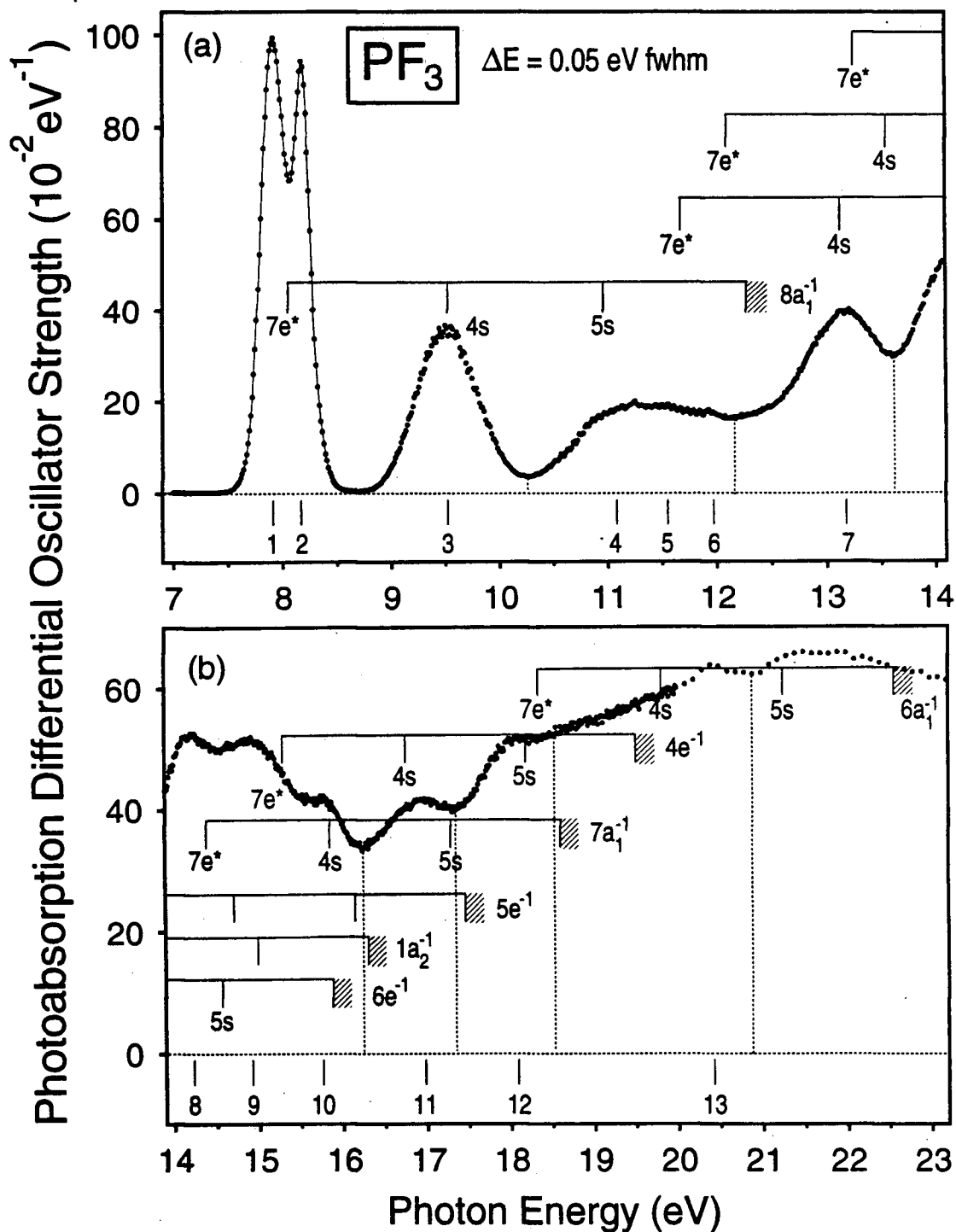


**Figure 5.3:** The features observed in the discrete high resolution (0.05 eV fwhm) valence-shell absolute photoabsorption spectrum from: (a) 7 to 14 eV and (b) 14 to 23 eV. The assignments are taken from ref. [101]. The integrated oscillator strengths for the eight energy regions separated by vertical dotted lines are given in table 5.2.

integrated oscillator strength value of 0.4604 (table 5.2) presently determined for this transition is very close to the value of 0.48 reported in the optical density study by McAdams and Russell [97].

**Table 5.2**

Absolute photoabsorption oscillator strengths for regions of the valence-shell spectrum of PF<sub>3</sub>

Integrated energy region <sup>1</sup> (eV)	Oscillator strength (10 <sup>-2</sup> )	
	Present work	Ref. [97]
7.39–8.68	46.04	48
8.68–10.26	25.42	28
10.26–12.16	28.42	
12.16–13.62	41.56	
13.62–16.24	117.43	
16.24–17.34	42.78	
17.34–18.54	58.23	
18.54–20.88	136.80	

<sup>1</sup> See figure 5.3 for the respective spectral regions.

Two vibronic progressions centered at 9.52 and 11.08 eV (figure 5.2(b)) are clearly observed in the presently reported spectrum. The relative [96] and absolute [97] optical absorption spectra previously measured in the very limited energy regions, 6.9–11.8 and 5–10 eV, respectively, also showed these vibrational structures. In the present work, 23 vibronic bands have been deconvoluted from the first progression and 29 have been identified from the second. The energy positions

for these vibronic bands are in good agreement with those reported by Humphries *et al.* [96] within experimental uncertainty. The average vibrational separation,  $460\text{ cm}^{-1}$  (0.058 eV), for both progressions corresponds closely to the  $\nu_2$  symmetric bending mode of  $\text{PF}_3$  ( $487\text{ cm}^{-1}$ ) in the infrared spectrum [125].

The HOMO ( $8a_1$ ) of  $\text{PF}_3$  is primarily the phosphorus lone-pair orbital [126], and ionization of an electron from the HOMO results in the manifestation of vibronic structures in the  $8a_1^{-1}$  ion ground state with an interval of  $470\text{ cm}^{-1}$  (averaged from  $\nu'=5$  to  $\nu'=20$ ) in the high resolution photoelectron spectrum reported by Maier and Turner [109]. The intensity distribution and width of the Franck-Condon vibrational envelope of the 9.52 eV band of the dipole ( $e,e$ ) excitation spectrum as shown in figure 5.2(b) corresponds very closely with that observed in the  $8a_1^{-1}$  photoelectron spectrum [109]. This similarity with ionization would be expected for a Rydberg transition since Rydberg orbitals are generally diffuse and atomic-like with the Rydberg electron viewing the positively charged ion core as a point charge. These observations therefore strongly support the assignment of the first vibronic progression centered at 9.52 eV solely to the  $4s \leftarrow 8a_1^{-1}$  Rydberg transition [97] with no underlying contribution from a  $9a_1 \leftarrow 8a_1^{-1}$  virtual valence transition. Sodhi and Brion [101], whose data are not sufficiently resolved to show any vibronic structures, had earlier suggested that the  $9a_1$  virtual valence transition might also be contributing to the band at 9.52 eV. Table 5.3 gives the absolute oscillator strength values for each of the 23 vibronic peaks shown in figure 5.2(b). The oscillator strength for the entire band from 8.68 to 10.26 eV, 0.2542 (table 5.2), is in good agreement with the value of 0.28 reported earlier [97]. This good agreement and also that for the band from 7.39 to 8.68 eV (see above) further supports the accuracy of the presently determined absolute oscillator strength scale and the resulting value of the static dipole polarizability (see Sec. 5.2.2.1).

Based on a quantum defect of 1.78 determined for the  $4s \leftarrow 8a_1^{-1}$  transition at

**Table 5.3**

Absolute oscillator strengths for the  $4s \leftarrow 8a_1^{-1}$  vibronic bands of the valence-shell photoabsorption spectrum of  $\text{PF}_3$

Vibrational quantum number ( $v'$ )	Photon energy (eV)	Oscillator strength ( $10^{-2}$ )
0	8.82	0.09
1	8.91	0.15
2	8.98	0.32
3	9.04	0.49
4	9.10	0.70
5	9.16	0.92
6	9.22	1.20
7	9.28	1.45
8	9.33	1.70
9	9.39	1.87
10	9.45	1.98
11	9.50	2.04
12	9.56	2.02
13	9.62	1.96
14	9.68	1.73
15	9.73	1.52
16	9.79	1.27
17	9.85	1.02
18	9.91	0.82
19	9.97	0.61
20	10.04	0.45
21	10.11	0.31
22	10.19	0.18

9.52 eV, the Rydberg formula (equation (2.41)) was used in ref. [101] to determine the position of the 5s Rydberg. This is shown on the  $8a_1^{-1}$  manifold in figure 5.3(a), and it can be seen that, as expected, the occurrence of a second vibronic envelope (feature 4) matches very well with the predicted position of the  $5s \leftarrow 8a_1^{-1}$  transition. Therefore, while the broad band at 11.08 eV also possibly has contributions from  $7e \leftarrow 6e^{-1}$  and  $1a_1^{-1}$ , the vibrational structures must presumably arise from the transition to the 5s Rydberg state. An oscillator strength value of 0.2842 has presently been obtained for this band (integrated over the 10.26–12.16 eV region). The oscillator strengths for five more energy regions, shown by the dotted vertical lines in figure 5.3, are listed in table 5.2. This represents an extension of the very limited absolute data (5–10 eV) [97] for the valence-shell photoabsorption of  $PF_3$  that is currently available in the literature. It should be noted that while the spectral features in figure 5.3 correspond well to the 7e and *ns* Rydberg assignments [101], transitions to the *np* and *nd* orbitals are also formally-allowed for  $PF_3$  and may be expected to contribute [40].

Recent theoretical investigations using continuum MS-X $\alpha$  calculations [43,127] suggested the presence of two shape resonances in each of the  $a_1$  and e continuum channels in the valence-shell ionization continuum. The partial photoionization cross sections were calculated over the electron kinetic energy range, 0–30 eV, for each of the three outermost valence orbitals,  $8a_1$ , 6e, and  $1a_2$  [43]. The lower energy resonance ( $9a_1 \leftarrow 8a_1^{-1}$ ), which was found to be characterized by *sp* type wavefunctions from the P atom and *p* type wavefunctions from the F ligand, was predicted [43,127] to be located ~3 eV above the ionization threshold. In contrast, the remaining  $a_1$  and e shape resonances were calculated to be dominated by *d* type continuum functions. This suggests that similar to the P 2*p* spectrum (see section 5.2.2.3 below), the broad continuum peak observed at ~35 eV in figure 5.1(b) can be attributed to valence-shell excitations to the  $10a_1$  virtual valence orbital.

### 5.2.2.3 P 2p,2s inner-shell spectra

In addition to the low resolution data shown in figure 5.1(a) and (c), the absolute differential oscillator strengths in the discrete P 2p inner-shell region of PF<sub>3</sub> have been further investigated in the present work at higher resolution (0.1 eV fwhm), and the data are shown as solid circles in figure 5.4(a) together with the optical work (line) of Ishiguro *et al.* [98], which matches closely with the dipole (*e,e*) data in both shape and magnitude.

The bands situated from 134 to 137 eV in figure 5.4(a) have been previously assigned [98,102] to the virtual valence transitions,  $7e \leftarrow 2p^{-1}$ . The phosphorus 2p orbitals of PF<sub>3</sub> transform as a<sub>1</sub> and 2e under C<sub>3v</sub> symmetry. The direct product of the initial 2p(*e*) and final 7e orbitals indicates the existence of two dipole-allowed excited states, <sup>1</sup>A<sub>1</sub> and <sup>1</sup>E, which are spin-orbit split into four transitions [98,102]. However, only three peaks are apparent in this energy region. The assignments in refs. [98,102] indicated that the center band represents the sum of  $7e(\sigma^*) : ^1E \leftarrow 2p_{3/2}^{-1}(e) : ^1A_1$  and  $7e(\sigma^*) : ^1A_1 \leftarrow 2p_{1/2}^{-1}(e) : ^1A_1$  [98,102]. It can be seen that the main peak energies of features 1–3 (134.93, 135.70, and 136.48 eV) also reflect the 2p<sub>3/2</sub> and 2p<sub>1/2</sub> spin-orbit splitting (0.86 eV [99]) for transitions to both the <sup>1</sup>E and <sup>1</sup>A<sub>1</sub> excited states. Recently, a high order *ab initio* calculation and synchrotron radiation study [100] predicts that feature 3 is in fact an LS coupled  $7e(\sigma^*) : ^1A_1 \leftarrow 2p_{3/2}^{-1}(e) : ^1A_1$  state which has no spin-orbit partner.

The series of absorption bands from 137 eV up to the P 2p ionization thresholds arise from transitions of the 2p core photoelectrons to Rydberg orbitals [102]. Features 5 and 7 at 138.60 and 139.40 eV, respectively, have been assigned to  $4s \leftarrow 2p_{3/2, 1/2}^{-1}$  [102] based on their splitting and also because of the sharpness of their profiles which is typical of Rydberg transitions [40]. The positions of the 4s Rydbergs correspond to larger term values than those expected for an *ns* quantum

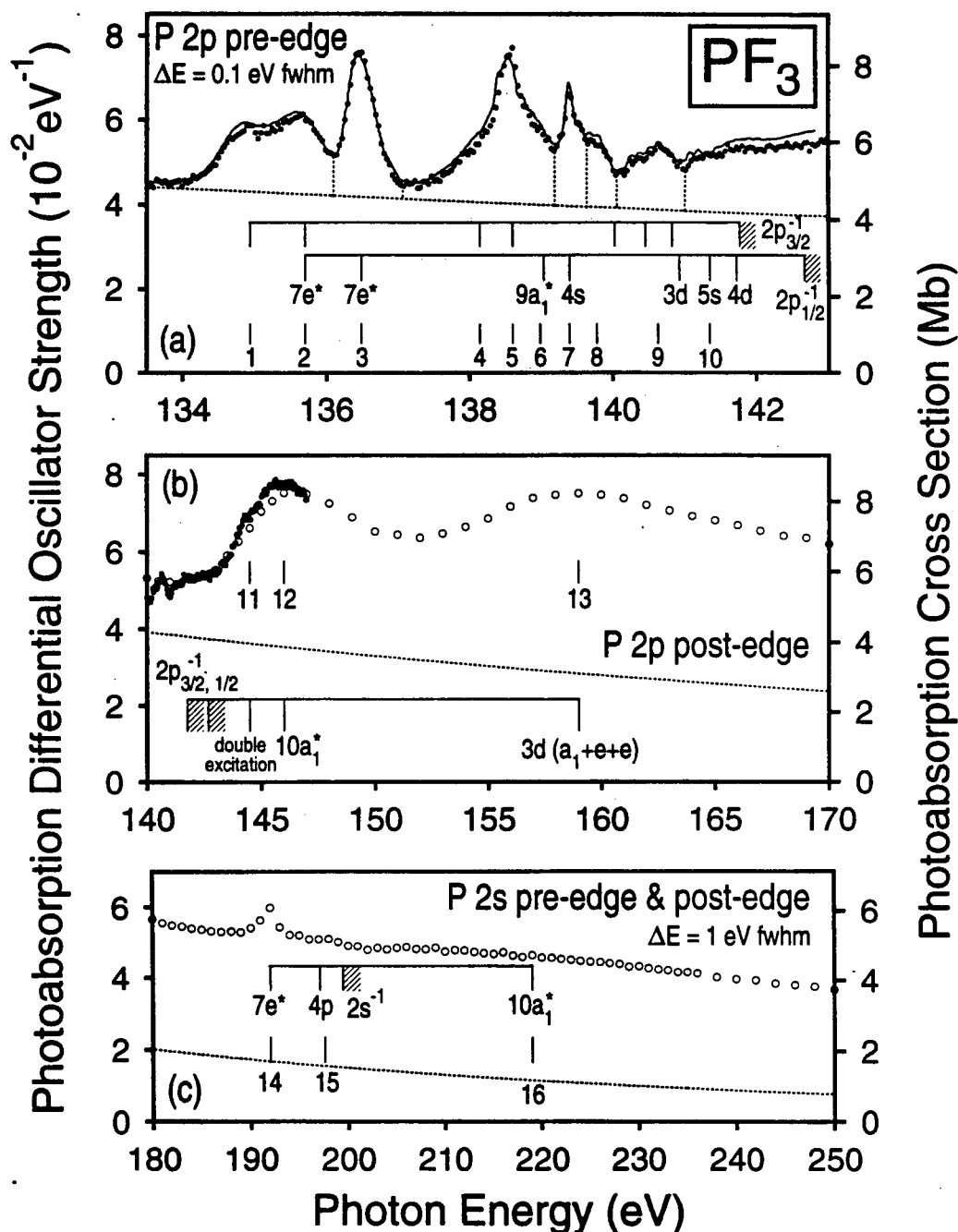


**Figure 5.4:** (a) The absolute photoabsorption differential oscillator strengths (0.1 eV fwhm) measured in the P 2p discrete region (solid circles) compared with the optical spectrum (line) previously obtained using synchrotron radiation [98]. The integrated oscillator strengths for the six energy regions separated by dotted vertical lines are given in table 5.4. Panels (b) and (c) show the P 2p post-edge and P 2s regions respectively: The solid circles represent the high resolution (0.1 eV fwhm) dipole ( $e,e$ ) data, while the open circles show the lower resolution (1 eV fwhm), long-range data. The dotted lines at the base of the spectra in panels (a)–(c) represent the contributions to the absolute oscillator strengths for inner-shell photoabsorption from the underlying valence-shell estimated from the fitting and extrapolation procedures (see sections 3.1.1 and 5.2 for details).

defect of 1.75 eV determined from the valence shell (see section 5.2.2.2 above). This can be attributed to Rydberg-valence mixing with the underlying virtual valence transition to the  $9a_1$  orbital (see below). Ishiguro *et al.* [98] later interpreted these two peaks as being due to transitions to the  $4p$  Rydberg orbitals based on an average term value of 2.5 eV and a quantum defect of 1.67. However, with the P  $2p_{3/2}$  and P  $2p_{1/2}$  VIP's occurring at 141.77 and 142.67 eV [102], the term value ( $T = \text{VIP} - E$ ) for each of the two sharp structures clearly cannot be 2.5 eV. Since VIP's of 141.04 and 141.97 eV were used in assigning the optical spectrum [98], it appears that the authors had misinterpreted the VIP's reported in ref. [114]. Minimal basis set *ab initio* calculations performed by Ishiguro *et al.* [98] predicted that  $np$  Rydbergs occur in the photoabsorption spectrum of  $\text{PF}_3$  because of the  $C_{3v}$  symmetry of the molecule. However, it has been found in previous studies that atomic-like selection rules are a useful guide to relative intensities in the interpretation of molecular core excitation spectra to Rydberg states, since the initial and final states are both essentially atomic in character. On this basis,  $4p \leftarrow 2p^{-1}$  transitions would not be expected to make a larger contribution than  $4s \leftarrow 2p^{-1}$ , and thus the latter assignments as in ref. [102] are preferred for peaks 5 and 7 on figure 5.4(a). The shapes of the two bands in the 137–139 eV region suggest that the shoulders on the lower energy sides of the  $4s$  Rydberg transitions (features 4 and 6) arise from the underlying  $9a_1 \leftarrow 2p_{3/2, 1/2}^{-1}$  transitions [102]. However, both the minimal basis set *ab initio* [98] and the MS-X $\alpha$  continuum [43] calculations in the literature predicted the  $9a_1$  virtual valence orbital to be situated near the continuum, but this is not experimentally observed. Nevertheless, it is possible that the  $a_1$  anti-bonding orbital theoretically determined [98,43] is in fact the  $10a_1$ .

The tentative assignments of the higher Rydberg features converging to the ionization continua in figure 5.4(a) have been guided by those in ref. [102]. Since the calculated term values and quantum defects used in ref. [102] were not given, the

positions of the  $5s$  and  $4d$  Rydbergs indicated on the manifolds have been determined in the present work using the Rydberg formula (equation (2.41)) with estimated quantum defects of 1.75 and 0.2, respectively. The value of 1.75 in the former case has been taken from the  $4s \leftarrow 8a_1^{-1}$  valence-shell transition, since there is no evidence of Rydberg-valence mixing in the valence spectrum in contrast to the P  $2p$  region. The  $nd$  quantum defect of 0.2 is as suggested by Robin [40] for transitions involving third row elements.

Table 5.4 compares the absolute oscillator strengths for the P  $2p$  discrete photoabsorption of  $\text{PF}_3$  (plus the underlying valence continuum) for the six regions separated by the vertical lines in figure 5.4(a) determined from the present measurements, with those of the optical work of Ishiguro *et al.* [98]. It can be seen that there is generally good agreement between the two sets of data in all regions within experimental error. Also given in table 5.4 are the partial oscillator strengths for the P  $2p$  shell component of the spectrum obtained by subtracting the valence-shell contributions estimated from the fitting and extrapolation procedures in section 5.2.

Two strong shape resonances are observed in the P  $2p$  ionization continuum at 146 and 159 eV (figure 5.4(b)). Recent continuum MS-X $\alpha$  calculations [43] have predicted that the first resonance structure (feature 12 at 146 eV) results from the  $a_1$  channel associated with the  $l=1$  component of the fluorine ligands. This is consistent with earlier *ab initio* calculations which suggested an assignment of  $10a_1 \leftarrow 2p(a_1)^{-1}$  [98]. However, the small shoulder (feature 11 at 144.5 eV) situated at the leading edge of this resonance has not been modeled by any of the theoretical methods [43,98,108]. This feature, which is also evident in the optical absorption [98] and electron-energy-loss [102] spectra, has been ascribed [102] to a double excitation process (i.e., simultaneous excitation of a  $2p$  and a valence electron).

In contrast, the broader resonance located ~16 eV above the P  $2p$  edge

**Table 5.4**

Absolute photoabsorption oscillator strengths for regions of the P 2*p* inner-shell spectra of PF<sub>3</sub>

Integrated energy region <sup>1</sup> (eV)	Oscillator strength (10 <sup>-2</sup> )		
	Present work		Ref. [98]
	Valence + P 2 <i>p</i> shells	P 2 <i>p</i> shell	Valence + P 2 <i>p</i> shells
133.60–136.10	13.29	2.53	13.52
136.10–137.07	5.81	1.72	5.84
137.07–139.19	11.69	3.09	12.20
139.19–139.64	2.66	0.86	3.22
139.64–140.06	2.20	0.54	2.27
140.06–141.01	4.79	1.12	4.88

<sup>1</sup> See figure 5.4 for the respective spectral regions.

(feature 13 at 159 eV) is attributed to excitation from the 2*p* core to the phosphorus continuum 3*d* orbitals according to the MS-X $\sigma$  calculations [43]. The ordering of the atomic-like 3*d*  $\leftarrow$  2*p*<sup>-1</sup> transitions, 3*d*<sub>z<sup>2</sup></sub>(11a<sub>1</sub>) < 3*d*<sub>xz,yz</sub>(8e) < 3*d*<sub>x<sup>2</sup>-y<sup>2</sup>,xy</sub>(9e) [108], is reflected by the relative energy positions of the a<sub>1</sub> and e channel partial photoionization cross sections theoretically determined in ref. [43].

The two pre-edge structures in the P 2*s* spectrum (figure 5.4(c)) have been previously observed in both the electron-energy-loss [102] and optical absorption [98] spectra. They were assigned to the 7e  $\leftarrow$  2*s*<sup>-1</sup> (192.0 eV) [98,102] and 4*p*  $\leftarrow$  2*s*<sup>-1</sup> (197.5 eV) [102] excitations. Above the P 2*s* threshold, the very broad resonance at ~219 eV arises from the a<sub>1</sub> continuum channel and is analogous to the 10a<sub>1</sub>  $\leftarrow$  2*p*<sub>3/2,1/2</sub><sup>-1</sup> transition in the P 2*p* spectrum [43]; therefore, it has been tentatively assigned to 10a<sub>1</sub>  $\leftarrow$  2*s*<sup>-1</sup> in the present work.

## 5.2.3 Phosphorus trichloride

### 5.2.3.1 Long range photoabsorption spectrum

The low resolution (1 eV fwhm), absolute photoabsorption spectrum of  $\text{PCl}_3$  obtained in the present work, spanning the valence and inner (P  $2p,2s$ ; Cl  $2p,2s$ ) shells from 5 to 350 eV, is shown in figure 5.5, and the data are presented in tables A.9 and A.10 in the appendix. The hatched lines indicate the positions of the P  $2p_{3/2,1/2}$ , P  $2s$ , Cl  $2p_{3/2,1/2}$ , and Cl  $2s$  ionization thresholds. The dashed curve represents the contribution of the valence-shell spectrum (determined from the VTRK sum rule normalization and extrapolation procedures discussed in sections 3.1.1 and 5.2) to the total photoabsorption above 130 eV.

The phosphorus trichloride electronic photoabsorption spectrum below 350 eV (figure 5.5) consists of three very distinct regions: (1) the valence shell, (2) the P  $2p,2s$  inner-shells, and (3) the Cl  $2p,2s$  inner-shells. The valence-shell differential oscillator strength rises to a maximum at 13.5 eV, followed by a steep decline to a Cooper minimum around 45 eV. This phenomenon, which is mainly due to the presence of a radial node in the atomic chlorine  $3p$  wavefunction, causes the valence-shell oscillator strengths to be concentrated to low energy (80% at photon energies less than 40 eV) [128,129]. This situation is very different from the corresponding  $\text{PF}_3$  spectrum (47% at < 40 eV) where the oscillator strength distribution is spread out over a much larger energy range (section 5.2.2.1). In contrast with the valence shell, the  $\text{PCl}_3$  oscillator strengths (figure 5.5) in the inner-shell spectral regions (P  $2p,2s$  and Cl  $2p,2s$ ) are distributed over a wider energy range as a result of the more spatially localized and less diffuse character of the  $2p$  and  $2s$  orbitals compared with those of the valence shell.

The absolute inner-shell photoabsorption spectra for  $\text{PCl}_3$  measured by Ishiguro *et al.* using synchrotron radiation [98] are shown in figure 5.5 in

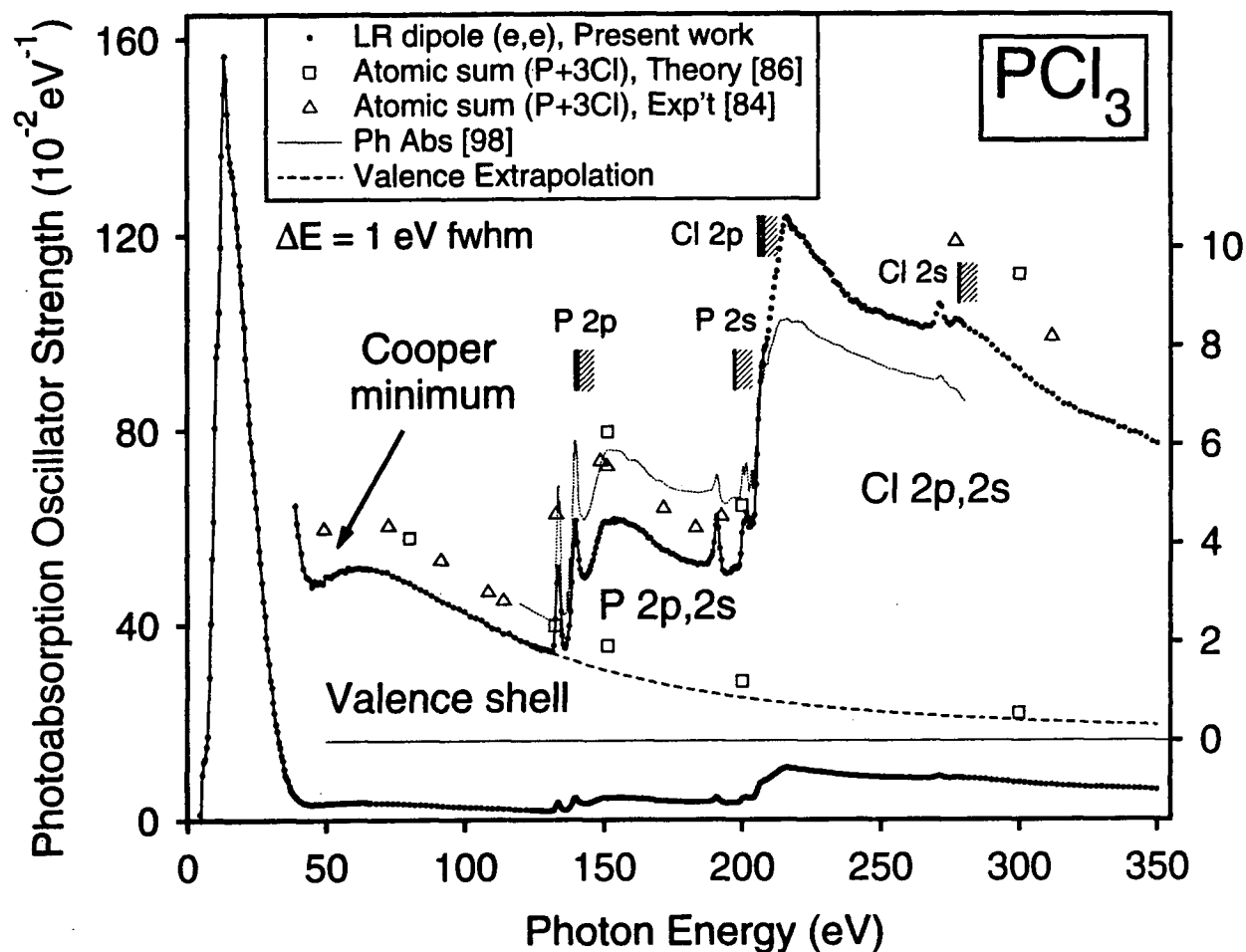


**Figure 5.5:** Absolute photoabsorption spectrum of  $\text{PCl}_3$  spanning the valence and inner (P 2p, 2s; Cl 2p, 2s) shell regions (5–350 eV). The positions of the VIP's for the P 2p, P 2s, Cl 2p, and Cl 2s edges are indicated by the hatched lines. The dashed line represents the valence-shell extrapolation curve obtained by fitting equation (3.1) to the high-energy portion of the valence spectrum (85–130 eV). Note that absolute cross sections in units of megabarns can be obtained by multiplication of the photoabsorption differential oscillator strengths ( $\text{eV}^{-1}$ ) by a factor of 109.75.

comparison with the present work. They are in serious disagreement with the presently obtained results, being ~30% higher than the present work in the P  $2p,2s$  region below 200 eV and ~15% lower in the Cl  $2p,2s$  region. If the synchrotron radiation data [98] were normalized down to the dipole ( $e,e$ ) data in the valence-shell continuum just below the P  $2p$  edge, the shape of the two spectra would then be in fairly good agreement between 130–200 eV (see figure 5.6 below). However, there would then be an even larger (40%) difference in intensity between the presently determined differential oscillator strengths for the Cl  $2p,2s$  shells and those reported in the same region by Ishiguro *et al.* [98]. These differences could be due to errors caused in the target density determination and/or by the presence of higher order radiation or stray light in the synchrotron radiation work [98].

Experimental [84] and theoretical [86] atomic differential oscillator strength sums (or AMR's) determined using the constituent atoms of  $\text{PCl}_3$  (P+3Cl) are plotted in figure 5.5 together with the present results in the valence and core continuum regions, where molecular effects are expected to become less important at higher energies away from near-edge fine structures or continuum resonances. The theoretical atomic data [86] are reasonably close to the present estimated valence contribution to the spectrum above 130 eV (as estimated by the extrapolated curve-fit discussed earlier). Since inner-shell spectra are generally atomic-like, AMR's can be useful for providing approximate estimates of the molecular oscillator strengths away from near-edge structures. From figure 5.5 it can be seen that the theoretical and experimental atomic sums are in fair agreement with one another but are uniformly ~20% higher than the experimental measurements presently obtained for  $\text{PCl}_3$ . However, it should be noted that the relative intensity increases in going from the valence to the P  $2p$  and to the Cl  $2p$  continua are in fair agreement between the atomic sums [84,86] and the dipole ( $e,e$ ) measurements. This lends some support to the relative intensities found in the present valence and inner shell spectra. The

accuracy of the absolute scale established in the present work further supports the S(-2) sum-rule analysis discussed below.

A method by which the accuracy of an absolute photoabsorption differential oscillator strength scale can be critically evaluated is by comparing the experimental or theoretical static electric-dipole polarizability ( $\alpha_N$ ) for a molecule with that derived from the oscillator strength data using the S(-2) sum rule (equation (2.29)). Since the absolute differential oscillator strengths for  $\text{PCl}_3$  have been measured over a sufficiently wide energy range (5–350 eV) to permit a determination of the S(-2) sum (dipole polarizability) for  $\text{PCl}_3$  using equation (2.29), the result can be compared directly with measured and calculated electric-dipole polarizability values from the literature. The value derived from the present data,  $106.01 \times 10^{-25} \text{ cm}^3$ , is found to be in excellent agreement with the experimental result of Hacket and Le Fèvre ( $104.9 \times 10^{-25} \text{ cm}^3$ ) [119] which was obtained using molar refractivity measurements, and also with the slightly lower value of  $103.03 \times 10^{-25} \text{ cm}^3$  reported by Grassi in 1933 [122]. The agreement is also quite good with theoretical dipole polarizabilities of  $107.8 \times 10^{-25} \text{ cm}^3$  [119] calculated using empirical equations involving structural data and  $102.98 \times 10^{-25} \text{ cm}^3$  [124] obtained using the delta-function potential model. These findings strongly support the accuracy of the presently determined absolute oscillator strength scale established using the VTRK sum-rule and the associated procedures of curve-fitting and extrapolation as well as correction for Pauli excluded transitions.

### 5.2.3.2 Valence-shell spectrum

The absolute differential oscillator strength spectrum for the valence-shell photoabsorption of  $\text{PCl}_3$  measured at high resolution (0.05 eV fwhm) in the present work is presented in figure 5.6(a) from 4 to 50 eV together with the optical

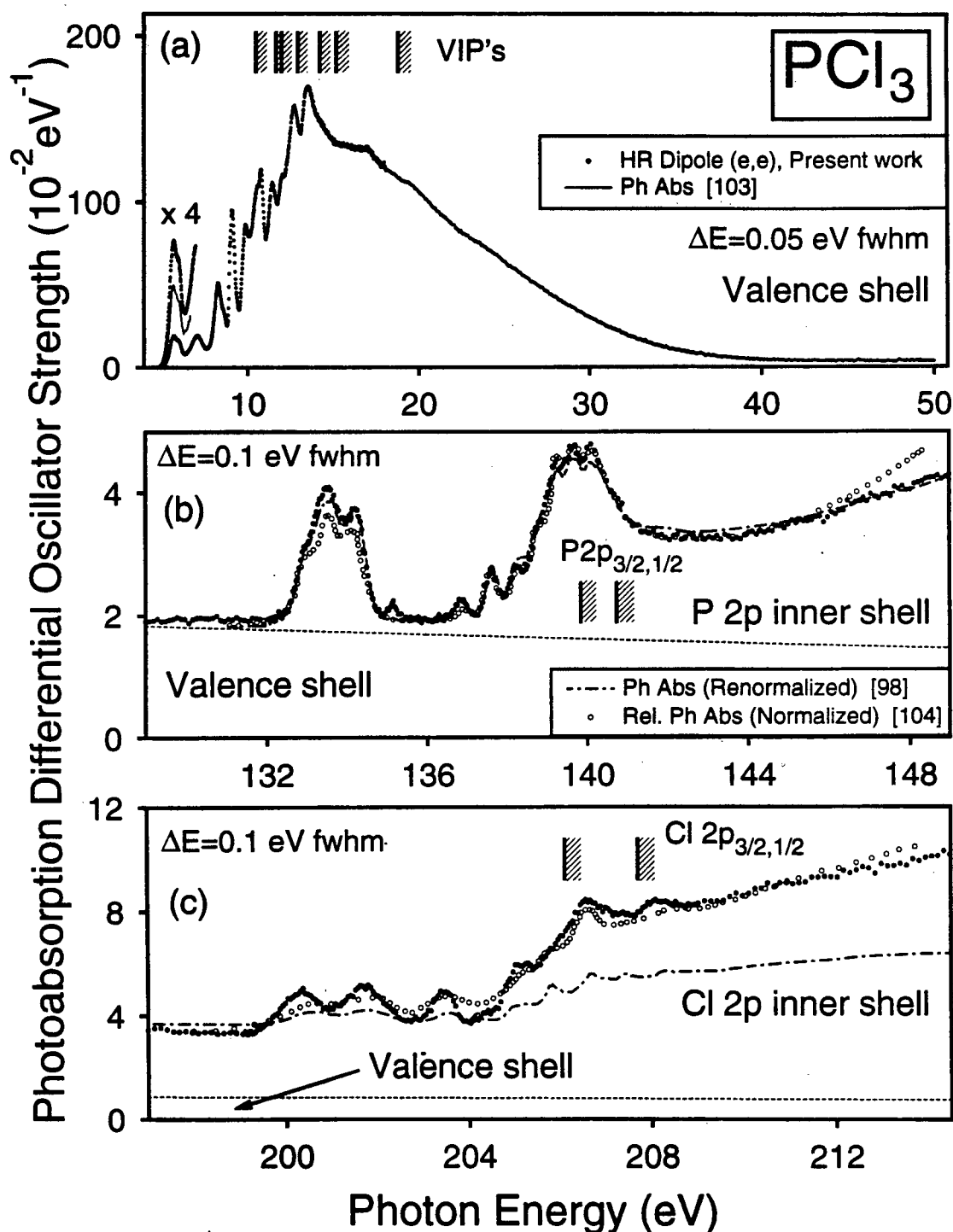


**Figure 5.6:** Absolute photoabsorption spectra of the (a) valence, (b) P 2p, and (c) Cl 2p regions of  $\text{PCl}_3$  obtained at resolutions of 0.05 eV (valence shell) and 0.1 eV fwhm (P 2p, Cl 2p shells). The hatched lines indicate positions of the VIP's, and the dotted lines in (b) and (c) represent the valence-shell contribution to the absolute oscillator strengths in the inner-shell excitation spectra. Note that the intensities of the dipole ( $e,e$ ) and the photoabsorption data [103] between 5–8 eV have been expanded by a factor of four for greater clarity.

absorption spectrum reported by Halmann [103] in the very limited 5.0–6.7 eV energy range. The discrete structures are shown in greater detail in figure 5.7. Spectral assignments to the dipole-allowed  $ns$ ,  $np$ , and  $nd$  Rydberg transitions have been calculated using the Rydberg formula with quantum defects of 1.85, 1.55, and 0, respectively, as given in ref. [101]. Features 1 and 2 have been previously assigned to the  $13a_1(\sigma^*)$  and  $11e(\sigma^*)$  respective virtual valence transitions [101] based on their perceived ordering in the phosphorus  $2p$  shell region [102]. However, both MS-X $\alpha$  [104] and more recent *ab initio* [98] calculations indicated that this ordering should be reversed, with the splitting between the excitations to the  $11e$  and  $13a_1$  orbitals being greater than 5 eV [98]. Using this ordering their positions on the manifolds in figure 5.7 have been taken from ref. [101] using term values of 4.83 eV ( $11e$ ) and 4.53 eV ( $13a_1$ ).

Table 5.5 compares the absolute oscillator strength values for the nine energy regions separated by vertical dotted lines in figure 5.7 with those reported by Halmann [103] and McAdams and Russell [97]. The oscillator strengths obtained by the two optical techniques are in general lower than those determined in the present work. These differences may be attributed to line-saturation (bandwidth) effects [5] occurring in the optical work [97], since the Beer-Lambert law method was used to obtain the absolute cross section data.

Humphries *et al.* [96] and McAdams and Russell [97] reported the presence of a long vibronic progression of 17 bands centered at 8.26 eV. The average band spacings of 261 [97] and 263  $\text{cm}^{-1}$  [96] (0.030 eV) correspond to the  $\nu_2$  symmetric bending mode (260  $\text{cm}^{-1}$ ) in the infrared spectrum [130]. The HOMO ( $12a_1$ ), which is primarily the phosphorus lone-pair orbital, shows similar vibrational structures separated by  $\sim 250 \text{ cm}^{-1}$  from one another [131] in the He (I) PES spectrum. The 8.26 eV vibronic progression is not identified in the present work due to the more modest resolution of the dipole ( $e,e$ ) spectrometer (0.05 eV fwhm).

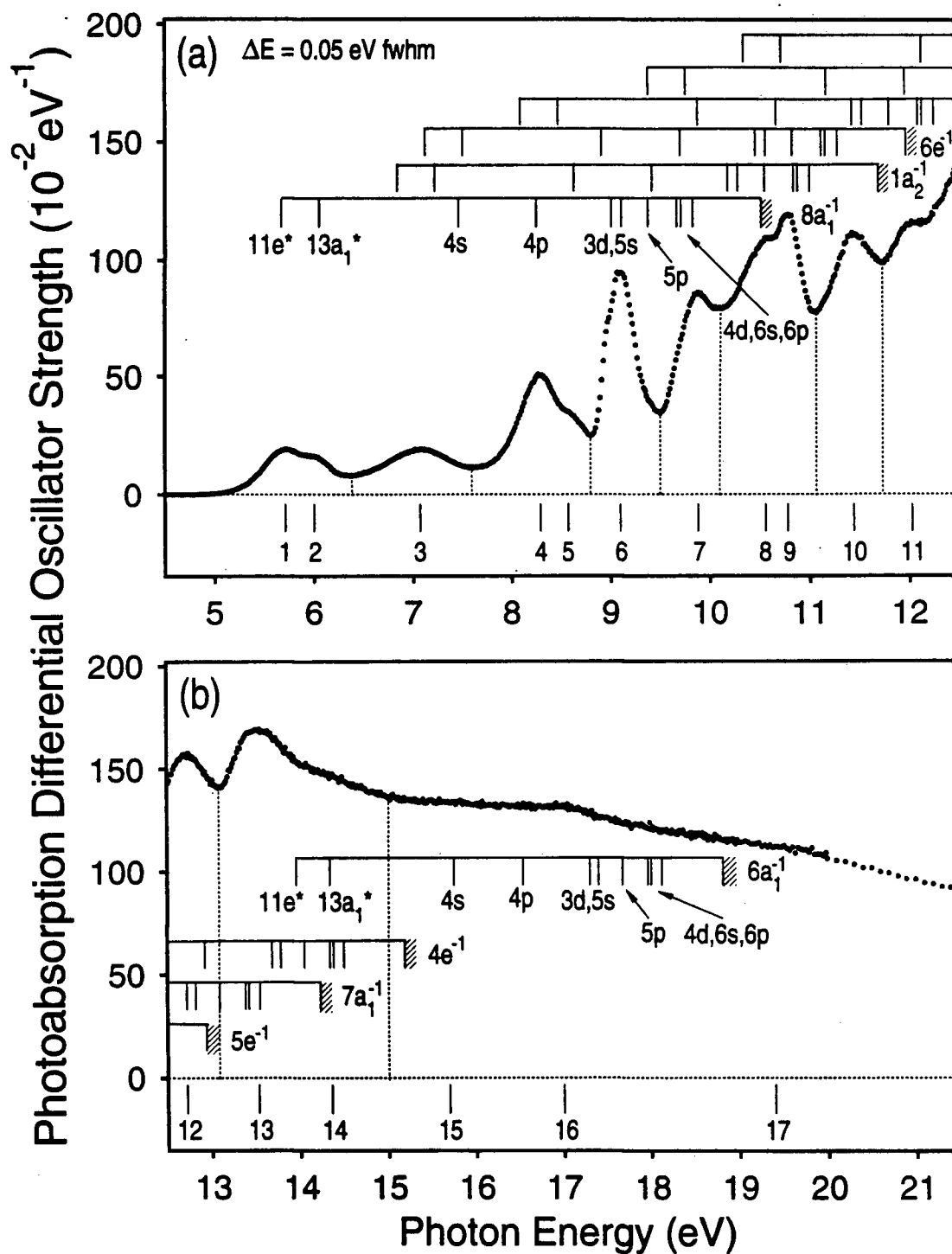


**Figure 5.7:** The features observed in the discrete high resolution (0.05 eV fwhm) valence-shell absolute photoabsorption spectrum of  $\text{PCl}_3$  from: (a) 5 to 12.5 eV and (b) 12.5 to 21.5 eV. The assignments are taken from ref. [102] (see text for details). Note that absolute cross sections in units of megabarns can be obtained by multiplication of the photoabsorption differential oscillator strengths ( $\text{eV}^{-1}$ ) by a factor of 109.75. The integrated oscillator strengths for the eight energy regions separated by vertical dotted lines are given in table 5.5.

**Table 5.5**

Absolute photoabsorption oscillator strengths for regions of the valence-shell spectrum of  $\text{PCl}_3$

Integrated energy region (eV)	Oscillator strength ( $10^{-2}$ )		
	Present work	Ref. [97]	Ref. [103]
4.92–6.38	14.92	10	9.21 <sup>1</sup>
6.38–7.60	17.46	7	
7.60–8.80	36.63	28	
8.80–9.50	41.85	48	
9.50–10.09	40.21	6	
10.09–11.05	94.60	62	
11.05–11.73	67.21	64	
11.73–13.09	179.17		
13.09–15.00	159.53		

<sup>1</sup> Integrated from 4.92 to 7.60 eV.

### 5.2.3.3 P 2p,2s inner-shell spectra

The absolute phosphorus 2p and 2s inner-shell photoabsorption spectra obtained at a resolution of 0.1 eV fwhm in the present work are presented in figure 5.6(b) together with previously recorded absolute [98] and relative [104] optical absorption spectra. In order to provide a better comparison of the shapes and energy positions of the excitation bands in the inner-shell region, the work of Ishiguro *et al.* [98], which has cross sections ~30% higher than the present

measurements in the phosphorus  $2p$  and  $2s$  shell regions (see figure 5.5 and Sec. 5.2.3.1 above), has been renormalized down to the present data at the valence-shell leading edge. A similar normalization has been performed for the relative spectrum [104]. In general, the shapes of all three measurements are similar. The absolute oscillator strength values for the three fitted gaussian bands as well as the six energy regions separated by the vertical dotted lines in figure 5.8(a) are given in table 5.6.

The first group of broad absorption bands from 132 to 136 eV (fig 5.8(a)) have been assigned to the  $13a_1(\sigma^*)$  and  $11e(\sigma^*)$  virtual valence excitations in the electron energy-loss (EELS) work [102]. However, *ab initio* calculations in a more recent optical study [98] indicated that the  $13a_1$  orbital is situated at least 5 eV above the  $11e$  orbital. Consequently, features 1–3 must arise from the  $11e \leftarrow 2p_{3/2, 1/2}^{-1}(e)$  transitions which have been split by molecular interactions [98]. Under  $C_{3v}$  symmetry the P  $2p$  core orbitals transform as  $a_1$  and  $2e$ . The direct product for the  $2p^{-1}(e)$  initial and  $11e$  virtual valence final orbitals ( $e \otimes e = a_1 + a_2 + e$ ) indicates that two excited states ( $^1A_1$  and  $^1E$ ) are dipole-allowed. These are represented by the spin-orbit split bands labeled as features 1–3 in figure 5.8(a). Compared to the present measurements, feature 4 (135.14 eV) is present at relatively higher intensity in the earlier reported EELS spectrum [102] and at slightly lower intensity in a recent total ion yield spectrum obtained by synchrotron radiation [132]; however, this peak at 135.14 eV is not observed in the other optical spectra [98,104]. It was suggested by Sodhi and Brion that feature 4 results from a dipole-forbidden transition to the  $^3A_2$  state since its intensity was found to increase with momentum transfer ( $\mathbf{K}$ ) when the scattering angle was varied over the range from  $1^\circ$  to  $8^\circ$  at an impact energy of 1500 eV [102]. The experimental conditions employed in the present work (i.e., high incident electron impact energies ( $E_0$ ) with  $E \ll E_0$ , where  $E_0$  is 3000 eV for the high resolution spectrometer, and a mean scattering angle of

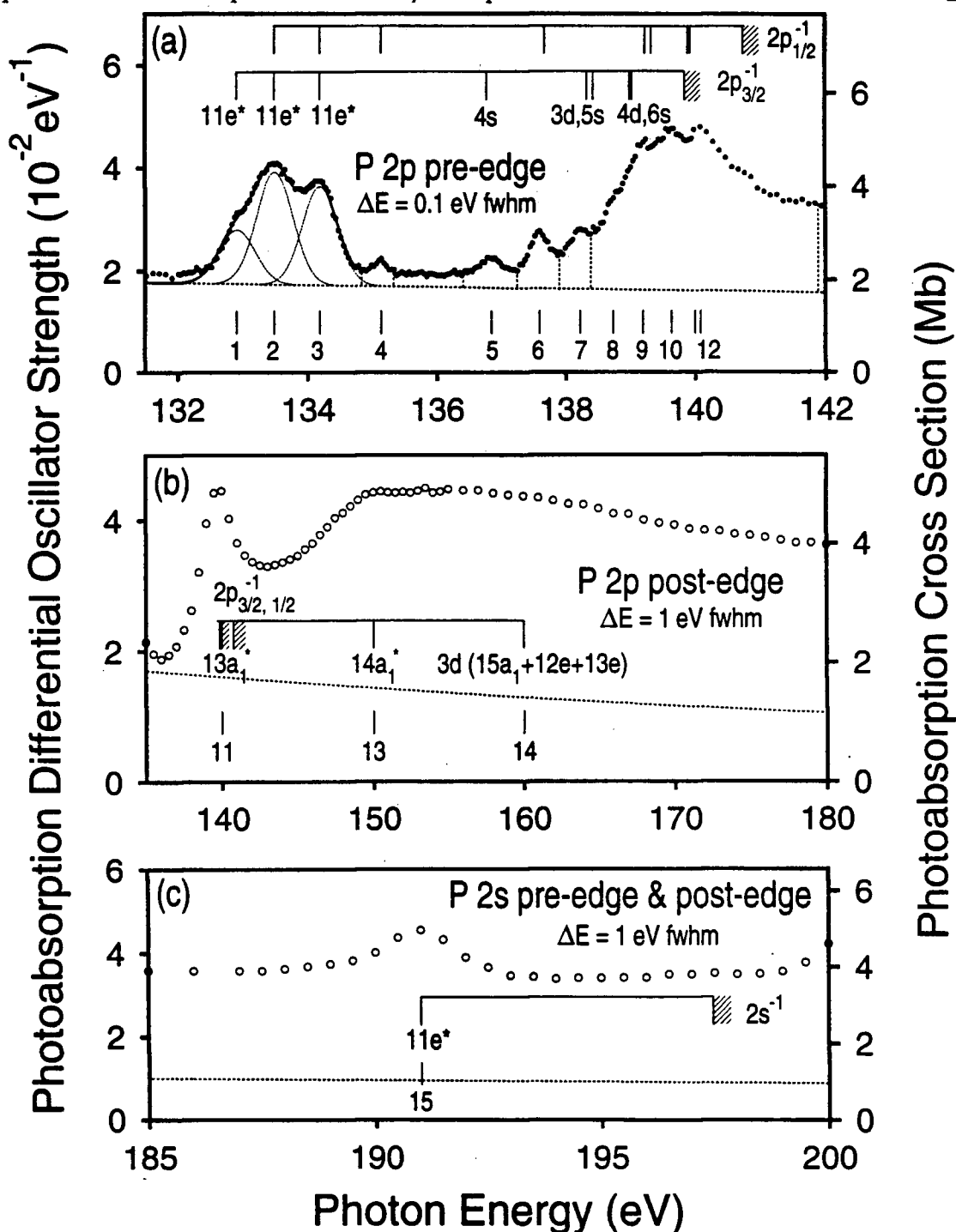


**Figure 5.8:** (a) Absolute photoabsorption differential oscillator strengths (0.1 eV fwhm) for  $\text{PCl}_3$  measured in the P 2p discrete region. The integrated oscillator strengths for the fitted gaussian peaks and the five energy regions separated by vertical dotted lines are given in table 5.6. Panels (b) and (c) show the P 2p post-edge and P 2s regions respectively at 1 eV fwhm. The dotted lines at the base of the spectra in panels (a)–(c) represent the contributions to the absolute oscillator strengths for the inner-shell photoabsorption from the underlying valence-shell estimated from the fitting and extrapolation procedures.

**Table 5.6**

Absolute photoabsorption oscillator strengths for regions of the P 2*p* spectrum of PCl<sub>3</sub>

Integrated energy region (eV)	Oscillator strength (10 <sup>-2</sup> )	
	P 2 <i>p</i> shells	Valence + P 2 <i>p</i> shells
132.91 <sup>1</sup>	0.73	7.83 (132.36–134.83 eV) <sup>2</sup>
133.49 <sup>1</sup>	1.53	
134.19 <sup>1</sup>	1.30	
134.83–135.38	0.21	1.13
135.38–136.39	0.26	1.95
136.39–137.25	0.37	1.81
137.25–137.88	0.50	1.54
137.88–138.39	0.49	1.34
138.39–141.90	8.16	13.78

<sup>1</sup> Main peak energy of fitted gaussian curve.

<sup>2</sup> Integrated energy region.

zero degree) result in an even smaller momentum transfer than that in ref. [102], and contributions from non-dipole transitions are expected to be very small [2,5]. Nevertheless, small contributions from dipole-forbidden transitions cannot be entirely ruled out, since the scattering angles can never be exactly zero degree because of the finite acceptance angle ( $3.0 \times 10^{-5}$  steradians) [5,14] subtended about zero degree by the effective entrance aperture to the electron analyzer. For example, an extremely small contribution from the dipole forbidden transition to the helium 2<sup>1</sup>S state from the ground state of helium (less than 0.5 % of the oscillator

strength for the  $2^1\text{P}$  state) was observed earlier [133]. Since the analogous P  $2p$  spectrum of  $\text{PF}_3$ , which also has  $\text{C}_{3v}$  geometry, (see section 5.2.2.3 and figure 5.4) does not show the presence of a similar excitation as that observed in  $\text{PCl}_3$  at 135.14 eV, the transition moment for the  $^3\text{A}_2$  excited state in  $\text{PCl}_3$  must be very sensitive to changes in the momentum transfer, and this unusual phenomenon is not understood. A momentum transfer of 0.12 a.u. ( $\text{\AA}^{-1}$ ) has been calculated based on the experimental conditions for the present study. This value is much smaller than that of 0.72 a.u. reported in the EELS study which utilized a one degree scattering angle and 1500 eV impact energy [102].

The next set of absorption bands from 136 to 141 eV have been attributed to overlapping Rydberg transitions superimposed on top of a shape resonance [98,102] which occur near the ionization edge. The assignments of features 5–10 and 12 as indicated on the manifolds have been taken from ref. [102] with quantum defects of 1.89 and 0 for the  $ns$  and  $nd$  Rydberg orbitals, respectively. In contrast, Ishiguro *et al.* [98] interpreted these structures as excitations to the  $ns$  and  $np$  series based on the fact that while  $p \leftarrow p$  transitions are formally forbidden in atomic systems,  $p$  orbitals transform as  $a_1$  and  $2e$  under  $\text{C}_{3v}$  symmetry for molecular  $\text{PCl}_3$ , and thus transitions to  $np$  Rydberg orbitals are formally dipole-allowed. Nevertheless, there is no clear evidence for any significant contribution from the  $4p$  Rydberg in the spectrum of Ishiguro *et al.* (see figure 4 of ref. [98]) despite the fact that it was collected with even higher resolution than the present work. Similarly, in the somewhat lower resolution spectrum reported by Sodhi and Brion [102], there is no evidence of the  $4p$  transition at the expected energy around the ionization edge.

The shape resonances located near and above the P  $2p$  ionization thresholds (features 11, 13, and 14 in figure 5.8(b)) can be assigned by analogy with the  $\text{PF}_3$  P  $2p$  shell spectrum (section 5.2.2.3 and figure 5.4). In the  $\text{PF}_3$  spectrum, the  $13a_1$  virtual valence orbital was determined to be situated close to the ionization

threshold [98,43], and by analogy the intense resonance embedded under the Rydberg structures for  $\text{PCl}_3$  (feature 11) must result from  $13a_1 \leftarrow \text{P } 2p^{-1}$ . The next resonance at  $\sim 150$  eV can be attributed to  $14a_1 \leftarrow \text{P } 2p^{-1}$ , while the very broad resonances extending from 150 to 170 eV arise from the phosphorus continuum  $3d$  orbitals ( $15a_1+12e+13e$ ) [43]. The ordering of the atomic-like  $3d \leftarrow \text{P } 2p^{-1}$  transitions,  $3d_{z^2}(a_1) < 3d_{xz,yz}(e) < 3d_{x^2-y^2,xy}(e)$  [108], is reflected by the relative positions of the  $a_1$  and  $e$  channel partial cross sections theoretically determined in ref. [43].

The structure (features 15) observed in the P  $2s$  spectrum in figure 5.8(c) has been previously assigned to the  $11e \leftarrow \text{P } 2s^{-1}$  transition [98,102].

### 5.2.3.4 Cl $2p,2s$ inner-shell spectra

The chlorine  $2p$  and  $2s$  inner-shell spectra for  $\text{PCl}_3$  measured at high resolution (0.1 eV fwhm) in the present work are shown in figure 5.6(c) together with previously recorded absolute [98] and relative [104] optical absorption spectra, which have been normalized to the present data in the phosphorus  $2s$  shell ionization continuum. Table 5.7 contains the absolute oscillator strength values ( $f$ ) for the Cl  $2p$  discrete transitions of  $\text{PCl}_3$  (plus the underlying P  $2p,2s$  continuum) in the seven energy regions indicated by the vertical dotted lines in figure 5.9(a).

The first two absorption bands observed at 200.27 and 201.72 eV in the Cl  $2p$  spectrum (fig. 5.9(a)) have been attributed to the  $11e \leftarrow \text{Cl } 2p^{-1}$  excitations [98]. Sodhi and Brion [102] suggested a different final orbital,  $13a_1$ , for these bands and assigned features 2 and 3 to  $11e \leftarrow \text{Cl } 2p^{-1}$  instead. However, based on the large energy separation between the  $11e$  and  $13a_1$  orbitals as shown by the P  $2p$  spectral assignments in figure 5.8 (based on the *ab initio* calculations of Ishiguro *et al.* [98]), it is unlikely that the  $13a_1 \leftarrow \text{Cl } 2p^{-1}$  absorption bands are located so far away from

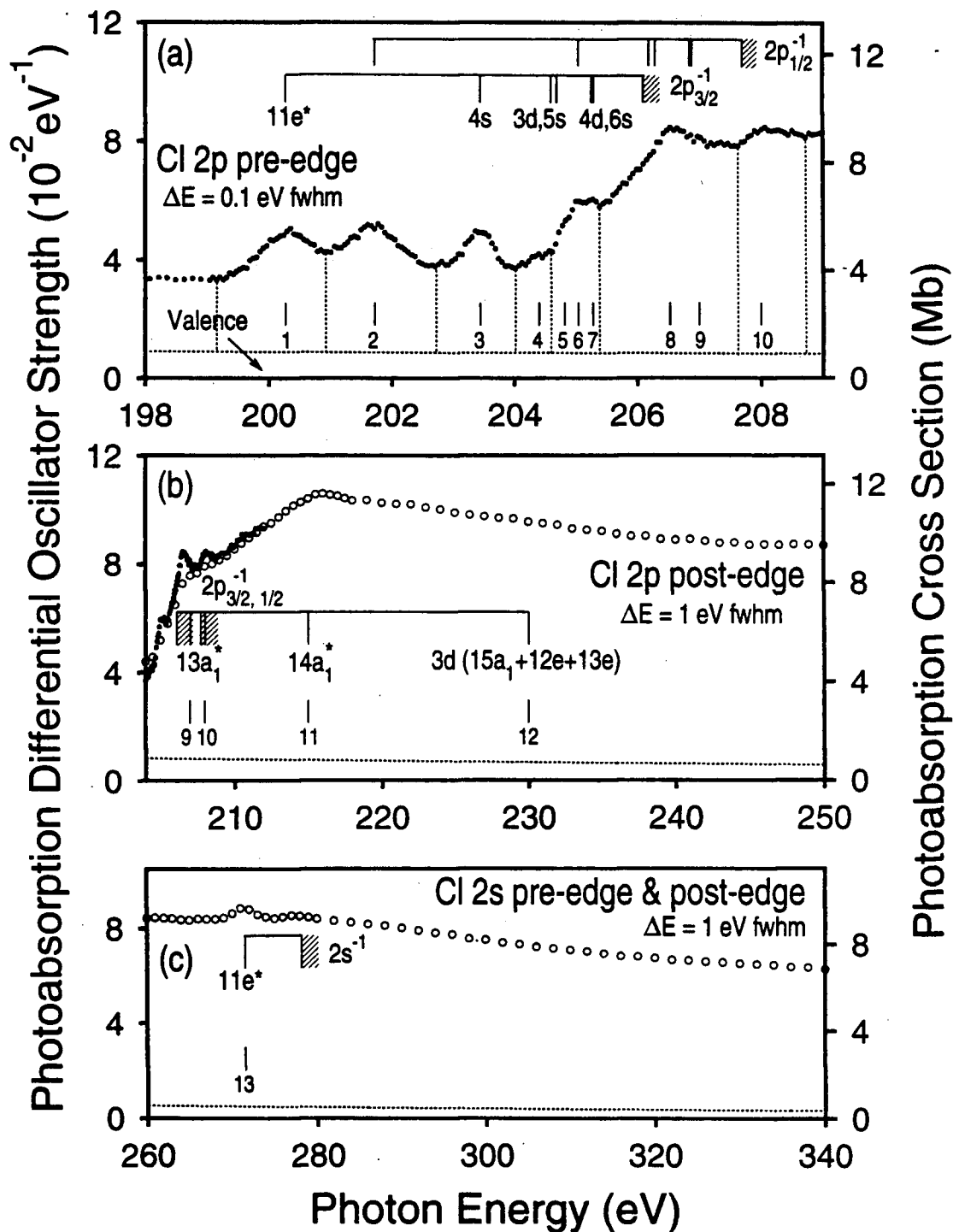


**Figure 5.9:** (a) Absolute photoabsorption differential oscillator strengths (0.1 eV fwhm) for  $\text{PCl}_3$  measured in the Cl 2p discrete region. The integrated oscillator strengths for the seven energy regions separated by vertical dotted lines are given in table 5.7. Panels (b) and (c) show the Cl 2p post-edge and Cl 2s regions respectively at 1 eV fwhm. The dotted lines at the base of the spectra in panels (a)–(c) represent the contributions to the absolute oscillator strengths for the inner-shell photoabsorption from the underlying valence-shell estimated from the fitting and extrapolation procedures.

**Table 5.7**

Absolute photoabsorption oscillator strengths for regions of the Cl 2p spectrum of PCl<sub>3</sub> (plus the underlying P 2p,2s continuum)

Integrated energy region (eV)	Oscillator strength (10 <sup>-2</sup> )	
	P 2p,2s + Cl 2p shells	Valence + P 2p,2s + Cl 2p shells
199.16–200.93	6.01	7.53
200.93–202.71	6.53	8.03
202.71–204.01	4.45	5.57
204.01–204.61	1.92	2.42
204.61–205.39	3.68	4.31
205.39–207.64	15.26	16.93
207.64–208.73	8.14	8.96

the ionization threshold. Similar to the electron energy-loss spectrum reported earlier [102], there is no indication of a third peak arising from the <sup>3</sup>A<sub>2</sub> dipole-forbidden state, in contrast to the situation in the phosphorus 2p spectrum.

The structures between 203 to 207 eV in figure 5.9(a) which are superimposed over the 13a<sub>1</sub> shape resonance have been previously assigned to *ns* Rydberg transitions in the electron energy-loss work [102], and these are shown on the manifolds in figure 5.9(a). The higher instrumental resolution of the dipole (*e,e*) spectrometer used in the present work allows the detection of an additional shoulder at ~204.4 eV (feature 4) as well as more defined structures between 204.5–205.5 eV (features 5–7). This is in fair agreement with the high resolution synchrotron radiation study [98]. Ishiguro *et al.* [98] has ascribed feature 4 to the 4p Rydberg ←

Cl  $2p^{-1}$  transitions; however, based on the assignments of the phosphorus  $2p$  spectrum [102] (see Sec. 5.2.3.3), it is more likely to be a  $3d$  Rydberg with a quantum defect of zero.

In the Cl  $2p$  post-edge region (figure 5.9(b)), the first resonance structure near the ionization threshold (207 eV) comes from the  $13a_1 \leftarrow \text{Cl } 2p^{-1}$  virtual valence transition, while the other two broader shape resonances at ~215 and 230 eV arise from excitations to  $14a_1$  and to the chlorine continuum  $3d$  orbitals, respectively [102].

From figures 5.8 and 5.9 it can be seen that the intensity distributions of the phosphorus and chlorine  $2p$  shell discrete spectra differ considerably from one another. The stronger pre-edge transitions to virtual valence orbitals than to Rydberg orbitals and the more prominent post-edge resonances in the P  $2p$  spectrum arise from the presence of the electronegative chlorine atoms, which form a partial "cage" about the phosphorus atom in  $\text{PCl}_3$  in the electrostatic potential well model [134,135]. The strong repulsive force acting on the escaping electron near the electronegative chlorine ligands would be expected to result in the existence of an effective Coulombic potential barrier [135], which separates the molecular field into an inner-well region which traps discrete virtual valence excited states below and above the ionization threshold, as well as an outer-well region where Rydberg states are located. The virtual valence orbitals located in the inner-well region would have a strong overlap with the P  $2p$  core orbital, resulting in enhanced spectral features or resonances. In contrast, the more diffuse Rydberg orbitals located in the outer-well region would be isolated from the molecular core, causing less pronounced Rydberg and ionization continuum transitions. It can be seen that the virtual valence transitions in the Cl  $2p$  pre-edge region are relatively much less prominent than in the P  $2p$  spectrum, while the Rydberg states and ionization continuum are relatively more pronounced in the Cl  $2p$  spectrum. In

addition, the Cl  $2p$  post-edge resonances are less prominent than those in the P  $2p$  spectrum. These observations can be attributed to the fact that the Cl ligands are not surrounded by electronegative species, in contrast to the situation for the P atom.

In the Cl  $2s$  spectrum (figure 5.9(c)), feature 13 results from the  $11e$  virtual valence transition [102].

## 5.2.4 Phosphorus pentafluoride

### 5.2.4.1 Long range photoabsorption spectrum

Figure 5.10 shows the absolute photoabsorption spectrum of  $PF_5$  spanning the valence, P  $2p$ , and P  $2s$  regions, and tables A.11 and A.12 in the appendix give the data in numerical form. The dotted line represents the valence shell extrapolation curve obtained as described in sections 3.1.1 and 5.2.

Atomic mixture rules (AMR's) have been used to provide an approximate means of assessing the shape and absolute values of photoabsorption spectra when no other experimental measurements are available for comparison, as is the case for  $PF_5$ . Such comparisons with atomic data are likely to be most valid in continuum regions of the spectra away from near edge molecular effects. In figure 5.10, experimental [84] and theoretical [86] atomic differential oscillator strength sums (P+5F) for  $PF_5$  are compared above 40 eV with the present measurements. The theoretical data [86] have also been used to model the valence contribution to the photoabsorption above 135 eV (the onset of P  $2p$  ionization and excitation). It can be seen that in the case of  $PF_5$  such atomic sums provide good estimates of the oscillator strengths in the valence continuum above 50 eV and in the P  $2p,2s$  continua.

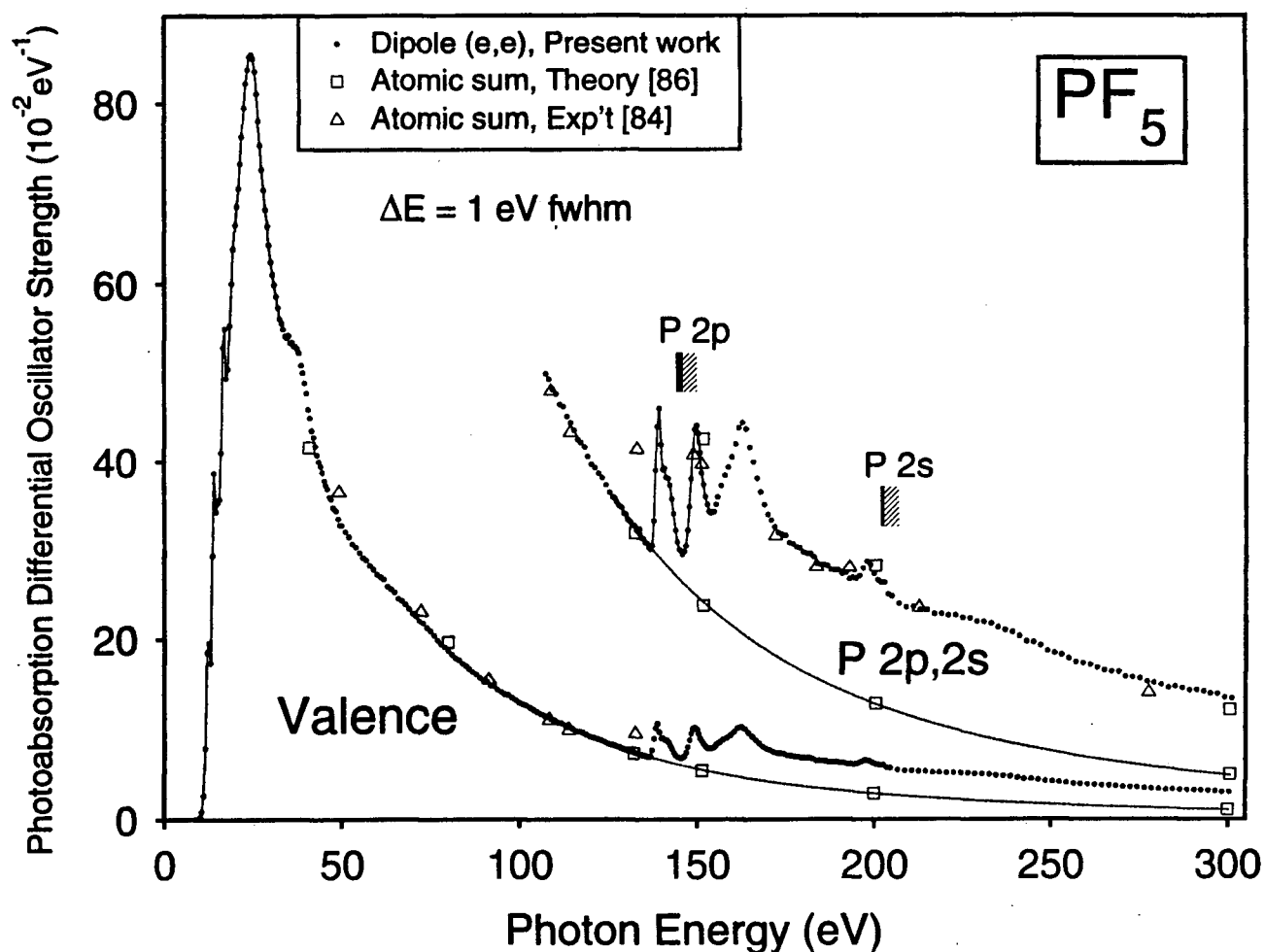


**Figure 5.10:** Absolute photoabsorption differential oscillator strengths for  $\text{PF}_5$  obtained at a resolution of 1 eV fwhm from 10 to 300 eV. The hatched lines show the positions of the P 2p and P 2s thresholds, and the dotted lines represent the valence-shell extrapolation curve obtained by fitting equation (3.1) to the high-energy portion of the valence spectrum (90–135 eV).

Using the  $S(-2)$  sum rule and the absolute photoabsorption differential oscillator strength data in tables A.11 and A.12, a static electric-dipole polarizability of  $39.14 \times 10^{-25} \text{ cm}^3$  has been derived for  $\text{PF}_5$ . This value is in good agreement with the refractivity work of Batsanov,  $36.455 \times 10^{-25} \text{ cm}^3$ , [121] and the theoretical calculation performed by Nagarajan,  $38.549 \times 10^{-25} \text{ cm}^3$ , [120] using the delta-function potential model. These findings provide additional support for the accuracy of the absolute differential oscillator strength scale obtained in the present work using the dipole ( $e, e$ ) method and the VTRK sum rule.

#### 5.2.4.2 Valence-shell spectrum

The valence-shell absolute photoabsorption spectrum from 10 to 50 eV measured at higher resolution (0.05 eV fwhm) is presented in figure 5.11(a), while figure 5.12 shows the 10–23 eV discrete region in greater detail. The assignments shown on the manifolds (figure 5.12) have been taken from ref. [101], where they were determined by transferring term values from the outermost ion state to all remaining ion states. It can be seen that the  $\text{PF}_5$  valence-shell spectrum is generally characterized by strong transitions to the  $9a'_1$  and  $7e'$  virtual valence orbitals, overlapping the much weaker  $ns$  Rydbergs [101]. The energy positions of the features observed in figure 5.12 are in good agreement with those reported by Sodhi and Brion [101]. The absolute oscillator strength values for the six energy regions separated by dotted vertical lines in figure 5.12 are given in table 5.8.

The two shape resonances present in the ionization continuum at ~37 and 65 eV in figures 5.10 and 5.11 can be attributed to valence-shell excitations to the phosphorus continuum  $3d$  orbitals by analogy with those observed in the  $\text{PF}_3$  valence-shell spectrum (cf. ~35 and 60 eV in figure 5.1) and the presence of similar structures in the  $\text{PF}_5$   $P 2p$  post-edge region (see figure 5.13(b) below).

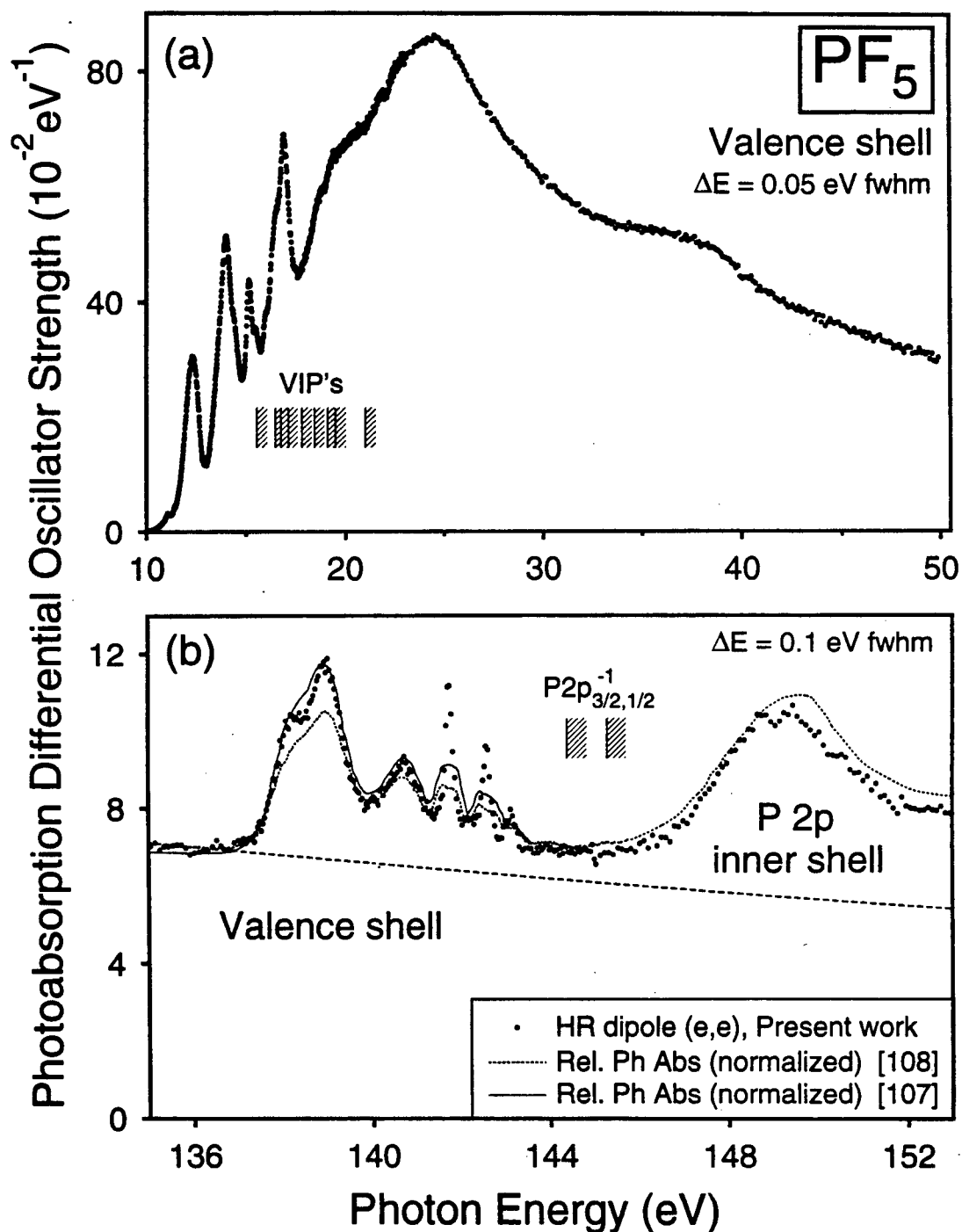


**Figure 5.11:** Absolute high resolution photoabsorption spectra of (a) the valence shell region of PF<sub>5</sub> (0.05 eV fwhm) and (b) the P 2p region of PF<sub>5</sub> (0.1 eV fwhm). The hatched lines indicate positions of the VIP's as determined by PES [112,117] and XPS [111]. The dashed line in (b) represents the contribution to the absolute oscillator strengths in the P 2p inner-shell region from the underlying valence-shell estimated from the fitting and extrapolation procedures. The relative intensities of the optical spectra [107,108] have been normalized to the present data at the valence-shell continuum for comparison.

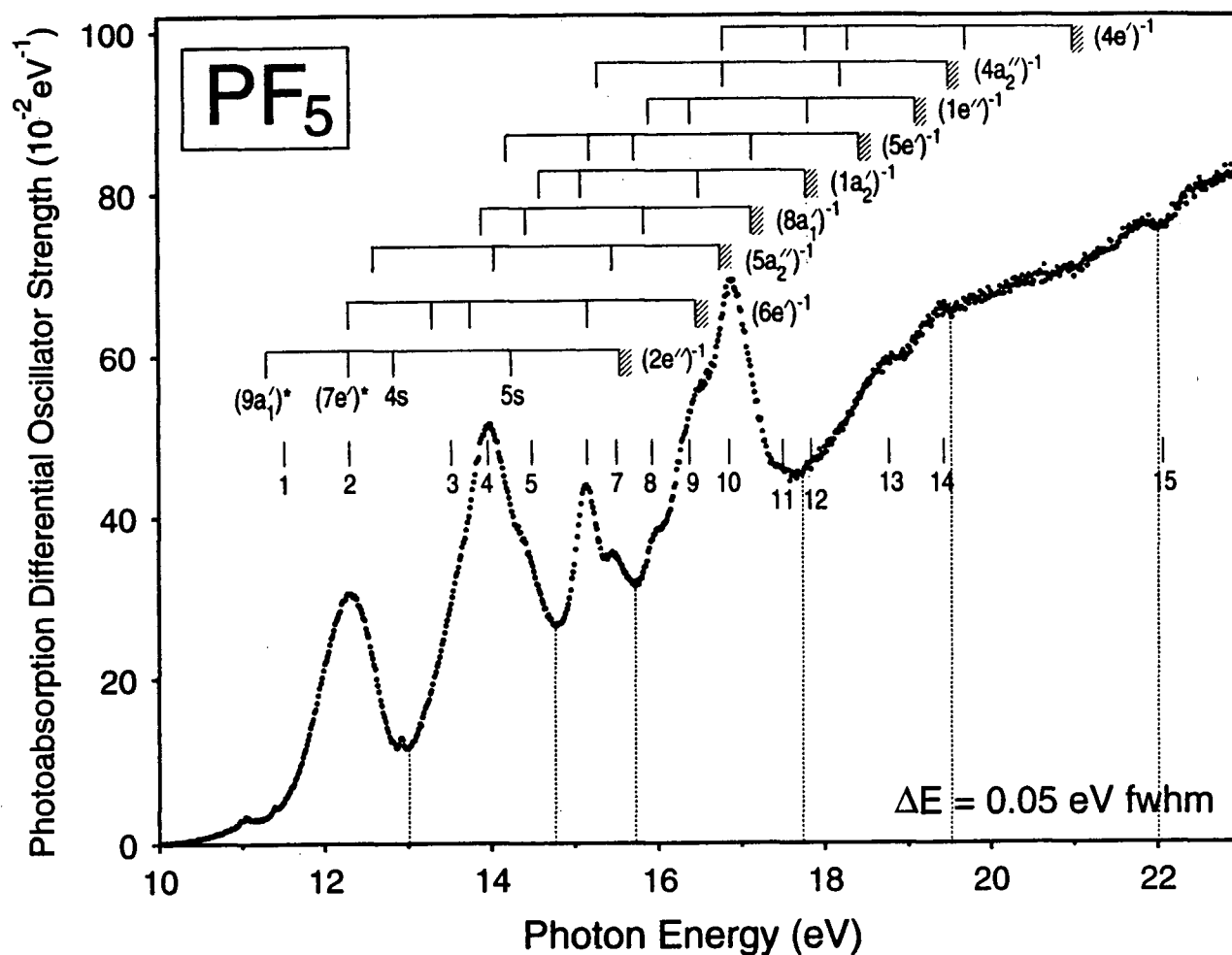


**Figure 5.12:** The high resolution (0.05 eV fwhm) valence-shell absolute photoabsorption spectrum of PF<sub>5</sub> from 10 to 23 eV. The assignments have been taken from ref. [101]. Note that absolute cross sections in units of megabarns can be obtained by multiplication of the photoabsorption differential oscillator strengths (eV<sup>-1</sup>) by a factor of 109.75. The integrated oscillator strengths for the six energy regions separated by vertical dotted lines are given in table 5.8.

**Table 5.8**

Absolute photoabsorption oscillator strengths for regions of the valence-shell spectrum of PF<sub>5</sub>

Integrated energy region (eV)	Oscillator strength (10 <sup>-2</sup> )
10.00–13.00	30.55
13.00–14.78	59.02
14.78–15.73	33.16
15.73–17.73	100.75
17.73–19.53	101.66
19.53–22.0	173.76

### 5.2.4.3 P 2*p*,2*s* inner-shell spectra

The absolute photoabsorption differential oscillator strengths for the P 2*p* and 2*s* inner-shells of PF<sub>5</sub> measured at 1 eV fwhm resolution in the present work are presented in figure 5.10. The discrete structures in the P 2*p* region have also been studied at higher resolution (0.1 eV fwhm), and these are shown in figure 5.11(b). The lower resolution relative optical spectra of Tse and Liu [107] and Liu *et al.* [108], also shown for comparison in figure 5.11(b), have been normalized to the present work in the valence-shell continuum. It can be seen that the energy positions of the peaks and the general shapes of the spectra taken from refs. [107,108] are in excellent agreement with the present results.

Strong virtual valence and sharp *ns* Rydberg transitions comprise the P 2*p* discrete spectrum of PF<sub>5</sub> (see figure 5.13(a)) [106–108]. This is in contrast to the

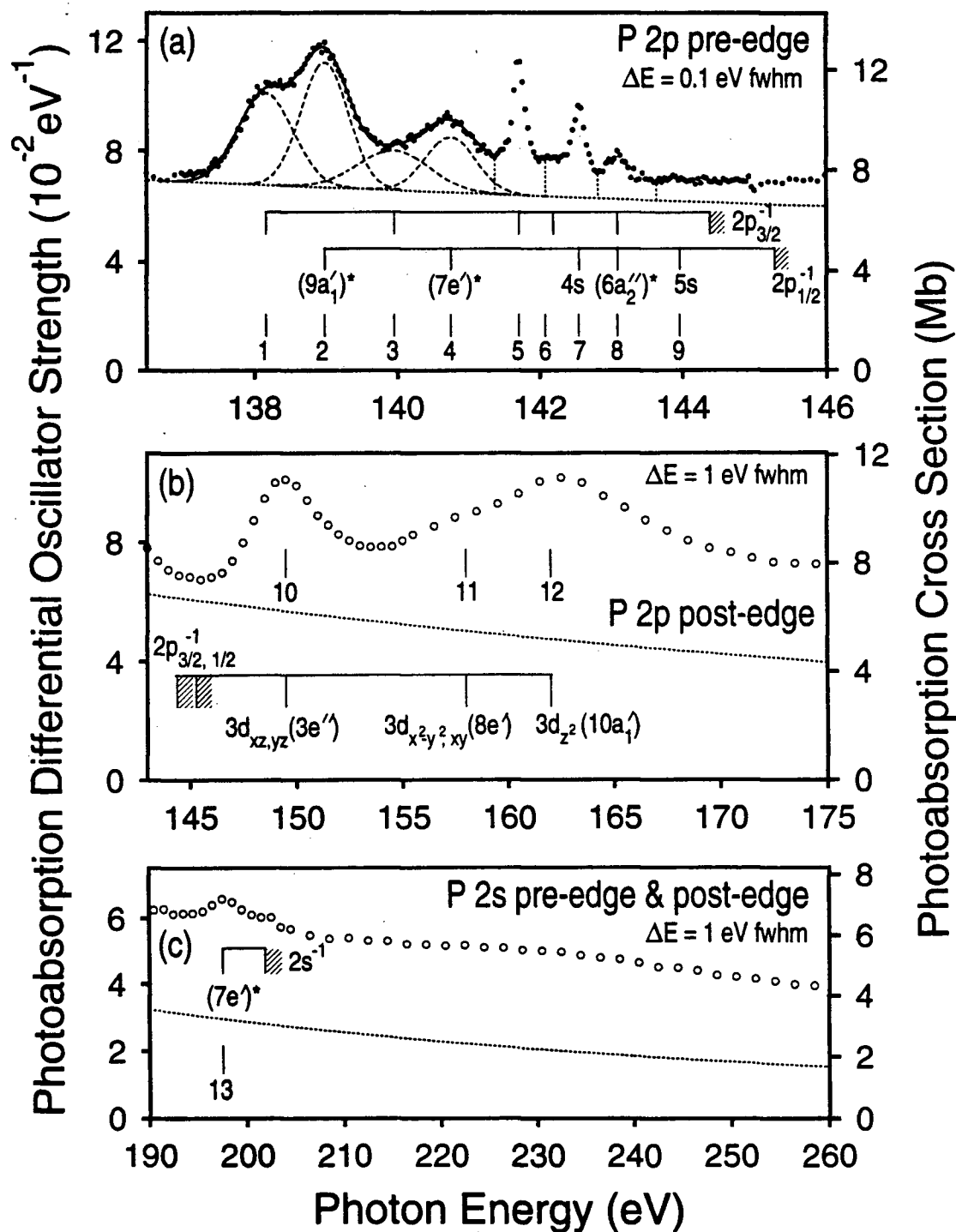


**Figure 5.13:** (a) Absolute photoabsorption differential oscillator strengths of  $\text{PF}_5$  (0.1 eV fwhm) measured in the P 2p discrete region. The integrated oscillator strengths for the four fitted gaussian curves and the three energy regions separated by vertical dotted lines are given in table 5.9. Panels (b) and (c) show the P 2p post-edge and P 2s regions respectively. The dotted lines at the base of the spectra in panels (a)–(c) represent the contributions to the absolute oscillator strengths in the respective inner-shell regions from the underlying valence-shell estimated from the fitting and extrapolation procedures.

S 2*p* spectrum of the isoelectronic molecule SF<sub>6</sub> [136,137], where the intensities of the Rydbergs are much smaller than those of the very strong virtual valence transitions. While both the SF<sub>6</sub> and PF<sub>5</sub> molecules are surrounded by a cage of electronegative fluorine atoms, the difference of just one fluorine atom in going from SF<sub>6</sub> to PF<sub>5</sub> dramatically increases the relative contribution of the Rydberg transitions in the spectrum. The four absorption bands at low energy (features 1–4) are predominantly virtual valence in character and have been previously assigned to the  $9a'_1 \leftarrow 2p_{3/2,1/2}^{-1}$  and  $7e' \leftarrow 2p_{3/2,1/2}^{-1}$  spin-orbit split transitions [106–108]. Using the energy positions of the virtual valence transitions as reported in refs.[106–108] as a guide, four gaussian curves have been fitted to the P 2*p* pre-edge spectrum. The absolute oscillator strengths (*f*) for the fitted peaks corresponding to features 1–4 are given in table 5.9.

**Table 5.9**

Absolute photoabsorption oscillator strengths for regions of the P 2*p* spectrum of PF<sub>5</sub>

Integrated energy region (eV)	Oscillator strength (10 <sup>-2</sup> )	
	P 2 <i>p</i> shell	Valence + P 2 <i>p</i> shells
138.16 <sup>1</sup>	3.19	26.18 (137.04–139.80 eV) <sup>2</sup>
138.98 <sup>1</sup>	3.72	
139.95 <sup>1</sup>	1.78	
140.75 <sup>1</sup>	1.75	13.42 (139.80–141.37 eV) <sup>2</sup>
141.37–142.08	1.69	6.23
142.08–142.84	1.37	6.18
142.84–143.62	0.85	5.76

<sup>1</sup> Peak energy of fitted gaussian curve.

<sup>2</sup> Integrated energy range.

Based on a recent study [107] that compared the relative intensities of the discrete profiles observed in gas-phase and solid-phase photoabsorption spectra, the features in the 141.5–145 eV energy region of the  $\text{PF}_5$  photoabsorption spectrum were found to be largely due to Rydberg transitions plus a small contribution from virtual valence transitions underlying the two sharp bands at 141.71 and 142.55 eV (features 5 and 7). Sodhi and Brion [106] have attributed these bands to  $4s \leftarrow 2p_{3/2}^{-1}$  and  $4s \leftarrow 2p_{1/2}^{-1}$ , respectively, with an average term value of 2.74 eV, which is in good agreement with that of 2.70 eV obtained in the present work. The positions of the  $4s$  and  $5s$  Rydbergs as determined in ref. [106] using the Rydberg formula are shown on the manifolds in figure 5.13(a). Two additional bands at 141.95 and 142.85 eV, which were not observed in the electron energy-loss spectrum [106], are present in the relative spectrum reported by Liu *et al.* [108], and theoretical MS-X $\alpha$  calculations [108] have suggested that these can be attributed to transitions to the  $10a'_1$  virtual valence orbital. In the present work, it is clear from figure 5.13(a) that additional transitions (i.e., features 6 and part of feature 8) are present in the vicinity of the  $4s$  Rydbergs. However, such transitions are more likely to be due to the  $6a''_2$  virtual valence orbital rather than the  $10a'_1$  orbital since the latter has P  $3d$  character [108], and transitions to the  $10a'_1$  are therefore expected to be observed at higher energy (see below). The absolute oscillator strength values ( $f$ ) for the energy regions separated by the vertical dotted lines in figure 5.13(a) are given table 5.9.

Three intense shape resonances are observed in the P  $2p$  ionization continuum at 149.5, 158, and 162 eV (see figure 5.13(b)). Based on recent MS-X $\alpha$  calculations [108], these structures arise from excitations of electrons from the P  $2p$  core to the phosphorus continuum  $3d$  orbitals, and crystal field theory indicates that the atomic-like transitions are split in the following order:  $3d_{xz,yz}(e'') < 3d_{x^2-y^2,xy}(e') < 3d_{z^2}(a'_1)$ .

The relatively weak pre-edge structure at 197.5 eV in the P  $2s$  spectrum

(figure 5.13(c)) has been assigned to the dipole-allowed virtual valence transition,  $7e' \leftarrow 2s^{-1}$  [106] based on the similarity of its term value to that of  $7e' \leftarrow 2p^{-1}$  in the P  $2p$  spectrum.

## Chapter 6

# Photoionization Studies of Phosphorus Halides

### 6.1 Introduction

As with the situation of phosphorus halide photoabsorption, there have been very few experimental or theoretical studies reported for the photoionization of  $\text{PF}_3$ ,  $\text{PCl}_3$ , and  $\text{PF}_5$ . Moreover, most of these studies have been focused on the determination of binding energies of valence and inner shell orbitals using PES and XPS. No absolute partial oscillator strengths for the molecular and dissociative photoionization of  $\text{PF}_3$ ,  $\text{PCl}_3$ , and  $\text{PF}_5$  are available in the literature prior to the present study.

The outer valence ionization of  $\text{PF}_3$  has been studied extensively by photoelectron spectroscopy [99,109,112,131,138,139] and photoelectron-photoion-coincidence (PEPICO) spectroscopy [140–142]. Both the PES studies by Green *et al.* [139] and Väyrynen *et al.* [99], obtained using synchrotron radiation, reported photoelectron branching ratio data for the seven outer valence bands of  $\text{PF}_3$ . In contrast, no data are available for the inner valence ion states,  $3e^{-1}$  and  $5a_1^{-1}$ , other than the theoretical ionization energies determined using SCF- $X\alpha$ -SW [113] and continuum MS- $X\alpha$  [43] calculations. Photoionization mass spectroscopy [143,144], electron impact [145–147], and threshold-photoelectron-photoion-coincidence (TPEPICO) [148] measurements have contributed additional information on the appearance potentials and relative intensities of molecular and dissociative ions observed in the breakdown of phosphorus trifluoride.

In the inner-shell region of  $\text{PF}_3$ , the phosphorus L and fluorine K photoelec-

tron core binding energies have been recorded using XPS [111,114,149–151], and synchrotron radiation has been used to determine the spin-orbit splitting between the  $2p_{1/2}^{-1}$  and  $2p_{3/2}^{-1}$  components of the P  $2p^{-1}$  ionization [99]. In other work, the core photoionization of  $\text{PF}_3$  has also been studied by  $\text{L}_{2,3}\text{VV}$  Auger spectroscopy [99,152], synchrotron radiation [132], and photoion-photoion coincidence (PIPICO) spectroscopy [153].

In the case of  $\text{PCl}_3$ , the outer-valence photoelectron bands have been investigated using He (I) [112,131] resonance radiation, and X-ray photoelectron spectroscopy has been used to measure the core electron binding energies and Auger ( $\text{KL}_2\text{L}_3$ ) spectra [111,114,149,151,154]. Recently, Platania *et al.* [155] and Larkins *et al.* [152] reported the  $\text{L}_{2,3}\text{VV}$  (P  $2p$ , Cl  $2p$ ) Auger spectra of  $\text{PCl}_3$  using electron beam excitation and synchrotron radiation, respectively. Additional information on the photoion appearance potentials [63,148,156–159] and their relative yield curves [148] have been provided from electron impact [63,156,157,159] and TPEPICO [148] measurements.

In other work, ionization potentials for the outer-valence ion states of  $\text{PF}_5$  have been obtained using He (I) photoelectron spectroscopy [112,117], while the core (P  $2p, 2s$ ; F  $1s$ ) binding energies have been determined by X-ray photoelectron spectroscopy [111,114,149,150,160]. Falconer *et al.* [161] investigated the temperature-dependence of  $\text{PF}_5$  mass spectra using molecular-beam mass spectroscopy in which the molecular beam was directed through a Pierce-type ionizer, and recently, two theoretical studies provided insights to the electronic structure and stability of the  $\text{PF}_5$  molecule [162,163].

In the present work, dipole ( $e, e+\text{ion}$ ) coincidence spectroscopy has been used to obtain the photoionization efficiencies, photoion branching ratios, and absolute partial differential oscillator strengths for the molecular and dissociative photoionization of  $\text{PF}_3$ ,  $\text{PCl}_3$ , and  $\text{PF}_5$  over wide energy ranges, from the first ionization

threshold up to the P 2s (PF<sub>3</sub> and PF<sub>5</sub>) and Cl 2s (PCl<sub>3</sub>) thresholds. In the case of PF<sub>3</sub>, the valence-shell measurements have been used together with photoelectron branching ratios [99,139] and PEPICO [140,141] data in the literature to obtain quantitative information concerning the dipole-induced breakdown scheme for PF<sub>3</sub> under vacuum ultraviolet and soft X-ray radiation.

## 6.2 Results and Discussions

The photoionization efficiencies, photoion branching ratios, and absolute partial photoionization differential oscillator strengths (PPOS) for the molecular and dissociative photoionization of PF<sub>3</sub>, PCl<sub>3</sub>, and PF<sub>5</sub> presented in this chapter were determined using the experimental procedures for the low resolution dipole ( $e,e^+ion$ ) spectrometer described in section 3.1.2. The photoion branching ratios were determined by integrating the mass peaks in the background subtracted TOF mass spectra recorded at each energy loss (equivalent photon energy), correcting for the mass ( $m/e$ ) sensitivity of the microchannel plate ion detector [45], and normalizing the total area to 100%. The absolute scales for the photoionization efficiencies ( $\eta_i$ ) of these molecules were established by normalizing the  $\eta_i$  values to unity at high energies (i.e., above 17.5, 23.5, and 21.0 eV for PF<sub>3</sub>, PCl<sub>3</sub>, and PF<sub>5</sub>, respectively). Finally, the triple product of the absolute total photoabsorption differential oscillator strength (the low resolution data presented in chapter 5), the photoionization efficiency, and the photoion branching ratio for each ion, as a function of photon energy, yielded the absolute PPOS for the production of molecular and fragment ions. The numerical values of the PPOS and  $\eta_i$  data can be found in tables A.7 and A.13 (PF<sub>3</sub>), tables A.9 and A.14 (PCl<sub>3</sub>), and tables A.11 and A.15 (PF<sub>5</sub>) in the appendix.

## 6.2.1 Phosphorus trifluoride

### 6.2.1.1 Valence-shell photoionization

Valence-shell TOF mass spectra of phosphorus trifluoride have been recorded at low resolution (1 eV fwhm) as a function of energy loss (equivalent photon energy) from the first ionization threshold up to the onset of excitation from the P  $2p$  shell (130 eV). The positive ions formed from the molecular and dissociative photoionization of  $\text{PF}_3$  are  $\text{PF}_x^+$ ,  $\text{PF}_x^{2+}$ , and  $\text{F}^+$  where  $x$  equals 0 to 3. Figure 6.1 shows a typical TOF spectrum obtained at 70 eV. The broadness of the peaks due to the smaller, singly-charged ions,  $\text{PF}^+$ ,  $\text{P}^+$ , and  $\text{F}^+$ , indicates that they are formed with appreciable kinetic energies of fragmentation either from direct dissociative photoionization or from Coulomb explosion of multiply charged ions. In particular, the  $\text{P}^+$  peak is quite broad when first formed at 26 eV, while the  $\text{F}^+$  peak further broadens above 55 eV. In the inner-shell region, these ion peaks become increasingly broad with increase in photon energy.

From the photoionization efficiencies ( $\eta_i$ ) shown in figure 6.2 (and given numerically in table A.7), it can be seen that these values rise to a local maximum at  $\sim 13$  eV before increasing quickly to unity at 17.5 eV. The leveling off of the  $\eta_i$  at  $\sim 13$  eV corresponds to a large peak in the low resolution total photoabsorption spectrum (figure 5.1(b)), and this indicates that fluorescence and/or dissociation to neutral products are competing with autoionization back down to the  $8a_1^{-1}$  continuum from the super excited states converging on the higher valence VIP's in this region (see figure 5.3 for details of the excited states at higher resolution).

The photoion branching ratios for  $\text{PF}_3$  are presented in figure 6.3. As the molecular ion decreases in abundance above 16 eV,  $\text{PF}_2^+$  becomes the dominant cation throughout the valence-shell photoionization of phosphorus trifluoride. Above 36 eV small amounts of stable, doubly-charged ions,  $\text{PF}_x^{2+}$  ( $x = 0-3$ ), are

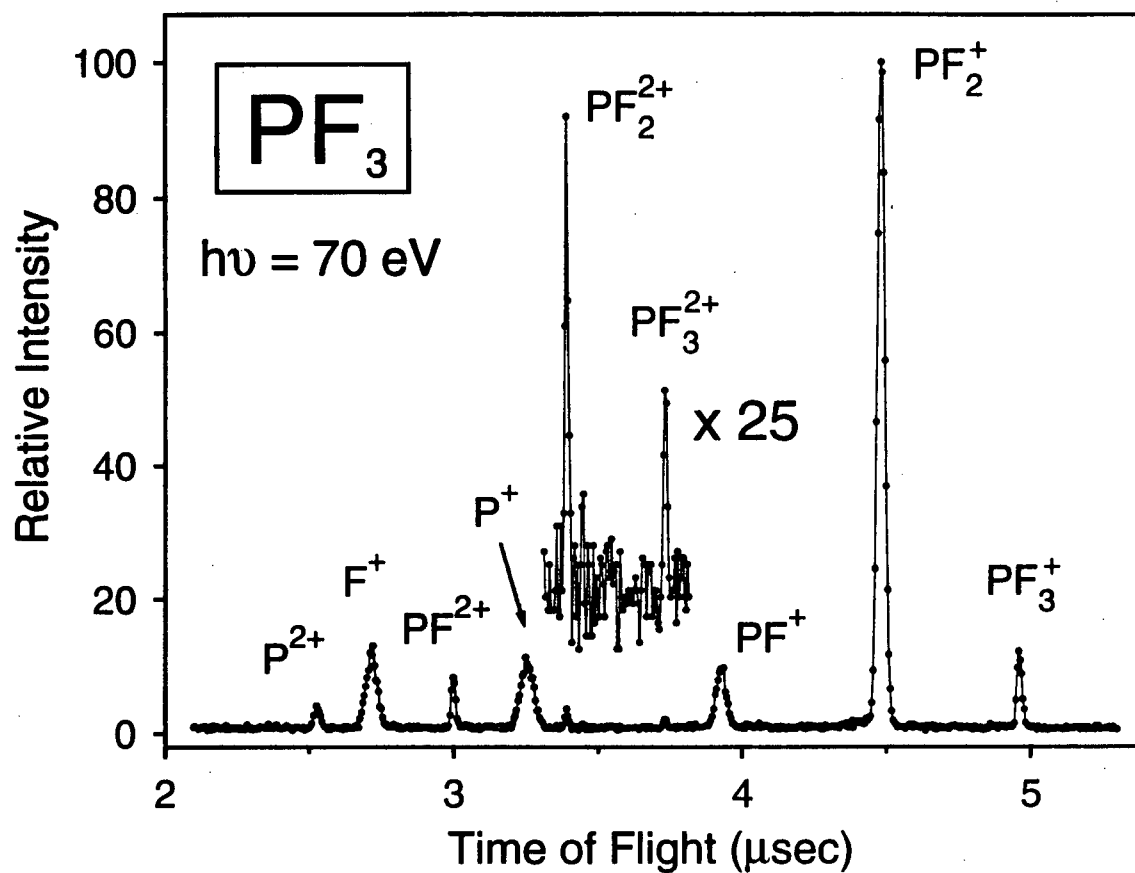


Figure 6.1: TOF mass spectrum of  $\text{PF}_3$  recorded at 70 eV.

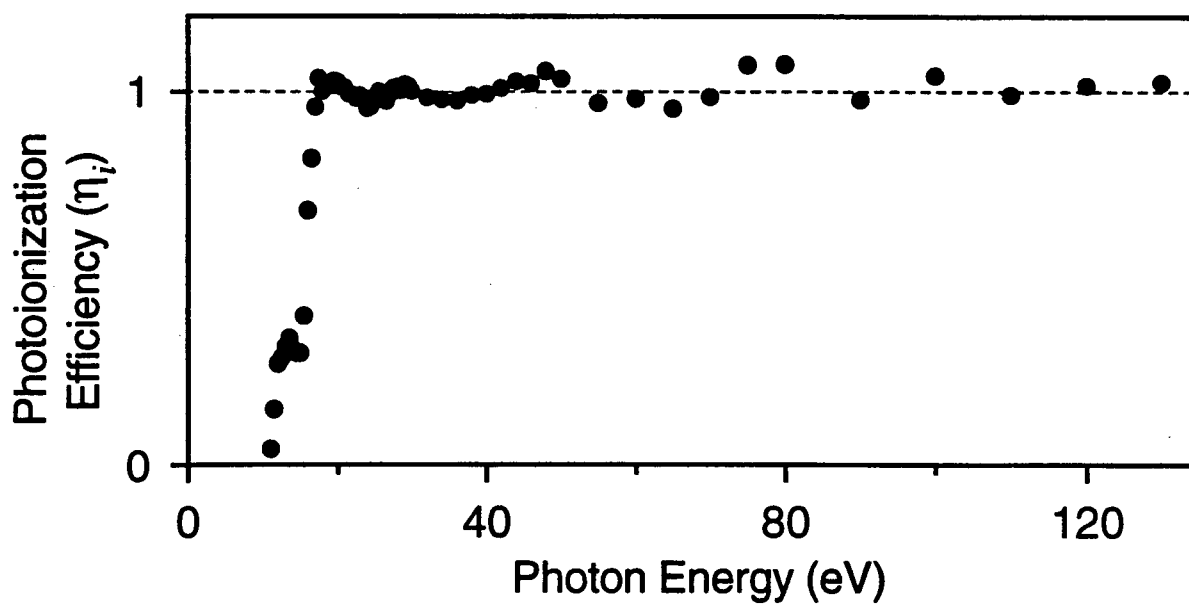
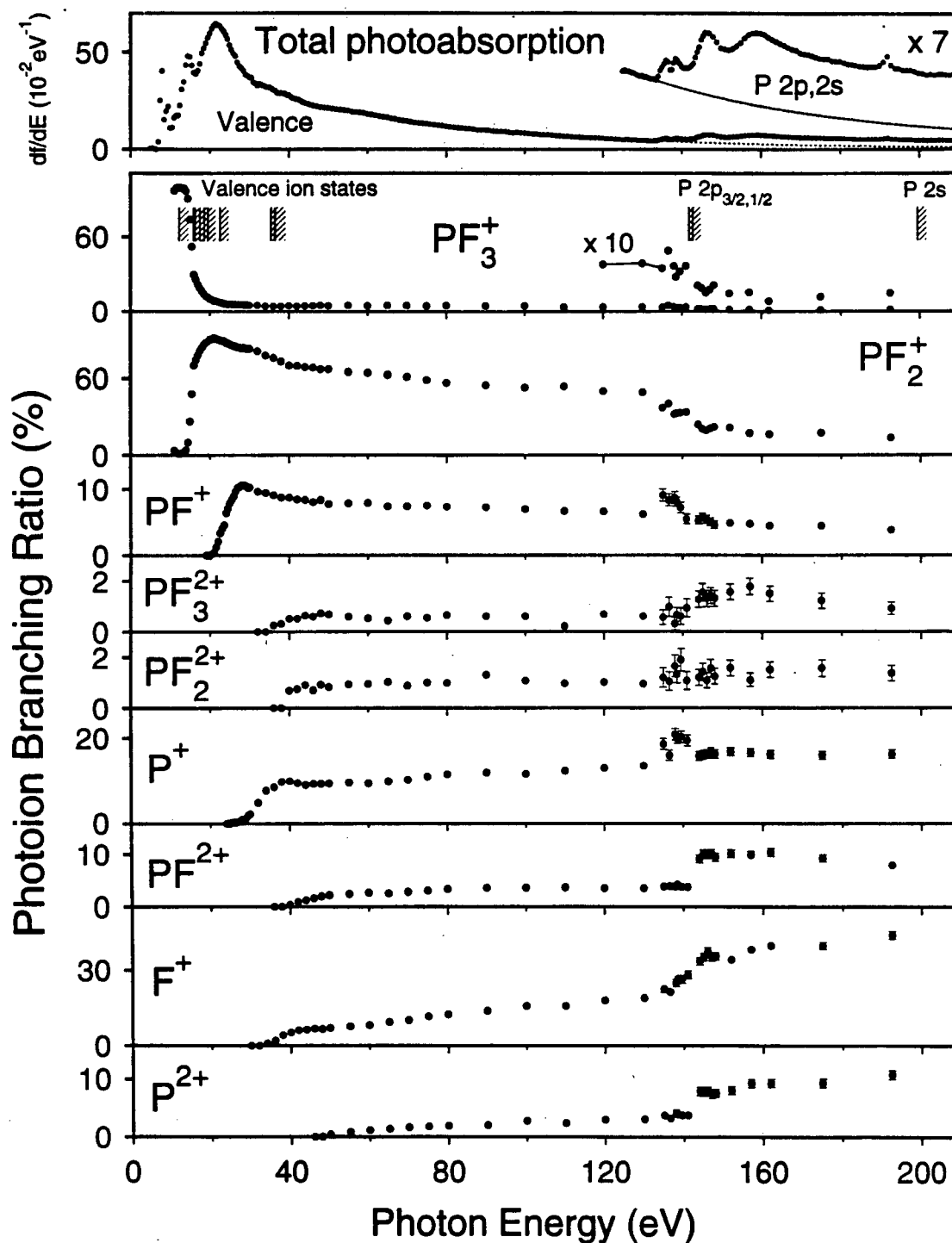


Figure 6.2: Photoionization efficiencies for  $\text{PF}_3$  (11–130 eV).



**Figure 6.3:** Branching ratios for the molecular and dissociative photoionization of  $\text{PF}_3$ . The positions of the seven outer-valence VIP's measured by PES [109], the average energies for the two inner-valence ionization processes determined using MS-X $\alpha$  calculations [43], and the P 2p and 2s VIP's derived from XPS [102] are denoted by the hatched lines in the  $\text{PF}_3^+$  panel. The absolute total photoabsorption spectrum from figure 5.1 is also shown in the top panel.

produced. It is clear that major changes occur in the ionic photofragmentation of  $\text{PF}_3$  in going from the valence to the inner-shell region. The data shown in figure 6.3 for the phosphorus  $2p$  and  $2s$  inner-shell regions above 130 eV are discussed in detail in section 6.2.1.3 below.

The appearance potentials (AP's) of the cations measured in the present work are given in table 6.1 in comparison with values from previously published work. The present results for the singly charged ions are reasonably consistent with previously reported values obtained from photoionization mass spectrometry (PIMS) [143] and electron impact [145,146,148] except in the case of the electron impact value [145] for  $\text{P}^+$ . No appearance potentials for the doubly charged ions are presently available in the literature. Table 6.1 also contains thermodynamic appearance potentials calculated for all possible processes leading to the production of singly charged ions from  $\text{PF}_3$  using heats of formation of neutral species and singly-charged ions [67], and assuming zero kinetic energy of fragmentation. These values for the singly-charged molecular and fragment ions are denoted by vertical arrows in figure 6.4 where the PPOS for  $\text{PF}_3$  are presented. Note that while negative ions cannot be detected from the dipole ( $e, e+\text{ion}$ ) experiment, the appearance of  $\text{PF}_2^+$  at 11 eV (see table 6.1 and branching ratios in fig. 6.3) corresponds to the resonant ion-pair formation process,  $\text{PF}_2^+ + \text{F}^-$  [145]. The main onset for  $\text{PF}_2^+$  production by dissociative photoionization is at 15.0 eV, which is in good agreement with the thermodynamic prediction. The observed onsets for  $\text{PF}^+$ ,  $\text{P}^+$ , and  $\text{F}^+$  formation correspond to extensive fragmentation of the molecule to the respective ions and dominantly atomic neutral fragments.

**Table 6.1**

Calculated and measured appearance potentials for the production of positive ions from  $\text{PF}_3$

Process	Appearance potential (eV)					
	Calc. <sup>1</sup>	Experimental				
		This work ( $\pm 1$ eV)	PIMS [143]	Electron impact		
			[145]	[146]	[148]	
$\text{PF}_3^+$	11.4	11.5	11.43	11.65	11.6	11.38
$\text{PF}_2^+ + \text{F}^-$	10.8	11.0				
$\text{PF}_2^+ + \text{F}$	14.7	15.0	14.55	15.5	13.5	14.27
$\text{PF}^+ + 2\text{F}^-$	13.1					
$\text{PF}^+ + \text{F} + \text{F}^-$	16.9					
$\text{PF}^+ + \text{F}_2$	19.1					
$\text{PF}^+ + 2\text{F}$	20.8	21.0		20.5		
$\text{P}^+ + 3\text{F}^-$	14.6					
$\text{P}^+ + \text{F} + 2\text{F}^-$	18.5					
$\text{P}^+ + \text{F}_2 + \text{F}^-$	20.7					
$\text{P}^+ + 2\text{F} + \text{F}^-$	22.3					
$\text{P}^+ + \text{F} + \text{F}_2$	24.5	26.0				
$\text{P}^+ + 3\text{F}$	26.2	28.5		32.3		
$\text{F}^+ + \text{PF}_2$	23.2					
$\text{F}^+ + \text{PF} + \text{F}$	28.5					
$\text{F}^+ + \text{P} + \text{F}_2$	31.5					
$\text{F}^+ + \text{P} + 2\text{F}$	33.1	33.0		36.0		
$\text{PF}_3^{2+}$		35.0				
$\text{PF}_2^{2+}$		39.0				
$\text{PF}^{2+}$		39.0				
$\text{P}^{2+}$		49.0				

<sup>1</sup> Calculated using thermochemical data [67] assuming zero kinetic energy of fragmentation.

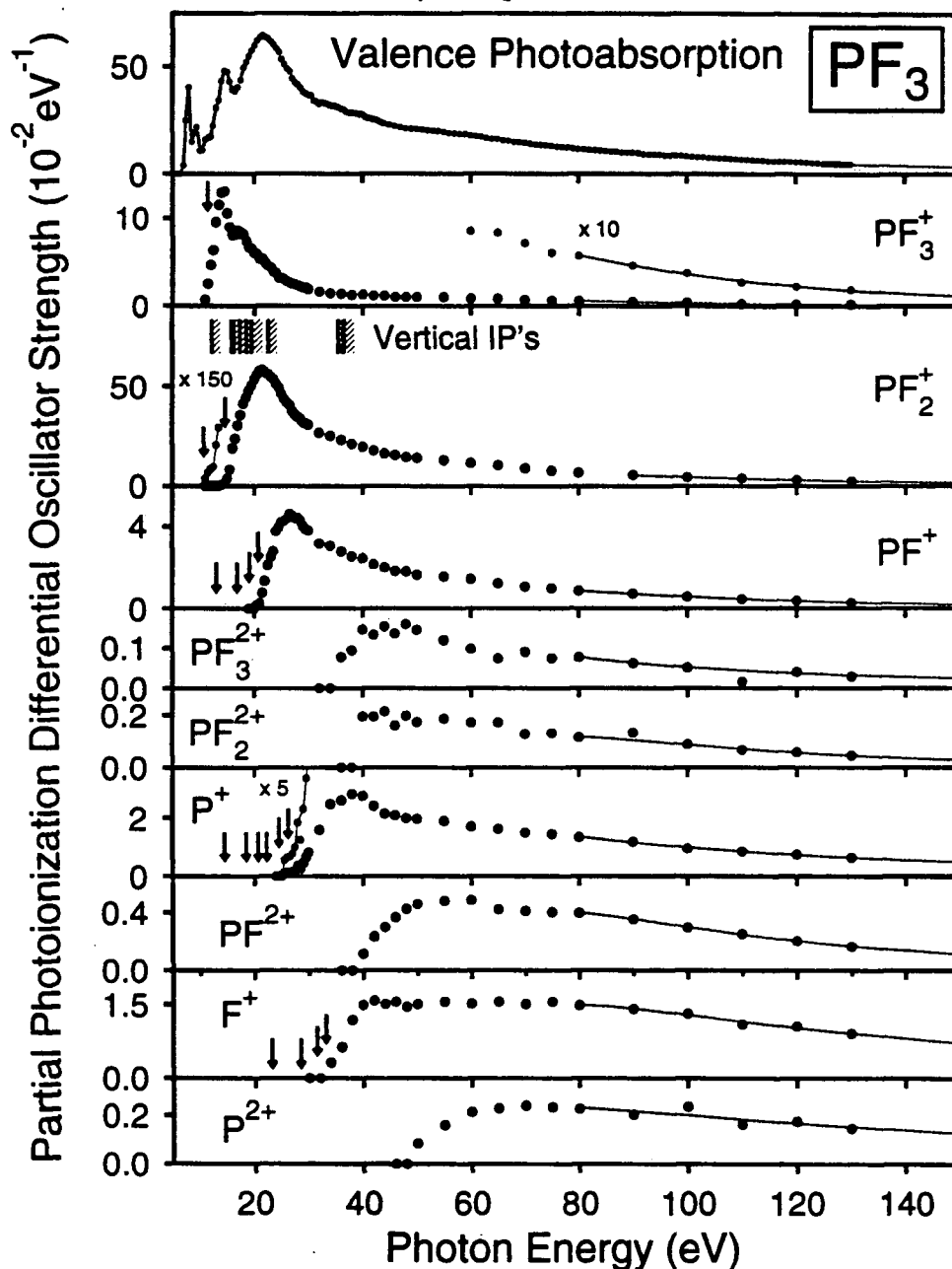


**Figure 6.4:** Absolute partial photoionization differential oscillator strengths for the valence-shell molecular and dissociative photoionization of  $\text{PF}_3$  (11–130 eV). The vertical arrows represent the calculated thermodynamic potentials [67] of the singly-charged cations (see table 6.1). The positions of the seven outer-valence VIP's measured by PES [109] and the average energies for the two inner-valence ionization processes determined using MS-X $\alpha$  calculations [43] are denoted by the hatched lines in the  $\text{PF}_2^+$  panel. The lower energy regions of the partial photoionization data for  $\text{PF}_2^+$  and  $\text{P}^+$  have also been plotted at 150 and five times the absolute intensities, respectively, in order to more clearly show the onsets of the multiple thresholds. The dotted curves represent valence-shell extrapolations used to estimate the differential oscillator strengths in the inner-shell region (see figure 6.9 below). The absolute total photoabsorption spectrum from figure 5.1 is also shown in the top panel.

### 6.2.1.2 Dipole-induced breakdown

Fragmentation ratios for dissociative photoionization from each electronic state of the molecular ion ( $\text{PF}_3^+$ ) should be constant when the photon energy exceeds the upper limit of the Franck-Condon region, except in local regions where autoionization effects are significant or where multiple photoionization is appreciable [39]. Therefore, the absolute PPOS for the production of each singly charged ion from  $\text{PF}_3$  can be expected to be a linear combination of PPOS of the contributing electronic ion states. This is the basis that permits the deduction of the dipole-induced breakdown pathways of phosphorus trifluoride by careful consideration of the experimental appearance potentials (table 6.1), valence-shell branching ratios (fig. 6.3), and absolute partial differential oscillator strengths for molecular and dissociative photoionization (fig. 6.4) measured in the present work, together with VIP's [139], Franck-Condon widths of the electronic ion states [139], photoelectron branching ratios [99,139], and He (I) PEPICO data [140] available in the literature.

The photoelectron branching ratios for production of the seven outer valence states for  $\text{PF}_3^+$  reported by Green *et al.* [139] and Väyrynen *et al.* [99] in the energy ranges 30–95 eV and 35–141 eV, respectively, have been used in conjunction with the presently obtained absolute total photoionization differential oscillator strengths (total photoabsorption differential oscillator strengths  $\times$  photoionization efficiencies, as given in table A.7) to derive electronic ion state PPOS for  $\text{PF}_3$  as follows: The contribution from the two inner valence ion states ( $3e^{-1}$  and  $5a_1^{-1}$ ), which were not reported in the photoelectron studies [99,139], have been approximated by using the sum of the presently measured  $\text{P}^+$  and  $\text{F}^+$  PPOS (see discussion below), and this sum was then subtracted from the total photoionization differential oscillator strength. This estimation using the sum of the  $\text{P}^+$  and  $\text{F}^+$  PPOS is based on the appearance potentials of these ions (table 6.1) which are above the upper limit of the

Franck-Condon region for production of the  $6a_1^{-1}$  ion state [139] (the last outer valence VIP). Since doubly charged ions are not in general expected to arise from the decomposition of singly charged ions (except in the case of VVV Auger processes [164]), the (relatively low intensity) PPOS for production of the  $PF_x^{2+}$  ( $x = 0-3$ ) ions were also subtracted from the total photoionization differential oscillator strength. The resulting modified "total" photoionization oscillator strengths were then multiplied by the photoelectron branching ratios [99,139] at each photon energy to yield PPOS for the production of each of the seven outer valence electronic states of  $PF_3^+$ . These PPOS are shown as open circles [139] and stars [99] on figure 6.5; the electronic state PPOS as given by ion sums (solid circles) have been derived from the presently obtained PPOS data using the dipole-induced breakdown scheme discussed below.

The appearance potential of the  $PF_3^+$  molecular ion (11.5 eV) is at the adiabatic ionization potential of the ground electronic state,  $8a_1^{-1}$  (VIP = 12.3 eV) [139], and the He (I) PEPICO data of Reynolds *et al.* [140] shows that  $PF_3^+$  is formed essentially only from the  $8a_1^{-1}$  state. The PPOS of  $PF_3^+$  are compared in figure 6.6(a) with the PPOS of the  $8a_1^{-1}$  state derived from the photoelectron branching ratios [99,139], and also with a calculation of the  $8a_1^{-1}$  ionization performed using the MS-X $\alpha$  method [141]. It can be seen that the PPOS of  $PF_3^+$  are in particularly good agreement with the  $8a_1^{-1}$  electronic state PPOS derived from the PES work of Green *et al.* [139] over the entire energy range of the latter measurements. The calculation [43], which shows two resonances centered at 14.5 and 22.0 eV, does not reproduce very well the PES [139] or the  $PF_3^+$  experimental results on figure 6.5(a).

Two appearance potentials were measured in the present work for  $PF_2^+$  (see figure 6.4). The first (low) onset at 11.0 eV corresponds to the thermodynamic AP calculated in table 6.1 for the ion pair formation,  $PF_3 \rightarrow PF_2^+ + F^-$ . The second  $PF_2^+$  onset at 15.0 eV is in the region of the ionization energies of the  $(6e^{-1} + 1a_2^{-1})$  states

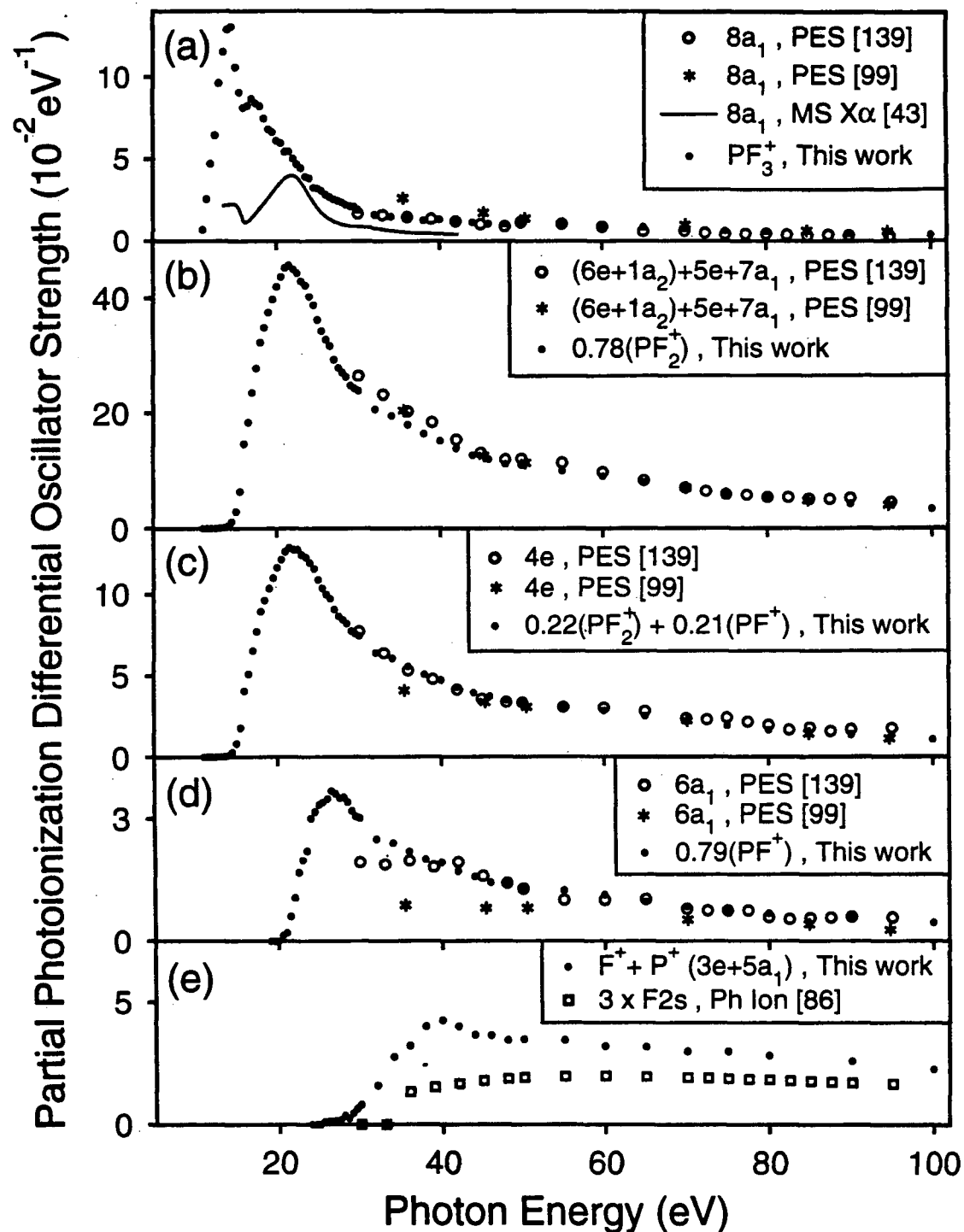


**Figure 6.5:** Absolute electronic ion state partial differential oscillator strengths (open circles and stars) derived from photoelectron branching ratios (30–95 eV) from refs. [99,139] and the presently measured total photoabsorption and photoionization efficiency data (see table 6.1). The solid circles represent estimates of electronic ion states PPOS derived from the absolute PPOS of the molecular and fragment ions obtained in the present work (see figure 6.4) as discussed in section 6.2.1.2.

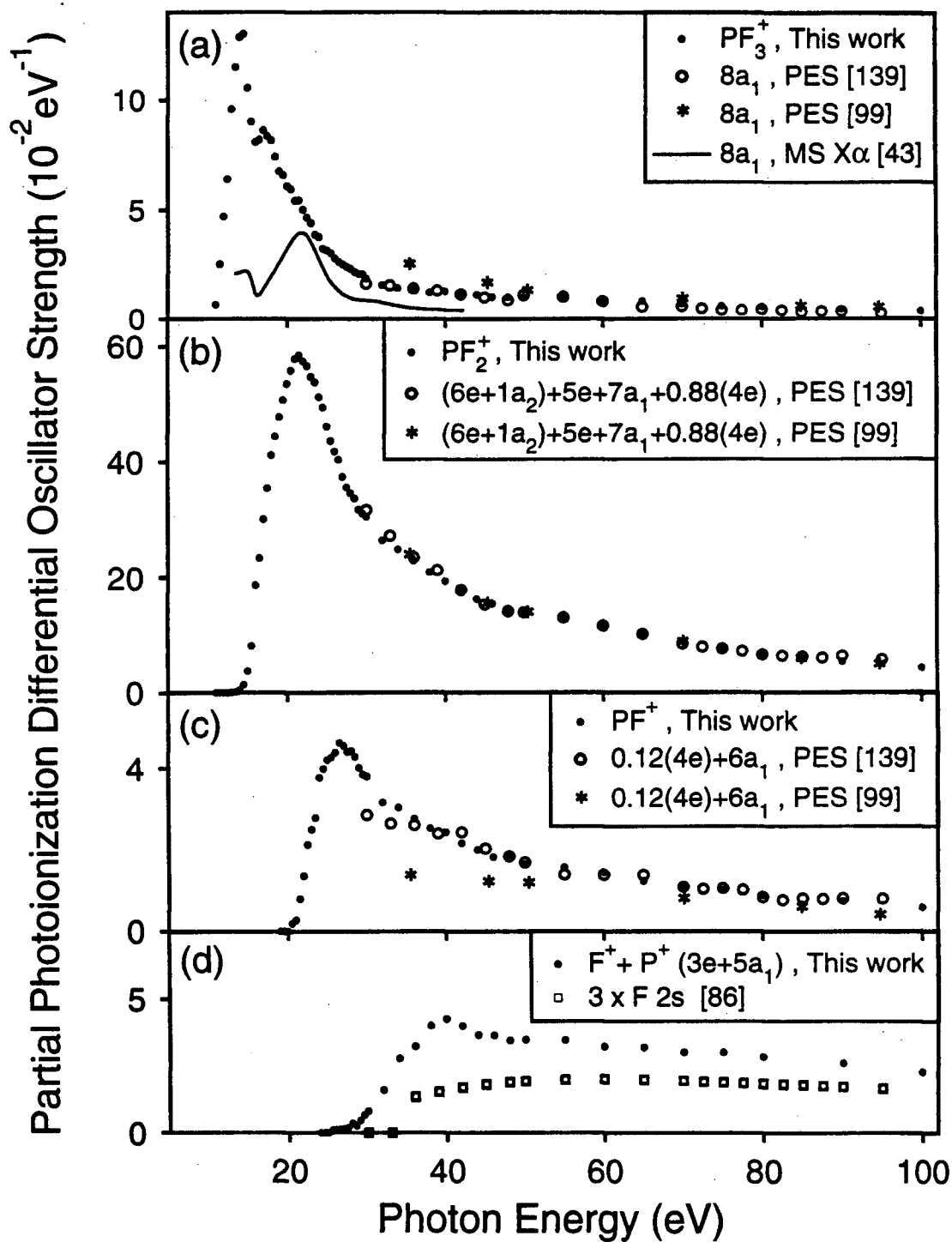


**Figure 6.6:** Differential oscillator strength sums determined from the proposed dipole-induced breakdown scheme for  $\text{PF}_3$  below 130 eV. The presently measured absolute partial photoionization differential oscillator strength sums for molecular and dissociative photoionization are compared with electronic ion state partial oscillator strength sums derived from PES branching ratio measurements [99,139] and MS-X $\alpha$  continuum calculations [43].

[139] and corresponds to dissociative photoionization to  $\text{PF}_2^+ + \text{F}$  (table 6.1). The PPOS curve for  $\text{PF}_2^+$  (fig. 6.4) continues to increase up to 21 eV, and all other ions appear at or above 21 eV. This, together with consideration of VIP's and Franck-Condon widths, suggests that further contributions must occur to  $\text{PF}_2^+$  from the  $5e^{-1}$ ,  $7a_1^{-1}$ , and  $4e^{-1}$  ion states. It can be seen from figure 6.6(b) that the electronic ion state PPOS sum ( $6e^{-1} + 1a_2^{-1} + 5e^{-1} + 7a_1^{-1} + 0.88(4e^{-1})$ ) using both PES data sets [99,139] is in excellent agreement with the shape of the  $\text{PF}_2^+$  partial differential oscillator strength curve. The PEPICO measurements [140] indicate that these five ion states dissociate exclusively to  $\text{PF}_2^+$  at the He (I) photon energy used.

The AP of the  $\text{PF}^+$  ion (21.0 eV) lies at the high energy limit of the  $4e^{-1}$  Franck-Condon width [139] and below the adiabatic ionization potential of the  $6a_1^{-1}$  state. This suggests a small contribution (~12 %) from the  $4e^{-1}$  and a dominant contribution from the  $6a_1^{-1}$  ion states.  $\text{PF}^+$  could not be observed to dissociate from the  $4e^{-1}$  in the PEPICO experiment [140], and this is to be expected since the upper photon energy limit of the He (I) PEPICO data (21 eV) [140] is situated right at the  $\text{PF}^+$  onset of 21 eV. Figure 6.6(c) shows that the agreement between the electronic ion state PPOS sum,  $0.12(4e) + 6a_1$ , derived from the PES data of Green *et al.* [139] is generally in very good agreement with the  $\text{PF}^+$  PPOS.

The  $\text{P}^+$  and  $\text{F}^+$  ions have AP's of 26 and 33 eV, respectively, which are well above the upper limit Franck-Condon width of the  $6a_1^{-1}$  state; therefore, these two ions must arise from inner valence ( $3e^{-1}$  and  $5a_1^{-1}$ ) photoionization [43] and/or dissociative multiple photoionization processes. Thus, the  $(\text{P}^+ + \text{F}^+)$  PPOS sum should provide a reasonable estimate of the summed  $(3e^{-1} + 5a_1^{-1})$  PPOS if the contributions to these two ions from dissociative multiple photoionization processes are relatively small. A crude estimate of the contribution from the inner-valence states may also be obtained from the calculated atomic F  $2s^{-1}$  photoionization differential oscillator strengths, since the  $3e$  and  $5a_1$  orbitals have predominantly

F 2s character [139]. As shown in figure 6.6(d), three times the differential oscillator strengths of F 2s<sup>-1</sup> [86] (from the three fluorine atoms in PF<sub>3</sub>) adds up to significantly less than the (P<sup>+</sup> + F<sup>+</sup>) PPOS sum. It can also be noted that 80% of (3 x F 2s) is similar in shape and magnitude to the F<sup>+</sup> PPOS. The differences are likely due to the molecular character in the inner-valence orbitals and/or contributions from dissociative multiple photoionization processes. The peak observed at 38 eV in the P<sup>+</sup> PPOS coincides with the shape resonance seen in the valence-shell photoabsorption (figure 5.1). This molecular phenomenon is not present in the (3 x F 2s) sum as expected. The dipole-induced breakdown scheme for production of singly charged cations from PF<sub>3</sub> in the valence shell region, according to the above deductions, is summarized in figure 6.7. Figure 6.5 illustrates the absolute electronic state PPOS derived from PES measurements [99,139] plus the total differential photoabsorption oscillator strengths from the present work, as described above, together with those estimated from sums of their corresponding dissociative ion products. It should be noted that the ion sums provide estimates of the electronic state PPOS at energies below the lower limit of the PES measurements [99,139] as well as at higher energies.

Turning to a consideration of the doubly charged ions, it can be seen that the shapes of the PPOS for production of PF<sub>3</sub><sup>2+</sup> and PF<sub>2</sub><sup>2+</sup> (figure 6.4) are quite similar, although their onsets are different. Similarly, the PF<sup>2+</sup> and P<sup>2+</sup> ions have different appearance potentials but similar partial differential oscillator strength shapes. Therefore, it is possible that these four dications arise at least in part from different VVV Auger processes involving groups of energy poles arising from many-body effects in the two inner-valence (3e<sup>-1</sup> and 5a<sub>1</sub><sup>-1</sup>) ionization processes. More complete information on the dipole-induced breakdown of the singly and doubly charged cations must await measurements of adiabatic and vertical double ionization potentials as well as further photoelectron-photoion coincidence (PEPICO) and

### Dipole Induced Breakdown Pathways for PF<sub>3</sub>

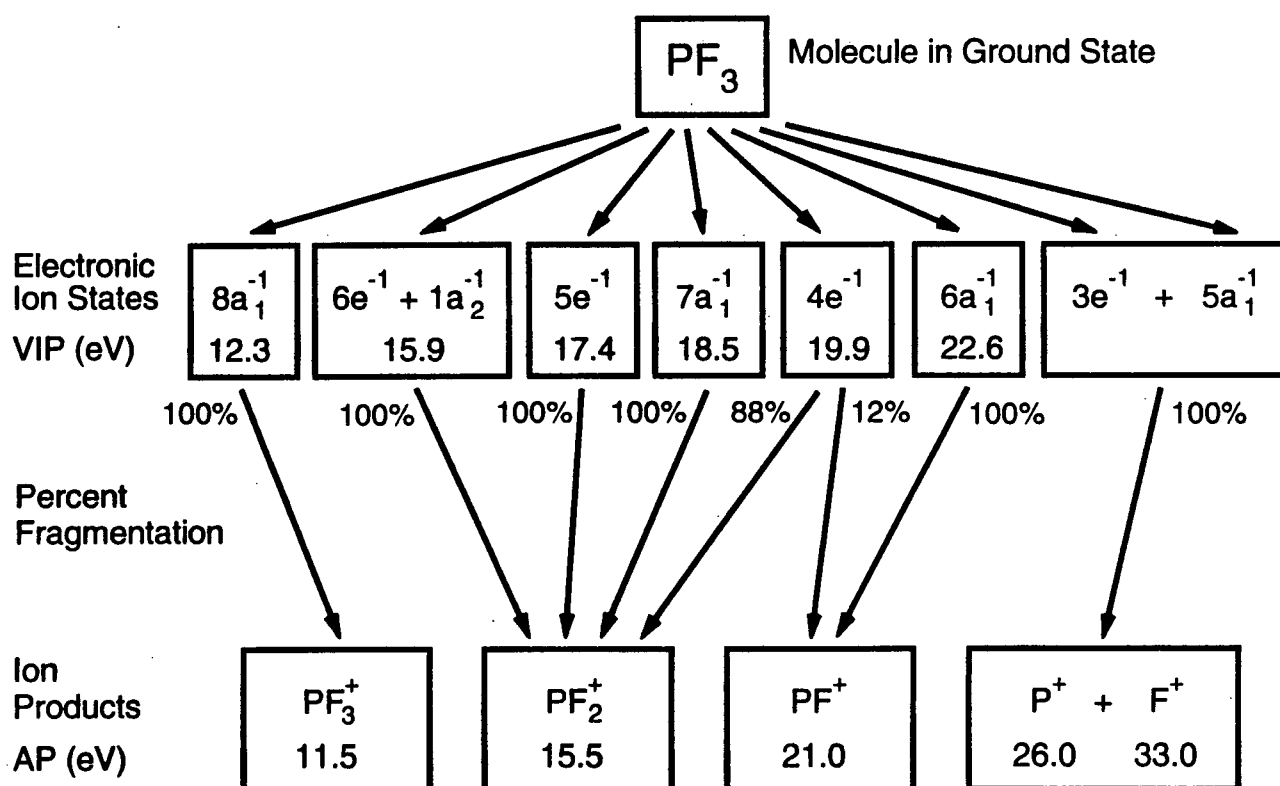


**Figure 6.7:** The dipole-induced breakdown pathways following valence-shell photoionization of PF<sub>3</sub> below 130 eV. The vertical ionization potentials (VIP's) for the seven outer-valence electronic ion states have been taken from PES [139].

photoion-photoion coincidence (PIPICO) studies. Many-body Greens' function calculations as well as further photoelectron and electron momentum spectroscopy experiments are required to elucidate the nature of the binding energy spectrum of  $\text{PF}_3$  in the inner-valence region and the role of many body (electron correlation) effects.

### 6.2.1.3 P $2p, 2s$ inner-shell photoionization

In order to investigate the changes in the dipole-induced breakdown of  $\text{PF}_3$  in going from valence-shell photoionization to phosphorus  $2p$  and  $2s$  excitation and ionization, TOF mass spectra have been recorded at a series of energies from 130 to 193 eV at a resolution of 1 eV fwhm. Typical spectra are shown in figure 6.8 at (a) 130 eV (pre-edge, valence-shell region) and in the inner-shell region at photon energies of (b) 136.5 eV corresponding to the virtual valence transitions ( $7e \leftarrow 2p$ ), (c) 138.5 eV (Rydbergs  $\leftarrow 2p$ ), (d) 147 and (f) 157 eV (the continuum shape resonances ( $9a_1 \leftarrow 2p$  and  $3d \leftarrow 2p$ , respectively), (e) 152 eV (the trough between the two shape resonances), (g) 169.5 eV (the  $2p$  ionization continuum), and (h) 193 eV ( $7e \leftarrow 2s$  excitation). Similar to the valence-shell case at 70 eV (see figure 6.1), five singly-charged ions ( $\text{PF}_3^+$ ,  $\text{PF}_2^+$ ,  $\text{PF}^+$ ,  $\text{P}^+$ , and  $\text{F}^+$ ) and four doubly-charged ions ( $\text{PF}_3^{2+}$ ,  $\text{PF}_2^{2+}$ ,  $\text{PF}^{2+}$ , and  $\text{P}^{2+}$ ) are detected at all energies, although the relative intensities are quite different in the P  $2p, 2s$  inner-shell regions. Recent PIPICO measurements for  $\text{PF}_3$  [153] in the P  $2p$  region have reported time correlated pairs of singly and doubly charged fragment species resulting from Coulomb explosion of dissociative doubly and triply charged ions. However, no stable triply charged ions were observed in the TOF mass spectra [153] in agreement with the present work. It can be seen from figure 6.8 that the most significant changes in the TOF mass spectra in going from the valence to the P  $2p, 2s$  region are the large increases in the

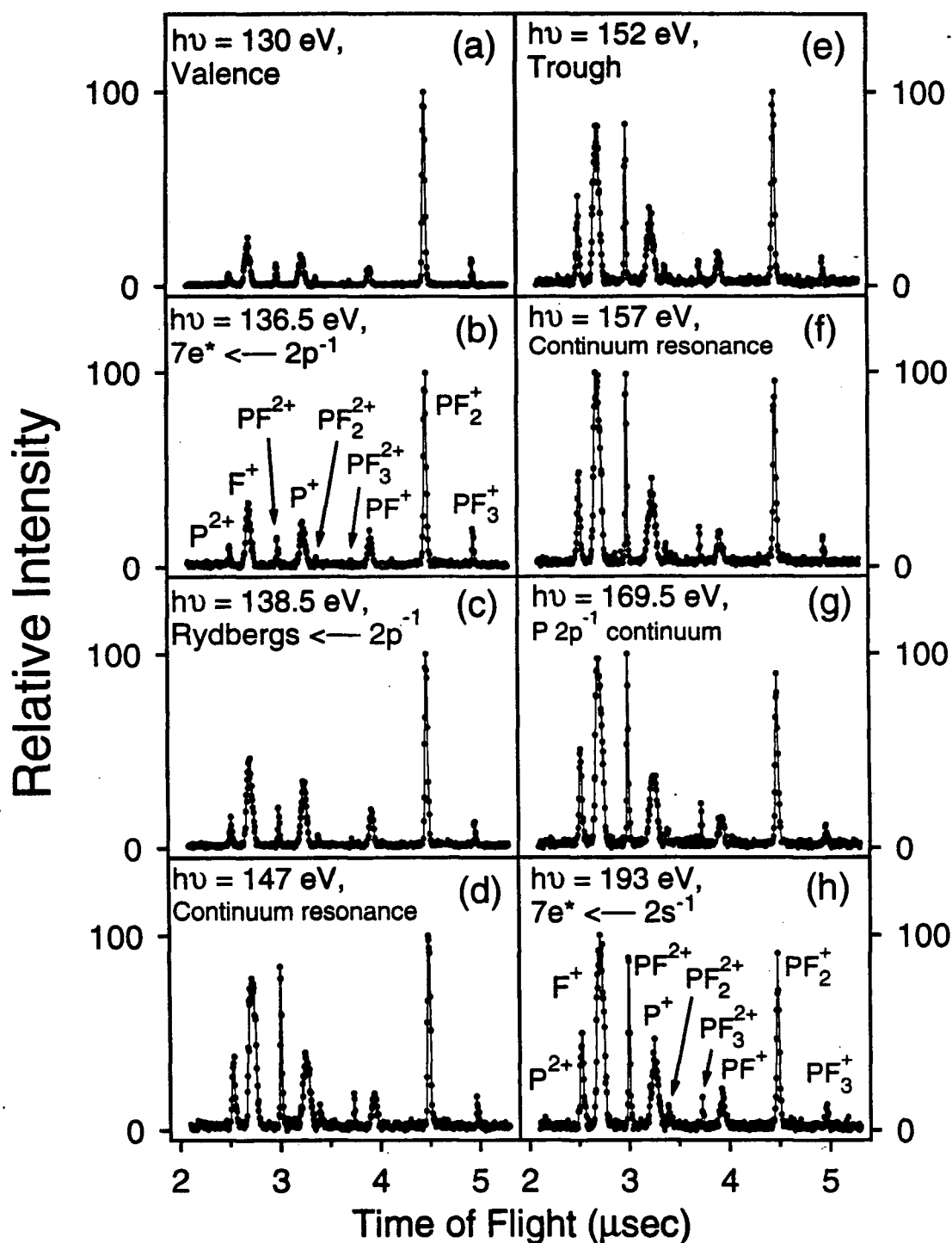


**Figure 6.8:** Time-of-flight mass spectra of  $\text{PF}_3$  recorded at selected energies in the P  $2p$  and P  $2s$  inner-shell region: (a) the valence-shell continuum at 130 eV, (b) 136.5 eV corresponding to the  $7e(\sigma^*) \leftarrow 2p_{3/2, 1/2}^{-1}$  virtual valence transition, (c) 138.5 eV corresponding to Rydbergs  $\leftarrow 2p_{3/2, 1/2}^{-1}$ , (d) 147 eV and (f) 157 eV corresponding to the two continuum shape resonances, (e) 152 eV corresponding to the trough in between the two continuum shape resonances, (g) 169.5 eV corresponding to the P  $2p$  continuum; and (h) 193 eV corresponding to the  $7e(\sigma^*) \leftarrow 2s^{-1}$  excitation.

relative abundances of  $F^+$ ,  $P^{2+}$ ,  $PF^+$ , and  $PF_3^{2+}$  at energies above 138.5 eV in the P 2*p* photoionization continuum region. In the P 2*p* virtual valence (136.5 eV, figure 6.8(b)) and Rydberg (138.5 eV, figure 6.8(c)) excitation regions, the most noticeable changes from the valence-shell spectra are in the relative abundances of  $PF^+$ ,  $P^+$ , and  $F^+$ . At higher photon energies in the P 2*p* continuum,  $F^+$  becomes the most abundant ion. The  $P^+$  and  $F^+$  peaks are very broad, particularly in the P 2*p* ionization continuum, indicating considerable kinetic energy of fragmentation. In assessing the measured data, it should be remembered that the TOF mass spectra show the abundances of the ions relative to the *highest* peak in the spectrum, whereas the photoion branching ratios (see below) indicate the percentages of the total photoionization contributed by each ion detected taking into account the *peak area* (i.e., considering both the width and height of each peak).

The photoion branching ratios for production of the singly and doubly charged cations obtained in the present work in the P 2*p*,2*s* regions (including the contribution from the underlying valence shell) are presented in the higher energy region of figure 6.3. The error bars are derived from the square roots of the total and background coincidence counts and represent statistical error only. In moving from the valence-shell to the 2*p* inner-shell continuum region, it can be seen from the photoion branching ratio curves that significant changes occur in the ionic photofragmentation of  $PF_3$ : The relative amount of  $PF_2^+$  decreases markedly, whereas the relative yield of  $PF_3^+$  shows little change. In contrast, the relative yields of  $PF^+$  and  $P^+$  show localized increases in the pre-edge excitation region, while  $F^+$  and all doubly charged ions generally show significant increases throughout the 2*p* inner-shell region. The largest changes are in the branching ratios of  $PF_2^+$ ,  $P^+$ ,  $PF^{2+}$ , and  $P^{2+}$ . However, it should be noted that since branching ratios are quantities relative to the total ionization, the branching ratio data of figure 6.3 do not show in a direct manner how the individual ionic photofragmenta-

tion channels are affected by the P  $2p$  discrete excitation and ionization continuum regions. Such detailed quantitative information is however provided by comparison of the individual PPOS ( $df/dE$ ) curves for molecular and dissociative photoionization with the P  $2p$  photoabsorption as shown below in figure 6.9. For example, even though the branching ratio for  $\text{PF}_2^+$  markedly decreases (figure 6.3), the PPOS (figure 6.9 below) shows no significant change in  $\text{PF}_2^+$  absolute yield in the P  $2p$  region.

The absolute partial photoionization differential oscillator strengths (figure 6.9, table A.13) for the production of molecular and fragment ions in the P  $2p$  and  $2s$  inner-shell regions of phosphorus trifluoride were determined from the product of the total photoabsorption differential oscillator strength and photoion branching ratio at each photon energy, and assuming photoionization efficiencies of unity (this assumes effects due to double or higher multiple photoionization, including dissociative processes such as Coulomb explosions, are small compared with direct single photoionization processes). The valence-shell PPOS contributions in the inner-shell region have been estimated by fitting polynomial curves (see dotted lines in figures 6.4 and 6.9) to the valence-shell PPOS data and then extrapolating them into the inner-shell region. The branching ratios (figure 6.3) and absolute partial differential photoionization oscillator strengths (figure 6.9) of the fragment ions can be discussed with reference to the total photoabsorption in the valence continuum, the P  $2p$  pre-edge excitation region, and the P  $2p$  post-edge continuum region (see top panels of figures 6.3 and 6.9). It can be seen that the largest cations,  $\text{PF}_3^+$  and  $\text{PF}_2^+$ , are produced almost exclusively from the underlying valence-shell continuum. Although some of the molecular ion,  $\text{PF}_3^+$ , and possibly a very small amount of  $\text{PF}_2^+$  is produced from the  $7e \leftarrow 2p^{-1}$  core excited virtual valence and Rydberg states, there appears to be no appreciable increase in these yields above the  $2p_{3/2,1/2}$  ionization edges. In contrast, the other three singly-charged ions ( $\text{PF}^+$ ,  $\text{P}^+$ , and  $\text{F}^+$ )

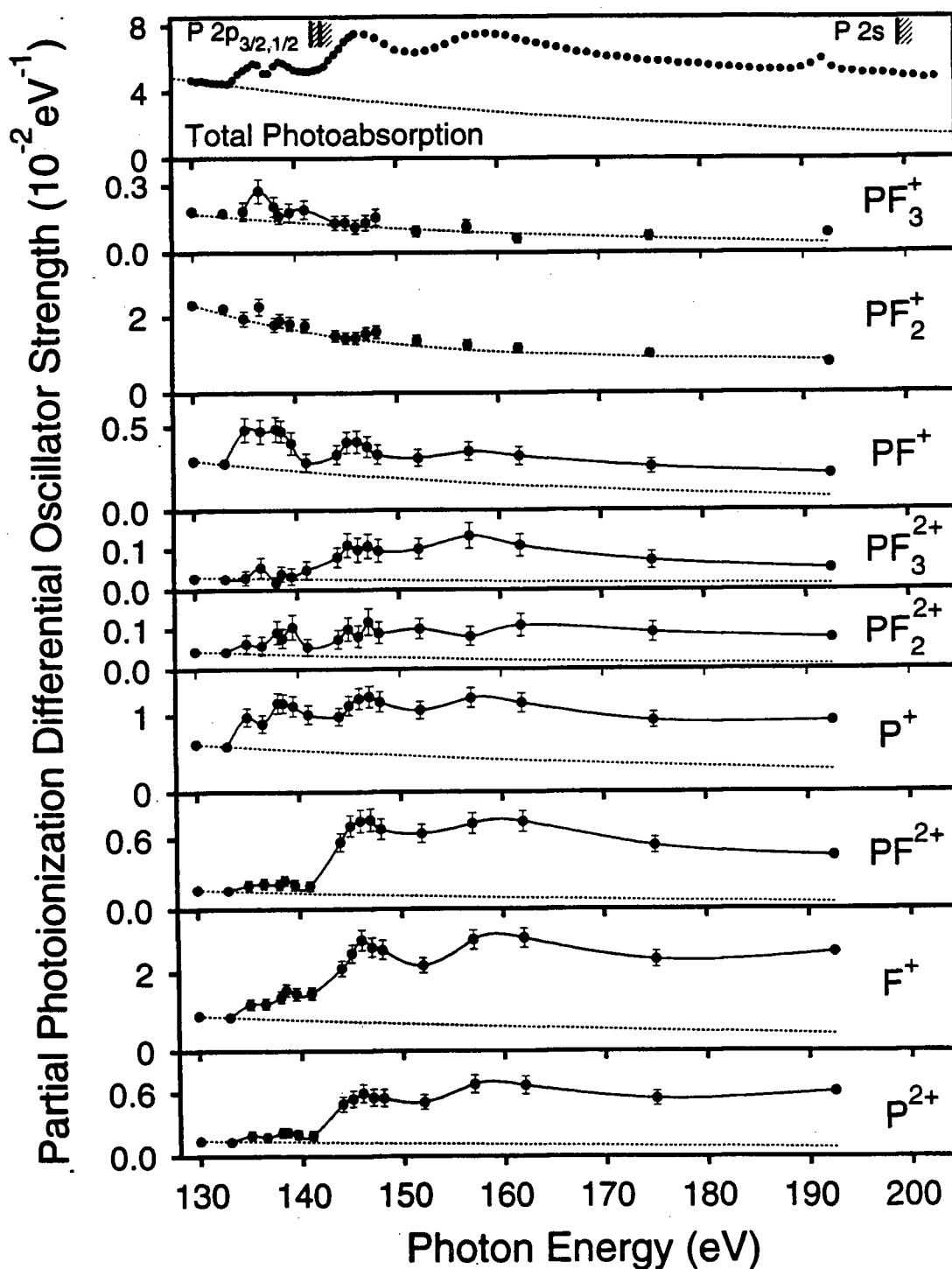


**Figure 6.9:** Absolute partial photoionization differential oscillator strengths for the molecular and dissociative photoionization of  $\text{PF}_3$  in the P  $2p$  and P  $2s$  regions from 130 to 193 eV. The dotted curves represent the estimated PPOS contributions from the underlying valence-shell continuum in the inner-shell region. The top panel presents the total (valence plus P  $2p, 2s$ ) absolute photoabsorption spectrum where the thresholds of the P  $2p$  and  $2s$  edges are shown as hatched lines.

are produced with increasing probability from P  $2p$  and  $2s$  excitation and ionization processes with decreasing size of the fragment ion. The singly charged ions,  $\text{PF}^+$ ,  $\text{P}^+$ , and  $\text{F}^+$ , and the doubly charged species,  $\text{PF}_3^{2+}$ ,  $\text{PF}_2^{2+}$ ,  $\text{PF}^{2+}$ , and  $\text{P}^{2+}$ , all show contributions from both the P  $2p$  neutral excited states and the ionization continuum. Above the P  $2p$  excitation threshold, the PPOS of all four doubly-charged ions ( $\text{PF}_3^{2+}$ ,  $\text{PF}_2^{2+}$ ,  $\text{PF}^{2+}$ , and  $\text{P}^{2+}$ ) arise primarily from inner-shell rather than valence shell processes. This observation can be attributed to autoionization decay (i.e., resonance Auger processes) being favored below the ionization threshold where the excited  $2p$  electron remains as a spectator or participates in the autoionizing decay of the  $2p^{-1}$  hole state to give singly-charged ions. In contrast, above the  $2p$  ionization threshold, Auger processes become the principal decay channels, giving rise to doubly-charged species [152]. In general, with the exceptions of  $\text{PF}_2^+$ ,  $\text{P}^+$ , and  $\text{F}^+$ , the singly-charged cations are the predominant species in the P  $2p$  pre-edge region, while all the dications make increased contributions in the post-edge continuum. In the P  $2p$  continuum, doubly-charged ions produced by Auger processes are expected in some cases to fragment by Coulomb explosion (i.e., dissociative double photoionization processes) to give two singly-charged species. This will lead to greater yield of the lighter ion products, and as shown in figure 6.9,  $\text{P}^+$  and  $\text{F}^+$  make the largest contributions from singly charged ions in the P  $2p$  ionization continuum. These fragments also possess considerable kinetic energy of fragmentation, as can be seen by the increasingly broad peaks of the  $\text{P}^+$  and  $\text{F}^+$  ions in the TOF mass spectra above 138.5 eV (figure 6.8). This interpretation is supported by the PIPICO studies of Hitchcock *et al.* [153] which reported increasing intensities of the ( $\text{F}^+$ ,  $\text{P}^+$ ), ( $\text{F}^+$ ,  $\text{PF}^+$ ), and ( $\text{F}^+$ ,  $\text{PF}_2^+$ ) ion pairs with increasing photon energy. At 145.6 eV small amounts of the ( $\text{F}^+$ ,  $\text{P}^{2+}$ ) and ( $\text{F}^+$ ,  $\text{PF}_2^{2+}$ ) ion pairs were also observed [153]. However, since the  $\text{P}^{2+}$  and  $\text{PF}_2^{2+}$  ion peaks observed in the present work are relatively sharp and narrow (figure 6.8) even at the higher photon

energies, it is unlikely that they are produced from triply dissociative photoionization to any large extent. The shape of the PPOS for  $\text{PF}_2^+$  in figure 6.9 suggests that the  $(\text{F}^+, \text{PF}_2^+)$  correlated pairs observed in the PIPICO experiments [153] arise principally from double ionization processes involving valence shell electrons even at 145.6 eV. In this regard, it should also be noted that the 10% detection efficiency of the presently used TOF mass spectrometer (see section 3.1.2) causes both ions formed in Coulomb explosions to contribute to the TOF mass spectra in approximately equal proportions. Finally, note that there is no way to relate the PIPICO intensities [153] quantitatively to those of the present TOF mass spectra measurements, and only qualitative comparisons can be made. In particular, it is not possible to deduce the relative contribution to a given fragment ions from dissociative single ionization and dissociative double (or higher) multiple photoionization processes. In both experiments the data also involve contributions from the underlying valence shell.

## 6.2.2 Phosphorus trichloride

### 6.2.2.1 Valence-shell photoionization

TOF mass spectra of phosphorus trichloride have been measured in the valence-shell region at 1 eV fwhm resolution in the equivalent photon energy range from the first ionization potential up to 130 eV, just below the onset of excitations arising from the phosphorus L shell. Figure 6.10 shows a typical TOF spectrum obtained at 40 eV. The splitting or asymmetry in the various chlorine-containing ion peaks reflect the 3:1 isotopic ratio ( $^{35}\text{Cl}$  to  $^{37}\text{Cl}$ ) of atomic chlorine. All four singly charged phosphorus-containing cations,  $\text{PCl}_x^+$  ( $x = 0-3$ ), and  $\text{Cl}^+$  were observed in the TOF spectra. In contrast with the case of  $\text{PF}_3$  where the doubly

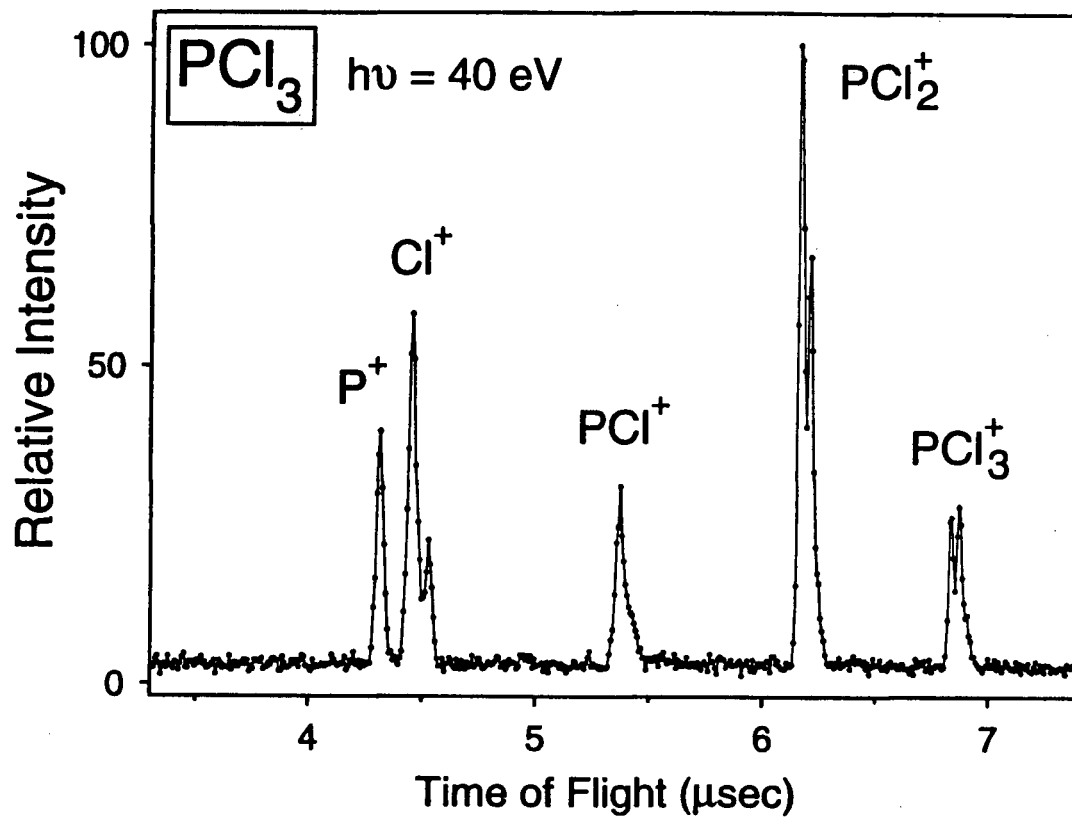


Figure 6.10: TOF mass spectrum of  $\text{PCl}_3$  recorded at 40 eV.

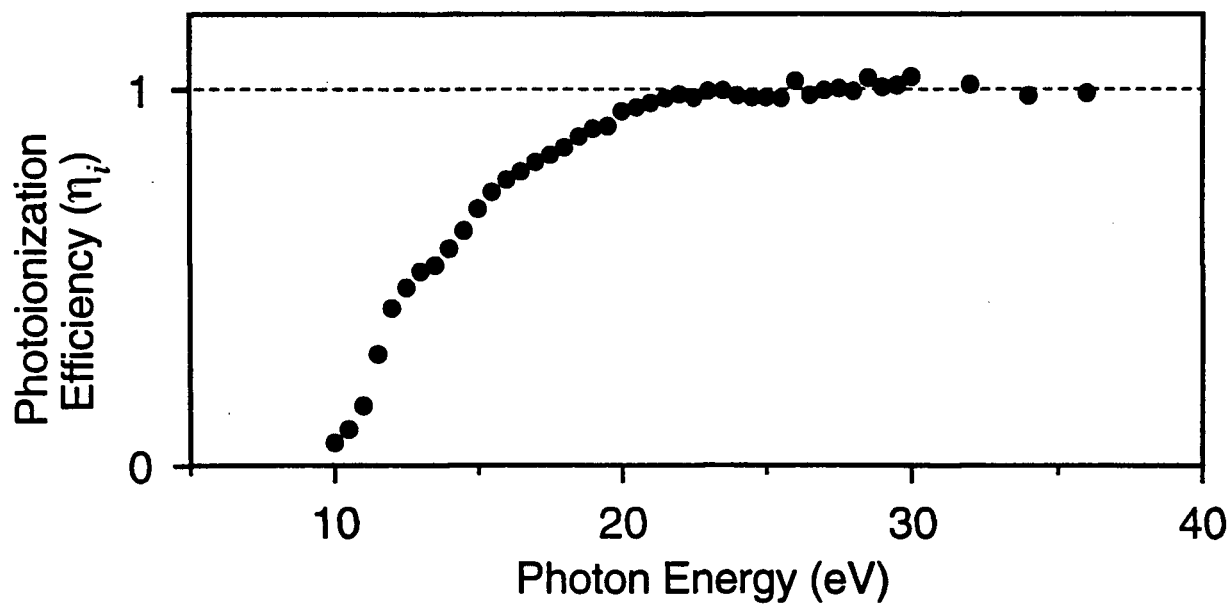


Figure 6.11: Photoionization efficiencies for  $\text{PCl}_3$  (10–36 eV).

charged ions  $\text{PF}_x^{2+}$  ( $x = 0-3$ ) were detected, no stable doubly charged ions are produced from  $\text{PCl}_3$  in the valence-shell region. Therefore, any doubly charged ions formed in the valence-shell region must involve repulsive states resulting in dissociative double photoionization processes which lead to singly charged products. These could be studied by PIPICO techniques, but no such measurements have been reported for  $\text{PCl}_3$ . The absolute photoionization efficiencies ( $\eta_i$ ) up to 36 eV are shown in figure 6.11 and listed in table A.9.

The photoion branching ratios for each of the ionic species are presented in figure 6.12. Since the TOF mass spectrometer was unable to fully resolve the isotopic bands of the four chlorine-containing ions, the branching ratio for each of the molecular and fragment ions represents the sum over all chlorine isotopes for that ion. Analogous to the situation in  $\text{PF}_3$  (section 6.2.1.1),  $\text{PCl}_2^+$  is the dominant fragment ion produced from  $\text{PCl}_3$  in valence-shell photoionization region below 50 eV. However, the dissociative photoionization of  $\text{PCl}_3$  differs in that  $\text{PCl}_2^+$  becomes much less abundant than  $\text{PF}_2^+$  with increasing photon energy, and above ~50 eV the  $\text{Cl}^+$  ion becomes dominant.  $\text{PCl}^+$  and  $\text{P}^+$  also make major contributions to the total valence-shell photoionization oscillator strengths.

The absolute valence-shell PPOS for the production of molecular and fragment ions from  $\text{PCl}_3$  are shown in figure 6.13 and listed numerically in table A.14. These represent the first absolute oscillator strength (cross section) measurements for the molecular and dissociative photoionization channels of  $\text{PCl}_3$  in the vacuum ultraviolet and soft X-ray regions (see also Sec. 6.2.2.3 for measurements in the P  $2p,2s$  and Cl  $2p,2s$  inner-shell regions). The hatched lines in figure 6.13 indicate the positions of the VIP's for the occupied valence orbitals [112] as given in section 5.2.1.

The appearance potentials (AP's) observed in the present work for the five singly-charged ions in the valence-shell region are summarized in table 6.2 together

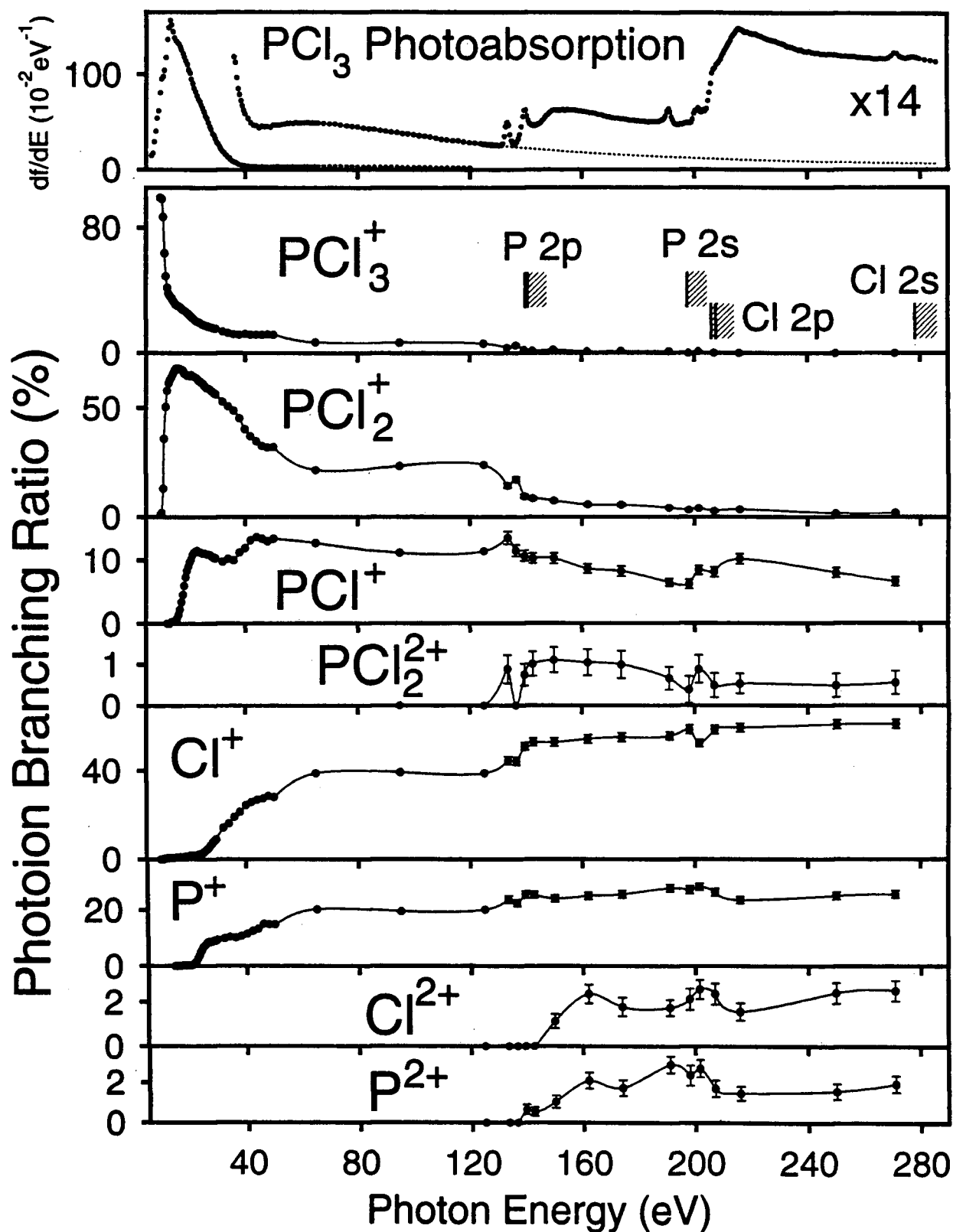


**Figure 6.12:** Branching ratios for the molecular and dissociative photoionization of  $\text{PCl}_3$ . The absolute total photoabsorption spectrum from figure 5.5 is also shown in the top panel.

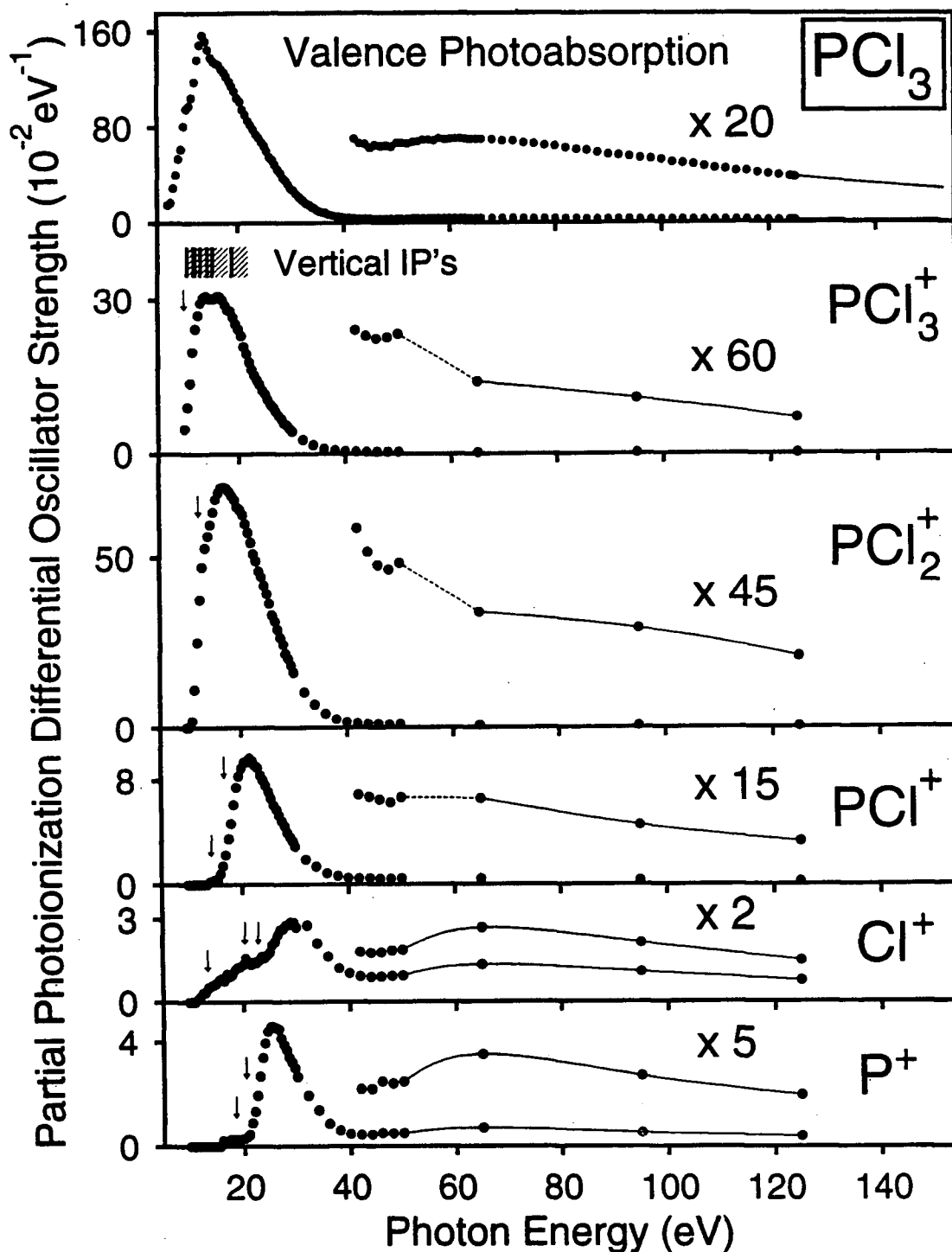


**Figure 6.13:** Absolute partial photoionization differential oscillator strengths for the valence-shell molecular and dissociative photoionization of  $\text{PCl}_3$  (10–125 eV). The arrows represent the calculated thermodynamic appearance potentials [67] of the singly charged cations given in table 6.2. The positions of vertical ionization potentials for the occupied valence orbitals [112] are denoted by the hatched lines. The absolute total photoabsorption spectrum from figure 5.5 is also shown in the top panel.

**Table 6.2**Calculated and measured appearance potentials for the production of positive ions from  $\text{PCl}_3$ 

Process	Appearance potential (eV)							
	Calculated <sup>1</sup>	Experimental						
		This work ( $\pm 1$ eV)	PIMS		Electron impact			
		[148]	[112]	[158]	[157]	[156]	[63]	[159]
$\text{PCl}_3^+$	9.9	10.0	9.90 $\pm$ 0.01	10.52 $\pm$ 0.03	10.58	10.75 $\pm$ 0.2	10.6 $\pm$ 0.2	12.2
$\text{PCl}_2^+ + \text{Cl}^-$		11.5	11.61 $\pm$ 0.01		8.68			
$\text{PCl}_2^+ + \text{Cl}$	12.27				12.15	12.32 $\pm$ 0.2	11.8 $\pm$ 0.5	12.5
$\text{PCl}^+ + \text{Cl}_2$	14.28							
$\text{PCl}^+ + 2\text{Cl}$	16.76	16.0	15.69 $\pm$ 0.02		16.93	16.83 $\pm$ 0.3	16.5 $\pm$ 0.5	17.5
$\text{Cl}^+ + \text{PCl}_2^-$	13.4 [156]	12.5					19.8 $\pm$ 0.4	
$\text{Cl}^+ + \text{PCl}_2$								
$\text{Cl}^+ + \text{PCl} + \text{Cl}$					19.77			
$\text{Cl}^+ + \text{P} + \text{Cl}_2$	20.4					20.2 $\pm$ 0.4		22.1
$\text{Cl}^+ + \text{P} + 2\text{Cl}$	22.9	24						
$\text{P}^+ + \text{Cl}^- + \text{Cl}_2$					14.47			
$\text{P}^+ + \text{Cl} + \text{Cl}_2$	18.4	16.5			18.22			
$\text{P}^+ + 3\text{Cl}$	20.4	21				21.2 $\pm$ 0.5	21.0 $\pm$ 0.5	
$\text{PCl}_2^{2+}$		134						
$\text{Cl}^{2+}$		150						
$\text{P}^{2+}$		140						

<sup>1</sup> Calculated using thermochemical data from ref. [67,165] assuming zero kinetic energy of fragmentation.

with previously reported [63,112,148,156–159] experimental AP's determined by photoionization mass spectrometry and electron impact methods. Table 6.2 also gives calculated thermodynamic appearance potentials for the formation of singly charged cations from  $\text{PCl}_3$  using thermochemical data where available [67,165], and assuming zero kinetic energy of fragmentation. These are shown as vertical arrows in figure 6.13.

Fragmentation ratios for dissociative photoionization from each electronic state of the molecular ion ( $\text{PCl}_3^+$ ) should be constant when the photon energy exceeds the upper limit of the Franck-Condon region [39]. This model will apply where contributions from effects such as autoionization and multiple ionization are small [39]. In this situation, the absolute PPOS for the production of each singly charged ion from  $\text{PCl}_3$  can be expressed as a linear combination of PPOS for the production of electronic ion states. The dipole-induced breakdown pathways of a molecule therefore can be investigated using ideas such as these, as reported earlier for  $\text{PF}_3$  (section 6.2.1.2). However, since photoelectron branching ratios, electronic ion state PPOS, and photoelectron-photoion coincidence data are not available as a function of photon energy in the literature for phosphorus trichloride, only very limited information can be deduced from the present data. Some qualitative information concerning the molecular and fragment ions produced from the nine valence-shell ion states of  $\text{PCl}_3$  can be deduced from a consideration of the experimental appearance potentials (table 6.2) and absolute partial differential oscillator strengths for molecular and dissociative photoionization (figure 6.13) measured in the present work, together with VIP's [112] and PES Franck-Condon widths of the electronic ion states [112] reported in the literature.

The  $\text{PCl}_3^+$  molecular ion first appears at the adiabatic ionization potential ( $\sim 10.0$  eV) of the ion electronic ground state,  $12a_1^{-1}$  [112] (see figure 6.13). A further increase in  $\text{PCl}_3^+$  yield occurs in the region of  $\sim 15$  eV, suggesting a contribution from

the  $8e^{-1}$  photoionization process. However, contributions from other less tightly bound outer valence ionization processes may also occur. Such contributions could be determined from PEPICO experiments, but to date no such data have been reported.  $\text{PCl}_2^+$  is first formed at 11.5 eV in good agreement with the appearance potential found using PIMS [148]. Since this energy (11.5 eV) is beyond the upper limits of the Franck-Condon width of the  $12a_1^{-1}$  ground state ion, it can be concluded that the  $12a_1^{-1}$  photoionization process produces exclusively  $\text{PCl}_3^+$ .

Two appearance potentials have been obtained in the present work for  $\text{PCl}_2^+$ . The first onset at 11.5 eV corresponds to the  $\text{PCl}_2^+ + \text{Cl}^-$  ion-pair formation [156,148]. This process occurs only in a localized energy region since it originates from dissociation of a neutral state of  $\text{PCl}_3$ . However, this first onset is also within the energy ranges of the Franck-Condon regions [112] of the  $1a_2^{-1}$  and  $10e^{-1}$  processes (which are likely to result in dissociation to  $\text{PCl}_2^+ + \text{Cl}$ ). An onset of 12.27 eV is calculated for the process  $\text{PCl}_3 \rightarrow \text{PCl}_2^+ + \text{Cl}$  (table 6.2) using thermodynamic data [67]. The  $\text{PCl}_2^+$  partial differential oscillator strength curve in figure 6.13 also shows some indication of a second higher onset at 14.5 eV, suggesting the possibility of a contribution from the  $11a_1^{-1}$  and/or  $8e^{-1}$  states.

The presently measured AP of the  $\text{PCl}^+$  ion (16.0 eV) lies near the upper energy limit of the  $8e^{-1}$  Franck-Condon width and below the VIP of the  $10a_1^{-1}$  state. Therefore, it is reasonable to conclude that  $\text{PCl}^+$  is first produced from the  $8e^{-1}$  process. This appearance potential is in reasonable agreement with earlier reported PIMS measurements [148] and in good agreement with an electron impact study [159].

The  $\text{Cl}^+$  ion is first observed at 12.5 eV in the dipole ( $e, e+\text{ion}$ ) experiment, but AP's ranging from 19.77 to 22.1 eV corresponding to the  $\text{PCl}_3^+ \rightarrow \text{Cl}^+ + \text{PCl} + \text{Cl}$  process have been reported from earlier electron impact measurements [156–158]. In a study of positive and negative ions produced from  $\text{PCl}_3$ , Halmann and Klein

[156] reported that  $\text{PCl}_2^-$  and  $\text{Cl}^+$  are formed together in an ion-pair process.  $\text{PCl}_2^-$  was found to have an appearance potential of 14 eV, but  $\text{Cl}^+$  was not observed until 19.8 eV [156]. The authors attributed the higher AP of  $\text{Cl}^+$  to poor collection efficiency of their mass spectrometer because the  $\text{Cl}^+$  ion is formed with high kinetic energy. In the present work, the ion extraction voltages and TOF analyzer lens system in the dipole ( $e, e+\text{ion}$ ) spectrometer ensure uniform collection of ions with up to ~20 eV excess kinetic energy of fragmentation [15], and thus a lower AP of 12.0 eV is observed. Any contribution from an ion-pair process is expected to be localized in energy due to the neutral state involved. Therefore, the present result strongly indicates that  $\text{Cl}^+$  is formed together with neutral products by direct dissociative photoionization at a much lower energy than previously observed in threshold electron impact studies [63,157,158]. In this connection, it is likely that dissociative photoionization to  $\text{Cl}^+$  first occurs from the  $1a_2^{-1} + 10e^{-1}$  and/or  $9e^{-1}$  states. The  $\text{Cl}^+$  partial differential oscillator strength curve in figure 6.13 also shows evidence of a further onset at ~24 eV, above the Franck-Condon region of the  $10a_1^{-1}$  process and in the region of the theoretically calculated average VIP's of the inner-valence ionization processes ( $7e^{-1}$  and  $9a_1^{-1}$ ) [113]. It can therefore be concluded that  $\text{Cl}^+$  ion must also come from dissociative ionization in the inner-valence region.

The  $\text{P}^+$  ion is first produced in very low abundance (figure 6.13) from 16.5 eV up to ~21 eV, after which the photoion branching ratio rapidly increases. The initial formation of  $\text{P}^+$  apparently comes from the upper Franck-Condon region of the  $8e^{-1}$  process with the subsequent higher energy formation arising from many-body ion states associated with inner-valence ionization, although contributions from the  $10a_1^{-1}$  process cannot be excluded.

Further information on the dipole-induced breakdown of  $\text{PCl}_3$  must await measurements of electronic state PPOS by variable energy photoelectron spectroscopy and data from PEPICO and PIPICO experiments.

### 6.2.2.2 P 2*p*,2*s* and Cl 2*p*,2*s* inner-shell photoionization

Time-of-flight mass spectra of  $\text{PCl}_3$  have been recorded at a series of energies from 130 to 271 eV (1 eV fwhm) in order to investigate changes in the molecular and dissociative photoionization in moving from the valence-shell continuum to the inner-shell virtual valence and Rydberg excited state regions as well as the ionization continua in the phosphorus 2*p*,2*s* and chlorine 2*p*,2*s* inner-shell regions. Typical spectra are shown in figure 6.14 at (a) 125 eV (pre-edge and valence-shell region) and in the inner-shell region at photon energies of (b) 133.5 eV corresponding to the virtual valence transitions  $11e \leftarrow \text{P } 2p^{-1}$ , (c) 136.5 eV (Rydbergs  $\leftarrow \text{P } 2p^{-1}$ ), (d) 139.5 and (f) 150 eV (the continuum shape resonances  $13a_1 \leftarrow \text{P } 2p^{-1}$  and  $14a_1 \leftarrow \text{P } 2p^{-1}$ , respectively), (e) 142.5 eV (the trough between the two shape resonances), (g) 162 eV (the broad  $3d \leftarrow \text{P } 2p^{-1}$  resonance), and (h) 174 eV (the P 2*p* continuum). Additional spectra are shown in figure 6.15 at (a) 191 eV ( $11e \leftarrow \text{P } 2s^{-1}$ ), (b) 198 eV (the P 2*s* continuum), (c) 201.5 eV ( $11e \leftarrow \text{Cl } 2p^{-1}$ ), (d) 207 eV (the  $13a_1 \leftarrow \text{Cl } 2p^{-1}$  resonance and Rydbergs  $\leftarrow \text{Cl } 2p^{-1}$  transitions), (e) 216 eV ( $14a_1 \leftarrow \text{Cl } 2p^{-1}$ ), (f) 250 eV (the broad  $3d \leftarrow \text{Cl } 2p^{-1}$  continuum resonance), and (g) 271 eV ( $11e \leftarrow \text{Cl } 2s^{-1}$  excitation). It should be noted that at each of these energies, there are also varying contributions from the relevant underlying valence and inner shells. In addition to the five singly-charged ions ( $\text{PCl}_3^+$ ,  $\text{PCl}_2^+$ ,  $\text{PCl}^+$ ,  $\text{P}^+$ , and  $\text{Cl}^+$ ) observed in the valence-shell region (figure 6.10), three stable doubly-charged ions ( $\text{PCl}_2^{2+}$ ,  $\text{Cl}^{2+}$ , and  $\text{P}^{2+}$ ) are also detected. Similar to the situation in  $\text{PF}_3$  (section 6.2.1.3), no stable triply-charged ions were observed in the present work. The photoion branching ratios for production of the molecular and fragment ions in the phosphorus 2*p*,2*s* and chlorine 2*p*,2*s* inner-shell regions are shown in figure 6.12 together with the valence shell data. The error bars were derived from the square roots of the total and background coincidence counts and thus represent only the statistical errors.

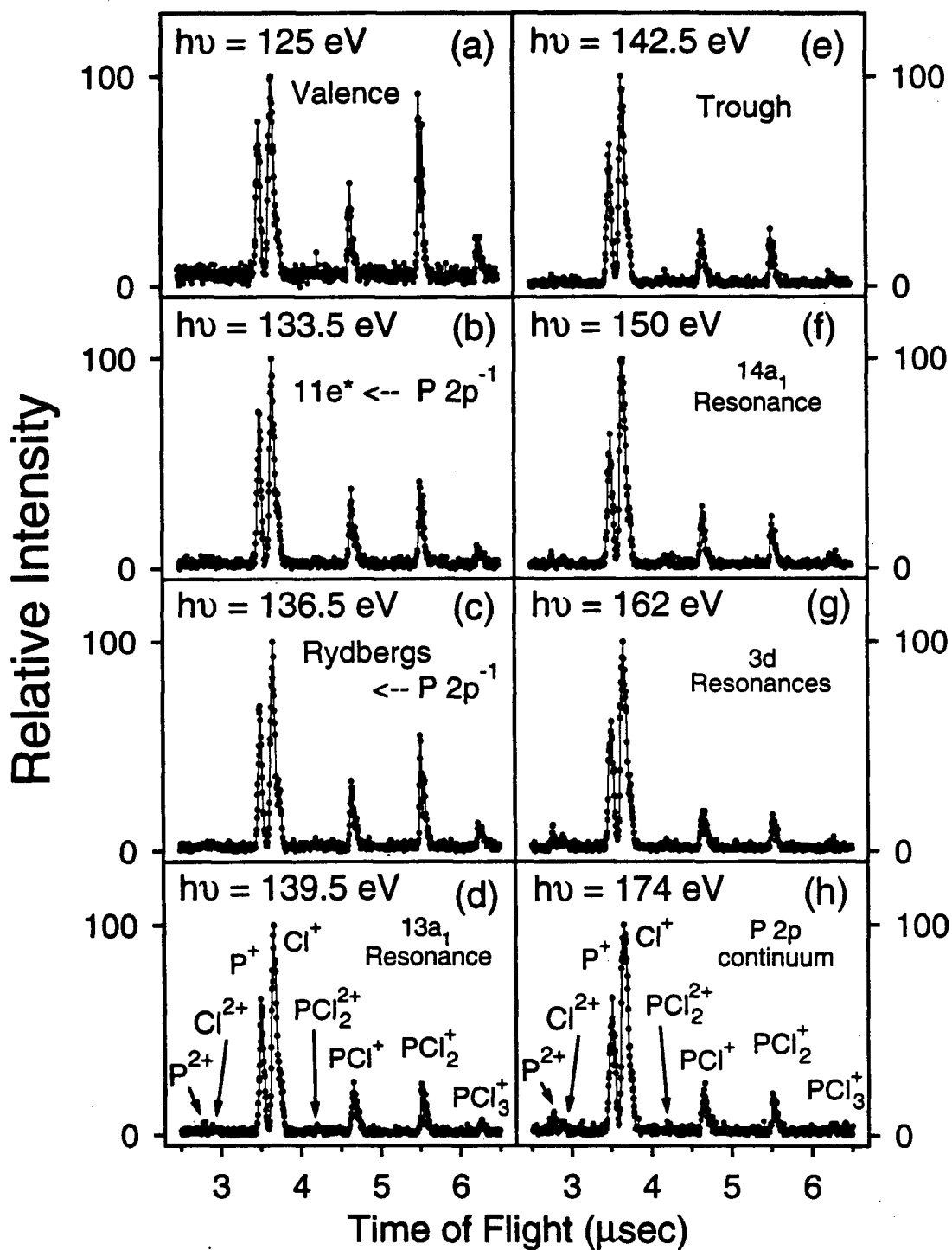


**Figure 6.14:** Time-of-flight mass spectra of  $\text{PCl}_3$  recorded at selected energies in the  $\text{P } 2p$  inner-shell region: (a) the valence-shell continuum at 125 eV, (b) 133.5 eV corresponding to the  $11e \leftarrow \text{P } 2p^{-1}$  virtual valence transition, (c) 136.5 eV corresponding to Rydbergs  $\leftarrow \text{P } 2p^{-1}$ , (d) 139.5 eV and (f) 150 eV corresponding to the two shape resonances ( $13a_1 \leftarrow \text{P } 2p^{-1}$  and  $14a_1 \leftarrow \text{P } 2p^{-1}$ , respectively), (e) 142.5 eV corresponding to the trough between the two resonances, (g) 162 eV corresponding to the broad  $3d \leftarrow \text{P } 2p^{-1}$  resonances, and (h) 174 eV corresponding to the  $\text{P } 2p$  continuum.

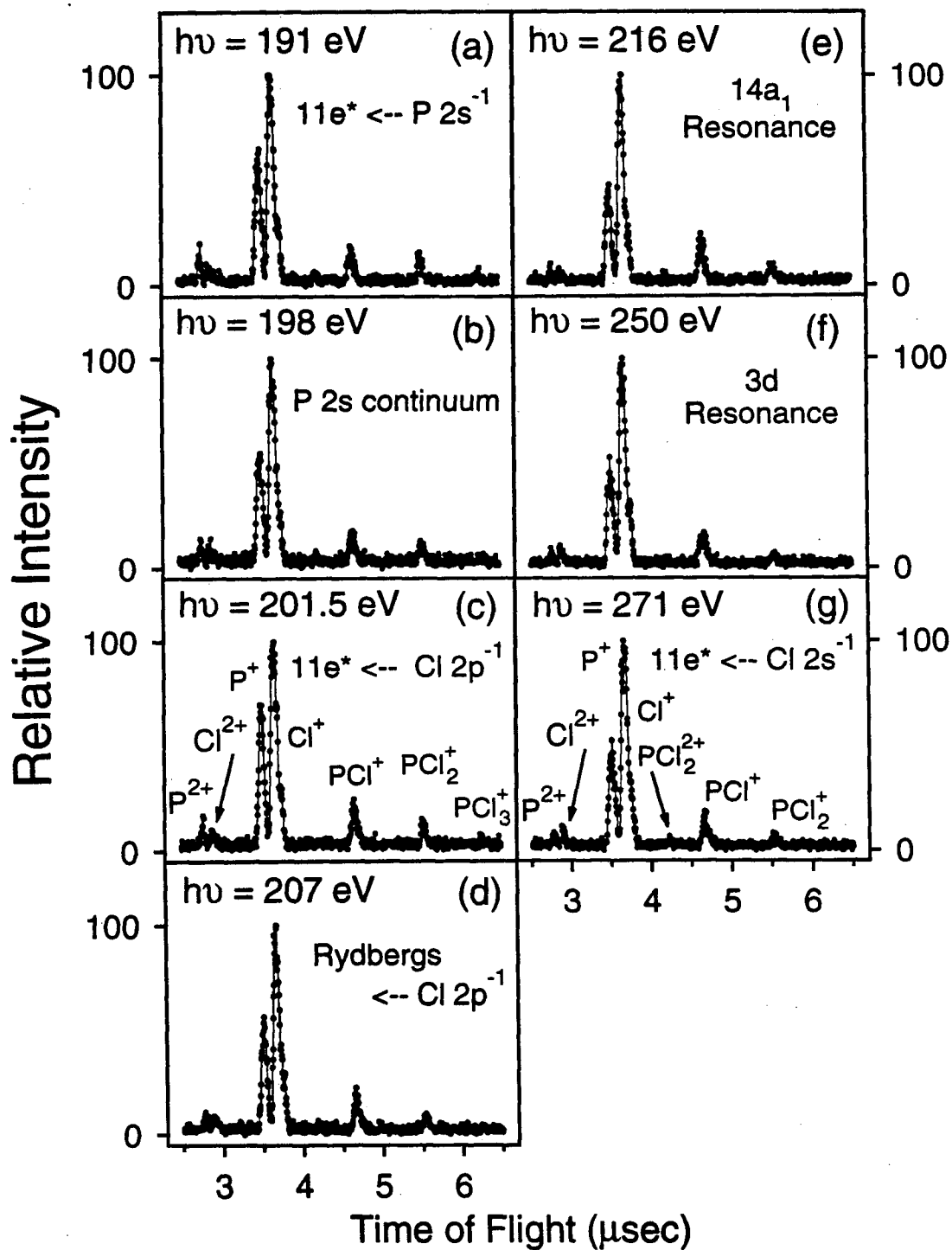


**Figure 6.15:** Time-of-flight mass spectra of  $\text{PCl}_3$  recorded at selected energies in the P  $2s$  and Cl  $2p, 2s$  inner-shell regions: (a) 191 eV corresponding to  $11e \leftarrow \text{P } 2s^{-1}$  virtual valence transition, (b) 198 eV corresponding to the P  $2s$  continuum, (c) 201.5 eV corresponding to  $11e \leftarrow \text{Cl } 2p^{-1}$ , (d) 207 eV corresponding to  $13a_1$  Rydbergs  $\leftarrow \text{Cl } 2p^{-1}$ , (e) 216 eV corresponding to the  $14a_1 \leftarrow \text{Cl } 2p^{-1}$  resonance, (f) 250 eV corresponding to the broad  $3d \leftarrow \text{Cl } 2p^{-1}$  resonances, and (g) 271 eV corresponding to the  $11e \leftarrow \text{Cl } 2s^{-1}$  excitation.

From the TOF mass spectra (figures 6.14 and 6.15) and the photoion branching ratio curves (figure 6.12), it can be seen that there are significant changes in the fragmentation in moving from the pre-edge valence shell to the P 2*p* region and from the P 2*p* continuum to the Cl 2*p* region. In particular, the most noticeable changes in the P 2*p* virtual valence and Rydberg excitation regions (figure 6.14(b,c)) are in the decreased relative abundances of the large ions,  $\text{PCl}_3^+$  and  $\text{PCl}_2^+$ . Once the P 2*p* photoionization continuum is accessed (figure 6.15(d)), doubly charged ions ( $\text{PCl}_2^{2+}$ ,  $\text{Cl}^{2+}$ , and  $\text{P}^{2+}$ ) start to appear, while the relative yield of  $\text{PCl}^+$  begins to decrease. In moving to the P 2*s* and Cl 2*p* regions (figures 6.11 and 6.15), the relative yields of  $\text{Cl}^+$  and  $\text{P}^+$  further increase, and the relative amounts of the larger ions generally decrease. Consideration of the total photoabsorption (top panel in figure 6.12) together with the changes in the photoion branching ratio curve in the P 2*p*,2*s* and Cl 2*p*,2*s* regions indicate that  $\text{PCl}^+$  formation is relatively enhanced when an inner-shell electron hole is made in a Cl ligand. These large changes occurring in the photoion branching ratios of all ions in the respective inner-shell regions indicate contributions from additional photoionization channels associated with the production of the various core excited and ionized states. However, it should be noted that the branching ratio is a quantity relative to the total ionization, and therefore direct information on any particular ion yield is best obtained from the individual partial photoionization differential oscillator strength curves (see figure 6.16 below).

Absolute partial photoionization differential oscillator strengths (figure 6.16, table A.14) for the production of the eight cations formed in the region of the P 2*p*,2*s* and Cl 2*p*,2*s* shells of  $\text{PCl}_3$  were determined from the product of the total photoabsorption differential oscillator strength and photoion branching ratio at each photon energy, and assuming photoionization efficiencies of unity (this assumes effects due to double or higher dissociative photoionization, i.e., Coulomb explosion, are small

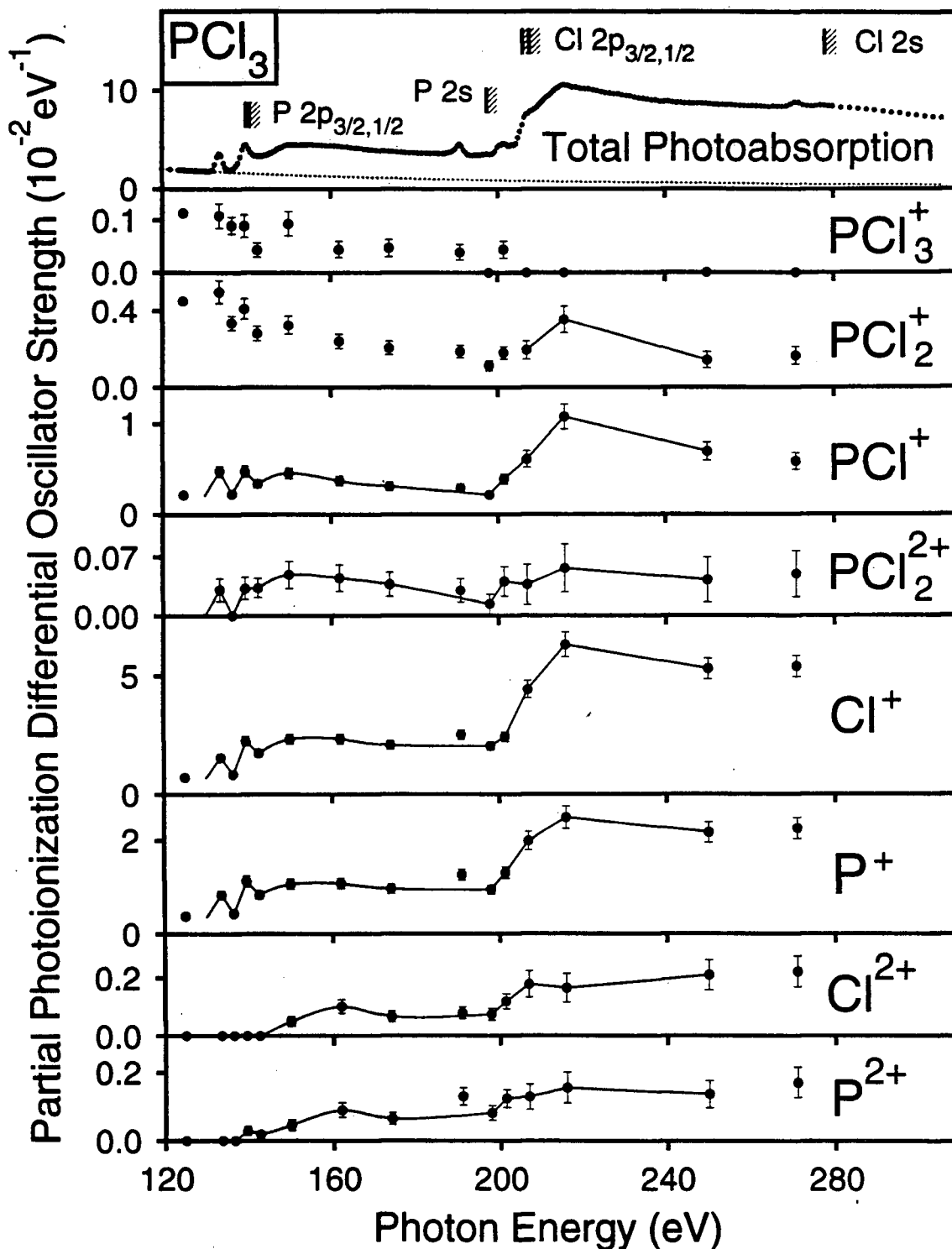


**Figure 6.16:** Absolute partial photoionization oscillator strengths for the molecular and dissociative photoionization of  $\text{PCl}_3$  in the phosphorus  $2p, 2s$  and chlorine  $2p, 2s$  shell regions from 120 to 271 eV. The top panel presents the total (valence plus  $\text{P } 2p, 2s$  and  $\text{Cl } 2p, 2s$ ) absolute differential oscillator strength spectrum, where the thresholds of the  $\text{P } 2p, 2s$  and  $\text{Cl } 2p, 2s$  ionization edges are shown as hatched lines.

compared with direct photoionization processes). This approximation is likely to become less good as the photoionization energy increases, especially in the Cl  $2p$  and  $2s$  regions. From the monotonically decreasing PPOS curve of the molecular ion, it is reasonable to conclude that  $\text{PCl}_3^+$  is produced essentially entirely from the underlying valence continuum since its shape seems to mimic the shape of the valence-shell extrapolation curve (top panel in figure 6.16). This indicates that essentially all electronic ion states formed from P  $2p,2s$  and Cl  $2p,2s$  core hole excitation and ionization states are dissociative in nature. In contrast, the PPOS of the other four singly-charged ions ( $\text{PCl}_2^+$ ,  $\text{PCl}^+$ ,  $\text{P}^+$ , and  $\text{Cl}^+$ ) all show contributions from the various inner-shell states, although the production of  $\text{PCl}_2^+$  from the phosphorus and chlorine core regions is very small compared with that from the underlying valence-shell continuum. Similar to the singly charged fragment ions, the dications ( $\text{PCl}_2^{2+}$ ,  $\text{Cl}^{2+}$ , and  $\text{P}^{2+}$ ) all show contributions from the phosphorus and chlorine  $2p$  shell neutral excited states and ionization continua. This can be seen by the similar shapes of the fragment ion PPOS curves compared with that of the total photoabsorption curve at the top panel of figure 6.16.

The absolute yields of the  $\text{PCl}_3$  fragments ions can be discussed with reference to autoionization and Auger decay processes occurring in core hole excitation and ionization. Below the P  $2p$  ionization threshold the singly-charged cations ( $\text{PCl}_2^+$ ,  $\text{PCl}^+$ ,  $\text{P}^+$ , and  $\text{Cl}^+$ ) are produced with reasonable yield. In this region the excited  $2p$  electron either remains as a spectator or participates in the autoionization (resonance Auger) decay of the P  $2p^{-1}$  excited hole state to give the singly-charged ions. The  $\text{PCl}_2^{2+}$  dication is also produced in small but significant yield throughout the P  $2p,2s$  and Cl  $2p$  regions, presumably from Auger type processes involving the inner-shell holes since no stable doubly charged cations are found from the valence shell (figure 6.12). Above the P  $2p$  edges normal Auger processes become the principal decay channels, giving rise to doubly-charged species

[155,152]. Since the appearance potentials for  $\text{Cl}^{2+}$  and  $\text{P}^{2+}$  are in the P  $2p$  post-edge region, both of these dications must be formed almost exclusively by Auger processes and not as a result of core hole excitation processes. In the phosphorus and chlorine  $2p$  and  $2s$  inner-shell continua, doubly-charged ions produced by Auger processes are also expected to fragment by Coulomb explosion (i.e., double dissociative photoionization processes) to give two singly-charged species. Such processes contribute to the relatively larger yields of the lighter ion products (especially  $\text{P}^+$  and  $\text{Cl}^+$ ) which may possess considerable kinetic energy of fragmentation (as exemplified by the relatively broad TOF  $m/e$  peaks of the  $\text{PCl}^+$ ,  $\text{P}^+$ , and  $\text{Cl}^+$  ions in figures 6.14 and 6.15).

## 6.2.3 Phosphorus pentafluoride

### 6.2.3.1 Valence-shell photoionization

TOF mass spectra of phosphorus pentafluoride have been measured as a function of photon energy spanning the entire valence-shell photoionization region from 15–130 eV. The cations produced from the molecular and dissociative photoionization of  $\text{PF}_5$  observed in the present work are  $\text{PF}_x^+$ ,  $\text{PF}_x^{2+}$ , and  $\text{F}^+$  ( $x = 0-4$ ). The  $\text{PF}_5^+$  parent ion is not detected which is consistent with the result of an earlier mass spectral study [161]. Similarly, the parent doubly charged ion ( $\text{PF}_5^{2+}$ ) is not observed. Figure 6.17 shows a typical TOF spectrum obtained at 80 eV. The broadness of the smaller singly charged ions,  $\text{F}^+$ ,  $\text{P}^+$ , and  $\text{PF}^+$ , indicates that they are formed with considerable kinetic energies of fragmentation. Very small impurity peaks ( $\text{POF}_3^+$  and  $\text{POF}_2^+$ ) resulting from the presence of  $\text{POF}_3$  in the sample were detected in the mass spectra, and corrections have been made as discussed in section 3.3. The absolute photoionization efficiencies for  $\text{PF}_5$  measured

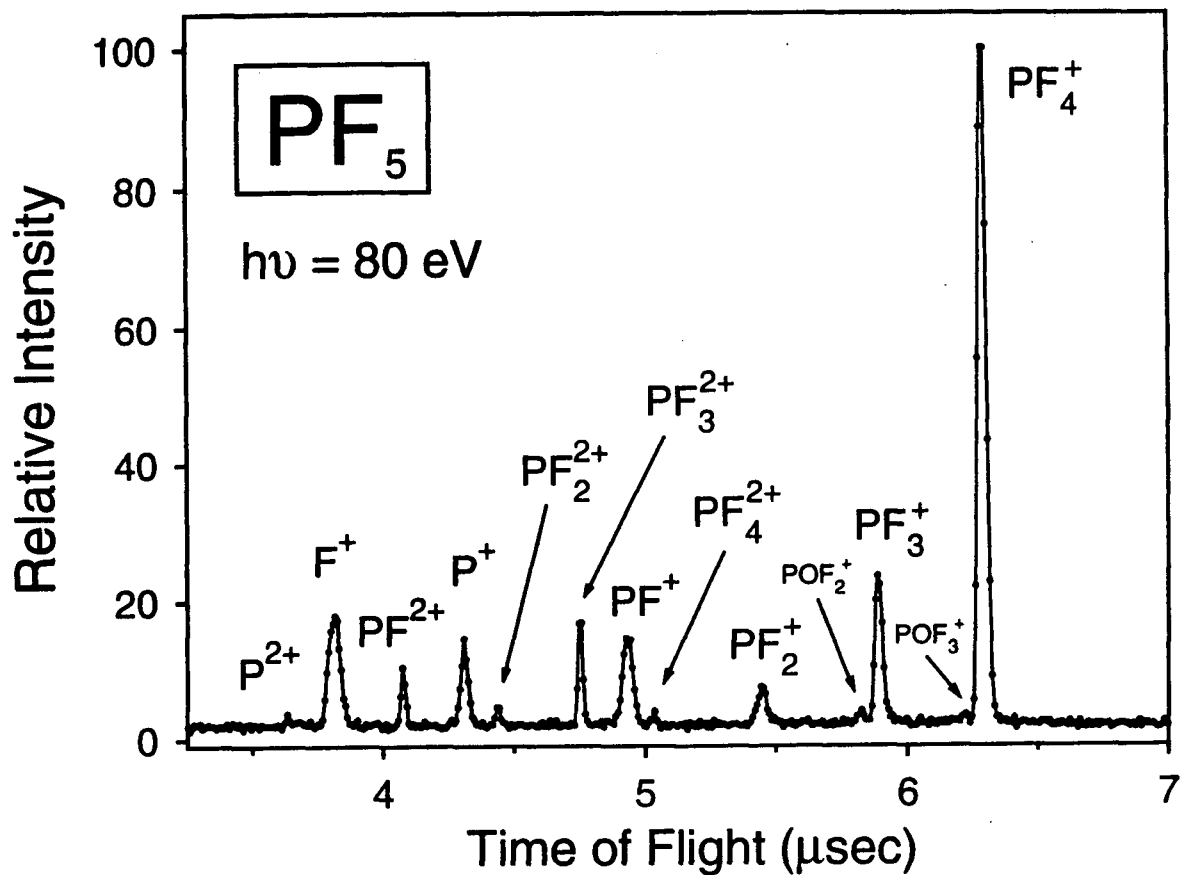


Figure 6.17: TOF mass spectrum of  $\text{PF}_5$  recorded at 80 eV.

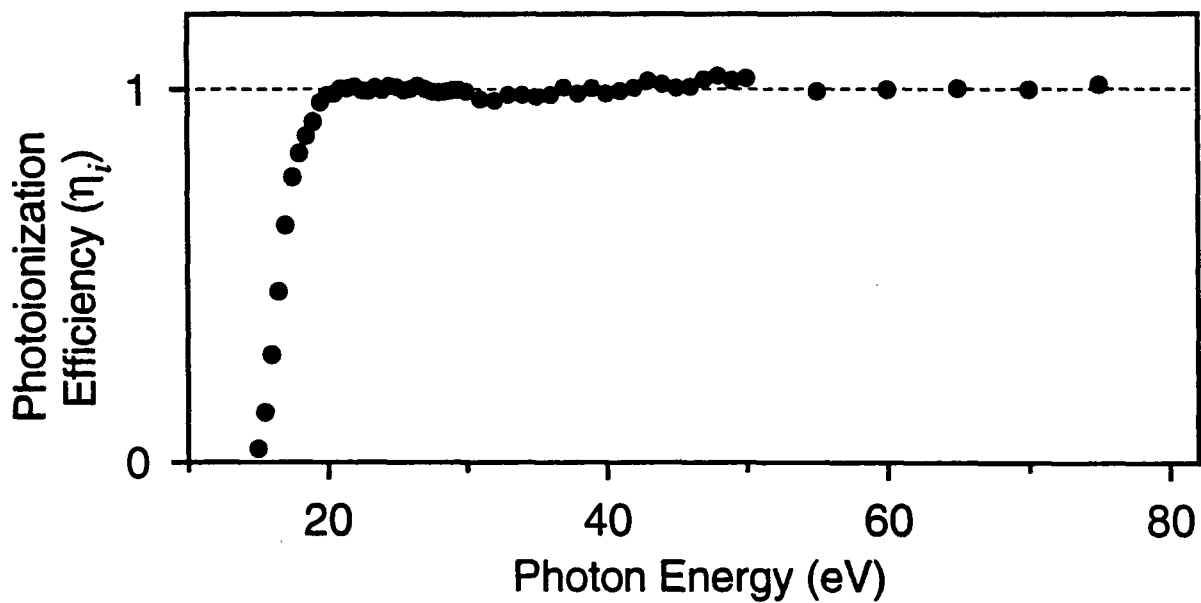


Figure 6.18: Photoionization efficiencies for  $\text{PF}_5$  (15–75 eV).

from 15 to 75 eV are shown in figure 6.18, while the photoion branching ratios determined from the TOF spectra are presented in figure 6.19.

Absolute partial photoionization differential oscillator strengths (PPOS) for the production of the fragment ions from  $\text{PF}_5$  have been obtained from the triple product of the absolute total photoabsorption differential oscillator strength (see section 5.2.4.1), the photoionization efficiency, and photoion branching ratio for each ionic species, as a function of photon energy. The results are shown graphically in figure 6.20 and are given numerically in table A.11. The hatched lines in figure 6.20 indicate the positions of the VIP's for the first nine occupied outer valence orbitals of  $\text{PF}_5$  as given in section 5.2.1. The appearance potentials (AP's) for all eleven ions observed in the present work are listed in table 6.3.

Using the model in which fragmentation ratios for dissociative photoionization from each electronic state of the molecular ion ( $\text{PF}_5^+$ ) should be constant when the photon energy exceeds the upper limit of the Franck-Condon region (except in local regions where autoionization effects are significant or where multiple photoionization is appreciable) [39], the absolute PPOS for the production of each singly charged ion from  $\text{PF}_5$  can be expressed as a linear combination of PPOS of electronic ion states. However, since photoelectron branching ratios, electronic state PPOS, and photoelectron-photoion coincidence data are not available in the literature for phosphorus pentafluoride, it is not possible to quantitatively investigate the dipole-induced breakdown scheme of  $\text{PF}_5$ . Such measurements will present a considerable challenge since the outer valence ion states are generally situated very close to one another, with the first five excited ion states not being resolved even by high resolution PES [112,117].

A consideration of the outer-valence VIP's and Franck-Condon widths (see section 5.2.1) [112] and the high values of the appearance potentials of the  $\text{P}^+$  (37 eV) and  $\text{F}^+$  (30 eV) atomic ions suggests that these two ions arise from inner-valence

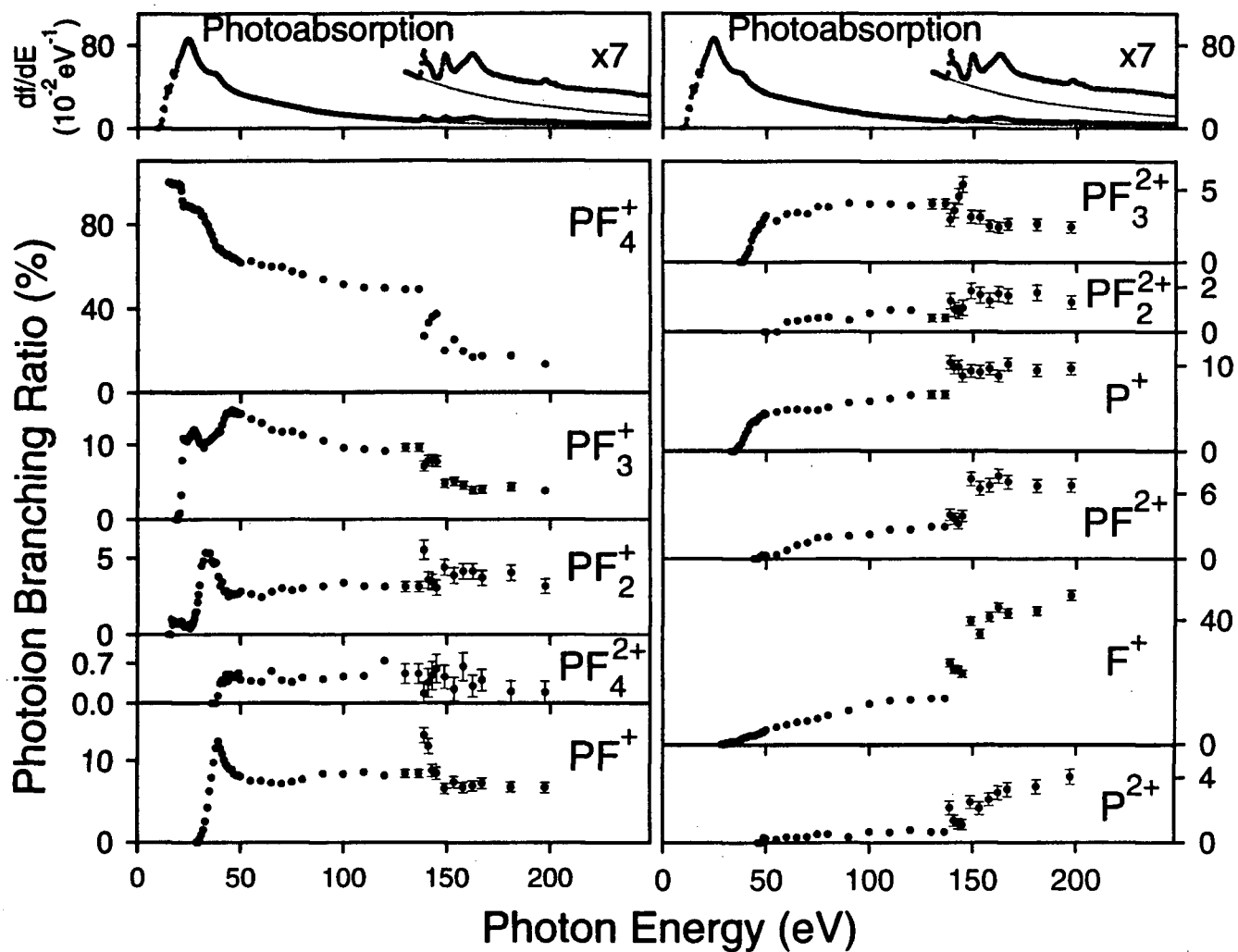


**Figure 6.19:** Branching ratios for the dissociative photoionization of  $\text{PF}_5$ . The absolute total photoabsorption spectrum from figure 5.10 is also shown in the top panel.

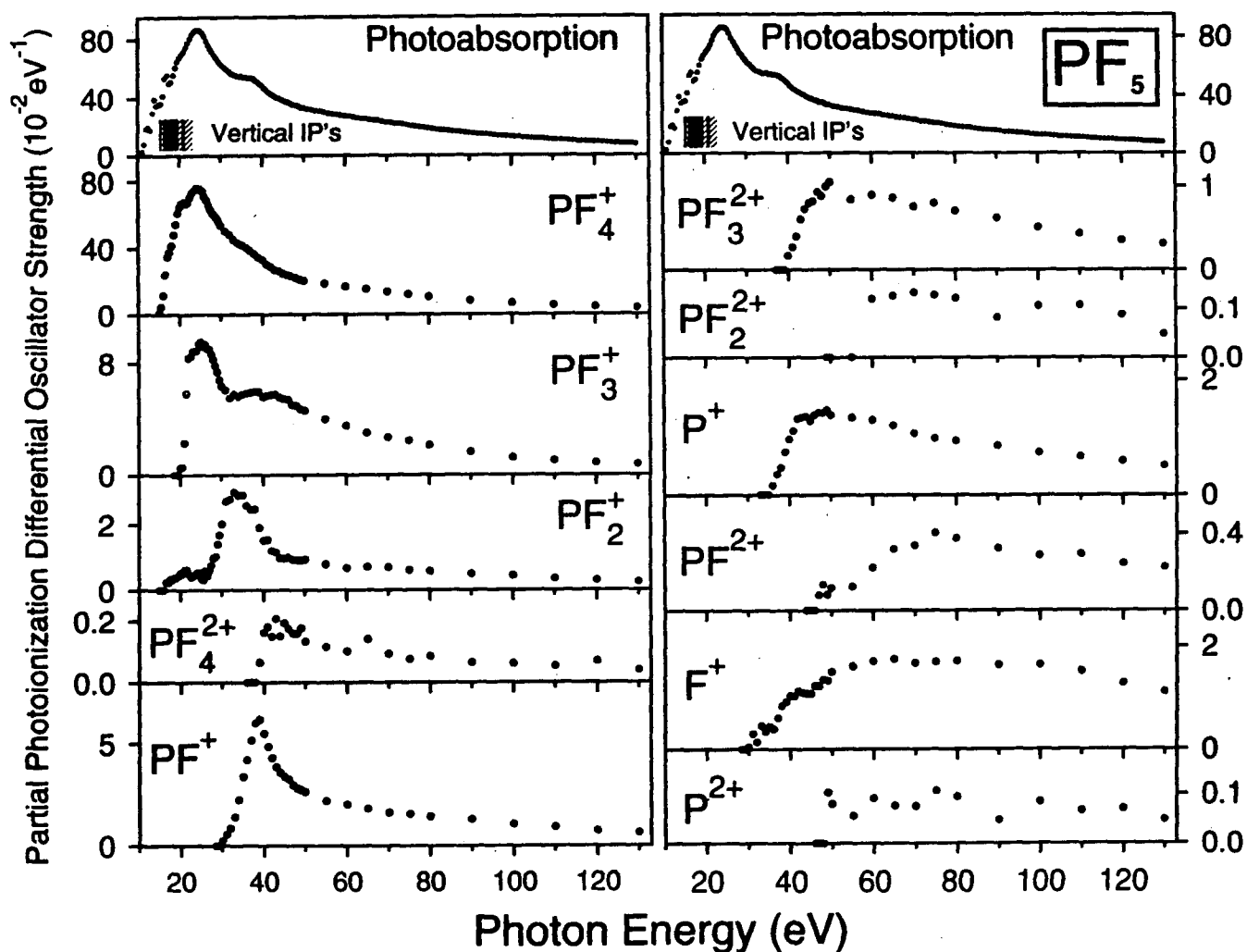


**Figure 6.20:** Absolute partial photoionization differential oscillator strengths for the valence-shell dissociative photoionization of  $\text{PF}_5$  (15–130 eV). The absolute total photoabsorption spectrum from figure 5.10 is also shown in the top panels. The positions of the nine outermost outer-valence VIP's measured by PES [112,117] are denoted by the hatched lines.

ionization processes. Since the inner-valence orbitals ( $6a'_1$ ,  $5a'_1$ ,  $3a''_2$ , and  $3e'$ ) are expected to have considerable F 2s character, it is of interest to compare the measured, summed ( $P^+ + F^+$ ) differential oscillator strengths with five times the theoretical values of the F 2s photoionization oscillator strengths for atomic fluorine [86]. Such procedures have sometimes been used [44] to provide estimates of the contributions from inner-valence photoionization. Figure 6.21 shows that the shape of the ( $P^+ + F^+$ ) summed differential oscillator strengths is well reproduced by the calculated F 2s atomic sum, but the magnitudes differ by ~12%. This contrasts with the analogous situation in  $PF_3$  where three times the calculated atomic F 2s differential oscillator strengths was considerably less (20%) and of a different shape from the ( $P^+ + F^+$ ) oscillator strength sum. This clearly indicates that such procedures for estimating inner-valence electronic ion state oscillator strengths are at best very approximate. It should also be noted that the high appearance potential of  $PF^+$  (30 eV) suggests that this ion may also arise from inner-valence photoionization of  $PF_5$ . The strong resonance structure evident in the  $PF^+$  PPOS curve at 39 eV is not observed in the F 2s theoretical oscillator strengths but corresponds in energy to the phosphorus 3d resonance in the valence shell photo-absorption continuum.

In addition to the singly-charged cations, five dications,  $PF_x^{2+}$  ( $x = 0-4$ ), are also produced from the valence-shell photoionization of  $PF_5$ . While doubly charged ions are not in general expected to arise from the decomposition of singly charged ions, it is possible that some can be formed by VVV Auger processes involving inner-valence primary hole states [164]. For  $PF_5$ , the occurrence of this is suggested by the measured appearance potentials of the dications (table 6.3), which are at energies where inner-valence ionization processes may be expected to occur. From figure 6.21 it can be seen that the appearance potentials and shapes of the PPOS for production of  $PF_4^{2+}$  and  $PF_3^{2+}$  are quite similar, and it is possible that these doubly

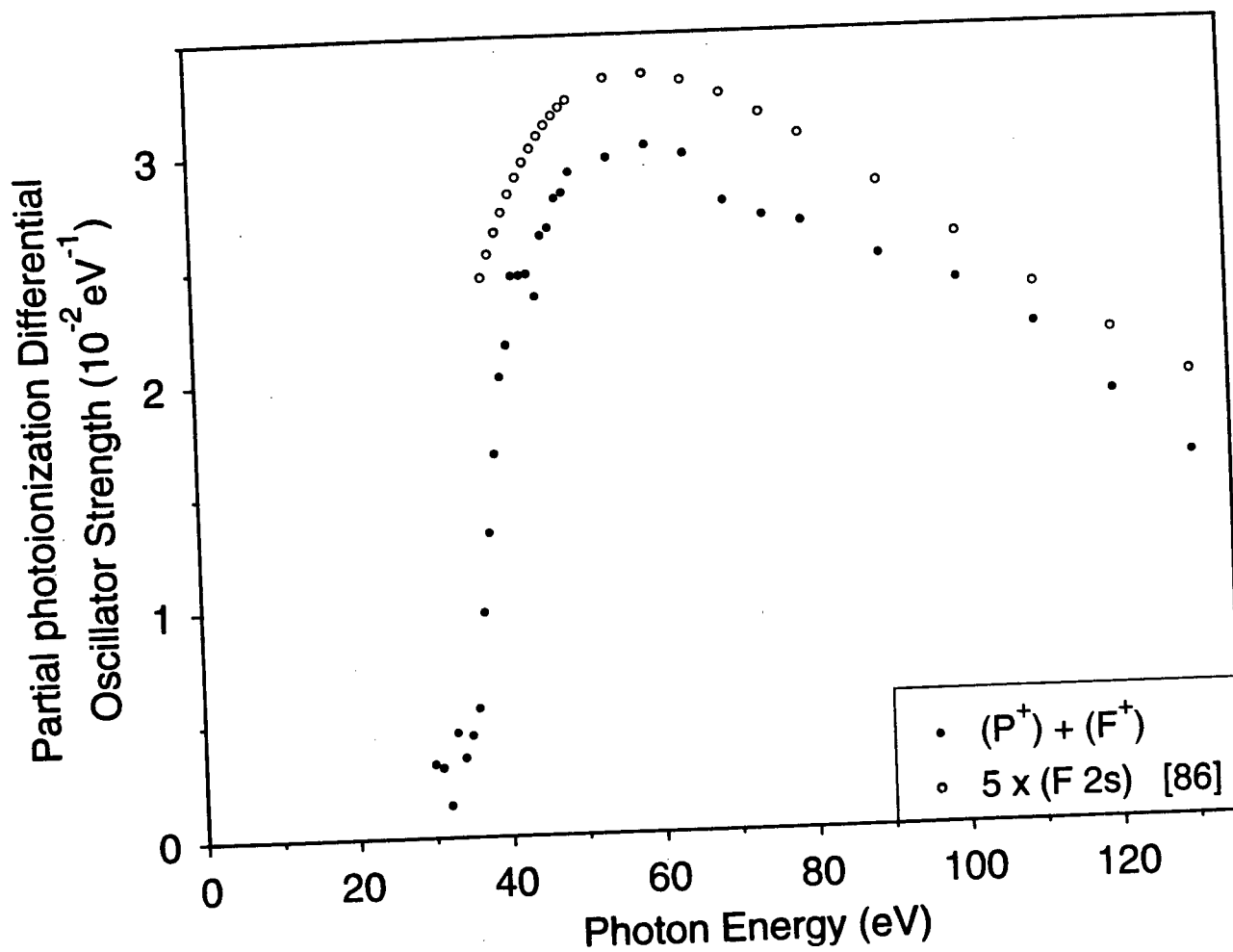


**Figure 6.21:** Comparison of the summed  $(\text{P}^+ + \text{F}^+)$  differential oscillator strengths with five times the theoretical values of the F 2s photoionization differential oscillator strengths for atomic fluorine [86].

**Table 6.3**Appearance potentials for the production of positive ions from  $\text{PF}_5$ 

Fragment ion	Appearance potential (eV) ( $\pm 1$ eV)
$\text{PF}_4^+$	15.5
	17.5
	22.0
$\text{PF}_3^+$	20.5
	32
$\text{PF}_2^+$	17.0
$\text{PF}_4^{2+}$	39
$\text{PF}^+$	30
$\text{PF}_3^{2+}$	40
$\text{PF}_2^{2+}$	60
$\text{P}^+$	36
$\text{PF}^{2+}$	47
$\text{F}^+$	30
$\text{P}^{2+}$	49

charged ions are formed primarily by dissociation of the same doubly ionized state(s). More complete information on the dipole-induced breakdown of the singly and doubly charged cations must await measurements of adiabatic and vertical double-ionization potentials as well as PEPICO and PIPICO studies.

### 6.2.3.2 P 2p,2s inner-shell photoionization

In order to investigate the changes in the ion fragmentation of PF<sub>5</sub> in going from valence-shell photoionization to phosphorus 2p and 2s excitation and ionization, time-of-flight mass spectra (figures 6.22 and 6.23) have been recorded at a series of energies from 130 to 197.5 eV at a resolution of 1 eV fwhm. Typical spectra are shown in figure 6.22 at (a) 130 eV (pre-edge, valence-shell region) and in the inner-shell region at photon energies of (b) 139 eV corresponding to the virtual valence transitions  $9a'_1 \leftarrow P 2p^{-1}$ , (c) 141 eV ( $7e' \leftarrow P 2p^{-1}$ ), (d) 143 eV (Rydbergs  $\leftarrow P 2p^{-1}$ ), and (e) 149 eV (shape resonance). Additional TOF spectra are shown in figure 6.23 at (a) 158 and (b) 162.5 eV corresponding to the 3d continuum resonances, (c) 181 eV (the P 2p continuum), and (d) 197.5 eV ( $7e' \leftarrow P 2s^{-1}$ ). All eleven of the ions observed in the valence-shell region, PF<sub>x</sub><sup>+</sup>, PF<sub>x</sub><sup>2+</sup>, and F<sup>+</sup> (x = 0–4), are also detected at all energies in these spectra, but with very different relative intensities. In the virtual valence (139 and 141 eV) and Rydberg (143 eV) excitation regions, the most noticeable changes from the valence-shell fragmentation are in the relative abundances of F<sup>+</sup>, PF<sup>+</sup>, PF<sub>3</sub><sup>+</sup>, and PF<sub>4</sub><sup>+</sup>. Above the P 2p threshold F<sup>+</sup> becomes the most abundant ion (149 eV, figure 6.22(e)). It can also be seen that the most significant changes in the TOF mass spectra in the P 2p continuum above 145 eV are the large increases in the relative abundances of F<sup>+</sup>, P<sup>2+</sup>, and PF<sup>2+</sup>. The F<sup>+</sup> and PF<sup>+</sup> peaks are very broad, with the F<sup>+</sup> becoming increasingly so at higher energies, indicating that these ions are formed with considerable kinetic energy of fragmentation.

The photoion branching ratios for production of the singly and doubly charged cations in the P 2p,2s regions are presented in figure 6.19. The error bars are derived from the square roots of the total and background coincidence counts and represent statistical error only. In moving from the valence-shell to the 2p inner-

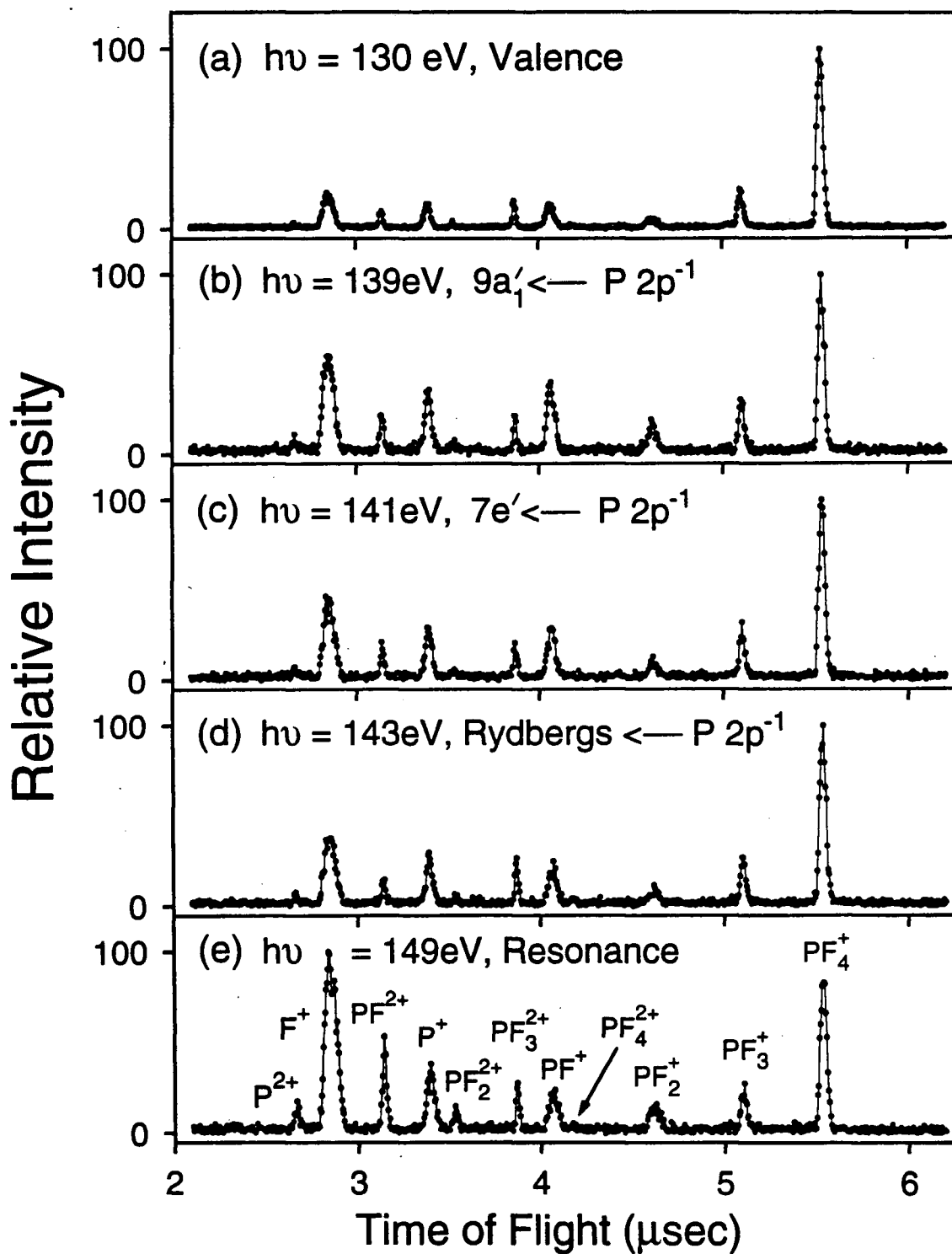


**Figure 6.22:** Time-of-flight mass spectra of  $\text{PF}_5$  recorded at selected energies in the P  $2p$  inner-shell region: (a) the valence-shell continuum at 130 eV, (b) 139 eV corresponding to the virtual valence transitions  $9a_1' \leftarrow \text{P } 2p^{-1}$ , (c) 141 eV corresponding to  $7e' \leftarrow \text{P } 2p^{-1}$ , (d) 143 eV corresponding to Rydbergs  $\leftarrow \text{P } 2p^{-1}$ , and (e) 149 eV corresponding to the shape resonance.

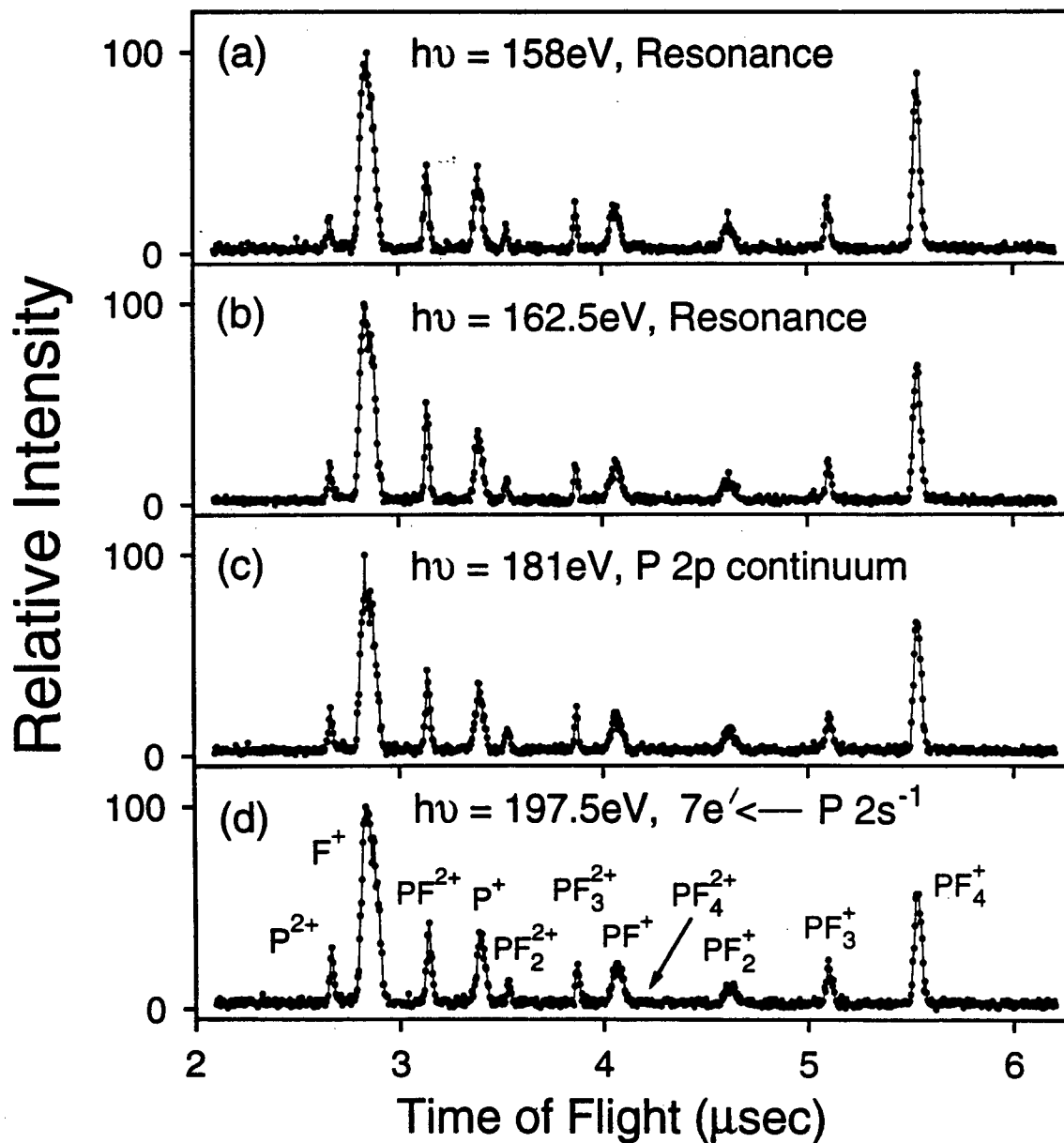


**Figure 6.23:** Time-of-flight mass spectra of  $\text{PF}_5$  recorded at selected energies in the P 2p and P 2s inner-shell regions: (a) 158 and (b) 162.5 eV corresponding to the 3d continuum resonances, (c) 181 eV corresponding to the P 2p continuum, and (d) 197.5 eV corresponding to  $7e' \leftarrow \text{P } 2s^{-1}$  transition.

shell region, the relative yields of  $\text{PF}_4^+$  and  $\text{PF}_3^+$  decrease markedly, while those of  $\text{P}^{2+}$ ,  $\text{F}^+$ ,  $\text{PF}^{2+}$ ,  $\text{P}^+$ , and  $\text{PF}_2^{2+}$  show significant increases throughout the  $2p$  inner-shell region. Localized increases in the relative amounts of  $\text{PF}_3^{2+}$ ,  $\text{PF}^+$ , and  $\text{PF}_2^+$  in the pre-edge excitation region are also observed. It should be noted that while the branching ratios are quantities relative to the total ionization, they do not directly show how the individual fragmentation channels are affected by the P  $2p$  discrete excitations and ionization continuum regions. Such information can only be obtained by considering the absolute PPOS ( $df/dE$ ) curves for molecular and dissociative photoionization along with the P  $2p$  photoabsorption spectrum as shown in figure 6.24.

Absolute partial photoionization differential oscillator strengths for the production of fragment ions from the P  $2p$  and  $2s$  inner-shell regions of phosphorus pentafluoride are presented in figure 6.24 and given numerically in table A.15. From the monotonically decreasing PPOS curve of  $\text{PF}_4^+$ , which seems to mimic the shape of the valence-shell photoabsorption extrapolation curve (top panel in figure 6.24), it is reasonable to conclude that  $\text{PF}_4^+$  is produced almost exclusively from the underlying valence-shell continuum. In contrast, all remaining ions show contributions from both the P  $2p$  neutral excited states and the ionization continuum. Judging by the oscillator strengths of the valence-shell photoionization at 130 eV, and the shapes of the ion PPOS, the total photoabsorption, and the extrapolation curves of the valence-shell photoabsorption, it can be seen that the relative contributions from the P  $2p, 2s$  excitation and ionization region to the ion oscillator strengths is very small for  $\text{PF}_3^+$  and  $\text{PF}_3^{2+}$ , but large for the smaller ions,  $\text{P}^{2+}$ ,  $\text{F}^+$ ,  $\text{PF}^{2+}$ ,  $\text{P}^+$ ,  $\text{PF}^+$ , and  $\text{PF}_2^{2+}$ . In particular, it should be noted that in the P  $2p$  region,  $\text{PF}^+$  arises almost exclusively from the  $2p$  excited neutral states.

In general, with the exception of  $\text{PF}_4^+$  and  $\text{F}^+$ , which have large intensities at all energies studied, the singly charged ions are the predominant species in the P  $2p$

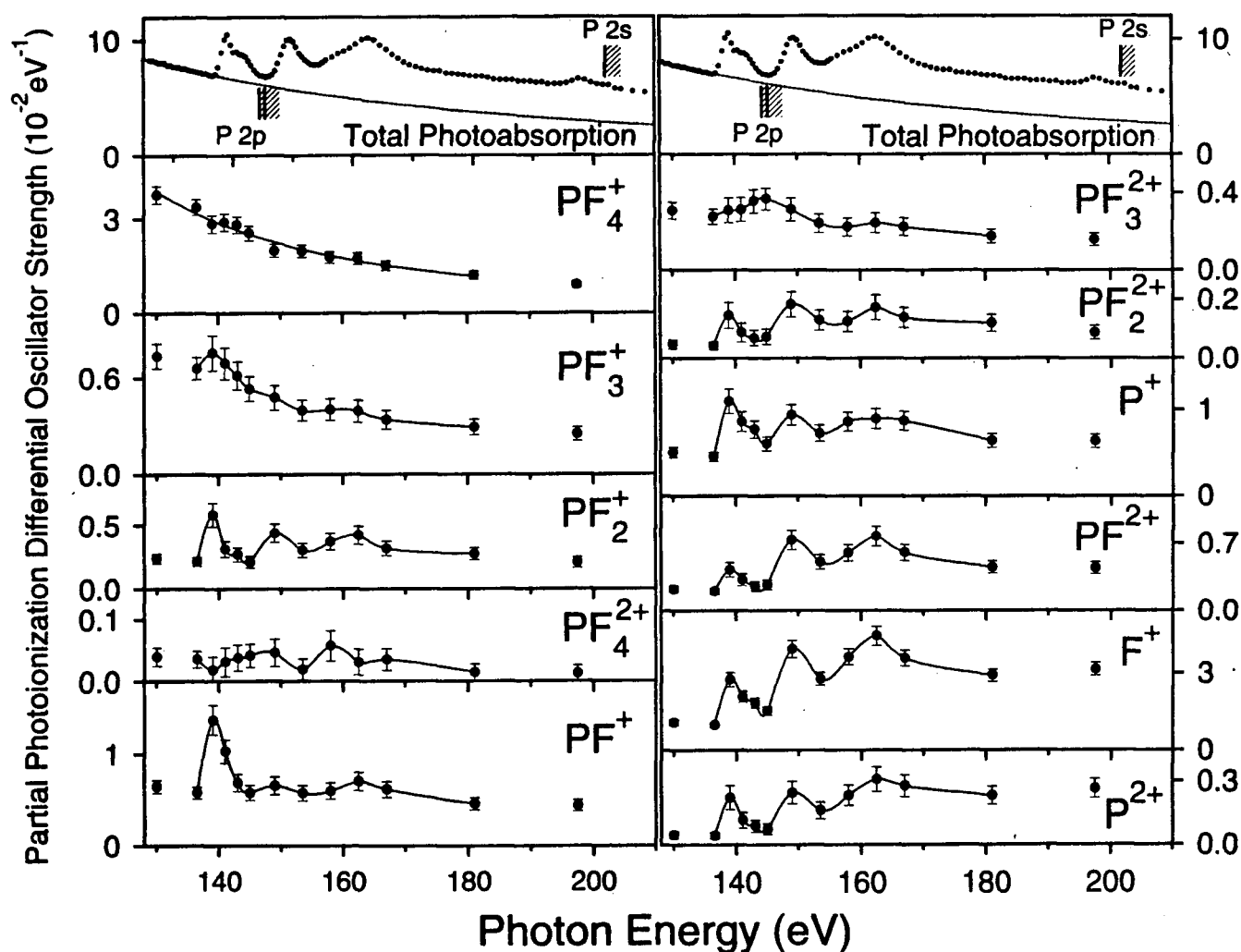


**Figure 6.24:** Absolute partial photoionization differential oscillator strengths for the dissociative photoionization of  $\text{PF}_5$  in the P 2p and P 2s regions from 130 to 197.5 eV. The top panel presents the total (valence plus P 2p, 2s) absolute photoabsorption spectrum where the thresholds of the P 2p and 2s edges are shown as hatched lines.

pre-edge region, while the doubly charged ions are dominant in the post-edge ionization continuum. This phenomenon can be attributed to autoionization decay of the  $2p^{-1}$  hole state (i.e., resonance Auger processes) being favored in the excitation region, thereby giving rise to singly charged ions, whereas above the  $2p$  ionization threshold, Auger processes become the principal decay channels, which results in the formation of predominantly doubly charged ions [152]. The subsequent fragmentation of these dications by Coulomb explosion (i.e., double dissociative photoionization processes) would result in the production of two singly charged ions. Such processes can therefore contribute to the yield of the lighter ion products (e.g.,  $F^+$ ). Considerable ion kinetic energy can be generated in the Coulomb explosion process, as exemplified by the increasingly broad peaks of  $F^+$  with increase in energy (see figures 6.22 and 6.23).

## Chapter 7

# Photoabsorption and Photoionization Studies of Nitrogen Dioxide

### 7.1 Introduction

Nitrogen dioxide ( $\text{NO}_2$ ) has become one of the major atmospheric pollutants in our society as a result of its production from the combustion of fuels used for heat, power, and transportation [33]. At higher elevations in the stratosphere,  $\text{NO}_2$  is also involved in the cyclic catalytic decomposition of atmosphere ozone ( $\text{O}_3$ ) [30–32]:



The overall result of these reactions is the net conversion of ozone into molecular oxygen. Therefore, quantitative data for the photoabsorption and photoionization of  $\text{NO}_2$  is of interest in atmospheric phenomena as well as in fundamental science. From a theoretical standpoint, calculations for open shell molecules [166] such as  $\text{NO}_2$  are particularly challenging.

The electronic spectrum of nitrogen dioxide up to 25 eV has been extensively studied and analyzed both by theory [167–170] and by experiment [3,4,171–201]. Relative measurements obtained using conventional optical techniques [171–176,180–189], time-resolved excitation [190], two-photon absorption [191,192], and electron energy-loss spectroscopy [177–179] have provided insights into the assignment of virtual valence and Rydberg transitions to discrete bands observed between 1.6–25 eV, as well as rotational lines and vibronic progressions associated

with these transitions. In addition, the electronic excitations at low energy ( $\sim 1.5$ – $6.7$  eV) have been reviewed in refs. [202–204]. In contrast, although many measurements of absolute photoabsorption cross sections have been made in the visible region up to  $3.4$  eV [193–201], absolute data reported in the UV and VUV regions are very limited, and the overlaps between the various data sets are very small. Following the absolute measurements of Hall and Blacet [194] from  $2.5$  to  $5.2$  eV, absorption coefficients at higher energies from  $4.6$  to  $11.5$  eV were reported by Nakayama *et al.* [3] in 1959, and nineteen years later Morioka *et al.* [4] extended the data from  $11$  to  $25$  eV using monochromated synchrotron radiation. However, above  $25$  eV no absolute cross sections for the photoabsorption of nitrogen dioxide are available in the literature.

In photoionization work, Frost *et al.* [205] reported the relative photoionization yield of the nitrogen dioxide molecular ion ( $\text{NO}_2^+$ ) up to  $14$  eV, while Weissler *et al.* [206] and Dibeler *et al.* [207] determined relative photoionization yield curves for  $\text{NO}_2^+$  as well as for the  $\text{NO}^+$  and  $\text{O}^+$  fragment ion between  $\sim 11$ – $25$  eV. However, to date no absolute photoionization cross sections have been published. In other work, electron impact ionization [208–210] has contributed additional information on the appearance potentials of the molecular and dissociative ions produced from nitrogen dioxide, and a multiphoton study [211] in 1981 reported the detection of  $\text{O}_2^+$  cations not previously observed in the photoionization mass spectrometry (PIMS) [205–207] and electron impact [208–210] studies.

In the present work, dipole ( $e, e$ ) spectroscopy has been used to obtain the first wide range valence-shell absolute photoabsorption spectrum and absolute differential oscillator strengths (cross sections) of  $\text{NO}_2$  spanning the visible to the soft X-ray regions ( $2$ – $200$  eV) at  $1$  eV resolution. The discrete features have also been studied at higher resolution ( $0.05$  eV fwhm), from which absolute oscillator strength values have been determined for the  ${}^2\text{B}_1 \leftarrow {}^2\text{A}_1$  and  ${}^2\text{B}_2 \leftarrow {}^2\text{A}_1$  systems, as

well as for the Rydberg transitions at higher energies. In addition, dipole ( $e,e^+$ ion) coincidence spectroscopy has been used to obtain time-of-flight mass spectra of  $\text{NO}_2$  from the first ionization threshold up to 80 eV. The photoion branching ratios and absolute photoionization efficiencies determined from these spectra have been combined with the photoabsorption data in order to obtain, for the first time, the absolute partial photoionization differential oscillator strengths (PPOS) for the production of molecular and fragment ions from  $\text{NO}_2$ .

## 7.2 Results and Discussions

### 7.2.1 Electronic structures

The photoabsorption and photoionization data of nitrogen dioxide ( $\text{C}_{2v}$ ) will be discussed with reference to its electronic ground state ( ${}^2\text{A}_1$ ), valence-shell molecular orbital configuration in the independent particle model:

$$\underbrace{(3a_1)^2(2b_2)^2}_{\text{Inner valence}} \quad \underbrace{(4a_1)^2(3b_2)^2(1b_1)^2(5a_1)^2(1a_2)^2(4b_2)^2(6a_1)^1}_{\text{Outer valence}} \quad \underbrace{(2b_1)^0(7a_1)^0(5b_2)^0}_{\text{Virtual valence}}.$$

The vertical ionization potentials (VIP's) for the seven outer valence orbitals reported from He (I) and He (II) photoelectron spectroscopy [212] are:  $6a_1^{-1}$ , 11.23 eV ( ${}^1\text{A}_1$ );  $4b_2^{-1}$ , 13.01 eV ( ${}^3\text{B}_2$ ), 14.51 eV ( ${}^1\text{B}_2$ );  $1a_2^{-1}$ , 13.60 eV ( ${}^3\text{A}_2$ ), 14.06 eV ( ${}^1\text{A}_2$ );  $5a_1^{-1}$ , 17.45 eV ( ${}^3\text{A}_1$ );  $1b_1^{-1}$ , 17.64 eV ( ${}^3\text{B}_1$ );  $3b_2^{-1}$ , 18.86 eV ( ${}^3\text{B}_2$ ), 21.0 eV ( ${}^1\text{B}_2$ ); and  $4a_1^{-1}$ , 21.26 eV ( ${}^3\text{A}_1$ ). The two-hole-one-particle configuration interaction calculations of Schirmer *et al.* showed that the inner valence  $2b_2^{-1}$  and  $3a_1^{-1}$  ionization processes are predicted to be split by electron correlation effects into several many-body states [213]. The poles for the  $2b_2^{-1}$  ionization ( ${}^3,{}^1\text{B}_2$ ) extend from 36 to 40 eV with the dominant peak occurring at 38.6 eV [213]. Similarly, the  $3a_1^{-1}$  ionization ( ${}^3,{}^1\text{A}_1$ ) lines cover the 40–45 eV range with the main line situated at

43.1 eV [213]. The ordering of the three virtual valence orbitals given above is that determined by Mulliken [202].

## 7.2.2 Long range photoabsorption spectrum

The background subtracted EEL spectrum (6–200 eV) obtained in the dipole ( $e,e$ ) mode of the low resolution spectrometer was Bethe-Born converted to relative photoabsorption data, which was then put onto an absolute scale using the VTRK sum-rule. In the latter procedure, the proportion of the valence-shell oscillator strengths above 200 eV was estimated by fitting a polynomial of the form given by equation (3.1) to the relative photoabsorption data over 100–200 eV and extrapolating to infinite energy. The relative valence-shell photoabsorption spectrum was then integrated from the first excitation threshold to infinite energy, and the total area was set to an oscillator strength value of 17.57 (see sections 2.1.2 and 3.1.1 for details). Note that the low resolution data (6–200 eV) was extended down to 1.5 eV using the high resolution data (convoluted with a 1 eV fwhm gaussian function) before the above integration procedure, since the high background arising from the “tail” of the main electron beam precludes the measurement of EEL data below 6 eV using the low resolution dipole ( $e,e$ ) spectrometer.

The absolute photoabsorption spectrum (1 eV fwhm) of nitrogen dioxide spanning the valence-shell region from 1.5 to 200 eV is shown in figure 7.1, and the data are given numerically in tables A.16 and A.17 of the appendix. The solid line in panel (b) represents the polynomial curve that has been fitted to the data between 100–200 eV, as discussed above. The discrete structures observed between 1.6–22 eV in panel (a) will be presented and discussed in greater detail in section 7.2.3 below. Also shown for comparison in the continuum region of figure 7.1 are atomic differential oscillator strength sums (or atomic mixture rules (AMR's))

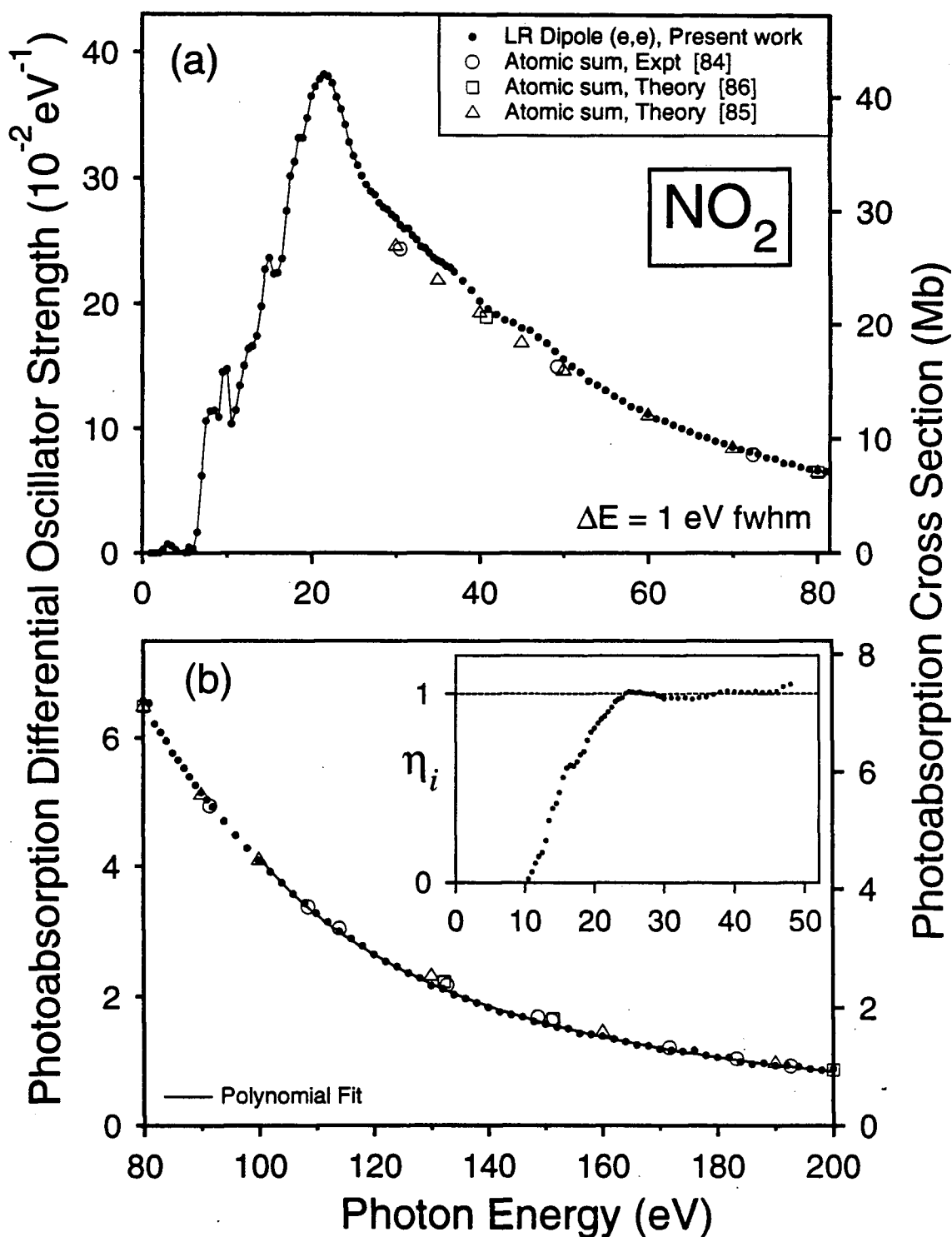


**Figure 7.1:** Absolute differential oscillator strengths for the valence-shell photoabsorption of nitrogen dioxide measured from 1.5 to 200 eV ( $\Delta E = 1 \text{ eV fwhm}$ ). Atomic sums for the constituent atoms (N+O+O) calculated using both experimental [84] and theoretical [85,86] atomic differential oscillator strength values are also shown for comparison in the continuum region. The inset to panel (b) shows the absolute photoionization efficiencies obtained from 10.5 to 50 eV.

determined using the sum of experimental [84] and theoretical [85,86] atomic differential oscillator strengths of the constituent atoms (i.e.,  $df/dE$  (N) + 2 [ $df/dE$  (O)]). It can be seen that there is very good agreement in both shape and magnitude between the present results and the AMR's obtained both from experimental [84] and theoretical [85,86] atomic sums particularly above 50 eV, where molecular effects are expected to become less prominent at higher energies away from near-edge fine structures or continuum resonances. However, it should be noted that although atomic mixture rules are useful in providing rough estimates of differential oscillator strengths for polyatomic molecules in regions where no experimental data exist, in some cases (e.g.,  $\text{PCl}_3$ ) the agreement with experiment is not as good as in the present case of  $\text{NO}_2$ .

In order to critically evaluate the accuracy of the absolute photoabsorption differential oscillator strength scale determined for nitrogen dioxide, the  $S(-2)$  sum rule [28], which is directly related to the static electric-dipole polarizability ( $\alpha_N$ ) for a molecule (see equation (2.29) and section 2.1.2), has again been applied to the present data. In this procedure, the absolute differential oscillator strengths measured over the wide energy range from 1.5 to 200 eV (using the high resolution data below 20 eV and the low resolution data at higher energies) have been used in equation (2.29) to obtain a dipole polarizability of  $29.13 \times 10^{-25} \text{ cm}^3$ . This value is in agreement within 3% with the experimental result of  $30.21 \times 10^{-25} \text{ cm}^3$  reported independently by Williams *et al.* [214] and by Schulz [215] from dielectric constant measurements, and also the value of  $30.25 \times 10^{-25} \text{ cm}^3$  reported earlier in 1933 [216] using the same technique. These findings strongly support the accuracy of the presently determined absolute oscillator strength scale established using the VTRK sum rule and the associated procedures of curve-fitting and extrapolation.

### 7.2.3 Valence-shell spectrum in the discrete region

An overview of the absolute differential oscillator strengths ( $df/dE$ ) for the valence-shell photoabsorption of nitrogen dioxide (1.6–30 eV) obtained in the present work at 0.05 eV resolution is presented in figure 7.2(a) together with the vertical ionization potentials (shown as hatched lines) for the seven outer valence orbitals [212] as given in section 7.2.1. Figure 7.2(b) shows an expanded view of the virtual valence transitions observed between 1.6–6.6 eV, while figure 7.3 illustrates the transitions at higher energies (6.3–22 eV) in greater detail. The discrete photoexcitation spectrum of nitrogen dioxide is very complex, as it is complicated by the open shell structure, vibronic coupling [186], predissociation [3,172,176], and many overlapping vibronic progressions [4,171,172,175]. The assignments given for the virtual valence transitions in figure 7.2(b) have been taken from Gangi and Burnelle [170] and Nakayama *et al.* [3] based on oscillator strength calculations [167,170] and the energy level diagram of NO<sub>2</sub> [202]. The Rydberg assignments for some of the prominent peaks observed in figure 7.3 have been obtained from refs. [4,174,192]. The oscillator strengths ( $f$ ) for band systems corresponding to these transitions between 1.6–22 eV are given in table 7.1.

The broad absorption band centered at 3.12 eV (figure 7.2(b)) has been the subject of many studies [167,170,173,176,181–183,187,188,190,193–204]. The energy level diagram of NO<sub>2</sub> reported by Mulliken [202] indicated that three dipole-allowed transitions can occur in this region:  $6a_1 \leftarrow 4b_2$  ( ${}^2B_2 \leftarrow {}^2A_1$ ),  $2b_1 \leftarrow 6a_1$  ( ${}^2B_1 \leftarrow {}^2A_1$ ), and  $7a_1 \leftarrow 6a_1$  ( ${}^2A_1 \leftarrow {}^2A_1$ ). Based on a rotational analysis of the long vibronic progression, this band was initially assigned to the  ${}^2B_1 \leftarrow {}^2A_1$  transition [176]. This assignment contrasts with that from an earlier semi-empirical calculation [167], which reported an oscillator strength of 0.0001 for the  ${}^2B_1 \leftarrow {}^2A_1$  transition and a much greater value (0.011) for the  ${}^2B_2 \leftarrow {}^2A_1$  transition. A high

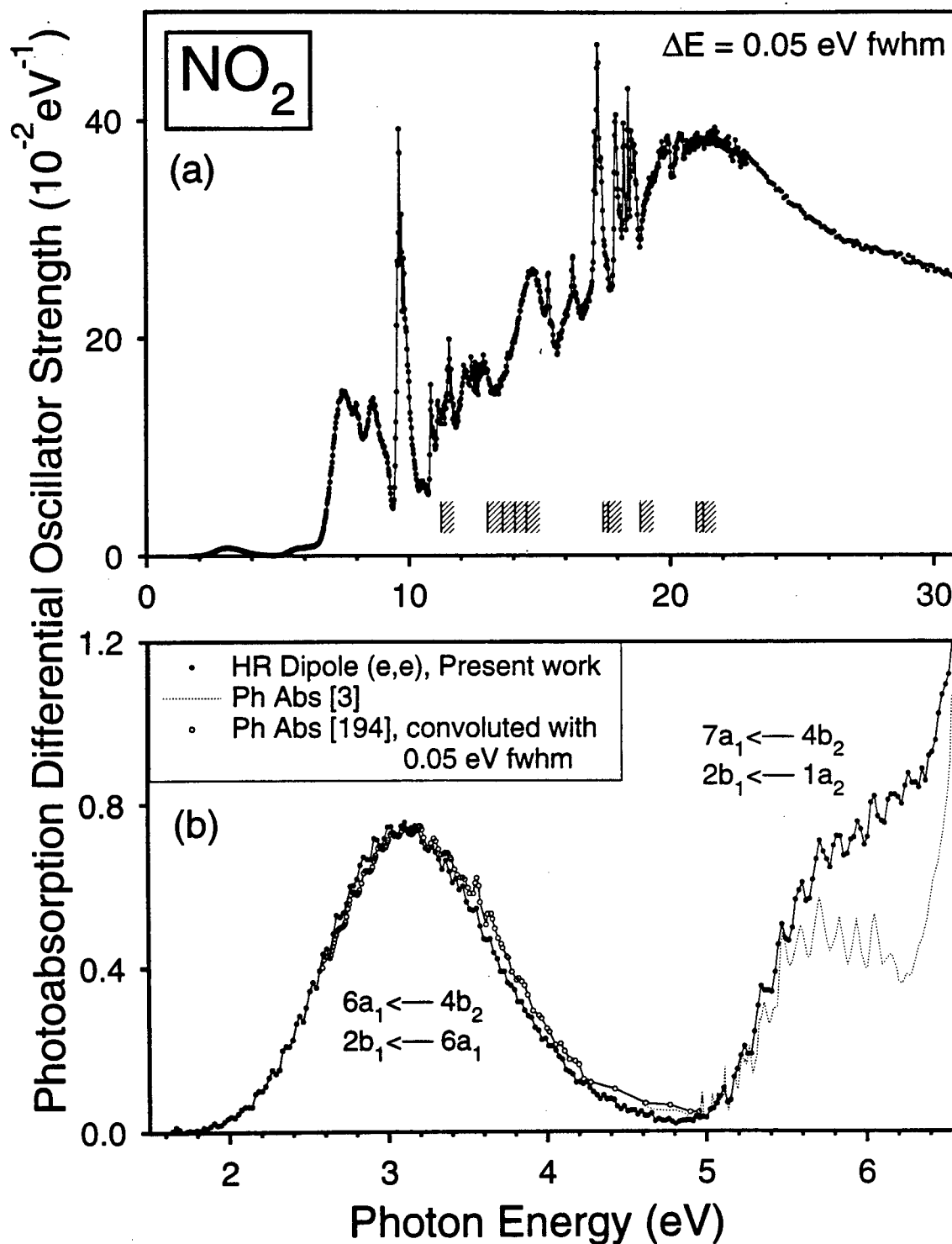


**Figure 7.2:** (a) Absolute photoabsorption differential oscillator strengths for nitrogen dioxide obtained at 0.05 eV resolution from 1.6 to 30 eV. (b) The  ${}^2B_1 \leftarrow {}^2A_1$  and  ${}^2B_2 \leftarrow {}^2A_1$  band systems in the visible and near UV regions (1.6–6.6 eV). Note that absolute photoabsorption cross sections in units of megabarns can be obtained by multiplication of the photoabsorption differential oscillator strength ( $\text{eV}^{-1}$ ) by a factor of 109.75.

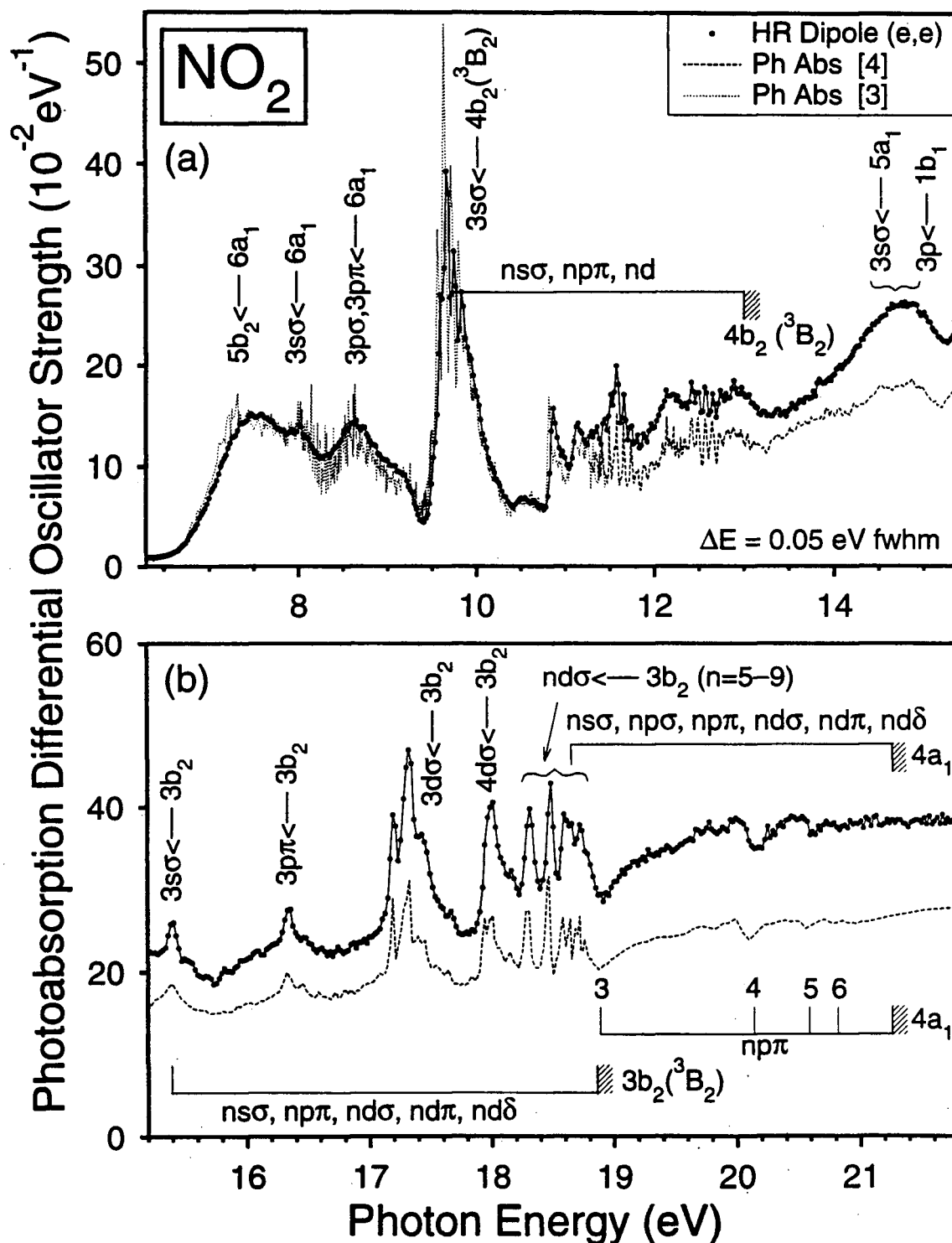


**Figure 7.3:** Discrete features observed in the high resolution (0.05 eV fwhm) valence-shell photoabsorption spectrum of nitrogen dioxide from: (a) 6.3 to 15.4 eV and (b) 15.2 to 21.8 eV. The assignments for some of the prominent profiles have been taken from refs. [3,4,167,174,192] (see text for details). Note that absolute photoabsorption cross sections in units of megabarns can be obtained by multiplication of the photoabsorption differential oscillator strength ( $\text{eV}^{-1}$ ) by a factor of 109.75.

**Table 7.1**

Absolute photoabsorption oscillator strengths ( $f$ ) for discrete regions of the valence-shell spectrum of nitrogen dioxide

Integrated energy region (eV)	Oscillator strength ( $10^{-2}$ )				
	Experiment			Theory	
	Present work	[3]	[4]	[193,194] <sup>1</sup>	[167] [170]
1.58–4.80	0.95			1.0	1.11 2.16
4.80–6.30	0.68	0.47			0.1
6.30–7.85	12.87	13.21			19.2
7.85–8.25	5.02	5.10			
8.25–9.38	12.28	11.34			
9.38–10.38	16.61	19.75			
10.38–10.74	2.32	2.27			
10.74–11.02	3.01	2.82			
11.02–11.24	2.70	2.47			
11.24–11.82	8.34		5.67		
11.82–13.27	23.31		17.29		
13.27–15.72	51.95		38.92		
15.72–16.66	21.71		15.87		
16.66–17.74	31.28		22.15		
17.74–18.21	14.60		10.23		
18.21–18.38	5.91		39.02		
18.38–18.53	5.20		3.56		
18.53–18.65	4.72		3.10		
18.65–18.89	7.88		5.16		
18.89–20.12	43.01		29.67		
20.12–20.59	17.70		11.98		
20.59–20.81	8.08		5.67		
20.81–22.00	45.57		32.16		

<sup>1</sup> Estimated in ref. [217].

order *ab initio* calculation [170] later supported the semi-empirical results [167], and oscillator strengths of 0.004924, 0.01670, and 0 for production of the  ${}^2B_1$  (1.75 eV),  ${}^2B_2$  (3.33 eV), and  ${}^2A_1$  states, respectively, were obtained. In view of this, the authors [170] attributed both the  ${}^2B_1 \leftarrow {}^2A_1$  and  ${}^2B_2 \leftarrow {}^2A_1$  transitions to the broad band, with the  ${}^2B_2$  state having a greater contribution to the photoabsorption. In the present work, an oscillator strength of 0.0095 has been obtained for this band (integrated over 1.58–4.80 eV). This value is in good agreement with the calculated value reported by McEwen (0.0111) [167] and the experimental value of  $\sim 0.010$  (estimated in ref. [217] based on the absorption coefficients measured by Dixon [193] from 1.8 to 2.5 eV and by Hall and Blacet [194] from 2.5 to 4.8 eV). The long vibronic progression observed in this region has been determined to have an average spacing of  $\sim 880 \text{ cm}^{-1}$  (0.11 eV) [176,182], corresponding to the  $\nu_2$  bending mode.

The next absorption band at  $\sim 5.8$  eV (figure 7.2(b)) has been attributed to the  $7a_1 \leftarrow 4b_2$  ( ${}^2B_2 \leftarrow {}^2A_1$ ) and  $2b_1 \leftarrow 1a_2$  ( ${}^2B_2 \leftarrow {}^2A_1$ ) transitions [3,172,203] based on Mulliken's energy-level diagram of nitrogen dioxide [202]. A multi-reference configuration interaction treatment [168] calculated a vertical excitation energy of 5.51 eV for the  $2b_1 \leftarrow 1a_2$  transitions, but no value was given for the other excitation. The series of twelve vibronic bands presently observed in this region from 4.80 to 6.30 eV has average spacings of  $\sim 0.12$  eV ( $940 \text{ cm}^{-1}$ ), which is in good agreement with the work of Nakayama *et al.* [3]. However, the oscillator strength of 0.0068 presently obtained for this region (see table 7.1) is 45% higher than that of 0.0047 reported by Nakayama *et al.* [3]. This is reflected by the rise in the differential oscillator strengths between 5.81–6.30 eV (figure 7.2(b)) which indicates the presence of an additional transition at  $\sim 6.1$  eV not observed in the optical study.

The much stronger series of absorption bands from 6.3 to 9.4 eV (figure 7.3(a)) results from excitations of the unpaired electron in the  $6a_1$  orbital to the  $5b_2$  virtual valence [167,3] and the  $3s\sigma$ ,  $3p\sigma$ , and  $3p\pi$  Rydberg [4,174,177,192] orbitals.

Nakayama *et al.* [3] suggested that the broad band centered at 7.55 eV is attributed to the  $5b_2 \leftarrow 6a_1$  ( ${}^2B_2 \leftarrow {}^2A_1$ ) transition, and this is supported by the quite reasonable agreement between the oscillator strength (see table 7.1) determined by theory (0.192) [167] and by experiment both in the present study (0.1287) and in ref. [3] (0.1321). The diffuse vibronic structures characteristic of this absorption band have previously been analyzed in a high resolution photographic study [172] and assigned to two progressions having frequency intervals of 930 and 540  $\text{cm}^{-1}$ . The peaks at 8.0 and 8.6 eV have been determined to arise from the  $3s\sigma \leftarrow 6a_1$  and  $(3p\sigma, 3p\pi) \leftarrow 6a_1$  Rydberg transitions, respectively [4,174,192]. The vibronic structures have also been identified, and these can be found in refs. [4,174,192]. Table 7.1 lists the absolute oscillator strengths corresponding to these excitations, and it can be seen that there is good agreement between the present work and the data of Nakayama *et al.* [3].

The photoabsorption spectrum of nitrogen dioxide from 9.4 to 21 eV is characterized by overlapping vibronic progressions of many Rydberg series [3,4,177,184,185]. Some of the prominent structures shown in figure 7.3 have been labeled based on the assignments for the absolute spectrum reported in ref. [4]. It can be seen that the energy positions of the observed profiles, including many of the vibronic progressions, are in good agreement with those of the only available absolute optical data [3,4]. One of the interesting features characteristic of  $\text{NO}_2$  photoabsorption is the series of window resonances (i.e., dips in the differential oscillator strengths) situated at 18.89, 20.14, 20.59, and 20.82 eV in the ionization continuum (see figure 7.3(b)), which arise from the  $np\pi \leftarrow 4a_1$  Rydberg transitions where  $n = 3-6$  [4]. In contrast to the other spectral features, photoexcitation to these Rydberg states caused the differential oscillator strengths to decrease in intensity due to destructive interference with the underlying  $3b_2^{-1}$  ionization continuum.

In general, the shape of the dipole ( $e,e$ ) spectrum matches well with those of

the optical data [3,4,194], but the magnitudes of the absolute cross sections reported by Morioka *et al.* [4] are systematically 30% lower than the present measurements. The higher resolution measurements of Nakayama *et al.* [3] are in good quantitative agreement with the present work except in the narrow region at higher energy (11.2–11.5 eV), where the cross sections overlap with those of Morioka *et al.* [4]. This difference may be attributed to problems and difficulties associated with accurate path length and target density determinations required in Beer-Lambert law photoabsorption. Moreover, the data obtained by monochromated synchrotron radiation [4] can also be susceptible to higher order radiation and stray light. In contrast, such problems are avoided in the determination of absolute cross sections using the dipole ( $e,e$ ) method [5], and the accuracy of the presently obtained data for NO<sub>2</sub> has been confirmed using the S(-2) sum rule (see section 7.2.2).

The broad structures observed between ~35–50 eV in the ionization continuum (see figure 7.1(a)) most likely arise from ionization processes associated with the two inner valence orbitals ( $2b_2$  and  $3a_1$ ), since the many-body poles for these processes are predicted to extend between 36–45 eV [213].

## 7.2.4 Molecular and dissociative photoionization

Valence-shell time-of-flight (TOF) mass spectra of nitrogen dioxide have been collected using dipole ( $e,e+\text{ion}$ ) coincidence spectroscopy as a function of equivalent photon energy from 10.5 to 80 eV ( $\Delta E = 1$  eV fwhm). Figure 7.4 shows a typical TOF mass spectrum recorded at 50 eV. A small amount of oxygen impurity was detected, as shown by the presence of an O<sub>2</sub><sup>+</sup> peak in the mass spectra which first appears at 13.0 eV (the VIP of molecular oxygen), which is 3.6 eV below the lowest calculated thermodynamic threshold for formation of O<sub>2</sub><sup>+</sup> from NO<sub>2</sub> (see table 7.2). Using the absolute partial photoionization differential oscillator strengths (PPOS) for the

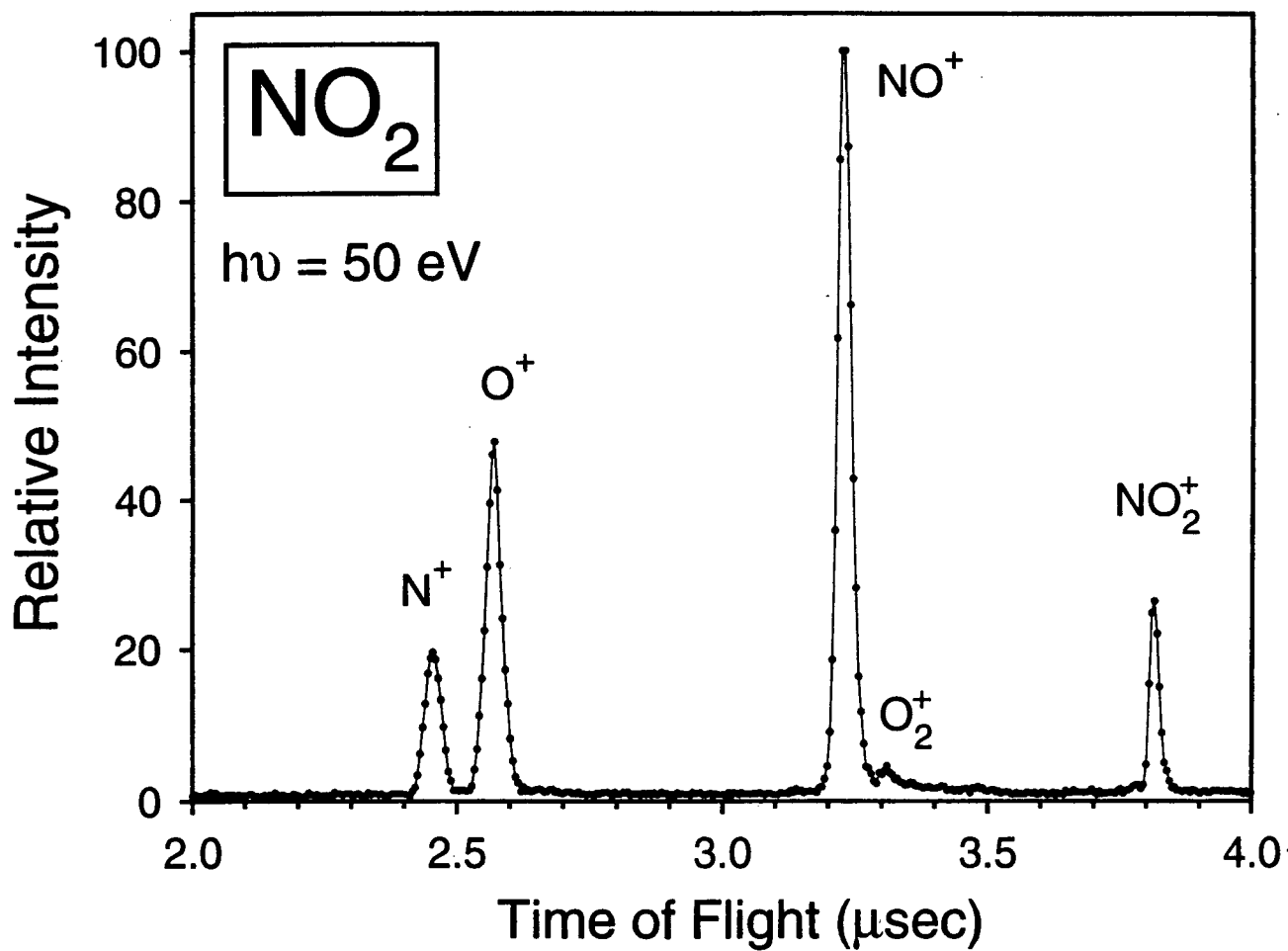


Figure 7.4: TOF mass spectrum of nitrogen dioxide recorded at 50 eV.

**Table 7.2**  
 Calculated and measured appearance potentials for the production of  
 positive ions from nitrogen dioxide

Process	Appearance potential (eV)						
	Calc. <sup>1</sup>	Experimental					
		This work ( $\pm 1$ eV)	PIMS		Electron impact		
		[207]	[206]	[209]	[208]	[210]	
NO <sub>2</sub> <sup>+</sup>	9.8	11.0 20.5 ~44	9.75	11.3 $\pm$ 0.4 20.0 $\pm$ 0.3	10.3	13.98 $\pm$ 0.12	10.4 $\pm$ 0.3
O <sub>2</sub> <sup>+</sup> + N	16.6	(13.0) <sup>2</sup> ~18					
NO <sup>+</sup> + O <sup>-</sup>	11.0	11.0		11.3 $\pm$ 0.4		10.1 $\pm$ 0.2	
NO <sup>+</sup> + O	12.4	13.0 16.5 ~44	12.34 13.01	12.5 $\pm$ 0.1 15.3 $\pm$ 0.4 16.5 $\pm$ 0.2 17.7 $\pm$ 0.3 20.3 $\pm$ 0.3	13.01		
O <sup>+</sup> + NO	16.8	17.0 18	16.82 18.82	17.6 $\pm$ 0.2 20.5 $\pm$ 0.2	16.82		
O <sup>+</sup> + N + O	23.3	31					
N <sup>+</sup> + O <sub>2</sub>	19.1	21.5			21.2		
N <sup>+</sup> + O + O	24.3	26.0 ~44					
NO <sub>2</sub> <sup>2+</sup>							35.0 $\pm$ 0.5

<sup>1</sup> Calculated using thermochemical data from ref. [67] assuming zero kinetic energy of fragmentation.

<sup>2</sup> O<sub>2</sub><sup>+</sup> formation from O<sub>2</sub> impurity (see text in section 7.2.4).

production of  $O_2^+$  and  $O^+$  from oxygen [2], corrections have presently been made to the branching ratios and PPOS for the production of  $O_2^+$  and  $O^+$  from nitrogen dioxide. Five stable positive ions are formed from the molecular and dissociative photoionization of nitrogen dioxide:  $NO_2^+$ ,  $O_2^+$ ,  $NO^+$ ,  $O^+$ , and  $N^+$ . The widths of the  $NO^+$ ,  $O^+$ , and  $N^+$  ion peaks are considerably larger than those of the other peaks in the spectrum obtained at 50 eV (figure 7.4), and this indicates that they are produced with significant kinetic energy of fragmentation either from direct dissociative photoionization or from Coulomb explosion of multiply charged ions. In particular, an examination of the TOF spectra shows that the  $NO^+$ ,  $O^+$ , and  $N^+$  peaks are fairly narrow when first formed but begin to broaden at 13, 20, and 28 eV, respectively. The  $NO^+$  ion peak reaches its maximum width at ~47 eV, while the  $O^+$  and  $N^+$  peaks continue to broaden up to 80 eV.

The photoion branching ratios as determined from the TOF mass spectra for  $NO_2$  are shown in figure 7.5. As the molecular ion decreases in abundance above 14 eV,  $NO^+$  becomes the dominant ion, making up 40–75 % of all the stable cations produced from  $NO_2$  from 14 to 80 eV. In contrast, the  $O_2^+$  ion is produced in very low abundance (~ 1 %). Above 30 eV the  $O^+$  ion gradually increases in relative intensity from 16% up to 35% at 80 eV, while the  $NO^+$  abundance correspondingly decreases in this region. The  $N^+$  photoion branching ratio also shows significant increases up to 38 eV but remains constant between 38–50 eV.

Relative photoionization efficiencies for  $NO_2$  were obtained by taking the ratio of the total coincidence ion signal to the number of forward scattered electrons as a function of energy loss (i.e., equivalent photon energy). The data become essentially constant above 24.5 eV, and assuming that the photoionization efficiency ( $\eta_i$ ) is unity at high energies, the  $\eta_i$  values at 24.5 eV and above have been normalized to one. The absolute photoionization efficiencies from 10.5 to 50 eV are shown in the inset to figure 7.1(b) and are given numerically in the last column of

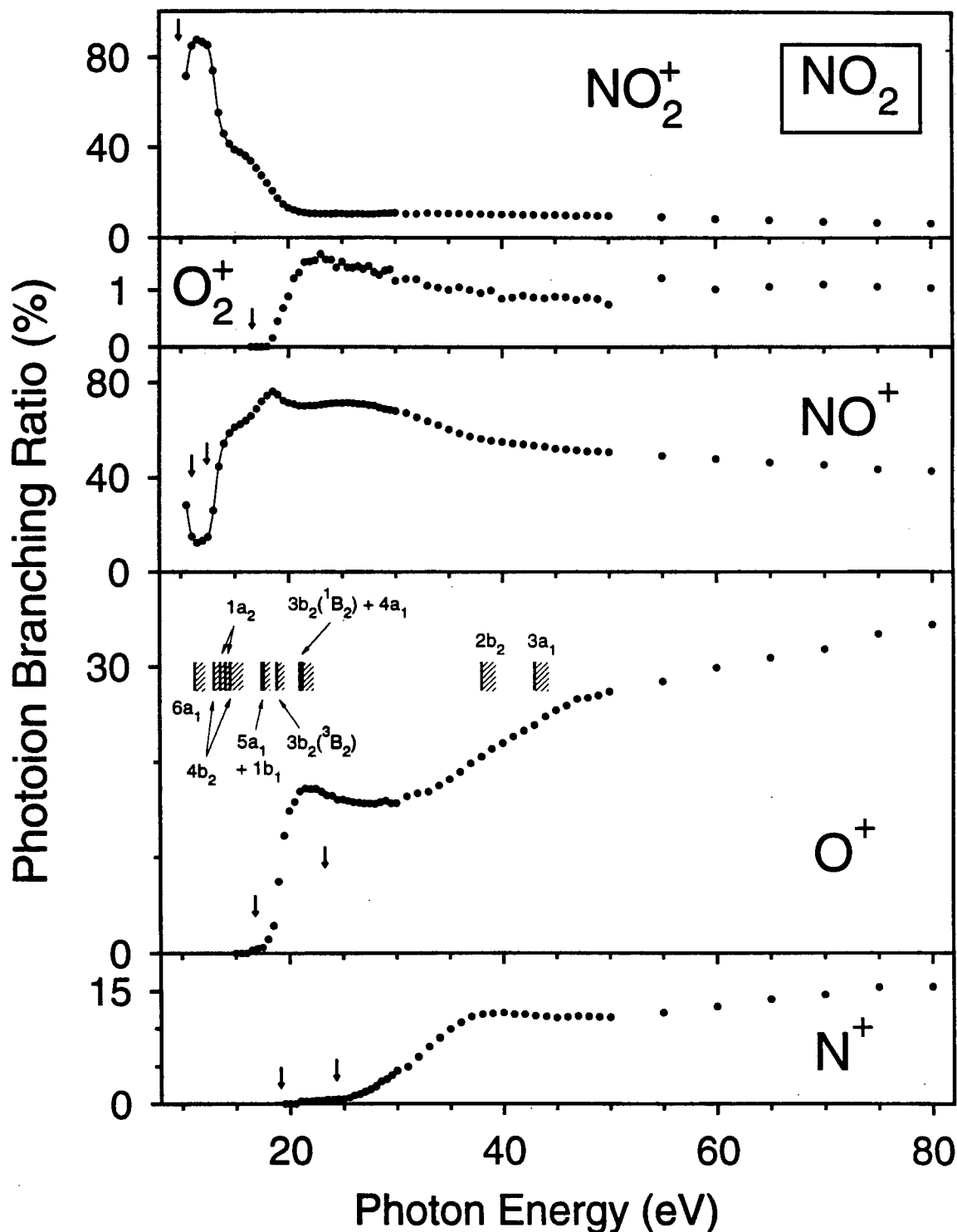


**Figure 7.5:** Photoion branching ratios for the molecular and dissociative photoionization of nitrogen dioxide ( $\Delta E = 1$  eV fwhm). The positions of the vertical ionization potentials for the seven outer valence orbitals [212] and the dominant poles for the two inner valence ionization processes [213] given in section 7.2.1 are denoted by the hatched lies, while the vertical arrows represent the calculated thermodynamic appearance potentials [67] given in table 7.2.

table A.16. Changes in the slope of the  $\eta_i$  curve are observed to occur at 13, 15, 17.5, and 20 eV, corresponding to shoulders and peaks in the low resolution total photoabsorption spectrum (see figure 7.1(a) and section 7.2.2). Details of the excited states can be found in section 7.2.3 and figure 7.3.

Absolute partial photoionization differential oscillator strengths (PPOS) for the production of the molecular and dissociative ions from nitrogen dioxide were obtained by multiplying the absolute photoabsorption differential oscillator strengths in figure 7.1 by the photoionization efficiency and the branching ratio for each ion, as a function of photon energy. These data are plotted in figure 7.6 and tabulated in table A.16. The hatched lines in figure 7.6 represent the vertical ionization potentials of the seven outer-valence orbitals determined from PES [212] and the dominant poles calculated for the inner valence ionization processes [213].

The appearance potentials (AP's) of the five cations measured in the present work are given in table 7.2 together with values from previously published experimental work [206–210] and values calculated from enthalpies of formation of ions and neutrals [67], assuming zero kinetic energy of fragmentation. The calculated values are denoted by vertical arrows in figures 7.5 and 7.6. The present appearance potential results for  $\text{NO}_2^+$ ,  $\text{NO}^+$ ,  $\text{O}^+$ , and  $\text{N}^+$  are in good agreement with the previously reported values obtained from PIMS [206,207] and electron impact [208–210] threshold studies within experimental uncertainty. Note that the  $\text{N}^+$  ion was observed in ref. [207], but its abundance was too low to permit an accurate threshold determination. The  $\text{O}_2^+$  ion detected in the present work at an appearance potential of 13 eV must be due to an impurity from molecular oxygen in the sample, since the thermodynamic threshold calculated for the  $\text{NO}_2 \rightarrow \text{O}_2^+ + \text{N}$  process is 16.6 eV. However, the present PPOS data for  $\text{O}_2^+$  clearly showed another AP at 18 eV. After corrections have been made for the contribution of  $\text{O}_2^+$  from oxygen [2], the resulting  $\text{O}_2^+$  PPOS curve (figure 7.6) indicates that a very small amount of this ion

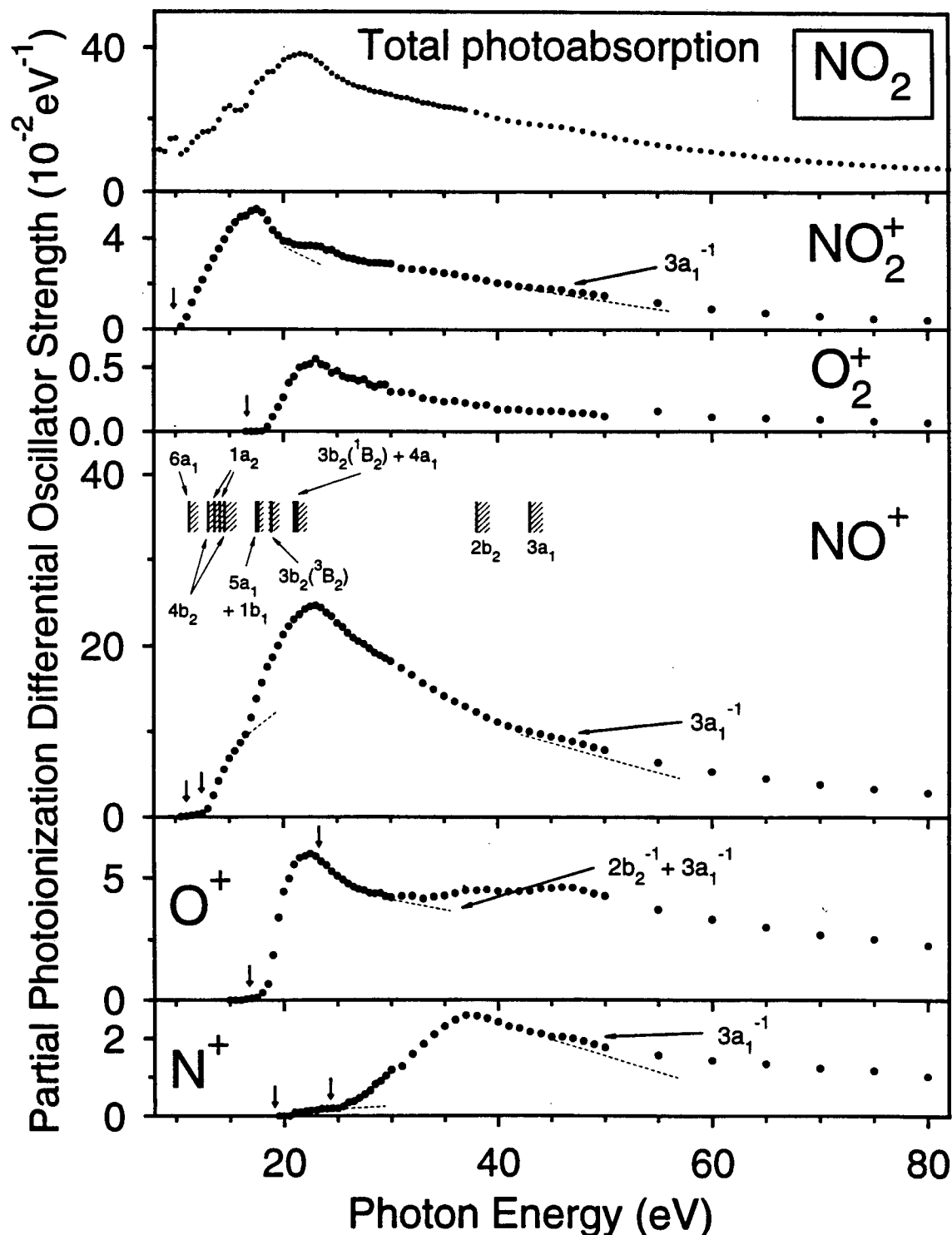


**Figure 7.6:** Absolute partial photoionization differential oscillator strengths for the valence-shell molecular and dissociative photoionization of nitrogen dioxide from 10.5 to 80 eV ( $\Delta E = 1$  eV fwhm). The positions of the vertical ionization potentials for the seven outer valence orbitals [212] and the dominant poles for the two inner valence ionization processes [213] given in section 7.2.1 are denoted by the hatched lines, while the vertical arrows represent the calculated thermodynamic appearance potentials [67] given in table 7.2.

is produced from nitrogen dioxide. This is supported by the work of Hodges *et al.* [211], which reported the presence of  $\text{O}_2^+$  at 16 eV in a multiphoton ionization experiment on  $\text{NO}_2$ . In a low energy electron scattering cross section study, Stephan *et al.* [210] detected the  $\text{NO}_2^{2+}$  dication in significant yield from 35 to 180 eV, but no ion peak at a  $m/e$  ratio of 23 is observed in any of the TOF mass spectra recorded in the present work (see for example, figure 7.4), where the flight times are even shorter than those in ref. [210]. The reason for this difference is not understood.

## 7.2.5 Dipole-induced breakdown

Fragmentation ratios for molecular and dissociative photoionization from any particular electronic ion state of a molecule should be constant at photon energies above the upper limit of the Franck-Condon region [39]. Using this model the absolute PPOS for the production of each cation from nitrogen dioxide can be expressed as a linear combination of PPOS for the production of electronic ion states, neglecting any contributions from autoionization processes and multiple ionization [39]. In the present work, some qualitative information concerning the dipole-induced breakdown of  $\text{NO}_2$  have been deduced from a careful consideration of the absolute PPOS for the molecular and fragment ions formed from  $\text{NO}_2$  (figure 7.6) together with the measured and calculated appearance potentials (table 7.2), vertical ionization potentials and Franck-Condon widths of the electronic ion states [212], and calculated pole strengths for the inner valence ionization processes [213] reported in the literature.

The  $\text{NO}_2^+$  molecular ion is first observed at 10.5 eV in the present work (figure 7.6). Correction for the 1 eV width of the electron beam used in this study yields an appearance potential of  $11.0 \pm 1$  eV, consistent with the vertical ionization potentials

of 11.23 [212] and 11.22 eV [177] obtained by high resolution PES. The AP's reported by Weessler *et al.* [206] and by two of the electron impact studies [209,210] (see table 7.2) are also in agreement with the present value within experimental uncertainty. The lower appearance potential observed by Dibeler *et al.* [207] corresponds to the adiabatic ionization potential of 9.75 eV in the photoelectron spectrum [212]. Additional onsets present in ref. [206] from 12.5 to 20.0 eV (not resolved in the present measurements) indicate contributions from the  $4b_2^{-1}$  ( $^3,^1B_2$ ),  $5a_1^{-1}$  ( $^3A_1$ ), and  $1b_1^{-1}$  ( $^3B_1$ ) states. The  $NO_2^+$  partial differential oscillator strengths in figure 7.6 also have a distinct onset at 20.5 eV, suggesting further contributions from the  $3b_2^{-1}$  ( $^3,^1B_2$ ) and/or  $4a_1^{-1}$  ( $^3A_1$ ) states based on the Franck-Condon widths of these peaks in the He (II) PE spectrum [212]. The  $NO_2^+$  PPOS curve also shows some indication of a higher onset at ~44 eV, and this may be attributed to some  $NO_2^+$  being formed from the  $3a_1^{-1}$  ( $^3,^1A_1$ ) inner valence ionization process.

The appearance potential of the  $O_2^+$  cation at 18 eV suggests an initial contribution from the  $3b_2^{-1}$  ( $^3B_2$ ) triplet state. At higher energies, the  $3b_2^{-1}$  ( $^1B_2$ ) and/or  $4a_1^{-1}$  ( $^3A_1$ ) states may also contribute to the production of  $O_2^+$  ions.

The first AP of the  $NO^+$  cation at 11 eV corresponds to the calculated thermodynamic threshold of the  $NO^+ + O^-$  ion pair formation. Since this process originates from dissociation of a neutral state of  $NO_2$ ,  $NO^+$  in this region could not have been produced from the  $6a_1^{-1}$  state. The thermodynamic threshold calculated for the  $NO_2 \rightarrow NO^+ + O$  process (12.4 eV) instead corresponds to the steep rise in the  $NO^+$  PPOS at 13 eV, which clearly indicates a contribution from the  $4b_2^{-1}$  ( $^3B_2$ ) and/or  $1a_2^{-1}$  ( $^3,^1A_2$ ) states. Another change in the slope of the PPOS curve at 16.5 eV suggests a further major contribution to the formation of  $NO^+$  from the  $5a_1^{-1}$  ( $^3A_1$ ), and  $1b_1^{-1}$  ( $^3B_1$ ) states. Similar to the situation in  $NO_2^+$ , the onset at ~44 eV can be attributed to higher energy formation from the  $3a_1^{-1}$  ( $^3,^1A_1$ ) inner valence ionization process.

The appearance potentials of the  $O^+$  cation at 17 and 18 eV lie within the Franck-Condon region of the  $5a_1^{-1}$  ( $^3A_1$ ), and  $1b_1^{-1}$  ( $^3B_1$ ) states, suggesting an initial dominant contribution from these processes. Above 31 eV, the structures and increases in the  $O^+$  partial differential oscillator strength curve fall within the series of poles calculated for the two inner-valence processes ( $2b_2^{-1}$  and  $3a_1^{-1}$ ) [213]. Therefore, it can be concluded that dissociative ionization in the inner valence region must contribute significantly to the production of  $O^+$ .

The  $N^+$  cation is first produced in very low abundance (figure 7.5) from 21.5 to ~26 eV, after which the photoion branching ratio increases at a much faster rate. Based on threshold considerations, the initial formation of  $N^+$  must come from the  $3b_2^{-1}$  ( $^1B_2$ ) and  $4a_1^{-1}$  ( $^3A_1$ ) processes with the subsequent higher energy formation arising from many-body ion states associated with the  $2b_2^{-1}$  ( $^3,^1B_2$ ) inner valence ionization. Above 44 eV, the small rise in the  $N^+$  PPOS curve (figure 7.6) suggests further contributions from the  $3a_1^{-1}$  ( $^3,^1A_1$ ) state.

More detailed information concerning the ionic photofragmentation breakdown pathways of nitrogen dioxide must await measurements of electronic ion state PPOS using tunable energy PES as well as PEPICO and PIPICO experiments.

## Chapter 8

### Photoabsorption Studies of Freons

#### 8.1 Introduction

Absolute photoabsorption oscillator strength (cross section) data for the single carbon Freons ( $\text{CFCl}_3$ ,  $\text{CF}_2\text{Cl}_2$ ,  $\text{CF}_3\text{Cl}$ , and  $\text{CF}_4$ ) are of considerable interest because of their role in the catalytic decomposition of atmospheric ozone in the stratosphere [29,30]. In this process  $\text{CFCl}_3$  and  $\text{CF}_2\text{Cl}_2$ , which are widely used in industry as aerosols and refrigerants, dissociate by solar UV radiation in the stratosphere to release chlorine atoms. This in turn sets off a chain reaction that results in the net conversion of ozone into oxygen [30]. While  $\text{CF}_4$  (which is used in the plasma etching of semiconductor materials [218,219]) does not contain chlorine atoms, fluorine radicals can similarly breakdown ozone. However,  $\text{CF}_4$  is not as destructive to the ozone layer as the other Freons because the chain-ending reactions involving fluorine radicals with  $\text{CH}_4$  and  $\text{H}_2$  occur much more readily than in the case of chlorine radicals [30]. Nevertheless, the production of the end product HF in the stratosphere is also of much concern.

In view of the importance of quantitative data for the photoexcitation of Freons, these molecules have been investigated by a number of groups, and the valence-shell absolute photoabsorption spectra of  $\text{CFCl}_3$ ,  $\text{CF}_2\text{Cl}_2$ ,  $\text{CF}_3\text{Cl}$ , and  $\text{CF}_4$  reported prior to 1990–1991 have been summarized by Zhang *et al.* in earlier articles [220–223] reporting low resolution dipole ( $e,e$ ) measurements. Since then no additional absolute photoabsorption cross section data have been published in the valence-shell region. This is surprising since large discrepancies for all four Freons

are evident between the various data sets [220–223] with differences of up to 40% in the vicinity of the spectral maximum ( $\sim 20$  eV) in the case of  $\text{CF}_2\text{Cl}_2$  [221].

However, shortly after the publication of the low resolution dipole ( $e,e$ ) photoabsorption measurements for Freons by Zhang *et al.* [220–223], it was discovered that certain types of gases (e.g., acetylene [224], ethylene [225], and silane [226]) seriously affected the emission characteristic of the indirectly heated oxide cathode in the low resolution spectrometer in a pressure-dependent fashion. Oxide cathodes are extremely susceptible to “poisoning” by certain types of compounds, and for such reactive target species, significant errors in the shapes and magnitudes of the measured differential oscillator strengths can occur due to the quarter pressure background subtraction procedures (see section 3.1.1). These background subtraction errors have since been eliminated by installation of an additional stage of differential pumping [44] between the electron gun chamber and the collision chamber shown in figure 3.1. After this modification was installed, the absolute acetylene [224], ethylene [225], and silane [226] have been remeasured, and the accuracy of these new results has been confirmed by the accurate dipole polarizabilities from  $S(-2)$  analyses [28,224–226]. It should be noted that background subtraction errors do not occur in the high resolution dipole ( $e,e$ ) spectrometer since this instrument has a well differentially pumped, directly heated, thoriated tungsten cathode, which is much more stable than the oxide cathode employed in the low resolution spectrometer.

In the course of the present work, large inconsistencies were found between the shapes of the presently measured high resolution dipole ( $e,e$ ) spectra (see section 8.2.3 below) and those of the previously published [220–223] low resolution spectra for  $\text{CFCl}_3$ ,  $\text{CF}_2\text{Cl}_2$ ,  $\text{CF}_3\text{Cl}$ , and  $\text{CF}_4$ . In view of the above considerations, this strongly suggested that halogen-containing molecules such as the Freons were also possibly reacting with the oxide cathodes, resulting in incorrect background

subtraction. In such circumstances, erroneous oscillator strength distributions would be obtained and incorrect absolute scales would result from the VTRK sum rule [27] normalization. The existence of serious errors in the earlier reported low resolution spectra of the Freons [220–223] is confirmed by the unacceptably low values of the static dipole polarizabilities (see table 8.1 below) obtained by applying the S(-2) sum rule (equation 2.29) [28] to the photoabsorption data of Zhang *et al.* [220–223].

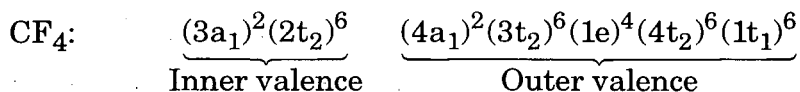
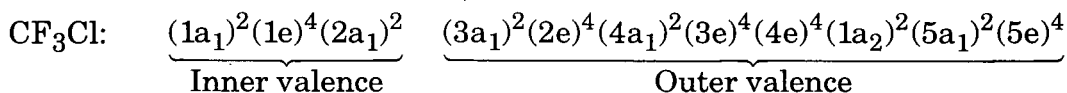
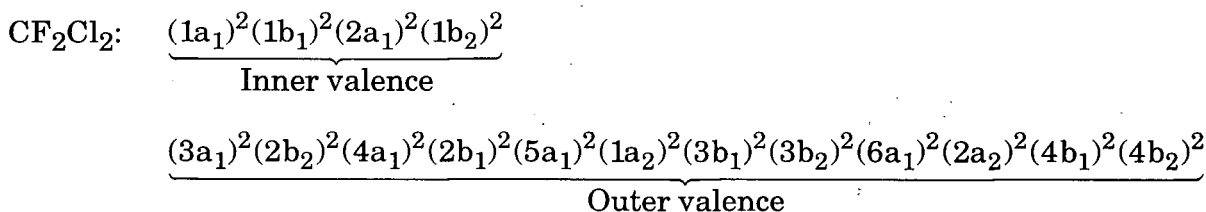
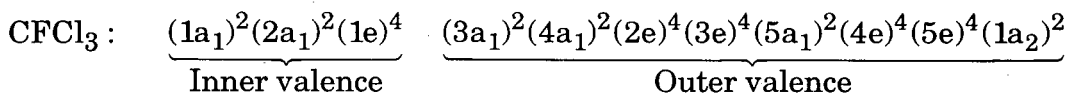
In the present work, new measurements of the absolute valence-shell photoabsorption spectra of  $\text{CFCl}_3$ ,  $\text{CF}_2\text{Cl}_2$ ,  $\text{CF}_3\text{Cl}$ , and  $\text{CF}_4$  have been measured using both high resolution dipole ( $e,e$ ) spectroscopy from 5 to 60 eV (0.05 eV fwhm) and low resolution dipole ( $e,e$ ) spectroscopy from 5 to 200 eV (1 eV fwhm). The long range data spanning the valence-shell region (5–200 eV) up to the Cl  $2p$  ionization edge (~200 eV) have been remeasured for the four Freon molecules at 1 eV fwhm resolution using the improved differential pumping in the dipole ( $e,e$ ) spectrometer [44]. The absolute differential oscillator strength scales have been determined for the long range low resolution spectra using the valence-shell Thomas-Reiche-Kuhn (VTRK) sum-rule. The accuracy of the absolute differential oscillator strength scales has been investigated by comparing the results of the S(-2) sum rule analysis of the differential oscillator strength spectra with accurate literature values of the respective dipole polarizabilities.

## 8.2 Results and Discussions

### 8.2.1 Electronic structures

The photoabsorption spectra of  $\text{CFCl}_3$  ( $C_{3v}$ ),  $\text{CF}_2\text{Cl}_2$  ( $C_{2v}$ ),  $\text{CF}_3\text{Cl}$  ( $C_{3v}$ ), and  $\text{CF}_4$  ( $T_d$ ) are conveniently discussed with reference to the electronic ground state

( $^1A_1$ ), valence-shell molecular orbital configurations in the independent particle model as given in refs. [220–223]:



The outer and inner valence vertical ionization potentials (VIP's) have been determined for the above molecules by He (I) and He (II) photoelectron spectroscopy [227,228], synchrotron radiation [229,230], and X-ray photoelectron spectroscopy [231]. Note that each of the inner-valence ionization processes are expected to be split into a range of many-body photoelectron states [232].

### 8.2.2 Long range photoabsorption spectra

The long range absolute photoabsorption spectra obtained in the present work for  $\text{CFCl}_3$ ,  $\text{CF}_2\text{Cl}_2$ ,  $\text{CF}_3\text{Cl}$ , and  $\text{CF}_4$  from the first excitation threshold up to 200 eV at 1 eV fwhm resolution are shown in figure 8.1 and given numerically in tables A.18–A.21 in the appendix. These values can be converted to absolute photoabsorption cross sections using the relation,  $\sigma$  (Mb) = 109.75 x (df/dE) (eV $^{-1}$ ).

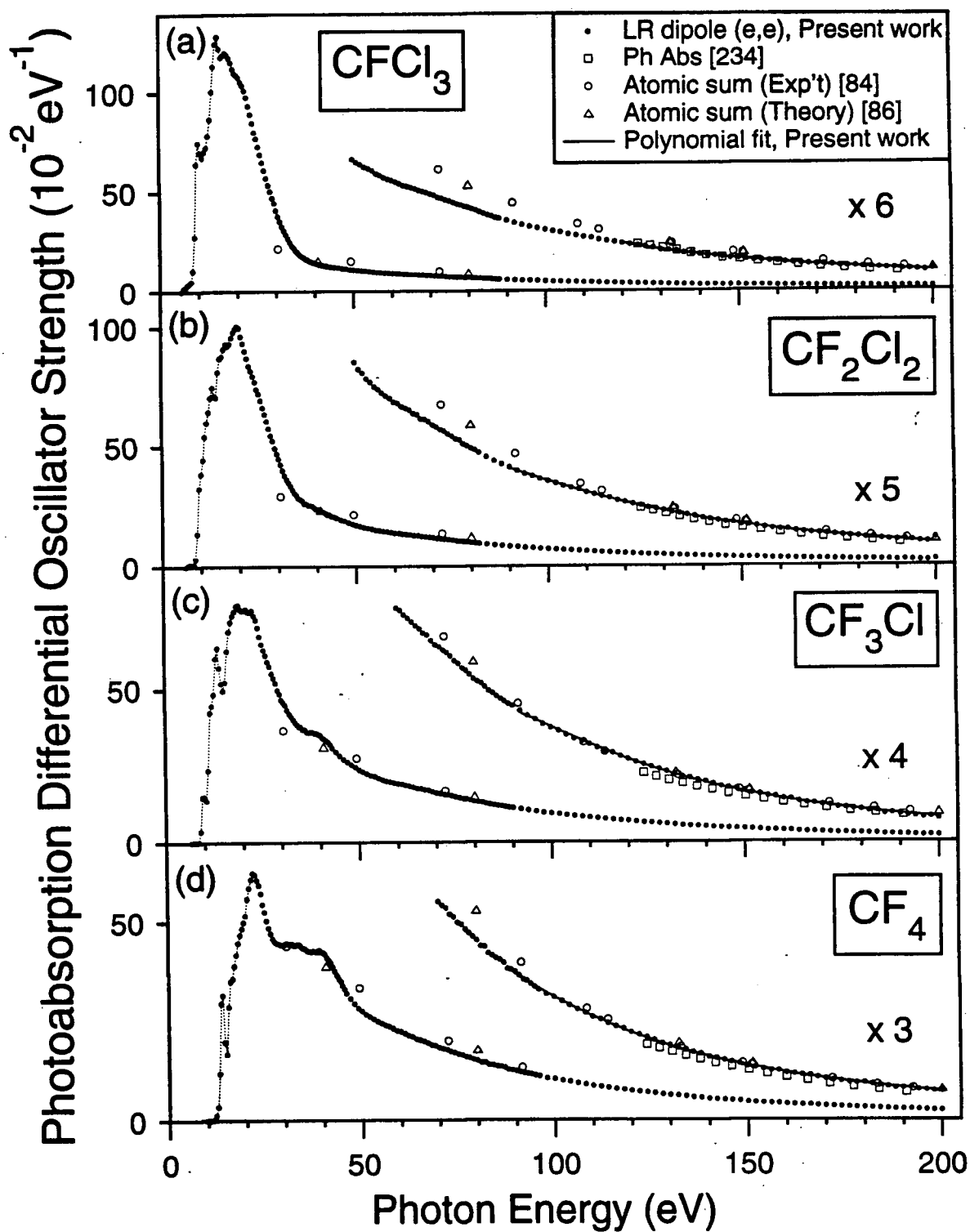


**Figure 8.1:** Absolute differential oscillator strengths (5–200 eV) for the valence-shell photoabsorption of (a)  $\text{CFCl}_3$ , (b)  $\text{CF}_2\text{Cl}_2$ , (c)  $\text{CF}_3\text{Cl}$ , and (d)  $\text{CF}_4$  obtained at 1 eV fwhm resolution.

The 8000 eV impact energy, low resolution dipole ( $e,e$ ) spectrometer [15,16, 39,45] with the additional differential pumping [44] between the electron gun chamber and the collision chamber was used to obtain background-subtracted, zero degree, EEL spectra (1 eV fwhm) in overlapping regions and normalized to one another to form long range spectra spanning the entire valence-shell region from 5 to 200 eV for each of  $\text{CFCl}_3$ ,  $\text{CF}_2\text{Cl}_2$ ,  $\text{CF}_3\text{Cl}$ , and  $\text{CF}_4$ . The EEL spectra were Bethe-Born converted to relative photoabsorption differential oscillator strength spectra and were then put onto an absolute scale using the VTRK sum-rule (see sections 2.1.2 and 3.1.1 for details). In the latter procedure, the extrapolated portion of the oscillator strengths from 198 eV to infinite energy for  $\text{CFCl}_3$ ,  $\text{CF}_2\text{Cl}_2$ ,  $\text{CF}_3\text{Cl}$ , and  $\text{CF}_4$  make up 12.2, 9.9, 6.6, and 11.4 % of the total area, respectively. The goodness of the least square polynomial fits to the data used in the determination of the absolute oscillator strength scales can be seen in figure 8.1 where the data at high energy have been shown on expanded scales. In contrast to the present work where 7–12 % of the oscillator strengths are found to be in the spectral regions above 198 eV, the curve-fitting and valence-shell extrapolation procedures used for the data in refs. [220–223] set 17–24 % of the oscillator strengths to these regions. Since the total oscillator strengths from the first excitation threshold to infinite energy must equal  $\sim 33.2$  according to the VTRK sum rule (see table 3.1) for each of the isoelectronic Freon molecules, this results in the earlier measurements [220–223] being lower by up to 20% at low photon energies.

The most noticeable difference in the spectra in going from  $\text{CFCl}_3$  to  $\text{CF}_4$  (panels (a) to (d) in figure 8.1) is the decrease in the absolute differential oscillator strength at the spectral maximum from  $1.21 \text{ eV}^{-1}$  in  $\text{CFCl}_3$  to  $0.62 \text{ eV}^{-1}$  in  $\text{CF}_4$ . Given that the valence-shell electron configurations of these molecules are isoelectronic, the distribution of increasing oscillator strengths to low photon energy with increase in the number of chlorine atoms in the molecule is attributed to the

presence of a radial node in the atomic chlorine  $3p$  wavefunction which results in a local (or Cooper) minimum around 40 eV. This effect causes the overall shape of the differential oscillator strengths for the  $3p$  subshell of chlorine to differ significantly from that for the  $2p$  subshell of fluorine [233].

The previously reported absolute photoabsorption cross sections of Cole and Dexter [234] in the valence-shell continuum (124–171 eV) are also shown in figure 8.1. Excellent agreement is observed between these data [234] and those of the present work in the case of  $\text{CFCl}_3$  (figure 8.1(a)). Good agreement in shape is also observed for each of the other Freon molecules (figures 8.1(b), (c), and (d)), with the magnitude of the differential oscillator strengths differing by only ~5 % from the present work.

Figure 8.1 also shows a comparison of the presently measured data with experimental [84] and theoretical [86] atomic differential oscillator strength sums (or atomic mixture rules (AMR's)) for the constituent atoms (e.g.,  $\text{C}+\text{F}+3\text{Cl}$  in the case of  $\text{CFCl}_3$ ). It can be seen that the atomic mixture rules generally provide good estimates at high energy (i.e., above 100 eV). However, at lower photon energy the agreement is not as good, especially in the cases of  $\text{CFCl}_3$  and  $\text{CF}_2\text{Cl}_2$ .

The accuracy of the absolute photoabsorption differential oscillator strengths presently determined for the Freons have been critically evaluated by comparison of the experimental and theoretical static electric-dipole polarizabilities ( $\alpha_N$ ) for the molecule of interest [71,72,235,236] with that derived from the differential oscillator strength data via the  $S(-2)$  sum rule. Using the absolute data presently obtained for the Freons and equation (2.29), electric-dipole polarizabilities of  $81.96 \times 10^{-25}$ ,  $63.94 \times 10^{-25}$ ,  $48.20 \times 10^{-25}$ , and  $28.42 \times 10^{-25} \text{ cm}^3$  have been derived for  $\text{CFCl}_3$ ,  $\text{CF}_2\text{Cl}_2$ ,  $\text{CF}_3\text{Cl}$ , and  $\text{CF}_4$ , respectively. From table 8.1 it can be seen that these values for  $\text{CFCl}_3$ ,  $\text{CF}_2\text{Cl}_2$ ,  $\text{CF}_3\text{Cl}$ , and  $\text{CF}_4$  are in excellent agreement (within 1–2 %) with experimental dipole polarizabilities directly obtained from dielectric constant

Table 8.1

Static electric-dipole polarizability values of  $\text{CFCl}_3$ ,  $\text{CF}_2\text{Cl}_2$ ,  $\text{CF}_3\text{Cl}$ , and  $\text{CF}_4$ 

Freon	Static electric-dipole polarizability ( $10^{-25} \text{ cm}^3$ )						
	Experiment				Calculation		
	From $df/dE$ <sup>1</sup>		From dielectric constants		From refractivity	From additivity	
	This work	Refs. [220–223] <sup>2</sup>	Ref. [71]	Ref. [72]	Ref. [235]	Ref. [72] <sup>3</sup>	Ref. [236] <sup>4</sup>
$\text{CFCl}_3$	81.96	63.27 [222]	82.39			84.44	83.03 87.12
$\text{CF}_2\text{Cl}_2$	63.94	49.46 [221]	63.42			65.01	62.83 68.82
$\text{CF}_3\text{Cl}$	48.20	36.44 [220]				45.20	42.71 50.55
$\text{CF}_4$	28.42	24.07 [223]	28.90	28.23	29.19		23.41 30.44

<sup>1</sup> Using the  $S(-2)$  sum rule (see equation (2.29)).

<sup>2</sup> These earlier  $df/dE$  measurements are clearly in error. See discussion in section 8.1 of the present work and also ref. [28].

<sup>3</sup> Atomic additivity of data tabulated in Landolt-Bornstein (5th ed.), as given in the compilation of Maryott and Buckley [72].

<sup>4</sup> Atomic hybridization: The first value is obtained using the ahp (atomic hybrid polarizability) method, while the second value is determined from the ahc (atomic hybrid component) method.

[71,72] and refractivity [235] measurements. Moreover, there is also quite good agreement for all four molecules with the molecular dipole polarizability values calculated using atomic additivity [72] and atomic hybridization additivity [236]. Two methods were used in the calculation of molecular polarizabilities in the latter procedure: atomic hybrid polarizability (ahp) and atomic hybrid component (ahc). The ahp method generally predicts a lower value than the ahc method, and the dipole polarizabilities derived from the absolute photoabsorption differential oscillator strength data measured in the present work are found to fall between these values. Consequently, the result of this comparison of dipole polarizability values lends further support to the accuracy of the presently determined photoabsorption data. In contrast, the static electric-dipole polarizabilities derived using the earlier dipole ( $e,e$ ) photoabsorption differential oscillator strength data of Zhang *et al.* [220–223] differ from the polarizability values reported in the literature [71,72,235] by ~15 % in the case of  $\text{CF}_4$  and by ~23 % in the cases of  $\text{CFCl}_3$ ,  $\text{CF}_2\text{Cl}_2$ , and  $\text{CF}_3\text{Cl}$ . This further confirms that the original measurements reported by Zhang *et al.* [220–223] are in error. These errors are most significant in  $\text{CFCl}_3$ ,  $\text{CF}_2\text{Cl}_2$ , and  $\text{CF}_3\text{Cl}$ , where one or more chlorine atoms are present in the molecule, indicating that the chlorine atoms in the Freon molecules react more readily with the oxide cathode of the electron gun than the fluorine atoms.

## 8.2.3 Discrete photoabsorption spectra

### 8.2.3.1 $\text{CFCl}_3$

The absolute photoabsorption spectrum of  $\text{CFCl}_3$  (Freon 11) obtained in the present work at a resolution of 0.05 eV fwhm is shown in figure 8.2. Figure 8.2(a) shows an overview of the spectrum from 5 to 60 eV, while figure 8.2(b) presents the

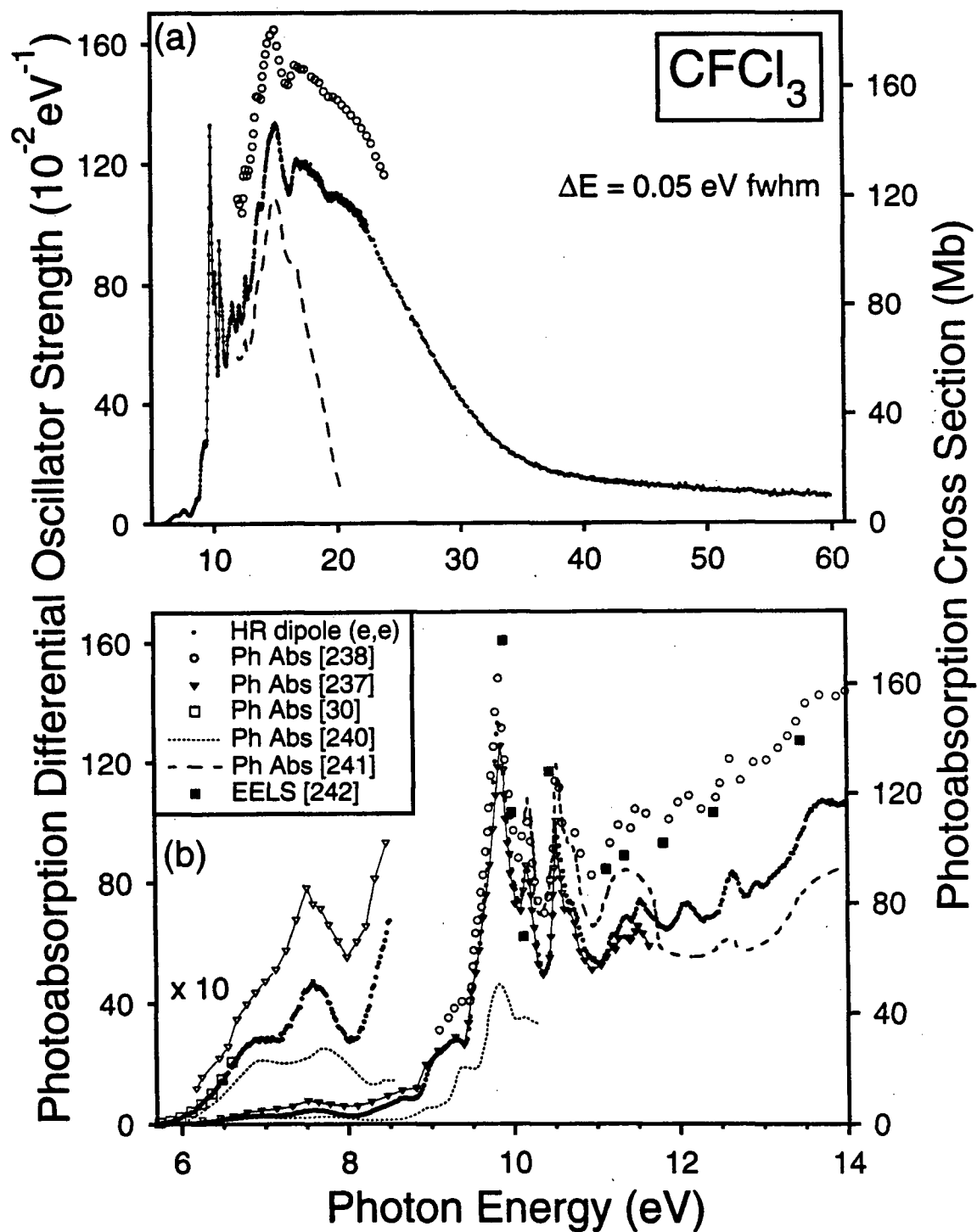


**Figure 8.2:** Absolute differential oscillator strengths ( $df/dE$ ) for the valence-shell photoabsorption of  $\text{CFCl}_3$ : (a) 5–60 eV, (b) 6–14 eV. The high resolution dipole ( $e,e$ ) measurements (0.05 eV fwhm) obtained in the present work are compared with data determined from both photon [30,237,238,240,241] and electron scattering [242] methods.

discrete region (6–14 eV) in greater detail. The energy positions of the observed structures are consistent with those obtained earlier using synchrotron radiation [237,238] and high resolution electron energy-loss spectroscopy [239]. The first two broad bands (6.70 and 7.62 eV) situated in the vicinity of the “ozone window” (~ 5–7 eV) [30] have been attributed to virtual valence transitions associated with electrons originating from the chlorine lone pair orbitals [240]. Ibuki *et al.* [237] assigned the 7.62 eV feature to  $\sigma^* \leftarrow 1a_2$ , but no reference was made to the lower energy transition, which was also observed in the high resolution data [237]. Figure 8.2(b) shows a comparison of the present measurements with data obtained by optical techniques [30,237,240]. There is excellent agreement between the present results and those reported in the limited energy region 5.5–6.7 eV by Rowland and Molina [30]. However, there are large disagreements with the measurements of Ibuki *et al.* [237] and Doucet *et al.* [240] in the 5.5–8.5 eV region.

The spectrum above 8 eV is dominated by Rydberg transitions originating from the chlorine lone pair molecular orbitals [237,239–241]. The assignments of these discrete features have been re-examined by Ibuki *et al.* [237] in 1989. Prior to that several authors [239–241] had proposed similar assessments of the Rydberg transitions up to 17 eV with quantum defects of 1.95, 1.75, and 0.14 for the *ns*, *np*, and *nd* Rydberg series, respectively [239]. The major difference between the two sets of assignments [237,239] is in the originating molecular orbital from which the electron is being excited. For example, King and McConkey attributed the band at 8.69 eV (figure 8.2(b)) to  $4s \leftarrow 1a_2$  [239], while Ibuki *et al.* proposed  $4s \leftarrow 4e$  [237]. The three sharp peaks at 9.83, 10.16, and 10.53 eV were also assigned very differently by the two authors. King and McConkey [239] interpreted these as arising from  $4s \leftarrow 4e$ ,  $4s \leftarrow 5a_1$ , and  $4p \leftarrow 4e$ , respectively, while the more recent work [237] attributed them to  $4p \leftarrow 5e$ ,  $3d \leftarrow 5e$ , and  $4p \leftarrow 4e$ . Unfortunately, since the VIP's for the four lowest molecular orbitals,  $1a_2$  (11.73 eV),  $5e$  (12.13 eV),  $4e$

(12.93 eV), and  $5a_1$  (13.45 eV), [227] are situated so closely to one another, the quantum defects determined by Ibuki *et al.* [237] for the *ns* (2.09), *np* (1.67), and *nd* (0.32) Rydberg series are found to be quite similar to those determined earlier [239], and therefore cannot be used to justify the validity of either set of assignments.

Figure 8.2(b) compares the differential photoabsorption oscillator strengths (cross sections) reported for  $\text{CFCl}_3$  in the literature [30,237,238,240,241,242] with the present measurements, while table 8.2 lists the absolute oscillator strengths for energy regions up to 60 eV. It can be seen from figure 8.2 that the previously published works cover only limited energy ranges. Between 9–11 eV where sharp peaks are observed, only the data of Ibuki *et al.* [237] are in good agreement with the present results. Most of the other measurements [238,239,241,242] are 12–25 % higher than the dipole (*e,e*) data. In contrast, the oscillator strengths reported by Doucet *et al.* [240] are typically 60% lower than the present data, and this difference likely arises from target density errors and/or line saturation effects (i.e., bandwidth /linewidth interactions) occurring in the optical work [240]. Such line saturation effects can occur for narrow, discrete peaks due to the logarithmic transform involved in the Beer-Lambert law used to obtain absolute photoabsorption cross sections [5]. Above 11 eV, the shape of the synchrotron radiation data [238] matches well with the present data, but the absolute values are systematically 35 % higher. In other work, the absolute oscillator strengths for  $\text{CFCl}_3$  reported by King and McConkey [239] in this region using lower impact energy (500 eV) EELS methods are higher but generally within 15% of the present values (see table 8.2), and this difference may be attributed to the fact that the relative spectra obtained by King and McConkey [239] were normalized onto an absolute scale using previously published absolute data [238,241]. Similarly, the EEL based data of Huebner *et al.* [242] also differ from the present measurements by 30–50 %. It should be noted that the variations in the oscillator strengths between the different data sets can be

**Table 8.2**

Absolute photoabsorption oscillator strengths for regions of the high resolution valence-shell spectrum of  $\text{CFCl}_3$

Energy range (eV) <sup>1</sup>	Oscillator strength ( $\times 10^{-2}$ )			
	This work	ref. [239]	ref. [237]	ref. [240]
5.58–7.08	1.84	2.5	2.79	1.25
7.08–8.11	3.71	4.8	6.49	2.22
8.11–8.85	4.66	5.2	6.83	1.31
8.85–9.43	13.44	15.2	14.29	5.54
9.43–10.32	71.17	87.0	68.09	29.51
10.32–11.05	47.77	59.3	46.57	
11.05–11.93	57.84	69.8		
11.93–12.23	21.37	24.3		
12.23–12.82	43.71	52.5		
12.82–16.20	378.54	512		
16.20–19.96	433.76	486		
19.96–36.51	956.24	1045		
36.51–47.00	153.39			
47.00–59.89	148.60			

<sup>1</sup> See figure 8.2.

caused by errors arising from sample pressure and path length measurements [5] and problems with reflection optics and higher order radiation in the optical studies. In electron impact based EELS measurements, non-dipole effects can become significant at higher momentum transfers. In particular, earlier EELS measurements [239,242] utilized relatively low incident electron impact energies (500 eV [239] and 100 eV [242]) and may therefore be complicated by significant contributions from dipole forbidden transitions. The high impact energy and zero degree scattering angle conditions used in the presently employed dipole ( $e,e$ ) spectrometers result in extremely small momentum transfers, and as such, contributions from non-dipole transitions have been found to be either negligible in the case of helium [133] or very small in the case of  $\text{PCl}_3$  (section 5.2.3.3).

### 8.2.3.2 $\text{CF}_2\text{Cl}_2$

The presently obtained absolute photoabsorption spectrum of  $\text{CF}_2\text{Cl}_2$  (Freon 12) at 0.05 eV resolution is shown in figure 8.3. Figure 8.3(a) shows an overview of the entire energy range measured from 6 to 60 eV, while figure 8.3(b) presents an expanded view of the discrete region (6–20 eV). The energy positions of the observed structures are consistent with those reported earlier by direct optical [237,238] and electron scattering [239] techniques.

The first two absorption bands (6.98 and 8.17 eV in figure 8.3(b)) observed in the  $\text{CF}_2\text{Cl}_2$  spectrum are very broad and weak. Similar to the case of  $\text{CFCl}_3$  (see section 8.2.3.1), these bands have been attributed to virtual valence transitions associated with electrons originating from the chlorine lone pair orbitals [240], while a more recent study assigned these to the  $4p \leftarrow 4b_2$  transitions [237]. It can be seen in figure 8.3(b) and table 8.3 that the present measurements of these bands (6–8.5 eV) are in excellent agreement with the data of Rowland and Molina [30].

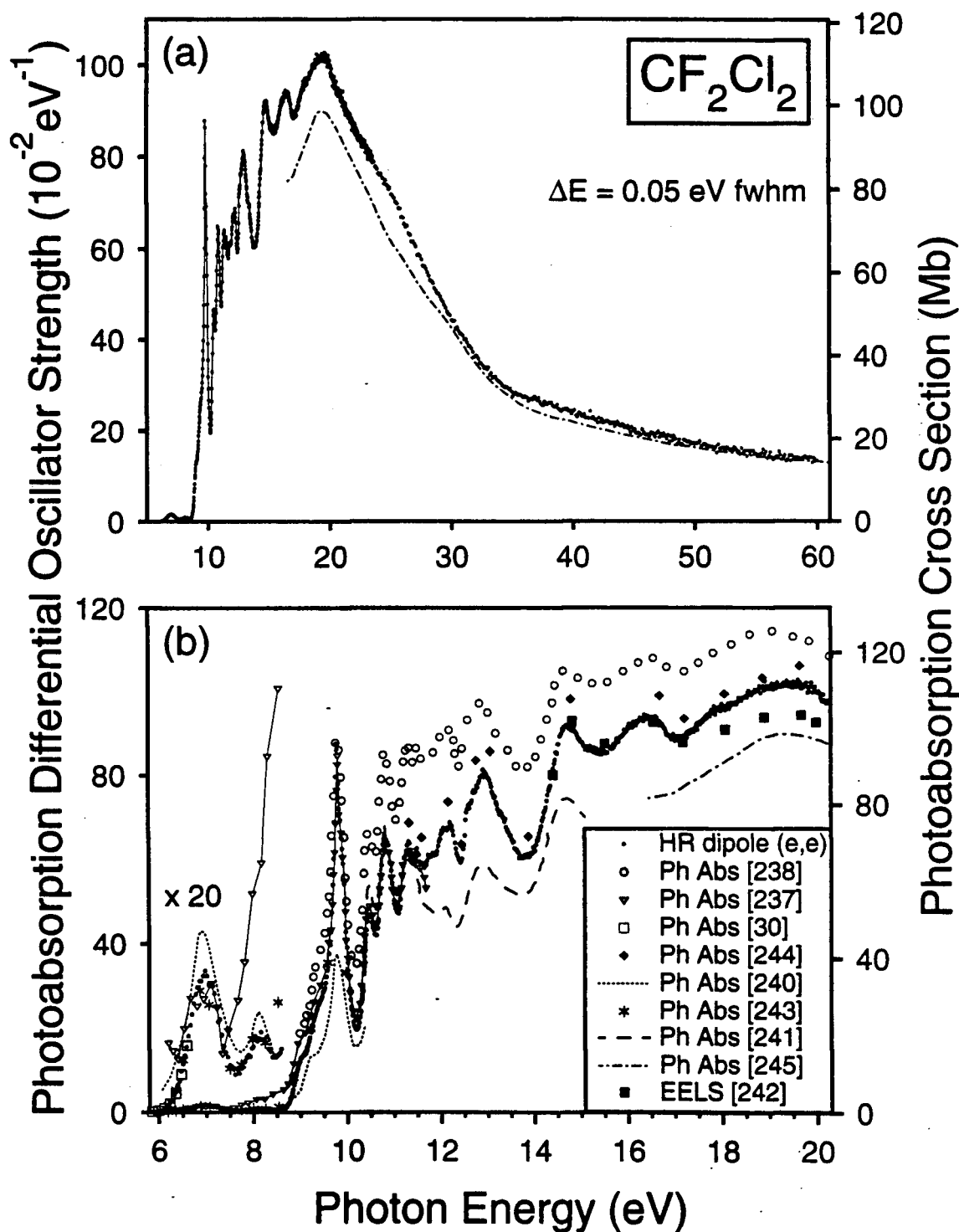


**Figure 8.3:** Absolute differential oscillator strengths ( $df/dE$ ) for the valence-shell photoabsorption of  $\text{CF}_2\text{Cl}_2$ : (a) 6–60 eV, (b) 6–20 eV. The high resolution dipole ( $e,e$ ) measurements (0.05 eV fwhm) obtained in the present work are compared with data determined from both photon [30,237,238,240,241,243–245] and electron scattering [242] methods. The data of Person *et al.* [244] were taken from ref. [239].

**Table 8.3**

Absolute photoabsorption oscillator strengths for regions of the high resolution valence-shell spectrum of  $\text{CF}_2\text{Cl}_2$

Energy range (eV) <sup>1</sup>	Oscillator strength ( $\times 10^{-2}$ )				
	This work	ref. [239]	ref. [237]	ref. [240]	ref. [243]
5.77-7.59	1.32	1.5	1.48	1.86	1.17
7.59-8.53	0.66	0.81	2.72	0.83	0.79
5.85-9.06	2.96	3.6	5.40	1.84	4.44
9.06-9.47	8.38	10.3	10.07	5.12	9.23
9.47-10.18	32.49	35.6	32.91	18.05	
10.18-10.59	14.39	16.5	15.50		
10.59-11.06	25.93	28.8	25.48		
11.06-11.38	17.89	16.5	18.02		
11.38-11.64	15.61	17.4	15.34		
11.64-11.85	12.73	11.6			
11.85-12.38	34.55	37.5			
12.38-13.87	104.26	113.4			
13.87-15.46	130.86	137.8			
15.46-17.13	150.15	157.8			
17.13-20.39	319.48	320.8			
20.39-23.09	237.63	234.7			
23.09-25.67	196.11	188.7			
25.67-28.25	154.39	151.3			
28.25-36.00	291.81	246.6			
36.00-46.04	234.15				
46.04-59.94	223.27				

<sup>1</sup> See figure 8.3.

Reasonably good agreement is also observed with the results in refs. [240,243]. The most notable difference between the various data sets is at the 8.17 eV band reported by Ibuki *et al.* [237] which is more intense than the band at lower energy. In particular, the oscillator strength for the 8.17 eV band reported in ref. [237] (0.0272) is over four times the value (0.0066) obtained in the present work (see table 8.3).

The structures situated in the discrete part of the  $\text{CF}_2\text{Cl}_2$  photoabsorption spectrum above 8.5 eV (figure 8.3(b)) largely arise from transitions to Rydberg orbitals [237,239–241]. Detailed assignments of the profiles up to 19 eV [239,241] have more recently been re-examined by Ibuki *et al.* based on a more highly resolved photoabsorption spectrum [237] together with newer and more accurate PES data [227]. In general, the new assignments [237] are fairly consistent with those of King and McConkey [239] and Gilbert *et al.* [241]. The most notable exception is that for the sharp, high intensity peak at 9.78 eV. Ibuki *et al.* interpreted this feature as  $4p \leftarrow 4b_2$  [237], while King and McConkey proposed  $4s \leftarrow 4a_2$  [239]. An oscillator strength of 0.3249 has presently been determined for this transition, and from table 8.3 it can be seen that it is in very good agreement with those determined by synchrotron radiation (0.3291) [237] and by EELS (0.356) [239]. Similar to the previous case of  $\text{CFCl}_3$ , the much lower oscillator strength reported in ref. [240] (0.1805) must arise from target density errors and/or line saturation effects in the optical work (see section 8.2.3.1). The next three sharp bands at 10.48, 10.84, and 11.31 eV have been attributed to  $4p \leftarrow 4a_2$ ,  $4p \leftarrow 4a_1$ , and  $4s \leftarrow 3b_2$ , respectively [237,239,241]. More detailed assignments of the  $\text{CF}_2\text{Cl}_2$  spectrum up to 19 eV can be found in refs. [237,239]. The absolute oscillator strengths for energy regions up to 60 eV obtained from the present work are given in table 8.3, and these values are generally consistent with those reported by King and McConkey [239] to within 5–10 %. It should be noted that the relative spectra obtained by King and McConkey

[239] were normalized using the previously published absolute data [244]. Between 9–11.5 eV, the present results agree well with those of refs. [237,241], but the data of Gilbert *et al.* [241] becomes 25% lower beyond 11.5 eV. From 11.5 to 20 eV, the shape and magnitude of the presently obtained spectrum match up fairly well with those of refs. [242,244]. Similar to the case of  $\text{CFCl}_3$  (see section 8.2.3.1), the data of Jochims *et al.* [238] are systematically higher than the present work, although the shape is similar. In the valence-shell continuum (figure 8.3(a)), the cross sections recorded using synchrotron radiation [245] are ~10% lower than the dipole ( $e,e$ ) data from 16 to 30 eV, but the agreement between the two data sets becomes progressively better above 30 eV.

### 8.2.3.3 $\text{CF}_3\text{Cl}$

The absolute photoabsorption spectrum of  $\text{CF}_3\text{Cl}$  (Freon 13) obtained in the present work at a resolution of 0.05 eV fwhm is shown in figure 8.4. Figure 8.4(a) presents an overview of the spectrum from 8 to 60 eV, while the discrete transitions (8–23 eV) are illustrated in greater detail in figure 8.4(b). The energy positions of the observed structures are in good agreement with those reported earlier [238,239,246].

In contrast to the previous cases of  $\text{CFCl}_3$  and  $\text{CF}_2\text{Cl}_2$ , the discrete bands observed between 9–18 eV are generally broad. Moreover, earlier studies indicated that Rydberg transitions comprise the entire spectrum of  $\text{CF}_3\text{Cl}$  [239,241]. The first two peaks at 9.69 and 10.64 eV have been determined to be the 4s and 4p respective Rydbergs of the HOMO (5e) [239,241], which essentially contains the lone pair electrons from the chlorine atom [227]. These assignments give quantum defects of 2.00 ( $\delta_s$ ) and 1.64 ( $\delta_p$ ) that are consistent with values generally expected from  $ns$  and  $np$  Rydberg series of third row atoms. The next intense peak at 11.60 eV also

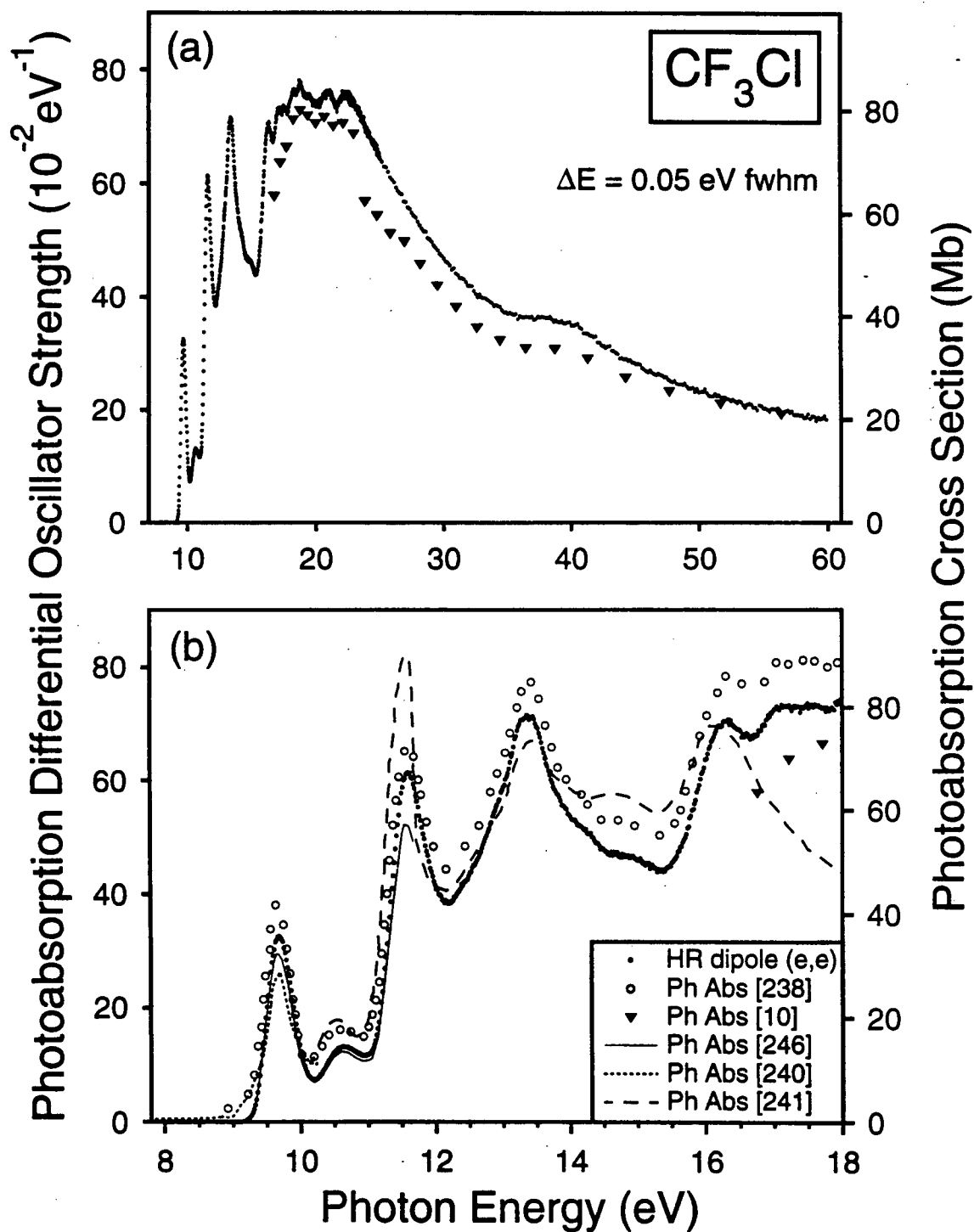


**Figure 8.4:** Absolute differential oscillator strengths ( $df/dE$ ) for the valence-shell photoabsorption of  $CF_3Cl$ : (a) 8–60 eV, (b) 8–18 eV. The high resolution dipole ( $e,e$ ) measurements (0.05 eV fwhm) obtained in the present work are compared with data determined using photon sources [10,238,240,241,246].

**Table 8.4**

Absolute photoabsorption oscillator strengths for regions of the high resolution valence-shell spectrum of  $\text{CF}_3\text{Cl}$

Energy range (eV) <sup>1</sup>	Oscillator strength ( $\times 10^{-2}$ )			
	This work	ref. [239]	ref. [240]	ref. [246]
9.04–10.18	16.25	22.0	15.16	15.03
10.18–10.95	8.65	11.9		8.05
10.95–12.23	51.10	67.6		
12.23–12.58	14.67	19.4		
12.58–13.07	25.68	34.2		
13.07–13.92	55.56	70.7		
13.92–14.70	38.88	49.9		
14.70–15.41	32.66	41.0		
15.41–16.68	77.27	95.8		
16.68–17.74	76.72	92.3		
17.74–19.16	107.96	124.55		
19.16–20.08	68.37	77.4		
20.08–20.57	36.74	40.6		
20.57–24.95	317.85	349.5		
24.95–29.99	278.53	302.1		
29.99–36.38	258.45	252.5		
36.38–46.00	316.28			
46.00–59.86	298.27			

<sup>1</sup> See figure 8.4.

arises from photoexcitation of electrons associated with the chlorine atom:  $5s,3d \leftarrow 5e$  and  $4s \leftarrow 5a_1$  [239]. In contrast, the broader band situated at 13.38 eV is predominantly  $3s \leftarrow 4e$  (F-CF<sub>2</sub>) [227]. More detailed discussions of the assignments of the transitions observed in the CF<sub>3</sub>Cl spectrum up to 18 eV can be found in ref. [239].

The differential photoabsorption oscillator strengths measured in the present work are compared with those reported earlier [10,238,240,241,246] in figure 8.4; more direct comparisons of oscillator strengths for regions of the spectrum [239,240,246] are given in table 8.4. From 9 to 11 eV, the present measurements are in fair agreement with the data of Suto and Lee [246] and Doucet *et al.* [240] within 7%, but the agreement is not so good with refs. [238,239,241], which are 20–30 % higher. However, it should be noted that the higher oscillator strengths reported by King and McConkey [239] may in part be attributed to the fact that their measurements were normalized to refs. [238,247] at 10.60 eV, and the data of Jochims *et al.* [238] are systematically higher than all studies to date (as with the previous cases of CFC1<sub>3</sub> and CF<sub>2</sub>Cl<sub>2</sub>). Between 11–17 eV there is a close correspondence between the relative intensities of the peaks appearing in the spectra of refs. [238,239,246] with those in the present work, but the relative intensities of the peaks in ref. [241] shows large deviations from other reported data. At the spectral maximum (~20 eV) and in the valence shell continuum at higher energies (figure 8.4(a)), the data of Lee *et al.* [10] fall below the present results, and this difference may be due to the contribution of higher-order radiation absorption or stray light in the synchrotron radiation measurements [10].

### 8.2.3.4 CF<sub>4</sub>

The absolute differential photoabsorption oscillator strengths of CF<sub>4</sub> (Freon 14) measured in the present work at high resolution (0.05 eV fwhm) is shown from 10 to 60 eV in figure 8.5(a). Figure 8.5(b) presents an expanded view of the discrete excitation region (12–24 eV) in greater detail.

The photoabsorption spectrum of CF<sub>4</sub> consists of fairly broad features (figure 8.5(b)), which have been attributed to overlapping transitions to Rydberg orbitals [10,239,248,249]. The first absorption band at 12.56 eV has been identified as the 3s Rydberg of the HOMO (1t<sub>1</sub>) [239,248,249], and its low intensity is the result of the 3s(a<sub>1</sub>) ← 1t<sub>1</sub> transition being symmetry forbidden. In contrast, the very strong and intense band at higher energy is composed of two dipole-allowed excitations, 3p ← 1t<sub>1</sub> (13.65 eV) and 3s(a<sub>1</sub>) ← 4t<sub>2</sub> (13.95 eV). An oscillator strength of 0.4781 has presently been determined over the 13.01–14.95 eV energy range, and it can be seen from table 8.5 that this value is in excellent agreement with those obtained by conventional photon methods [250,251]. Similarly good agreement is also observed for the next absorption band (14.95–16.27 eV), corresponding to the 3d ← 4t<sub>2</sub> and 3p ← 1e Rydberg transitions. However, although the data reported in both refs. [250,252] were obtained using a McPherson UV monochromator with the Hopfield He continuum photon source, it is unclear why the oscillator strengths between these data sets vary by 40% above 13 eV. The two earlier electron scattering studies [239,248] also reported oscillator strengths that are 25% lower, which can in part be attributed to the relatively low incident electron excitation energy used (500 eV) in refs. [239,248] as compared to the 3000 eV utilized in the present measurements. Such a low electron excitation energy can cause non-dipole transitions to appear in the spectrum while simultaneously lowering the intensities of dipole transitions. It should also be noted that King and McConkey [239] used the data from ref. [248] to

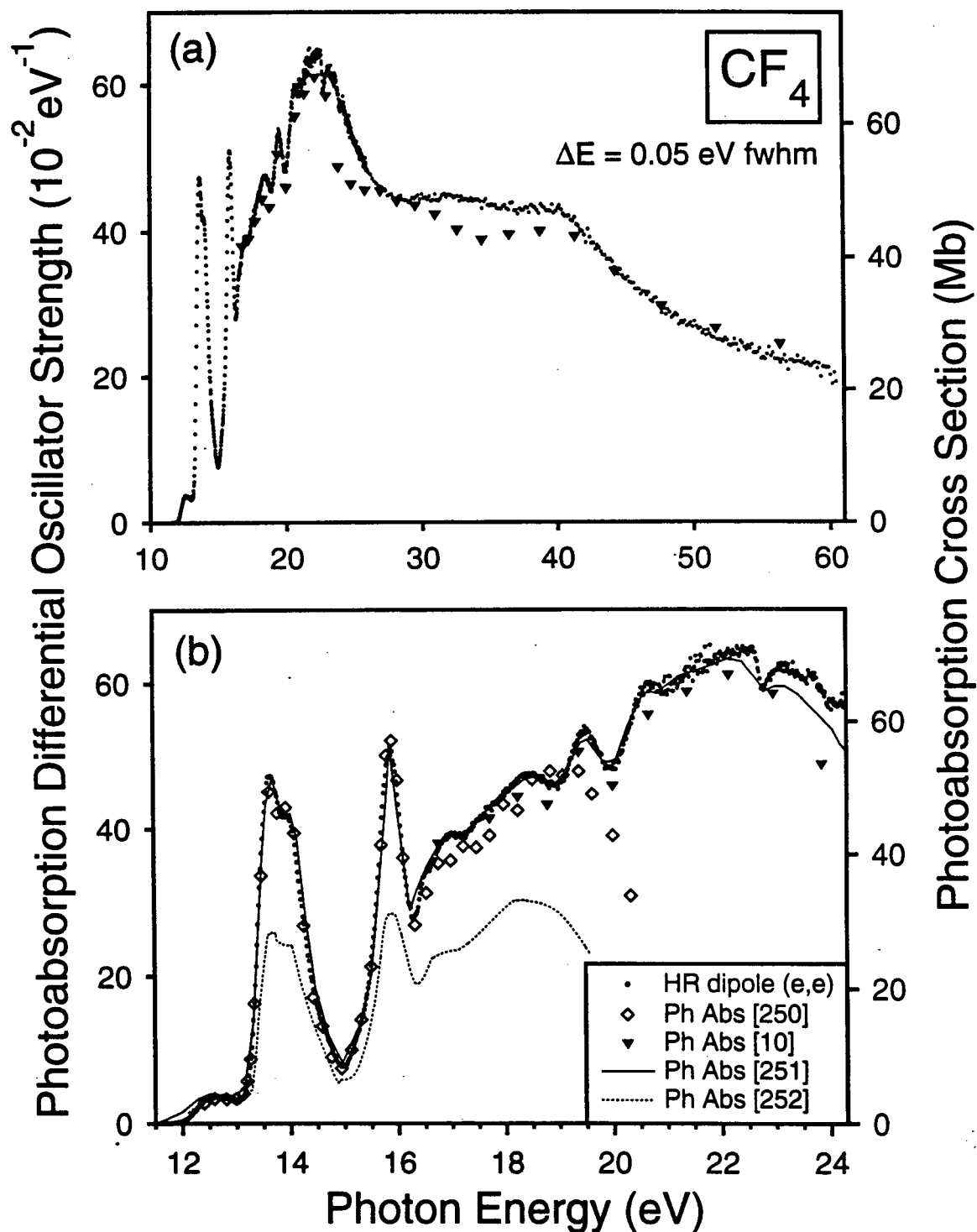


**Figure 8.5:** Absolute differential oscillator strengths ( $df/dE$ ) for the valence-shell photoabsorption of  $\text{CF}_4$ : (a) 10–60 eV, (b) 10–24 eV. The high resolution dipole ( $e,e$ ) measurements (0.05 eV fwhm) obtained in the present work are compared with data determined using photon sources [10,250–252].

**Table 8.5**

Absolute photoabsorption oscillator strengths for regions of the high resolution valence-shell spectrum of CF<sub>4</sub>

Energy range (eV) <sup>1</sup>	Oscillator strength (x 10 <sup>-2</sup> )					
	This work	ref. [239]	ref. [248]	ref. [250]	ref. [252]	ref. [251]
11.86–13.01	2.80	2.0	2.4	2.03	2.67	2.3
13.01–14.95	47.81	36.1	36.2	46.47	28.92	48.4
14.95–16.27	36.70	28.7		36.88	23.15	38.1
16.27–16.63	11.40	8.1		11.93	7.39	11.5
16.63–17.16	20.35	15.3		18.84	12.46	21.0
17.16–19.01	82.00	62.2		78.86	52.10	81.3
19.01–19.98	49.12	36.3		43.70		49.1
19.98–20.99	56.38	41.9				56.3
20.99–22.74	109.66	80.5				108.5
22.74–27.39	247.58	189.6				
27.39–31.85	197.85	156.9				
31.85–36.70	213.54	156.5				
36.70–46.03	370.17					
46.03–60.00	349.95					

<sup>1</sup> See figure 8.5.

set their absolute oscillator strength scale.

At higher energies above 17 eV in the valence-shell continuum, some very interesting features are observed in the  $\text{CF}_4$  photoabsorption spectrum. While many overlapping Rydberg transitions are expected to occur in this region, the broad, distinct peaks at 18.46, 19.49, and 20.70 eV (figure 8.5(b)) have been identified to arise predominantly from  $3s \leftarrow 3t_2$ ,  $3p \leftarrow 3t_2$ , and  $3d \leftarrow 3t_2$ , respectively [239,248,249]. The present work also confirms the presence of several vibronic progressions between 20.4–22.5 eV (see figure 8.6) observed earlier in a synchrotron radiation study [10]. These have been assigned to Rydberg transitions associated with the  $(3t_2)^{-1}$  and  $(4a_1)^{-1}$  ion states [10], which also exhibit vibrational structures with spacings of  $645 \text{ cm}^{-1}$  (0.077 eV) and  $730 \text{ cm}^{-1}$  (0.091 eV), respectively [228]. The vibronic bands in the  $\text{CF}_4$  excitation spectrum converge in the vicinity of the absorption minimum at 22.78 eV. This autoionization effect or window resonance results from the interaction of the  $(3t_2)^{-1}$  continuum ion state with the  $3d \leftarrow 4a_1$  bound state [239]. At high energies, the broad hump situated between  $\sim 30$ –40 eV in figure 8.5(a) likely arises from ionization of the two inner valence orbitals ( $2t_2$  and  $3a_1$ ). This is supported by the shape and onset (35 eV) of the electronic state partial photoionization oscillator strengths for the summed  $((2t_2)^{-1} + (3a_1)^{-1})$  ion states [223].

Comparison of the differential oscillator strengths (figure 8.5) and the oscillator strengths (table 8.5) of  $\text{CF}_4$  obtained in the present work with those reported earlier shows excellent agreement between the dipole ( $e,e$ ) data and the more recent synchrotron radiation data of Lee *et al.* [251] up to 22 eV. The earlier synchrotron radiation measurements [10] are also in reasonable agreement with the present work, but between 22–40 eV the former shows drastic differences in both shape and magnitude. This discrepancy is likely due to the contribution of second order radiation and/or stray light in the data of ref. [10], which the authors had

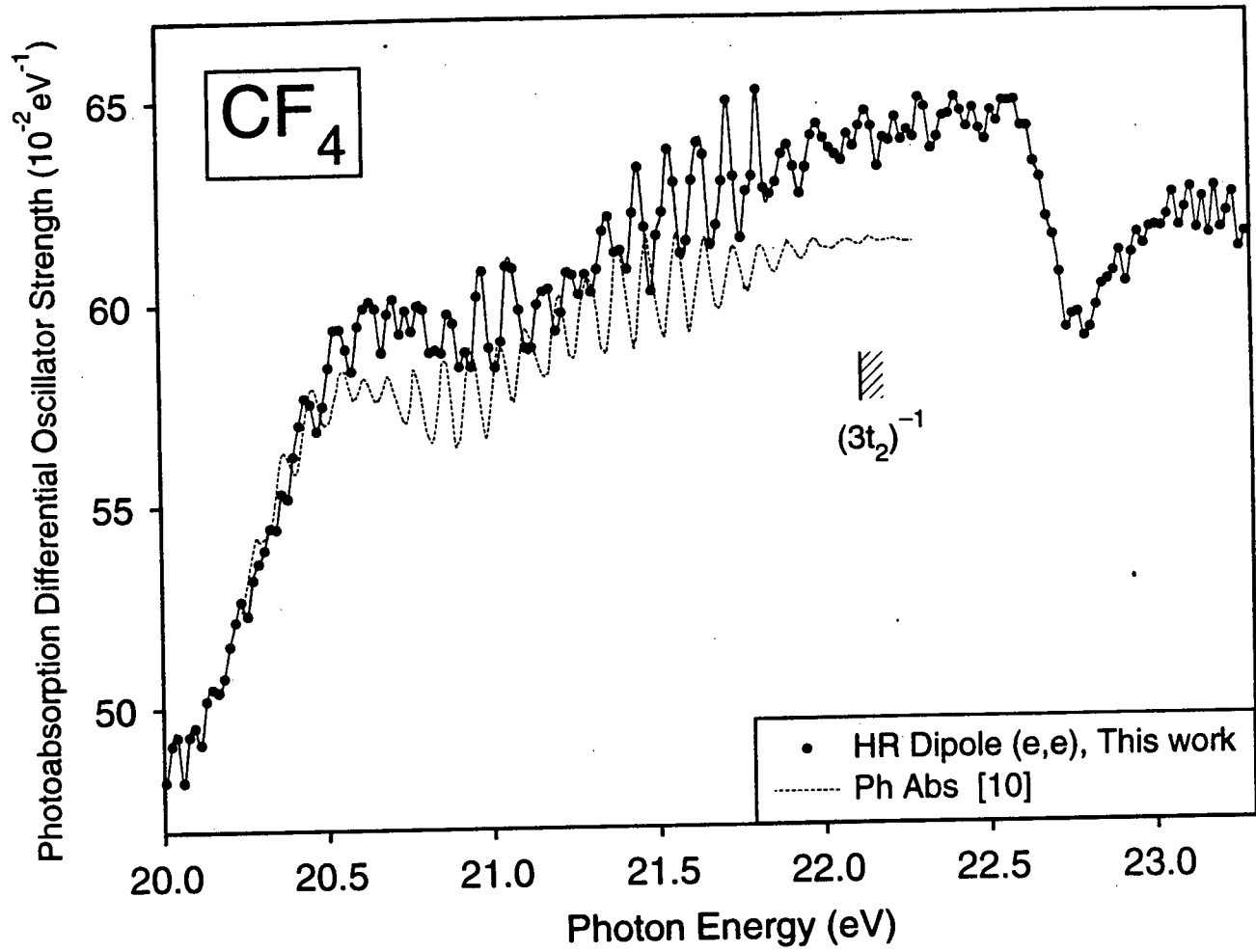


**Figure 8.6:** Absolute differential photoabsorption oscillator strengths of  $\text{CF}_4$  obtained at high resolution from 20 to 23.3 eV, showing the  $(3t_2)^{-1}$  autoionization region in detail.

estimated to have an experimental error of  $\pm 20\%$  in this region. Above 19 eV the downward deviation in the cross sections reported in ref. [250] can be attributed to uncertainties associated with the weakness of the Hopfield helium continuum photon source at high energies. It should be noted that the EELS data of King and McConkey [239] are systematically 25% lower than those of this work (see table 8.5), and this can be accounted for by the fact that King and McConkey normalized their data to those of ref. [248] between 13–15 eV.

## Chapter 9

### Conclusions

The present work has provided long range, absolute differential oscillator strengths (cross sections) for large normal alkanes ( $C_nH_{2n+2}$ ,  $n = 5-8$ ), phosphorus halides ( $PF_3$ ,  $PCl_3$ ,  $PF_5$ ), single-carbon Freons ( $CFCl_3$ ,  $CF_2Cl_2$ ,  $CF_3Cl$ ,  $CF_4$ ), and nitrogen dioxide ( $NO_2$ ) from the first excitation threshold up to 200–350 eV (1 eV fwhm), encompassing the valence-shell regions of all twelve molecules as well as the P  $2p,2s$  and Cl  $2p,2s$  inner shells of the phosphorus halides. These measurements have greatly extended the range of absolute oscillator strength data for these molecules currently available in the literature. Moreover, the valence-shell continuum photoabsorption spectrum of  $PF_3$  has also provided the first experimental test-bed for the theoretical MS-X $\alpha$  calculations reported earlier by Powis. The present measurements and the S(-2) sum rule have been used together to evaluate the accuracy of the absolute differential oscillator strength scales via comparison of the resulting static electric-dipole polarizability values with those reported in the literature. The good agreement lends further support to the reliability of the VTRK sum rule normalization procedure and the associated curve-fitting and extrapolation techniques.

The feasibility of using atomic and molecular mixture rules as well as group additivity concepts for predicting valence-shell photoabsorption differential oscillator strengths for normal alkane molecules has been investigated over a wide energy range (18–220 eV) using the experimental measurements presently reported for the large alkanes ( $C_nH_{2n+2}$ ,  $n = 5-8$ ) together with those obtained earlier in this laboratory for the smaller alkanes ( $n = 1-4$ ). Atomic mixture rules (AMR's) based on

either theoretical or experimental atomic oscillator strength sums are found to be unsatisfactory, giving very large errors at most photon energies. (Application of AMR's to other molecules reported in this thesis have also indicated that the accuracy of using AMR's to estimate molecular differential oscillator strengths is rather unpredictable, as they sometimes generate fairly good estimates (e.g., PF<sub>5</sub>, PF<sub>3</sub>, NO<sub>2</sub>) and sometimes they do not (e.g., PCl<sub>3</sub>, CFCI<sub>3</sub>, CF<sub>2</sub>Cl<sub>2</sub>)). A wide range of molecular mixture rules (MMR's) based on linear combinations of measured differential oscillator strength values for small "component" alkane molecules and molecular hydrogen have also been evaluated, and the results show that although good agreement with experiment is obtained with some linear combinations, many others result in substantial errors. MMR's constructed using differential oscillator strengths for larger component alkanes generally give better estimates of the experimentally measured data; however, since no other *a priori* physical or chemical reasons can be advanced for any particular choice of molecular mixture rule, this procedure is unsatisfactory for general application. In contrast, a group additivity procedure based on differential oscillator strength estimates for the methylene (CH<sub>2</sub>) and methyl (CH<sub>3</sub>) alkane fragments, derived entirely from the photoabsorption measurements for the smaller alkanes has been found to provide excellent agreement with the experimental data for C<sub>8</sub>H<sub>18</sub> over the entire energy range studied (18–220 eV). The absolute photoabsorption group oscillator strengths derived for the CH<sub>2</sub> and CH<sub>3</sub> fragments should be applicable to assessing the contributions from saturated hydrocarbon groupings to VUV and soft X-ray absorption in larger chemical and biochemical systems. Future studies could include group additivity assessments involving other functional groups such as amino and carboxyl groups.

Absolute photoabsorption spectra obtained at higher resolution (0.05–0.1 eV fwhm) have contributed additional oscillator strength information for discrete

profiles observed in the valence-shell and inner-shell regions. Comparisons have been made to previously reported optical measurements and theoretical calculations in those limited energy regions where such data exist. In the case of  $\text{PCl}_3$ , the high resolution spectrum obtained in the vicinity of the P  $2p$  inner-shell region has provided further insights on the dipole-forbidden transition situated at 134.15 eV.

Finally, absolute partial photoionization differential oscillator strengths (PPOS) for the valence-shell molecular and dissociative photoionization of propane, *n*-butane, nitrogen dioxide, and the phosphorus halides ( $\text{PF}_3$ ,  $\text{PCl}_3$ ,  $\text{PF}_5$ ) have been obtained from the first ionization threshold up to 50–270 eV. Together with photoelectron spectra and other data from the literature, these measurements have been used to gain a better qualitative and quantitative ( $\text{PF}_3$ ) understanding of the dipole-induced breakdown pathways of these molecules under VUV and soft X-ray radiation. Additional photoion PPOS data determined for the P  $2p, 2s$  and Cl  $2p, 2s$  inner-shells of the phosphorus halides have led to greater insights as to how the partial oscillator strengths for each of the fragment ions change in moving from valence-shell to inner-shell photoionization, with particular emphasis on the changes occurring in the vicinity of the different photoexcitation and photoionization processes observed in these spectra. A more detailed analysis of the breakdown pathways must await electronic ion state PPOS measurements using variable energy PES, photoelectron studies of the inner-valence orbitals, and PEPICO and PIPICO measurements in both the valence and inner shell regions.

## Bibliography

- [1] M. Inokuti (Ed.), *Proceedings of Workshop on Electronic and Ionic Collision Cross Sections Needed in the Modeling of Radiation Interaction with Matter*, Argonne, Illinois, 1983 (Argonne National Laboratory, Argonne, 1984), Report No. ANL-84-29.
- [2] J.W. Gallagher, C.E. Brion, J.A.R. Samson, and P.W. Langhoff, *J. Phys. Chem. Ref. Data*, **17** (1988) 9, and references therein.
- [3] T. Nakayama, M.Y. Kitamura, and K. Watanabe, *J. Chem. Phys.*, **30** (1959) 1180.
- [4] Y. Morioka, H. Masuko, M. Nakamura, M. Sasanuma, and E. Ishiguro, *Can. J. Phys.*, **56** (1978) 962.
- [5] W.F. Chan, G. Cooper, and C.E. Brion, *Phys. Rev. A*, **44** (1991) 186.
- [6] R.D. Hudson, *Rev. Geophys. Space Phys.*, **6** (1971) 305.
- [7] W.F. Chan, G. Cooper, and C.E. Brion, *Chem. Phys.*, **168** (1992) 375.
- [8] W.F. Chan, G. Cooper, R.N.S. Sodhi, and C.E. Brion, *Chem. Phys.*, **170** (1993) 81.
- [9] J.A.R. Samson, *Techniques of Vacuum Ultraviolet Spectroscopy* (John Wiley & Sons, New York, 1967).
- [10] L.C. Lee, E. Phillips, and D.L. Judge, *J. Chem. Phys.*, **67** (1977) 1237.
- [11] H. Bethe, *Ann. Phys.*, **5** (1930) 325.
- [12] M. Inokuti, *Rev. Mod. Phys.*, **43** (1971) 297.
- [13] M. Inokuti, Y. Itikawa, and J.E. Turner, *Rev. Mod. Phys.*, **50** (1978) 23.
- [14] W.F. Chan, G. Cooper, X. Guo, and C.E. Brion, *Phys. Rev. A*, **45** (1992) 1420.
- [15] C. Backx and M.J. Van der Wiel, *J. Phys. B*, **8** (1975) 3020.
- [16] C. Backx, G.R. Wight, R.R. Tol, and M.J. Van der Wiel, *J. Phys. B*, **8** (1975) 2050.
- [17] I.V. Hertel and K.J. Ross, *J. Phys. B*, **2** (1969) 1733.
- [18] E.N. Lassettre, *Can. J. Chem.*, **47** (1969) 1733.

- [19] E.N. Lassettre, A. Skerbele, and M.A. Dillon, *J. Chem. Phys.*, **52** (1970) 2797.
- [20] M.J. Van der Wiel, *Physica*, **49** (1970) 411.
- [21] M.J. Van der Wiel and G. Wiebes, *Physica*, **54** (1971) 411; **54** (1971) 225.
- [22] E.M. Zarate, G. Cooper, and C.E. Brion, *Chem. Phys.*, **148** (1990) 289.
- [23] G. Cooper, E.M. Zarate, R.K. Jones, and C.E. Brion, *Chem. Phys.*, **150** (1991) 251.
- [24] T.N. Olney, C.E. Brion, and T. Ibuki, *Chem. Phys.* **201** (1995) 505.
- [25] G.R. Burton, W.F. Chan, G. Cooper, and C.E. Brion, *Chem. Phys.*, **181** (1994) 147.
- [26] T. Ibuki, A. Hiraya, T.N. Olney, and C.E. Brion, *Chem. Phys.*, **203** (1996) 259.
- [27] G.R. Burton, W.F. Chan, G. Cooper, and C.E. Brion, *Chem. Phys.*, **177** (1993) 217.
- [28] T.N. Olney, N.M. Cann, G. Cooper, and C.E. Brion, *Chem. Phys.*, In press (1996).
- [29] M.J. Molina and F.S. Rowland, *Nature*, **249** (1974) 810.
- [30] F.S. Rowland and M.J. Molina, *Rev. Geophys. Space Phys.*, **13** (1975) 1.
- [31] T.G. Spiro and W.M. Stigliani, *Environmental Issues in Chemical Perspective* (State University of New York Press, Albany, 1980).
- [32] S. Elliott and F.S. Rowland, *J. Chem. Education*, **64** (1987) 387.
- [33] M. Katz, *Can. J. Chem. Eng.*, **48** (1970) 3.
- [34] P. Zurer. *Chemical & Engineering News*, **Nov. 25** (1991), 6.
- [35] *New Scientist*, 12 December 1974, p. 827.
- [36] J.W. Au, *B.Sc. Thesis* (University of British Columbia, Vancouver, 1992).
- [37] U. Fano and J.W. Cooper, *Rev. Mod. Phys.*, **40** (1968) 441.
- [38] G.D. Zeiss, W.J. Meath, J.C.F. MacDonald, and D.J. Dawson, *Radiation Res.*, **70** (1977) 284.
- [39] F. Carnovale and C.E. Brion, *Chem. Phys.*, **74** (1983) 253.

- [40] M.B. Robin, Higher Excited States of Polyatomic Molecules, Vol. I (Academic Press, New York, 1974).
- [41] J.L. Dehmer and D. Dill, *J. Chem. Phys.* **65** (1976) 5327.
- [42] J.L. Dehmer, D. Dill, and A.C. Parr, *Photophysics and Photochemistry in the Vacuum Ultraviolet* (Reidel, New York, 1985).
- [43] I. Powis, *Chem. Phys. Lett.*, 215 (1993) 269.
- [44] X. Guo, G. Cooper, W.F. Chan, G.R. Burton, and C.E. Brion, *Chem. Phys.*, **161** (1992) 453.
- [45] G. Cooper, Y. Zheng, G.R. Burton, and C.E. Brion, *Rev. Sci. Instrum.*, **64** (1993) 1140.
- [46] S. Daviel, C.E. Brion, and A.P. Hitchcock, *Rev. Sci. Instrum.*, **55** (1984) 182.
- [47] J.A. Wheeler and J.A. Bearden, *Phys. Rev.*, **46** (1934) 755.
- [48] M. Inokuti, private communication (1985).
- [49] W.L. Wiese, M.W. Smith, and B.M. Glenon, Atomic transition probabilities, Vol. 1. Hydrogen through neon NSRDS-NBS. Circular No. 4 (US GPO, Washington, DA, 1966).
- [50] R.L. Schoen. *J. Chem. Phys.*, **37** (1962), 2032.
- [51] R. Stockbauer. *J. Chem. Phys.*, **58** (1973), 3800.
- [52] W.A. Chupka and J. Berkowitz. *J. Chem. Phys.*, **47** (1967), 2921.
- [53] B. Steiner, C.F. Giese, and M.G. Inghram. *J. Chem. Phys.*, **34** (1961), 189.
- [54] S. Tsuda and W.H. Hamill. *J. Chem. Phys.*, **41** (1964), 2713.
- [55] C.E. Melton and W.H. Hamill. *J. Chem. Phys.*, **41** (1964), 546.
- [56] H.M. Rosenstock, K. Draxl, B.W. Steiner, and J.T. Herron. *J. Phys. Chem. Ref. Data*, **6** (1977).
- [57] B.A. Lombos, P. Sauvageau, and C. Sandorfy. *Chem. Phys. Letters*, **1** (1967), 42; *J. Mol. Spectry.*, 24 (1967), 253.
- [58] J.W. Raymonda and W.T. Simpson. *J. Chem. Phys.*, **47** (1967), 430.
- [59] J.C. Person and P.P. Nicole. *Argonne Natl. Lab. Radiolog. Environ. Res. Div.*

- Ann. Rep. 1973-74, ANL-75-3*, part I, 63.
- [60] B.L. Jhanwar, W.J. Meath, and J.C.F. MacDonald. *Can. J. Phys.*, **59** (1981), 185.
- [61] K. Kimura, S. Katsumata, Y. Achiba, T. Yamazaki, and S. Iwata. *Handbook of HeI Photoelectron Spectra of Fundamental Organic Molecules* (Japan Scientific Society, Tokyo, 1981).
- [62] A.W. Potts and D.G. Streets. *J.Chem.Soc. Faraday Trans. II*, **70** (1974), 875.
- [63] P. Kusch, A. Hustrulid, and J.T. Tate. *Phys. Rev.*, **52** (1937), 843.
- [64] F.H. Field and J.L. Franklin. *Electron Impact Phenomena and the Properties of Gaseous Ions* (Academic Press, New York, 1970).
- [65] G. Dujardin, S. Leach, O. Dutuit, P.M. Guyon, and M. Richard-Viard. *Chem. Phys.*, **88** (1984), 339.
- [66] D.A. Hagan and J.H.D. Eland. *Org. Mass Spectrom.*, **27** (1992), 855.
- [67] J.G. Lias, J.E. Bartmess, J.F. Liebman, J.L. Holmes, R.D. Levin, and W.G. Mallard. *J. Phys. Chem. Ref. Data*, **17** (1988), Suppl. No. 1.
- [68] J.C. Person and P.P. Nicole. *J. Chem. Phys.*, **49** (1968), 5421.
- [69] D. Beck and N. Niehaus. *J. Chem. Phys.*, **37** (1962), 2705.
- [70] R.H. Huebner, C.F. Fergurson, R.J. Celotta, and S.R. Mielczarek. *Argonne Natl. Lab. Radiolog. Environ. Res. Div. Ann. Rep. 1973-1974, ANL-75-3*, part I, 41.
- [71] H.A. Stuart, *Landolt-Bornstein, Atom und Molekularphysik* (Springer-Verlag, Berlin, Vol. 1, Part 3, p. 509, 1951).
- [72] A.A. Maryott and F. Buckley, *U.S. National Bureau of Standards Circular No. 537* (US GPO, Washington, DC, 1953).
- [73] G.D. Zeiss, W.J. Meath, J.C.F. MacDonald, and D.J. Dawson, *Mol. Phys.* **39** (1980) 1055.
- [74] B.L. Jhanwar, W.J. Meath, and J.C.F. MacDonald, *Can. J. Phys.* **61** (1983) 1027.
- [75] B.L. Jhanwar and W.J. Meath, *Can. J. Chem.* **62** (1984) 373.
- [76] G.F. Thomas and W.J. Meath, *Mol. Phys.* **34** (1977) 113.

- [77] G.R. Burton, W.F. Chan, G. Cooper, C.E. Brion, A. Kumar, and W.J. Meath, *Can. J. Chem.* **71** (1993), 341.
- [78] W.J. Meath, D.J. Margoliash, B.L. Jhanwar, A. Kiode, and G.D. Zeiss, *Intermolecular Forces*, Proc. 14th Jerusalem Symp. Quant. Chem. and Biochem. (1981) 101.
- [79] B.L. Jhanwar, W.J. Meath, and J.C.F. MacDonald, *Radiat. Res.* **96** (1983) 20.
- [80] B.L. Jhanwar, W.J. Meath, and J.C.F. MacDonald, *Radiat. Res.* **106** (1986) 288.
- [81] H.J. Grosse and H.K. Bothe, *Z. Naturforsch.*, **A23** (1968) 1583.
- [82] B.L. Schram, M.J. van der Wiel, F.J. de Heer, and H.R. Moustafa, *J. Chem. Phys.* **44** (1966), 49.
- [83] F.J. de Heer and M. Inokuti, in *Electron Impact Ionization*, ed. T.D. Märk and G.H. Dunn (New York, 1985).
- [84] B.L. Henke, P. Lee, T.J. Tanaka, R.L. Shimabukuro, and B.K. Fujikawa, *At. Data Nucl. Data Tables* **27** (1982) 1.
- [85] R.F. Reilman and S.T. Manson, *Astrophys. J. Suppl. Series* **40** (1979) 815.
- [86] J.J. Yeh and I. Lindau, *At. Data Nucl. Data Tables* **32** (1985) 1.
- [87] J.A.R. Samson, Z.X. He, L. Yin, and G.N. Haddad, *J. Phys. B* (1994). In press.
- [88] M. Sanchez, R. Daudel, P.D. Dacre, R. McWeeny, S. Kwun, and C. Valdemoro, *Int. J. Quantum Chem.* **11** (1977) 415.
- [89] T.N. Belyaeva, M.N. Krivchun, M.V. Sendyurev, A.V. Dogadina, V.V. Sokolov, B.I. Ionin, and A.A. Petrev, *Zh. Obshch. Khim.*, **56** (1986) 1184.
- [90] B.D. Sviridov, V.I. Porkhun, M.V. Serdobov, Yu. S. Ryabokobylko, G.M. Adamova, and R.V. Poponova, *Zh. Obshch. Khim.*, **56** (1986) 1268.
- [91] B.W. Moores and L. Andrews, *J. Phys. Chem.*, **93** (1989) 1902.
- [92] V.B. Yakovlev, N.I. Litsov, and A.A. Kachan, *Otkrytiya Izobret.*, **19** (1990) 110.
- [93] G.G. Bentini, M. Bianconi, L. Correra, R. Nipoti, D.A. Patti, and A. Gasparotto, *Appl. Surf. Sci.*, **36** (1989) 394.

- [94] T. Sugano, F. Arai, and H. Okazaki, *Sogo Shikensho Nenpo*, **49** (1990) 87.
- [95] S.J. Pearton, U.K. Chakrabarti, A. Katz, A.P. Perley, W.S. Hobson, and M. Geva, *Plasma Chem. Plasma Process.*, **11** (1991) 405.
- [96] C.M. Humphries, A.D. Walsh, and P.A. Warsop, *Discussions Faraday Soc.*, **35** (1963) 148.
- [97] M.J. McAdams and B.R. Russell, *Chem. Phys. Lett.*, **18** (1973) 402.
- [98] E. Ishiguro, S. Iwata, A. Mikuni, Y. Suzuki, H. Kanamori, and T. Sasaki, *J. Phys. B*, **20** (1987) 4725.
- [99] I.J. Väyrynen, T.A. Kaurila, R.G. Cavell, and K.H. Tan, *J. Electron Spectrosc. Relat. Phenom.*, **61** (1992) 55.
- [100] N. Kosugi, R.G. Cavell, and A.P. Hitchcock, *Chem. Phys. Lett.* Submitted (1996).
- [101] R.N.S. Sodhi and C.E. Brion, *J. Electron Spectrosc. Relat. Phenom.*, **37** (1985) 145.
- [102] R.N.S. Sodhi and C.E. Brion, *J. Electron Spectrosc. Relat. Phenom.*, **37** (1985) 97.
- [103] M. Halmann, *J. Chem. Soc.* (1963) 2853.
- [104] I.A. Topol, A.V. Kondratenko, and L.N. Mazalov, *Academy of Sciences USSR Bulletin, Physical Series*, **46** (1982) 143.
- [105] I.A. Topol, A.V. Kondratenko, V.D. Yumatov, L.N. Mazalov, A.V. Okotrub, A.A. Voityuk, and G.N. Dolenko, *Academy of Sciences USSR Bulletin, Physical Series*, **46** (1982) 137.
- [106] R.N.S. Sodhi and C.E. Brion, *J. Electron Spectrosc. Relat. Phenom.*, **37** (1985) 125.
- [107] J.S. Tse and Z.F. Liu, *Phys. Rev. A*, **44** (1991) 7838.
- [108] Z.F. Liu, J.N. Cutler, G.M. Bancroft, K.H. Tan, R.G. Cavell, and J.S. Tse, *Chem. Phys.*, **168** (1992) 133.
- [109] J.P. Maier and D.W. Turner, *J. Chem. Soc., Faraday Trans. 2*, **68** (1972) 711.
- [110] W. von Niessen, J. Schirmer, and L.S. Cederbaum, *Comp. Phys. Reports*, **1** (1984) 57.

- [111] R.N. Sodhi and R.G. Cavell, *J. Electron Spectrosc. Relat. Phenom.*, **32** (1983) 283.
- [112] P.A. Cox, S. Evans, A.F. Orchard, N.V. Richardson, and P.J. Roberts, *Discuss. Faraday Soc.*, **54** (1972) 26.
- [113] M. Xin, L.C. Chiu, D. Li, and Y. Pan, *J. Electron Spectrosc. Relat. Phenom.*, **33** (1984) 93.
- [114] R.G. Cavell, *Inorganic Chem.*, **14** (1975) 2828.
- [115] W.H.E. Schwarz, *Chem. Phys.*, **11** (1975) 217.
- [116] A. Barrie, I.W. Drummond, and Q.C. Herd, *J. Electron Spectrosc. Relat. Phenom.*, **5** (1974) 217.
- [117] D.W. Goodman, M.J.S. Dewar, J.R. Schweiger, and A.H. Cowley, *Chem. Phys. Lett.*, **21** (1973) 474.
- [118] R.S. Berry, M. Tamres, C.J. Ballhausen, and H. Johansen, *Acta Chem. Scand.*, **22** (1968) 231.
- [119] N. Hacket and R.J.W. Le Fèvre, *J. Chem. Soc.*, (1961) 2612.
- [120] G. Nagarajan, *Z. Naturforsch. a.*, **21** (1966) 238.
- [121] S.S. Batsanov, *Refractometry and Chemical Structure*, Consultants Bureau, New York, 1961.
- [122] U. Grassi, *Novo cimento*, **10** (1933) 3.
- [123] E.R. Lippincott, G. Nagarajan, and J.M. Stutmann, *J. Phys. Chem.*, **70** (1966) 78.
- [124] A.N. Pandey, A. Bigotto, and R.K. Gulati, *Acta Physica Polmica A*, **80** (1991) 503.
- [125] M.K. Wilson and R. Polo, *J. Chem. Phys.*, **20** (1952) 1716.
- [126] J. Rolke and C.E. Brion, *Chem. Phys.*, **207** (1996) 173.
- [127] I. Powis, *J. Chem. Phys.*, **103** (1995) 5570.
- [128] C.E. Brion, Y. Iida, and J.P. Thomson, *Chem. Phys.*, **101** (1986) 449.
- [129] S. Daviel, Y. Iida, F. Carnovale, and C.E. Brion, *Chem. Phys.*, **83** (1984) 319.

- [130] P.W. Davis and R.A. Oetyen, *J. Mol. Spectrosc.*, **2** (1958) 253.
- [131] A.W. Potts, H.J. Lempka, D.G. Streets, and W.C. Price, *Phil. Trans. Roy. Soc. Lond. A*, **268** (1970) 59.
- [132] A.P. Hitchcock, N. Kosugi, and R.G. Cavell. Manuscript in preparation.
- [133] W.F. Chan, G. Cooper, K.H. Sze, and C.E. Brion, *J. Phys. B*, **23** (1990) L523.
- [134] K.H. Sze and C.E. Brion, *Chem. Phys.*, **137** (1989) 353.
- [135] J.L. Dehmer, *J. Chem. Phys.*, **56** (1972) 4496.
- [136] B.M. Addison, K.H. Tan, and G.M. Bancroft, *Chem. Phys. Lett.*, **129** (1986) 468.
- [137] D. Blechschmidt, R. Haensel, E.E. Koch, U. Nielsen, and T. Sagawa, *Chem. Phys. Lett.*, **14** (1972) 33.
- [138] P.J. Bassett and D.R. Lloyd, *J. Chem. Soc., Dalton Trans.* (1972) 248.
- [139] J.C. Green, N. Kaltsoyannis, K.H. Sze, and M.A. MacDonald, *J. Chem. Soc., Dalton Trans.*, (1991) 2371.
- [140] D.J. Reynolds, E.H. van Kleef, and I. Powis, *J. Chem. Phys.*, **95** (1991) 8895.
- [141] I. Powis, *J. Chem. Phys.*, **99** (1993) 3436.
- [142] I. Powis, *Chem. Phys. Lett.*, **198** (1992) 473.
- [143] J. Berkowitz, J.P. Greene, J. Foropoulos, Jr., and O.M. Neskovic, *J. Chem. Phys.*, **81** (1984) 6166.
- [144] J. Berkowitz and J.P. Greene, *J. Chem. Phys.*, **81** (1984) 4328.
- [145] D.F. Torgerson and J.B. Westmore, *Can. J. Chem.*, **53** (1975) 933.
- [146] C.R.S. Dean, A. Finch, P.J. Gardner, and D.W. Payling, *J. Chem. Soc., Faraday Trans. 1*, **70** (1974) 1921.
- [147] W.H. Beattie, *Applied Spectroscopy*, **29** (1975) 334.
- [148] R. Rüede, H. Troxler, Ch. Beglinger, and M. Jungen, *Chem. Phys. Lett.*, **203** (1993) 477.
- [149] R.G. Cavell and R. Sodhi, *J. Electron Spectrosc. Relat. Phenom.*, **15** (1979) 145.

- [150] B.E. Mills, R.L. Martin, D.A. Shirley, *J. Am. Chem. Soc.*, **98** (1976) 2380.
- [151] W.L. Jolly and W.B. Perry, *Inorg. Chem.*, **13** (1974) 2686.
- [152] F.P. Larkins, E.Z. Chelkowska, Y. Sato, K. Ueda, E. Shigemasa, and A. Yagishita, *J. Phys. B*, **26** (1993) 1479.
- [153] A.P. Hitchcock, J. Bozek, F. Schlachter, T. Tyliczszak, D. Kilcoyne, and R. Cavell, unpublished results.
- [154] W.B. Perry, T.F. Schaaf, and W.L. Jolly, *J. Amer. Chem. Soc.*, **97** (1975) 4899.
- [155] R. Platania, F. Maracci, A.C.A. Souza, and G.G. B. de Souza, *Chem. Phys.*, **163** (1992) 381.
- [156] M. Halmann and Y. Klein, *J. Chem. Soc.* (1964) 4324.
- [157] A.A. Sandoval, H.C. Moser, and R.W. Kiser, *J. Phys. Chem.*, **67** (1963) 124.
- [158] M. Veljkovic, O. Neskovic, M. Miletic, D. Golobocanin, and K.F. Zmbov, *Vestn. Slov. Kem. Drus., Suppl.*, **33** (1963) 124.
- [159] K. Varmuza and P. Krenmayr, *Monatsh. Chem.*, **102** (1971) 1073.
- [160] R.W. Shaw, Jr., T.X. Carroll, and T.D. Thomas, *J. Amer. Chem. Soc.*, **95** (1973) 5870.
- [161] W.E. Falconer, G.R. Jones, W.A. Sunder, M.J. Vasile, A.A. Muentner, T.R. Dyke, and W. Klemperer, *J. Fluorine Chem.*, **4** (1974) 213.
- [162] H.H. Michels and J.A. Montgomery, Jr., *J. Chem. Phys.*, **93** (1990) 1805.
- [163] H. Wasada and K. Hirao, *J. Amer. Chem. Soc.*, **114** (1992) 16.
- [164] G.B. Armen and F.P. Larkins, *J. Phys. B*, **24** (1991) 741.
- [165] J.L. Franklin, J.G. Dillard, H.M. Rosenstock, J.T. Herron, K. Draxl, and F.H. Field, *NSRDS-NBS 26*, Nat. Bur. Stand. (U.S.), Washington, D.C., June 1969.
- [166] J. Rolke, N. Cann, Y. Zheng, B.P. Hollebone, C.E. Brion, Y.A. Wang, and E.R. Davidson, *Chem. Phys.*, **201** (1995) 1.
- [167] K.L. McEwen, *J. Chem. Phys.*, **32** (1960) 1801.
- [168] S. Shih, S.D. Peyerimhoff, and R.J. Buenker, *Chem. Phys. Lett.*, **46** (1977) 201.
- [169] C.F. Jackels and E.R. Davidson, *J. Chem. Phys.*, **65** (1976) 2941.

- [170] R.A. Gangi and L. Burnelle, *J. Chem. Phys.*, **55** (1971) 843; *J. Chem. Phys.*, **55** (1971) 851.
- [171] W.C. Price and D.M. Simpson, *Trans. Faraday Soc.*, **37** (1941) 106.
- [172] K. Mori, *Science of Light*, **3** (1954) 62; *Science of Light*, **4** (1955) 130.
- [173] G.W. Robinson, M. McCarty, and M.C. Keelty, *J. Chem. Phys.*, **27** (1957) 972.
- [174] R.K. Ritchie and A.D. Walsh, *Proc. Roy. Soc. A*, **267** (1962) 395.
- [175] Y. Tanaka and A.S. Jursa, *J. Chem. Phys.*, **36** (1962) 2493.
- [176] A.E. Douglas and K.P. Huber, *Can. J. Phys.*, **43** (1965) 74.
- [177] O. Edqvist, E. Lindholm, L.E. Selin, L. Åsbrink, C.E. Kuyatt, S.R. Mielczarek, J.A. Simpson, and I. Fischer-Hjalmars, *Physica Scripta*, **1** (1970) 172.
- [178] J.F. Rendina and R.E. Grojean, *Appl. Spectrosc.*, **25** (1971) 24.
- [179] J.S. Bulger and J.M. Goodings, *Can. J. Phys.*, **49** (1971) 1437.
- [180] J.C.D. Brand, J.L. Hardwick, R.J. Pirkle, and C.J. Seliskar, *Can. J. Phys.*, **51** (1973) 2184.
- [181] C.G. Stevens, M.W. Swagel, R. Wallace, and R.N. Zare, *Chem. Phys. Lett.*, **18** (1973) 465.
- [182] J.L. Hardwick and J.C.D. Brand, *Chem. Phys. Lett.*, **21** (1973) 458.
- [183] M. Krauss, R.J. Celotta, S.R. Mielczarek, and C.E. Kuyatt, *Chem. Phys. Lett.*, **27** (1974) 285.
- [184] Y. Morioka, H. Masuko, M. Nakamura, E. Ishiguro, and M. Sasanuma, *J. Phys. B*, **9** (1976) 2321.
- [185] S. Takezawa, *J. Mol. Spectrosc.*, **65** (1977) 109.
- [186] K.J. Hallin and A.J. Merer, *Can. J. Phys.*, **55** (1977) 2101.
- [187] N. Sugimoto, S. Takezawa, and N. Takeuchi, *J. Mol. Spectrosc.*, **102** (1983) 372.
- [188] A. Delon, R. Jost, and M. Lombardi, *J. Chem. Phys.*, **95** (1991) 5701.
- [189] F. Châteauneuf and H. Lefebvre-Brion, *J. Chem. Phys.*, **98** (1993) 7657.
- [190] T. Imasaka, T. Ogawa, and N. Ishibashi, *J. Chem. Phys.*, **70** (1979) 881.

- [191] V.S. Antonov, I.N. Knyazev, V.S. Letokhov, V.M. Matiuk, V.G. Movshev, and V.K. Potapov, *Optics Lett.*, **3** (1978) 37.
- [192] R.S. Tapper, R.L. Whetten, G.S. Ezra, and E.R. Grant, *J. Phys. Chem.*, **88** (1984) 1273.
- [193] J.K. Dixon, *J. Chem. Phys.*, **8** (1940) 157.
- [194] T.C. Hall and F.E. Blacet, *J. Chem. Phys.*, **20** (1952) 1745.
- [195] A.B. Harker, W. Ho, and J.J. Ratto, *Chem. Phys. Lett.*, **50** (1977) 394.
- [196] Z. Konefal, J. Heldt, D. Konderska-Okexinska, and S. Zachara, *Arch. Ochrony Srodowiska*, **1** (1979) 19.
- [197] J.B. Koffend, J.S. Holloway, M.A. Kwok, and R.F. Heidner, *J. Quant. Spectrosc. Radiat. Transfer*, **37** (1987) 449.
- [198] A. Amoruso, L. Crescentini, G. Fiocco, *J. Geophys. Res. Atmospheres*, **98** (1993) 16857.
- [199] T.C. Corcoran, E.J. Beiting, and M.O. Mitchell, *J. Mol. Spectrosc.*, **154** (1992) 119.
- [200] A.P. Zuev and A. Yu. Starikovskii, *J. Appl. Spectrosc.*, **52** (1990) 304.
- [201] G.J. Frost, L.M. Goss, and V. Vaida, *J. Geophys. Res.*, **101** (1996) 3869.
- [202] R.S. Mulliken, *Rev. Mod. Phys.*, **14** (1942) 204.
- [203] A.D. Walsh, *J. Chem. Soc.* (1953) 2266.
- [204] R.S. Mulliken, *Can. J. Chem.*, **36** (1958) 10.
- [205] D.C. Frost, D. Mak, and C.A. McDowell, *Can. J. Chem.*, **40** (1962) 1064.
- [206] G.L. Weissler, J.A.R. Samson, M. Ogawa, and G.R. Cook, *J. Optical Soc. Am.*, **49** (1959) 338.
- [207] V.H. Dibeler, J.A. Walker, and S.K. Liston, *J. Res. NBS*, **71A** (1967) 371.
- [208] J. Collin and F.P. Lossing, *J. Chem. Phys.*, **28** (1958) 900.
- [209] E. Lindholm and G. Sahlström, *Int. J. Mass Spectrom. Ion Phys.*, **4** (1970) 465.
- [210] K. Stephan, H. Helm, Y.B. Kim, G. Seykora, J. Ramier, M. Grössli, E. Märk, and T.D. Märk, *J. Chem. Phys.*, **73** (1980) 303.

- [211] R.V. Hodges, L.C. Lee, and J.T. Moseley, *Int. J. Mass Spectrom. Ion Phys.*, **39** (1981) 133.
- [212] C.R. Brundle, D. Neumann, W.C. Price, D. Evans, A.W. Potts, and D.G. Streets, *J. Chem. Phys.*, **53** (1970) 705.
- [213] J. Schirmer, L.S. Cederbaum, and W. von Niessen, *Chem. Phys.*, **56** (1981) 285.
- [214] J.W. Williams, C.H. Schwingel, and C.H. Winning, *J. Am. Chem. Soc.*, **58** (1936) 197.
- [215] R.W. Schulz, *Z. Physik*, **109** (1938) 517.
- [216] C.T. Zahn, *Physik. Z.*, **34** (1933) 461.
- [217] D. Neuberger and A.B.F. Duncan, *J. Chem. Phys.*, **22** (1954) 1693.
- [218] J.W. Coburn, *Plasma Etching and Reactive Etching*, Edited by N.R. Whetten, American Vacuum Society Monograph Series (American Institute of Physics, New York, 1982).
- [219] G.M. Reksten, W. Holber, and R.M. Osgood, Jr., *Appl. Phys. Lett.*, **48** (1986) 551.
- [220] W. Zhang, G. Cooper, T. Ibuki, and C.E. Brion, *Chem. Phys.*, **151** (1991) 343.
- [221] W. Zhang, G. Cooper, T. Ibuki, and C.E. Brion, *Chem. Phys.*, **151** (1991) 357.
- [222] W. Zhang, G. Cooper, T. Ibuki, and C.E. Brion, *Chem. Phys.*, **153** (1991) 491.
- [223] W. Zhang, G. Cooper, T. Ibuki, and C.E. Brion, *Chem. Phys.*, **137** (1989) 391.
- [224] G. Cooper, G.R. Burton, and C.E. Brion, *J. Elec. Spectrosc. Relat. Phenom.*, **73** (1995) 139.
- [225] G. Cooper, T.N. Olney, and C.E. Brion, *Chem. Phys.*, **194** (1995) 175.
- [226] G. Cooper, G.R. Burton, W.F. Chan, and C.E. Brion, *Chem. Phys.*, **196** (1995) 293.
- [227] T. Cvitas, H. Gusten, and L. Klasinc, *J. Chem. Phys.*, **67** (1977) 2687.
- [228] C.R. Brundle, M.B. Robin, and H. Basch, *J. Chem. Phys.*, **53** (1970) 2196.
- [229] A.W. Potts, I. Novak, F. Quinn, G.V. Marr, B. Dobson, I.H. Hillier, and J.B. West, *J. Phys. B*, **18** (1985) 3177.

- [230] G. Cooper, W. Zhang, C.E. Brion, and K.H. Tan, *Chem. Phys.*, **145** (1990) 117.
- [231] K. Siegbahn, C. Nordling, C. Johansson, J. Hedman, P.F. Heden, K. Hamrin, U. Gelius, T. Bergmark, L.O. Werme, R. Manne, and Y. Baer, *ESCA Applied to Free Molecules* (North-Holland, Amsterdam, 1969).
- [232] R. Cambi, G. Ciullo, A. Sgamelotti, F. Tarantelli, R. Fantoni, A. Giardini-Guidoni, M. Rosi, and R. Tiribelli, *Chem. Phys. Lett.*, **90** (1982) 131.
- [233] S.T. Manson, A. Msezane, A.F. Starace, and S. Shahabi, *Phys. Rev. A*, **20** (1979) 1005.
- [234] B.E. Cole and R.N. Dexter, *Quant. Spectrosc. Radiat. Transfer*, **19** (1978) 303.
- [235] H.E. Watson and K.L. Ramaswamy, *Proc. Roy. Soc. Lond. A*, **156** (1936) 130.
- [236] K.J. Miller, *J. Am. Chem. Soc.*, **112** (1990) 8533.
- [237] T. Ibuki, A. Hiraya, and K. Shobatake, *J. Chem. Phys.*, **90** (1989) 6290.
- [238] H. W. Jochims, W. Lohr, and H. Baumgärtel, *Ber. Bunsenges. Phys. Chem.*, **80** (1976) 130.
- [239] G.C. King and J.W. McConkey, *J. Phys. B*, **11** (1978) 1861.
- [240] J. Doucet, P. Sauvageau, and C. Sandorfy, *J. Chem. Phys.*, **58** (1973) 3708.
- [241] R. Gilbert, P. Sauvageau, and C. Sandorfy, *J. Chem. Phys.*, **60** (1974) 4820.
- [242] R.H. Huebner, D.L. Bushnell, R.J. Celotta, S.R. Mielczarek, and Kuyatt, *Nature*, **257** (1975) 376.
- [243] F. Bastien, P.A. Chatterton, E. Marode, and J.L. Moruzzi, *J. Phys. D*, **18** (1985) 1327.
- [244] J.C. Person, D.E. Fowler, and P.P. Nicole, *Argonne National Laboratory Report*, ANL-75-60, Part 1, as referenced by ref. [239]
- [245] C.Y.R. Wu, L.C. Lee, and D.L. Judge, *J. Chem. Phys.*, **71** (1979) 5221.
- [246] M. Suto and L.C. Lee, *J. Chem. Phys.*, **79** (1983) 1127.
- [247] R.H. Huebner, D.L. Bushnell, R.J. Celotta, S.R. Mielczarek, and C. Kuyatt, *Argonne National Laboratory Report*, ANL-75-60, Part 1, as referenced by ref. [239]
- [248] W.R. Harshbarger and E.N. Lassette, *J. Chem. Phys.*, **58** (1973) 1505.

- [249] W.R. Harshbarger, M.B. Robin, and E.N. Lassette, *J. Elec. Spectrosc. Relat. Phenom.*, **1** (1972/73) 319.
- [250] G.R. Cook and B.K. Ching, *J. Chem. Phys.*, **43** (1965) 1794.
- [251] L.C. Lee, X. Wang, and M. Suto, *J. Chem. Phys.*, **85** (1986) 6294.
- [252] P. Sauvageau, R. Gilbert, and P.P. Berlow, and C. Sandorfy, *J. Chem. Phys.*, **59** (1973) 762.

## Appendix

The numerical values of the absolute photoabsorption differential oscillator strengths, partial photoionization differential oscillator strengths (PPOS), and photoionization efficiencies ( $\eta_i$ ) obtained in the present work at 1 eV fwhm resolution are given in the following tables A.1 to A.21. The photoabsorption data were obtained by Bethe-Born conversion of background subtracted EEL measurements collected at a mean scattering angle of zero degrees and using high electron impact energy (8 keV). The absolute scales in all cases were established by valence-shell TRK sum-rule normalization (see section 3.1.1 for details). The PPOS for the molecular and dissociative ions were determined from the triple product of the photoabsorption differential oscillator strength, photoionization efficiency, and photoion branching ratio for the corresponding ions, as a function of photon energy. Therefore, these data can be used to regenerate the numerical values of the photoion branching ratios by taking the ratio of the PPOS for the ion of interest and the product of the photoabsorption differential oscillator strength and photoionization efficiency at each energy. Note that the differential oscillator strengths ( $df/dE$ ) given in these tables may be converted to absolute photoabsorption cross sections ( $\sigma_p$ ) in units of megabarns using equation (2.8).

Table A.1

Absolute partial differential oscillator strengths for the molecular and dissociative photoionization of propane

Photon Energy (eV)	Differential oscillator strength ( $10^{-2} \text{ eV}^{-1}$ )																		$\eta_i$
	$\text{C}_3\text{H}_8^+$	$\text{C}_3\text{H}_7^+$	$\text{C}_3\text{H}_6^+$	$\text{C}_3\text{H}_5^+$	$\text{C}_3\text{H}_4^+$	$\text{C}_3\text{H}_3^+$	$\text{C}_3\text{H}_2^+$	$\text{C}_3\text{H}^+$	$\text{C}_2\text{H}_5^+$	$\text{C}_2\text{H}_4^+$	$\text{C}_2\text{H}_3^+$	$\text{C}_2\text{H}_2^+$	$\text{C}_2\text{H}^+$	$\text{CH}_3^+$	$\text{CH}_2^+$	$\text{CH}^+$	$\text{H}_2^+$	$\text{H}^+$	
10.5	1.13	0.06								0.01									0.03
11.0	4.34	0.61							0.09	0.38									0.11
11.5	9.00	2.47	0.10						0.87	2.68									0.29
12.0	11.48	4.79	0.28						3.74	7.20									0.47
12.5	12.52	6.96	0.70						11.39	12.57									0.67
13.0	12.96	8.15	1.04						17.17	14.83									0.72
13.5	13.28	9.38	1.47	0.17					24.50	17.10									0.80
14.0	13.73	10.34	2.02	0.76					32.87	19.31	0.30								0.88
14.5	13.81	10.73	2.46	1.77	0.12				38.21	20.52	1.19	0.13							0.93
15.0	13.88	10.88	2.50	2.58	0.25				40.46	21.22	2.70	0.24							0.95
15.5	13.48	10.68	2.59	3.66	0.35				42.08	21.63	5.74	0.45							0.98
16.0	13.40	10.68	2.53	4.33	0.42				42.68	22.07	7.23	0.50							1.00 <sup>a</sup>
16.5	12.79	10.19	2.49	4.85	0.48	0.12			41.72	21.47	9.15	0.67							
17.0	12.30	9.79	2.40	5.01	0.51	0.19			39.36	20.52	9.33	0.70							
17.5	12.22	9.38	2.38	4.76	0.52	0.17			38.27	20.03	9.30	0.70							
18.0	11.97	9.28	2.35	4.99	0.56	0.25			38.13	19.70	9.46	0.70							
18.5	11.27	8.68	2.28	4.64	0.54	0.26			35.35	18.50	8.93	0.64							
19.0	11.18	8.44	2.24	4.65	0.53	0.51			34.42	17.95	8.98	0.66							
19.5	11.24	8.26	2.24	4.42	0.53	0.85			33.59	17.90	9.13	0.61							
20.0	10.20	7.62	2.02	4.25	0.55	1.04			30.96	16.36	8.61	0.65							
20.5	10.07	7.28	1.94	4.10	0.56	1.24			29.16	15.62	8.39	0.66			0.16				
21.0	9.73	6.99	1.94	3.96	0.57	1.35			27.77	15.30	8.27	0.65			0.20				
21.5	9.24	6.65	1.75	3.71	0.54	1.39			26.32	14.52	7.95	0.55			0.16				
22.0	8.88	6.42	1.67	3.66	0.56	1.50			24.83	13.64	7.75	0.59			0.23				0.15
22.5	8.34	5.96	1.52	3.26	0.53	1.55			22.96	13.05	7.43	0.57			0.22				0.17
23.0	7.85	5.68	1.46	3.17	0.55	1.59			21.73	12.19	7.16	0.59			0.23				0.16
23.5	7.67	5.37	1.39	3.17	0.53	1.79			20.39	11.61	7.08	0.57			0.29				0.17
24.0	7.34	5.14	1.33	2.95	0.48	1.76			19.44	11.22	6.99	0.59			0.23				0.19
24.5	6.89	4.80	1.23	2.76	0.51	1.89			18.01	10.51	6.68	0.64			0.24				0.16

Table A.1 (continued)

Photon Energy (eV)	Differential oscillator strength ( $10^{-2} \text{ eV}^{-1}$ )																		$\eta_i$
	$\text{C}_3\text{H}_8^+$	$\text{C}_3\text{H}_7^+$	$\text{C}_3\text{H}_6^+$	$\text{C}_3\text{H}_5^+$	$\text{C}_3\text{H}_4^+$	$\text{C}_3\text{H}_3^+$	$\text{C}_3\text{H}_2^+$	$\text{C}_3\text{H}^+$	$\text{C}_2\text{H}_5^+$	$\text{C}_2\text{H}_4^+$	$\text{C}_2\text{H}_3^+$	$\text{C}_2\text{H}_2^+$	$\text{C}_2\text{H}^+$	$\text{CH}_3^+$	$\text{CH}_2^+$	$\text{CH}^+$	$\text{H}_2^+$	$\text{H}^+$	
25.0	6.53	4.55	1.23	2.67	0.49	1.93			17.16	9.95	6.64	0.63		0.28	0.09			0.19	
25.5	6.05	4.37	1.13	2.61	0.51	1.97	0.07		16.27	9.54	6.41	0.62		0.30	0.07			0.21	
26.0	5.98	4.25	1.13	2.49	0.49	2.12	0.08		15.91	9.19	6.38	0.67		0.34	0.07			0.20	
26.5	5.46	3.77	1.02	2.33	0.44	2.05	0.10		14.16	8.51	5.95	0.66		0.40	0.11			0.21	
27.0	5.14	3.59	0.98	2.22	0.44	2.06	0.13		13.55	8.04	5.71	0.64		0.35	0.08			0.20	
27.5	4.90	3.40	0.91	2.15	0.44	2.14	0.14		12.94	7.74	5.71	0.65		0.37	0.11			0.19	
28.0	4.64	3.19	0.87	1.98	0.42	2.05	0.15		12.00	7.20	5.40	0.60		0.38	0.10			0.20	
28.5	4.37	3.07	0.79	1.94	0.39	2.03	0.17		11.51	6.94	5.23	0.66		0.36	0.09			0.19	
29.0	4.16	2.83	0.80	1.89	0.38	2.07	0.22	0.05	10.80	6.52	5.10	0.66		0.37	0.12			0.20	
29.5	3.97	2.75	0.76	1.84	0.39	2.07	0.21	0.06	10.35	6.31	5.02	0.68		0.40	0.11			0.19	
30.0	3.62	2.58	0.73	1.72	0.39	2.04	0.25	0.06	9.60	5.87	4.82	0.70		0.45	0.12			0.20	
31.0	3.21	2.29	0.62	1.61	0.34	1.85	0.25	0.12	8.60	5.14	4.47	0.73		0.61	0.17			0.23	
32.0	2.82	1.95	0.56	1.45	0.34	1.71	0.27	0.10	7.58	4.47	4.04	0.71	0.13	0.62	0.23			0.22	
33.0	2.55	1.67	0.50	1.27	0.30	1.65	0.27	0.12	6.70	3.94	3.78	0.65	0.14	0.70	0.21			0.23	
34.0	2.23	1.53	0.42	1.16	0.29	1.61	0.29	0.10	6.13	3.74	3.61	0.65	0.14	0.77	0.19			0.19	
35.0	1.97	1.37	0.44	1.12	0.24	1.49	0.28	0.13	5.53	3.29	3.37	0.64	0.15	0.85	0.23			0.24	
36.0	1.84	1.27	0.37	1.04	0.28	1.43	0.29	0.12	5.05	3.04	3.14	0.57	0.13	0.78	0.25			0.21	
37.0	1.64	1.09	0.35	0.89	0.23	1.38	0.29	0.14	4.55	2.75	2.99	0.60	0.11	0.80	0.24			0.25	
38.0	1.47	1.02	0.34	0.89	0.19	1.32	0.29	0.13	4.27	2.58	2.86	0.57	0.10	0.87	0.19			0.24	
39.0	1.33	0.93	0.30	0.82	0.21	1.23	0.25	0.15	3.81	2.31	2.70	0.52	0.09	0.84	0.20			0.22	
40.0	1.19	0.86	0.28	0.77	0.19	1.16	0.25	0.14	3.52	2.17	2.59	0.50	0.08	0.82	0.21	0.04		0.22	
41.0	1.12	0.74	0.25	0.72	0.18	1.10	0.24	0.13	3.29	2.01	2.44	0.51	0.11	0.83	0.21	0.02		0.24	
42.0	0.96	0.67	0.26	0.67	0.17	1.01	0.23	0.12	2.97	1.81	2.29	0.47	0.07	0.79	0.19	0.03		0.25	
43.0	0.90	0.63	0.20	0.64	0.17	0.98	0.19	0.12	2.80	1.66	2.13	0.46	0.08	0.79	0.19	0.02	0.05	0.26	
44.0	0.80	0.58	0.21	0.57	0.15	0.94	0.18	0.13	2.46	1.53	1.98	0.42	0.09	0.80	0.20	0.03	0.08	0.27	
45.0	0.77	0.51	0.20	0.54	0.15	0.87	0.18	0.11	2.28	1.42	1.91	0.39	0.06	0.76	0.20	0.02	0.06	0.22	
46.0	0.69	0.48	0.20	0.53	0.12	0.87	0.15	0.10	2.17	1.34	1.82	0.41	0.09	0.73	0.19	0.04	0.04	0.25	
47.0	0.64	0.45	0.18	0.50	0.14	0.84	0.16	0.11	2.06	1.26	1.71	0.38	0.06	0.73	0.19	0.03	0.05	0.27	
48.0	0.59	0.44	0.15	0.46	0.11	0.81	0.16	0.10	1.95	1.20	1.67	0.38	0.06	0.71	0.20	0.02	0.03	0.25	
49.0	0.53	0.39	0.13	0.42	0.12	0.75	0.14	0.09	1.78	1.08	1.53	0.36	0.06	0.68	0.20	0.01	0.05	0.26	
50.0	0.52	0.38	0.14	0.38	0.10	0.72	0.14	0.09	1.70	1.03	1.47	0.34	0.05	0.68	0.19	0.04	0.06	0.27	

Table A.1 (continued)

Photon Energy (eV)	Differential oscillator strength ( $10^{-2} \text{ eV}^{-1}$ )																		$\eta_i$
	$\text{C}_3\text{H}_8^+$	$\text{C}_3\text{H}_7^+$	$\text{C}_3\text{H}_6^+$	$\text{C}_3\text{H}_5^+$	$\text{C}_3\text{H}_4^+$	$\text{C}_3\text{H}_3^+$	$\text{C}_3\text{H}_2^+$	$\text{C}_3\text{H}^+$	$\text{C}_2\text{H}_5^+$	$\text{C}_2\text{H}_4^+$	$\text{C}_2\text{H}_3^+$	$\text{C}_2\text{H}_2^+$	$\text{C}_2\text{H}^+$	$\text{CH}_3^+$	$\text{CH}_2^+$	$\text{CH}^+$	$\text{H}_2^+$	$\text{H}^+$	
55.0	0.39	0.28	0.10	0.30	0.09	0.57	0.13	0.07	1.19	0.77	1.14	0.23	0.02	0.54	0.12	0.03	0.02	0.26	
60.0	0.29	0.21	0.08	0.22	0.06	0.46	0.10	0.06	0.92	0.54	0.93	0.25	0.01	0.43	0.14	0.05	0.03	0.22	
65.0	0.21	0.15	0.05	0.17	0.05	0.39	0.08	0.04	0.70	0.42	0.70	0.18	0.02	0.36	0.12	0.03	0.04	0.23	
70.0	0.15	0.12	0.04	0.14	0.04	0.32	0.07	0.05	0.57	0.35	0.57	0.15	0.02	0.30	0.11	0.03	0.02	0.22	
75.0	0.13	0.09	0.03	0.12	0.03	0.26	0.06	0.03	0.44	0.26	0.47	0.12	0.02	0.27	0.08	0.02	0.02	0.19	
80.0	0.10	0.08	0.03	0.09	0.03	0.22	0.04	0.03	0.33	0.23	0.37	0.11	0.02	0.22	0.07	0.02	0.03	0.18	

<sup>a</sup> The photoionization efficiency is normalized to unity above 15.5 eV.

Table A.2

Absolute partial differential oscillator strengths for the molecular and dissociative photoionization of *n*-butane

Photon Energy (eV)	Differential oscillator strength ( $10^{-2} \text{ eV}^{-1}$ )																				$\eta_i$			
	$\text{C}_4\text{H}_{10}^+$	$\text{C}_4\text{H}_9^+$	$\text{C}_4\text{H}_8^+$	$\text{C}_4\text{H}_7^+$	$\text{C}_4\text{H}_5^+$	$\text{C}_4\text{H}_4^+$	$\text{C}_4\text{H}_2^+$	$\text{C}_4\text{H}^+$	$\text{C}_3\text{H}_7^+$	$\text{C}_3\text{H}_6^+$	$\text{C}_3\text{H}_5^+$	$\text{C}_3\text{H}_4^+$	$\text{C}_3\text{H}_3^+$	$\text{C}_3\text{H}_2^+$	$\text{C}_3\text{H}^+$	$\text{C}_2\text{H}_5^+$	$\text{C}_2\text{H}_4^+$	$\text{C}_2\text{H}_3^+$	$\text{C}_2\text{H}_2^+$	$\text{CH}_3^+$		$\text{CH}_2^+$	$\text{H}^+$	
10.0	1.39								0.13	0.02								0.01						0.04
10.5	5.02	0.06	0.01						1.62	0.29								0.02						0.15
11.0	8.69	0.14	0.08						7.87	1.30								0.15						0.32
11.5	9.90	0.32	0.08						18.62	2.48						0.13	0.83							0.50
12.0	10.17	0.73	0.17						33.80	3.68						1.03	3.46							0.72
12.5	10.99	1.17	0.23						44.52	4.56	0.15					2.55	6.09							0.84
13.0	12.96	1.77	0.38						58.01	5.95	0.77					4.87	8.96							0.88
13.5	13.06	1.91	0.57						61.91	6.69	3.02					8.04	10.68	0.23						0.95
14.0	12.97	1.97	0.60						63.37	7.94	7.06	0.21				12.25	12.48	1.29						1.00 <sup>a</sup>
14.5	12.72	1.94	0.57	0.25					62.50	7.83	10.19	0.23				14.78	12.93	2.33						
15.0	11.36	1.91	0.65	0.27					58.11	7.99	12.19	0.34				16.33	13.43	3.70						
15.5	10.90	2.00	0.68	0.41					58.44	7.99	13.10	0.35				18.03	14.16	4.65						
16.0	10.62	1.75	0.61	0.52					56.93	7.79	14.75	0.43				19.42	14.70	6.31						
16.5	10.29	1.96	0.57	0.65					55.49	7.67	15.47	0.48				20.07	14.99	6.52						
17.0	9.61	1.94	0.61	0.61					52.88	7.50	15.06	0.40	0.24			19.66	14.45	6.82						
17.5	9.44	1.80	0.60	0.45					50.16	7.21	14.86	0.55	0.32			19.19	13.74	6.89						
18.0	9.08	1.72	0.56	0.51					49.15	7.16	14.61	0.55	0.39			19.35	13.57	6.95						
18.5	9.04	1.59	0.59	0.48					46.20	6.50	13.44	0.46	0.48			18.06	13.08	6.68						
19.0	8.81	1.49	0.56	0.51					45.28	6.42	13.47	0.48	0.76			18.32	12.64	6.60						
19.5	8.92	1.52	0.39	0.41					43.85	6.37	13.12	0.55	1.03			17.46	12.36	6.59						
20.0	8.27	1.35	0.39	0.46					40.13	5.83	12.27	0.49	1.04			16.18	11.51	6.23						
20.5	7.85	1.38	0.45	0.43					38.54	5.76	11.81	0.55	1.26			15.52	11.00	6.63	0.19					
21.0	7.57	1.23	0.37	0.44					36.90	5.42	11.04	0.55	1.35			15.27	10.60	6.37	0.20					
21.5	7.48	1.15	0.33	0.42					33.88	5.05	10.52	0.55	1.42			13.96	10.07	6.16	0.11					
22.0	7.30	1.17	0.38	0.47					32.78	4.98	10.48	0.56	1.33			13.89	9.67	5.99	0.19				0.19	
22.5	6.67	1.19	0.33	0.37					30.63	4.53	9.48	0.47	1.43			12.68	9.25	6.03	0.20				0.18	
23.0	6.57	0.98	0.40	0.35					29.16	4.32	9.31	0.53	1.57			12.15	8.86	6.10	0.19				0.15	
23.5	6.17	0.90	0.38	0.32					28.17	4.15	8.82	0.60	1.61			11.71	8.66	5.94	0.18	0.19			0.16	
24.0	5.97	0.87	0.33	0.35					26.49	4.06	8.65	0.47	1.74			11.33	8.23	5.99	0.22	0.20			0.21	
24.5	5.81	0.86	0.26	0.27					25.01	3.83	8.07	0.50	1.83			10.57	7.81	5.94	0.20	0.17			0.18	

Table A.2 (continued)

Photon Energy (eV)	Differential oscillator strength ( $10^{-2} \text{ eV}^{-1}$ )																					$\eta_i$
	$\text{C}_4\text{H}_{10}^+$	$\text{C}_4\text{H}_9^+$	$\text{C}_4\text{H}_8^+$	$\text{C}_4\text{H}_7^+$	$\text{C}_4\text{H}_5^+$	$\text{C}_4\text{H}_4^+$	$\text{C}_4\text{H}_2^+$	$\text{C}_4\text{H}^+$	$\text{C}_3\text{H}_7^+$	$\text{C}_3\text{H}_6^+$	$\text{C}_3\text{H}_5^+$	$\text{C}_3\text{H}_4^+$	$\text{C}_3\text{H}_3^+$	$\text{C}_3\text{H}_2^+$	$\text{C}_3\text{H}^+$	$\text{C}_2\text{H}_5^+$	$\text{C}_2\text{H}_4^+$	$\text{C}_2\text{H}_3^+$	$\text{C}_2\text{H}_2^+$	$\text{CH}_3^+$	$\text{CH}_2^+$	
25.0	5.38	0.80	0.24	0.29					23.80	3.78	7.69	0.50	1.80			9.97	7.47	5.84	0.18	0.17		0.20
25.5	5.28	0.75	0.30	0.33					22.56	3.50	7.27	0.53	1.97			9.42	7.09	5.94	0.23	0.23		0.18
26.0	5.00	0.75	0.31	0.29	0.15				21.91	3.33	7.12	0.46	2.04			9.29	7.07	6.02	0.30	0.22		0.19
26.5	4.67	0.65	0.17	0.25	0.09				20.25	3.16	6.64	0.44	1.95			8.86	6.60	5.77	0.23	0.27		0.12
27.0	4.35	0.60	0.25	0.32	0.15				18.85	2.82	6.22	0.45	1.97			8.34	6.15	5.51	0.26	0.35		0.17
27.5	4.29	0.59	0.20	0.25	0.08				18.29	2.86	6.14	0.40	2.07			8.24	6.15	5.55	0.29	0.23		0.13
28.0	3.93	0.58	0.27	0.21	0.09	0.11			17.08	2.57	5.73	0.45	2.05			7.72	5.84	5.43	0.37	0.45		0.15
28.5	3.77	0.54	0.17	0.22	0.10	0.08			16.20	2.42	5.52	0.37	1.95			7.26	5.50	5.27	0.32	0.30		0.10
29.0	3.46	0.52	0.15	0.20	0.13	0.07			15.20	2.36	5.27	0.41	1.96	0.12		7.00	5.41	5.17	0.35	0.34		0.21
29.5	3.38	0.47	0.18	0.19	0.10	0.08			14.45	2.22	5.16	0.36	2.01	0.08		6.67	5.15	5.26	0.40	0.39	0.09	0.20
30.0	3.14	0.45	0.15	0.18	0.09	0.10		0.08	13.38	2.17	4.77	0.37	2.00	0.09		6.43	4.86	5.11	0.39	0.47	0.09	0.17
31.0	2.86	0.43	0.17	0.17	0.07	0.05		0.08	12.28	1.98	4.48	0.34	1.79	0.12		6.08	4.27	4.87	0.40	0.51	0.09	0.12
32.0	2.40	0.37	0.09	0.18	0.13	0.08		0.05	10.47	1.80	4.00	0.37	1.86	0.10		5.32	3.90	4.50	0.35	0.60	0.16	0.14
33.0	2.08	0.29	0.13	0.14	0.06	0.03	0.07	0.05	9.34	1.52	3.67	0.29	1.71	0.08		4.84	3.77	4.30	0.40	0.74	0.10	0.06
34.0	1.85	0.30	0.15	0.13	0.08	0.07	0.07	0.03	8.35	1.37	3.39	0.30	1.78	0.17		4.74	3.47	4.18	0.42	0.85	0.16	0.15
35.0	1.71	0.24	0.09	0.14	0.07	0.05	0.05	0.11	7.61	1.32	3.18	0.29	1.58	0.09		4.29	3.09	4.06	0.38	0.86	0.12	0.16
36.0	1.56	0.21	0.07	0.14	0.08	0.06	0.08	0.08	6.71	1.11	2.88	0.27	1.57	0.09		3.86	2.90	3.75	0.33	0.92	0.15	0.14
37.0	1.35	0.26	0.04	0.10	0.06	0.04	0.08	0.05	6.05	1.08	2.67	0.23	1.47	0.15		3.53	2.67	3.69	0.38	0.87	0.14	0.18
38.0	1.27	0.17	0.07	0.08	0.05	0.05	0.08	0.08	5.43	1.01	2.49	0.30	1.28	0.11		3.29	2.44	3.53	0.37	0.97	0.14	0.15
39.0	1.13	0.17	0.06	0.13	0.02	0.05	0.06	0.06	4.99	0.91	2.34	0.27	1.26	0.11	0.05	3.17	2.33	3.43	0.34	0.92	0.15	0.21
40.0	1.01	0.14	0.07	0.11	0.04	0.03	0.05	0.06	4.54	0.77	2.06	0.22	1.20	0.13	0.05	2.93	2.11	3.14	0.29	0.89	0.13	0.19
41.0	0.93	0.13	0.06	0.09	0.07	0.03	0.06	0.07	4.15	0.74	2.06	0.19	1.17	0.11	0.05	2.67	1.97	2.95	0.34	0.86	0.18	0.18
42.0	0.77	0.12	0.05	0.06	0.02	0.05	0.05	0.08	3.80	0.71	1.91	0.22	1.13	0.11	0.04	2.57	1.82	2.79	0.35	0.95	0.12	0.15
43.0	0.72	0.12	0.06	0.09	0.04	0.04	0.05	0.09	3.26	0.65	1.70	0.18	1.02	0.10	0.04	2.19	1.70	2.64	0.30	0.89	0.15	0.18
44.0	0.70	0.10	0.05	0.08	0.04	0.03	0.07	0.08	3.00	0.55	1.59	0.21	1.06	0.10	0.04	2.03	1.56	2.49	0.34	0.90	0.16	0.16
45.0	0.61	0.11	0.05	0.06	0.04	0.03	0.06	0.07	2.86	0.52	1.47	0.18	0.93	0.09	0.05	1.96	1.49	2.40	0.30	0.87	0.19	0.19
46.0	0.60	0.11	0.04	0.07	0.04	0.04	0.06	0.06	2.66	0.49	1.36	0.15	0.97	0.10	0.04	1.77	1.43	2.27	0.33	0.85	0.18	0.19
47.0	0.53	0.08	0.04	0.04	0.03	0.03	0.06	0.07	2.45	0.43	1.32	0.19	0.94	0.08	0.04	1.70	1.37	2.20	0.32	0.85	0.20	0.19
48.0	0.50	0.07	0.04	0.07	0.01	0.03	0.04	0.05	2.30	0.45	1.22	0.16	0.89	0.08	0.06	1.65	1.23	2.13	0.30	0.84	0.19	0.22
49.0	0.47	0.09	0.02	0.04	0.03	0.02	0.03	0.05	2.16	0.44	1.12	0.14	0.87	0.07	0.02	1.56	1.27	2.06	0.29	0.79	0.18	0.18
50.0	0.44	0.06	0.03	0.04	0.04	0.03	0.03	0.08	1.95	0.37	1.06	0.14	0.78	0.08	0.07	1.37	1.15	1.87	0.28	0.72	0.20	0.20

<sup>a</sup> The photoionization efficiency is normalized to unity above 13.5 eV.

**Table A.3**

Absolute differential oscillator strengths for the valence-shell photoabsorption of *n*-pentane from 7.5 to 220 eV

Photon energy (eV)	Differential oscillator strength ( $10^{-2}$ eV $^{-1}$ )	Photon energy (eV)	Differential oscillator strength ( $10^{-2}$ eV $^{-1}$ )	Photon energy (eV)	Differential oscillator strength ( $10^{-2}$ eV $^{-1}$ )	Photon energy (eV)	Differential oscillator strength ( $10^{-2}$ eV $^{-1}$ )
7.5	0.00	20.5	124.82	33.5	38.76	53.0	11.56
8.0	5.95	21.0	121.45	34.0	37.06	54.0	10.95
8.5	19.89	21.5	114.86	34.5	36.11	55.0	10.08
9.0	37.35	22.0	110.83	35.0	34.36	56.0	9.90
9.5	43.34	22.5	103.83	35.5	33.19	57.0	9.38
10.0	49.39	23.0	100.04	36.0	31.79	58.0	9.08
10.5	58.59	23.5	96.26	36.5	31.07	59.0	8.61
11.0	72.29	24.0	93.56	37.0	29.96	60.0	8.42
11.5	84.62	24.5	88.00	37.5	28.39	61.0	7.79
12.0	99.35	25.0	84.59	38.0	27.98	62.0	7.40
12.5	109.56	25.5	80.57	38.5	26.10	63.0	7.22
13.0	123.48	26.0	79.54	39.0	25.92	64.0	6.81
13.5	134.20	26.5	74.07	39.5	25.95	65.0	6.58
14.0	145.01	27.0	69.35	40.0	24.51	66.0	6.27
14.5	151.92	27.5	67.54	41.0	22.60	67.0	6.08
15.0	157.60	28.0	63.87	42.0	20.90	68.0	5.77
15.5	163.04	28.5	61.19	43.0	19.90	69.0	5.70
16.0	165.01	29.0	58.27	44.0	19.03	70.0	5.35
16.5	166.24	29.5	56.65	45.0	17.64	71.0	5.13
17.0	161.87	30.0	51.39	46.0	16.71	72.0	4.90
17.5	155.67	30.5	52.43	47.0	15.76	73.0	4.75
18.0	155.32	31.0	46.55	48.0	15.15	74.0	4.53
18.5	146.36	31.5	48.09	49.0	14.19	75.0	4.41
19.0	143.07	32.0	43.87	50.0	13.37	76.0	4.19
19.5	140.47	32.5	41.92	51.0	12.86	77.0	4.22
20.0	130.67	33.0	40.08	52.0	12.21	78.0	3.91

Table A.3 (continued)

Photon energy (eV)	Differential oscillator strength ( $10^{-2} \text{ eV}^{-1}$ )	Photon energy (eV)	Differential oscillator strength ( $10^{-2} \text{ eV}^{-1}$ )	Photon energy (eV)	Differential oscillator strength ( $10^{-2} \text{ eV}^{-1}$ )	Photon energy (eV)	Differential oscillator strength ( $10^{-2} \text{ eV}^{-1}$ )
79.0	3.84	114.0	1.59	150.0	0.91	186.0	0.62
80.0	3.67	116.0	1.53	152.0	0.89	188.0	0.61
82.0	3.42	118.0	1.54	154.0	0.86	190.0	0.60
84.0	3.16	120.0	1.42	156.0	0.84	192.0	0.57
86.0	2.99	122.0	1.39	158.0	0.82	194.0	0.58
88.0	2.79	124.0	1.35	160.0	0.79	196.0	0.57
90.0	2.66	126.0	1.29	162.0	0.77	198.0	0.56
92.0	2.53	128.0	1.29	164.0	0.78	200.0	0.55
94.0	2.43	130.0	1.21	166.0	0.75	202.0	0.54
96.0	2.30	132.0	1.18	168.0	0.75	204.0	0.54
98.0	2.20	134.0	1.14	170.0	0.71	206.0	0.53
100.0	2.07	136.0	1.10	172.0	0.70	208.0	0.53
102.0	2.05	138.0	1.07	174.0	0.68	210.0	0.51
104.0	1.91	140.0	1.03	176.0	0.67	212.0	0.52
106.0	1.82	142.0	1.00	178.0	0.67	214.0	0.50
108.0	1.79	144.0	0.99	180.0	0.65	216.0	0.49
110.0	1.75	146.0	0.96	182.0	0.64	218.0	0.47
112.0	1.64	148.0	0.93	184.0	0.62	220.0	0.48

Table A.4

Absolute differential oscillator strengths for the valence-shell photoabsorption of *n*-hexane from 7 to 220 eV

Photon energy (eV)	Differential oscillator strength ( $10^{-2}$ eV $^{-1}$ )	Photon energy (eV)	Differential oscillator strength ( $10^{-2}$ eV $^{-1}$ )	Photon energy (eV)	Differential oscillator strength ( $10^{-2}$ eV $^{-1}$ )	Photon energy (eV)	Differential oscillator strength ( $10^{-2}$ eV $^{-1}$ )
7.0	0.21	20.0	153.48	33.0	48.64	52.0	14.41
7.5	1.89	20.5	147.96	33.5	46.78	53.0	13.61
8.0	9.66	21.0	143.94	34.0	44.91	54.0	13.08
8.5	24.72	21.5	135.90	34.5	42.29	55.0	11.85
9.0	43.00	22.0	132.00	35.0	41.44	56.0	11.42
9.5	51.47	22.5	124.11	35.5	39.04	57.0	11.06
10.0	58.98	23.0	117.95	36.0	38.25	58.0	10.73
10.5	69.46	23.5	114.72	36.5	36.86	59.0	10.03
11.0	84.52	24.0	111.37	37.0	35.80	60.0	9.79
11.5	98.51	24.5	104.68	37.5	33.50	61.0	9.12
12.0	118.70	25.0	99.54	38.0	33.51	62.0	8.79
12.5	132.32	25.5	96.27	38.5	30.96	63.0	8.41
13.0	151.18	26.0	94.58	39.0	30.79	64.0	8.03
13.5	164.32	26.5	86.58	39.5	29.55	65.0	7.75
14.0	175.89	27.0	83.10	40.0	28.90	66.0	7.39
14.5	185.57	27.5	79.56	41.0	27.08	67.0	6.99
15.0	190.16	28.0	76.04	42.0	24.67	68.0	6.78
15.5	194.80	28.5	72.50	43.0	23.32	69.0	6.66
16.0	195.76	29.0	68.64	44.0	22.14	70.0	6.30
16.5	195.20	29.5	66.72	45.0	20.79	71.0	5.94
17.0	188.10	30.0	63.57	46.0	19.77	72.0	5.75
17.5	181.60	30.5	61.47	47.0	18.57	73.0	5.72
18.0	181.22	31.0	59.17	48.0	18.05	74.0	5.28
18.5	172.51	31.5	56.89	49.0	16.59	75.0	5.14
19.0	169.28	32.0	53.57	50.0	15.75	76.0	4.90
19.5	165.86	32.5	49.35	51.0	15.11	77.0	4.73

Table A.4 (continued)

Photon energy (eV)	Differential oscillator strength ( $10^{-2} \text{ eV}^{-1}$ )	Photon energy (eV)	Differential oscillator strength ( $10^{-2} \text{ eV}^{-1}$ )	Photon energy (eV)	Differential oscillator strength ( $10^{-2} \text{ eV}^{-1}$ )	Photon energy (eV)	Differential oscillator strength ( $10^{-2} \text{ eV}^{-1}$ )
78.0	4.57	114.0	1.84	152.0	1.03	190.0	0.71
79.0	4.45	116.0	1.76	154.0	1.00	192.0	0.69
80.0	4.25	118.0	1.75	156.0	0.99	194.0	0.68
82.0	3.96	120.0	1.67	158.0	0.95	196.0	0.67
84.0	3.65	122.0	1.59	160.0	0.93	198.0	0.65
86.0	3.46	124.0	1.53	162.0	0.92	200.0	0.64
88.0	3.26	126.0	1.51	164.0	0.90	202.0	0.64
90.0	3.10	128.0	1.47	166.0	0.89	204.0	0.65
92.0	2.92	130.0	1.41	168.0	0.85	206.0	0.62
94.0	2.77	132.0	1.37	170.0	0.84	208.0	0.61
96.0	2.64	134.0	1.35	172.0	0.82	210.0	0.60
98.0	2.56	136.0	1.30	174.0	0.80	212.0	0.60
100.0	2.43	138.0	1.26	176.0	0.81	214.0	0.58
102.0	2.39	140.0	1.23	178.0	0.78	216.0	0.58
104.0	2.22	142.0	1.19	180.0	0.77	218.0	0.58
106.0	2.16	144.0	1.16	182.0	0.76	220.0	0.58
108.0	2.06	146.0	1.13	184.0	0.72		
110.0	2.05	148.0	1.10	186.0	0.74		
112.0	1.88	150.0	1.06	188.0	0.73		

Table A.5

Absolute differential oscillator strengths for the valence-shell photoabsorption of *n*-heptane from 7 to 220 eV

Photon energy (eV)	Differential oscillator strength ( $10^{-2} \text{ eV}^{-1}$ )	Photon energy (eV)	Differential oscillator strength ( $10^{-2} \text{ eV}^{-1}$ )	Photon energy (eV)	Differential oscillator strength ( $10^{-2} \text{ eV}^{-1}$ )	Photon energy (eV)	Differential oscillator strength ( $10^{-2} \text{ eV}^{-1}$ )
7.0	0.00	20.0	176.49	33.0	56.82	52.0	16.32
7.5	2.50	20.5	171.09	33.5	54.76	53.0	15.68
8.0	12.96	21.0	165.64	34.0	51.68	54.0	15.19
8.5	30.48	21.5	157.81	34.5	51.07	55.0	14.20
9.0	50.62	22.0	152.06	35.0	47.57	56.0	13.16
9.5	59.72	22.5	144.63	35.5	45.36	57.0	12.64
10.0	68.48	23.0	138.78	36.0	44.23	58.0	12.14
10.5	82.25	23.5	132.75	36.5	43.22	59.0	11.78
11.0	101.28	24.0	129.03	37.0	41.10	60.0	10.96
11.5	116.56	24.5	121.42	37.5	38.46	61.0	10.35
12.0	139.78	25.0	116.60	38.0	38.47	62.0	10.11
12.5	156.60	25.5	113.07	38.5	35.40	63.0	9.53
13.0	179.45	26.0	110.67	39.0	35.41	64.0	9.28
13.5	192.34	26.5	100.77	39.5	33.54	65.0	8.90
14.0	203.56	27.0	95.95	40.0	33.01	66.0	8.54
14.5	211.72	27.5	93.20	41.0	31.14	67.0	8.09
15.0	215.29	28.0	88.18	42.0	29.36	68.0	7.83
15.5	220.46	28.5	86.43	43.0	26.95	69.0	7.53
16.0	219.12	29.0	81.53	44.0	25.05	70.0	7.27
16.5	218.82	29.5	78.35	45.0	24.09	71.0	7.00
17.0	212.44	30.0	74.97	46.0	22.52	72.0	6.65
17.5	207.96	30.5	71.84	47.0	21.07	73.0	6.27
18.0	208.47	31.0	67.81	48.0	20.13	74.0	6.14
18.5	196.72	31.5	66.71	49.0	19.66	75.0	5.84
19.0	193.61	32.0	61.72	50.0	18.29	76.0	5.73
19.5	190.28	32.5	58.07	51.0	17.58	77.0	5.61

Table A.5 (continued)

Photon energy (eV)	Differential oscillator strength ( $10^{-2} \text{ eV}^{-1}$ )	Photon energy (eV)	Differential oscillator strength ( $10^{-2} \text{ eV}^{-1}$ )	Photon energy (eV)	Differential oscillator strength ( $10^{-2} \text{ eV}^{-1}$ )	Photon energy (eV)	Differential oscillator strength ( $10^{-2} \text{ eV}^{-1}$ )
78.0	5.29	114.0	2.12	152.0	1.19	190.0	0.82
79.0	5.25	116.0	2.08	154.0	1.18	192.0	0.80
80.0	4.92	118.0	2.04	156.0	1.13	194.0	0.79
82.0	4.62	120.0	1.94	158.0	1.10	196.0	0.77
84.0	4.23	122.0	1.86	160.0	1.08	198.0	0.75
86.0	4.04	124.0	1.81	162.0	1.05	200.0	0.74
88.0	3.80	126.0	1.78	164.0	1.03	202.0	0.75
90.0	3.59	128.0	1.70	166.0	1.02	204.0	0.73
92.0	3.43	130.0	1.63	168.0	1.00	206.0	0.73
94.0	3.27	132.0	1.58	170.0	0.97	208.0	0.72
96.0	3.08	134.0	1.54	172.0	0.96	210.0	0.70
98.0	2.98	136.0	1.51	174.0	0.95	212.0	0.68
100.0	2.84	138.0	1.45	176.0	0.92	214.0	0.69
102.0	2.75	140.0	1.40	178.0	0.90	216.0	0.66
104.0	2.61	142.0	1.37	180.0	0.88	218.0	0.67
106.0	2.58	144.0	1.33	182.0	0.89	220.0	0.67
108.0	2.43	146.0	1.29	184.0	0.85		
110.0	2.36	148.0	1.25	186.0	0.84		
112.0	2.23	150.0	1.23	188.0	0.83		

Table A.6

Absolute differential oscillator strengths for the valence-shell photoabsorption of *n*-octane from 7.5 to 220 eV

Photon energy (eV)	Differential oscillator strength ( $10^{-2}$ eV $^{-1}$ )	Photon energy (eV)	Differential oscillator strength ( $10^{-2}$ eV $^{-1}$ )	Photon energy (eV)	Differential oscillator strength ( $10^{-2}$ eV $^{-1}$ )	Photon energy (eV)	Differential oscillator strength ( $10^{-2}$ eV $^{-1}$ )
7.5	2.35	20.5	191.08	33.5	60.61	53.0	18.21
8.0	13.30	21.0	186.14	34.0	58.64	54.0	17.04
8.5	32.65	21.5	177.89	34.5	55.83	55.0	16.59
9.0	56.07	22.0	171.04	35.0	53.54	56.0	15.28
9.5	66.06	22.5	161.53	35.5	51.75	57.0	14.71
10.0	76.32	23.0	154.77	36.0	50.32	58.0	14.05
10.5	90.82	23.5	149.41	36.5	48.66	59.0	13.58
11.0	112.79	24.0	144.67	37.0	46.17	60.0	12.71
11.5	132.10	24.5	135.79	37.5	45.21	61.0	12.49
12.0	158.28	25.0	131.93	38.0	43.57	62.0	11.63
12.5	177.67	25.5	125.55	38.5	40.59	63.0	11.52
13.0	206.33	26.0	123.67	39.0	40.83	64.0	10.70
13.5	220.31	26.5	115.31	39.5	37.93	65.0	10.04
14.0	231.49	27.0	108.13	40.0	37.64	66.0	9.84
14.5	240.72	27.5	105.33	41.0	35.55	67.0	9.62
15.0	243.44	28.0	98.41	42.0	32.95	68.0	9.07
15.5	248.72	28.5	95.22	43.0	30.61	69.0	8.63
16.0	247.05	29.0	92.42	44.0	28.84	70.0	8.39
16.5	246.65	29.5	87.57	45.0	27.39	71.0	7.83
17.0	239.21	30.0	83.83	46.0	25.66	72.0	7.61
17.5	233.36	30.5	81.01	47.0	24.47	73.0	7.45
18.0	232.66	31.0	78.01	48.0	23.27	74.0	7.01
18.5	220.31	31.5	75.17	49.0	22.49	75.0	6.54
19.0	218.13	32.0	68.50	50.0	20.83	76.0	6.52
19.5	212.05	32.5	64.40	51.0	19.95	77.0	6.36
20.0	197.40	33.0	64.16	52.0	18.93	78.0	6.06

Table A.6 (continued)

Photon energy (eV)	Differential oscillator strength ( $10^{-2} \text{ eV}^{-1}$ )	Photon energy (eV)	Differential oscillator strength ( $10^{-2} \text{ eV}^{-1}$ )	Photon energy (eV)	Differential oscillator strength ( $10^{-2} \text{ eV}^{-1}$ )	Photon energy (eV)	Differential oscillator strength ( $10^{-2} \text{ eV}^{-1}$ )
79.0	6.02	116.0	2.31	154.0	1.30	192.0	0.90
80.0	5.64	118.0	2.31	156.0	1.28	194.0	0.91
82.0	5.25	120.0	2.21	158.0	1.24	196.0	0.89
84.0	4.83	122.0	2.11	160.0	1.21	198.0	0.89
86.0	4.59	124.0	2.10	162.0	1.23	200.0	0.87
88.0	4.30	126.0	1.92	164.0	1.18	202.0	0.87
90.0	4.07	128.0	1.96	166.0	1.15	204.0	0.87
92.0	3.92	130.0	1.85	168.0	1.12	206.0	0.83
94.0	3.71	132.0	1.87	170.0	1.10	208.0	0.81
96.0	3.52	134.0	1.73	172.0	1.08	210.0	0.81
98.0	3.36	136.0	1.67	174.0	1.06	212.0	0.79
100.0	3.17	138.0	1.62	176.0	1.05	214.0	0.80
102.0	3.10	140.0	1.57	178.0	1.03	216.0	0.79
104.0	2.94	142.0	1.52	180.0	1.04	218.0	0.80
106.0	2.81	144.0	1.49	182.0	0.99	220.0	0.81
108.0	2.75	146.0	1.45	184.0	0.97		
110.0	2.68	148.0	1.43	186.0	0.97		
112.0	2.54	150.0	1.39	188.0	0.95		
114.0	2.42	152.0	1.35	190.0	0.92		

Table A.7

Absolute differential oscillator strengths for the total photoabsorption and the dissociative photoionization of PF<sub>3</sub> up to 130 eV

Photon energy (eV)	Differential oscillator strength ( $10^{-2} \text{ eV}^{-1}$ )										Photoionization Efficiency $\eta_i$
	Photo-absorption	PF <sub>3</sub> <sup>+</sup>	PF <sub>2</sub> <sup>+</sup>	PF <sup>+</sup>	PF <sub>3</sub> <sup>2+</sup>	PF <sub>2</sub> <sup>2+</sup>	P <sup>+</sup>	PF <sup>2+</sup>	F <sup>+</sup>	P <sup>2+</sup>	
5.0	0.50										
5.5	0.59										
6.0	0.16										
6.5	0.13										
7.0	4.00										
7.5	24.96										
8.0	40.27										
8.5	15.14										
9.0	19.46										
9.5	22.02										
10.0	11.03										
10.5	11.21										
11.0	16.21	0.69	0.03								0.04
11.5	17.22	2.54	0.04								0.15
12.0	17.48	4.71	0.06								0.27
12.5	22.56	6.41	0.06								0.29
13.0	30.75	9.61	0.14								0.32
13.5	34.46	11.53	0.19								0.34
14.0	43.23	12.88	0.53								0.31
14.5	47.92	13.03	1.41								0.30
15.0	47.50	10.57	3.76								0.30
15.5	43.00	9.03	8.21								0.40
16.0	39.29	8.09	18.72								0.68
16.5	38.60	8.20	23.51								0.82
17.0	40.44	8.64	30.10								0.96
17.5	43.84	8.36	35.48								1.00 <sup>a</sup>
18.0	49.41	8.18	41.23								
18.5	51.89	7.43	44.46								
19.0	54.61	6.77	47.84								
19.5	57.37	6.60	50.77								
20.0	59.69	6.09	53.61								
20.5	61.97	5.95	55.84	0.18							
21.0	63.54	5.43	57.85	0.27							
21.5	64.67	5.44	58.46	0.77							
22.0	63.85	5.02	57.48	1.34							
22.5	63.40	4.66	56.63	2.12							
23.0	61.76	4.42	54.85	2.49							
23.5	60.56	3.89	53.89	2.77							

Table A.7 (continued)

Photon energy (eV)	Differential oscillator strength ( $10^{-2} \text{ eV}^{-1}$ )										Photoionization Efficiency $\eta_i$
	Photo-absorption	PF <sub>3</sub> <sup>+</sup>	PF <sub>2</sub> <sup>+</sup>	PF <sup>+</sup>	PF <sub>3</sub> <sup>2+</sup>	PF <sub>2</sub> <sup>2+</sup>	P <sup>+</sup>	PF <sup>2+</sup>	F <sup>+</sup>	P <sup>2+</sup>	
24.0	58.90	3.79	51.34	3.77							
24.5	56.72	3.24	49.50	3.98							
25.0	53.58	3.18	46.20	4.20							
25.5	51.09	3.04	43.67	4.27			0.11				
26.0	49.13	2.81	41.81	4.38			0.13				
26.5	47.82	2.65	40.42	4.62			0.13				
27.0	44.62	2.52	37.40	4.54			0.16				
27.5	42.61	2.42	35.58	4.40			0.20				
28.0	41.71	2.34	34.58	4.42			0.37				
28.5	40.36	2.19	33.63	4.28			0.25				
29.0	38.29	2.09	31.73	4.01			0.46				
29.5	37.67	2.07	31.08	3.84			0.67				
30.0	36.97	1.88	30.48	3.80			0.82				
32.0	32.77	1.60	26.43	3.15			1.59				
34.0	32.15	1.46	24.89	3.03			2.47		0.31		
36.0	30.39	1.38	22.96	2.76	0.08		2.60		0.63		
38.0	28.86	1.26	20.97	2.52	0.09		2.81		1.19		
40.0	27.82	1.30	19.40	2.42	0.15	0.19	2.75	0.11	1.49		
42.0	25.60	1.16	17.74	2.15	0.13	0.19	2.41	0.23	1.58		
44.0	23.73	1.15	16.28	1.99	0.15	0.21	2.14	0.30	1.51		
46.0	22.62	1.05	15.46	1.81	0.14	0.16	2.09	0.37	1.55		
48.0	21.47	1.05	14.40	1.80	0.16	0.20	1.99	0.42	1.45		
50.0	21.10	1.02	14.12	1.63	0.14	0.17	1.97	0.46	1.51	0.08	
55.0	19.88	1.01	12.90	1.56	0.12	0.19	1.90	0.48	1.56	0.16	
60.0	18.14	0.86	11.66	1.43	0.10	0.17	1.70	0.49	1.51	0.21	
65.0	16.53	0.84	10.39	1.22	0.07	0.17	1.62	0.42	1.56	0.23	
70.0	14.63	0.72	8.96	1.08	0.09	0.13	1.49	0.41	1.51	0.24	
75.0	13.20	0.61	7.75	0.99	0.07	0.13	1.44	0.40	1.56	0.23	
80.0	11.77	0.58	6.68	0.86	0.08	0.12	1.35	0.40	1.48	0.23	
90.0	10.03	0.46	5.49	0.73	0.06	0.13	1.19	0.35	1.41	0.20	
100.0	8.27	0.38	4.38	0.58	0.05	0.09	0.95	0.30	1.32	0.24	
110.0	6.84	0.26	3.69	0.46	0.02	0.07	0.84	0.25	1.09	0.16	
120.0	5.79	0.22	2.91	0.38	0.04	0.06	0.75	0.20	1.05	0.17	
130.0	4.73	0.18	2.33	0.29	0.03	0.04	0.63	0.17	0.90	0.15	

<sup>a</sup> The photoionization efficiency is normalized to unity above 17.5 eV.

Table A.8

Absolute differential oscillator strengths for the total photoabsorption<sup>a</sup>  
of PF<sub>3</sub> in the P 2p,2s inner-shell region from 125 to 300 eV

Photon energy (eV)	Differential oscillator strength (10 <sup>-2</sup> eV <sup>-1</sup> )	Photon energy (eV)	Differential oscillator strength (10 <sup>-2</sup> eV <sup>-1</sup> )	Photon energy (eV)	Differential oscillator strength (10 <sup>-2</sup> eV <sup>-1</sup> )	Photon energy (eV)	Differential oscillator strength (10 <sup>-2</sup> eV <sup>-1</sup> )
125.0	5.02	135.5	5.48	146.0	7.51	167.0	6.54
125.5	5.11	136.0	5.73	147.0	7.48	168.0	6.41
126.0	5.04	136.5	5.63	148.0	7.24	169.0	6.36
126.5	5.02	137.0	5.11	149.0	6.88	170.0	6.20
127.0	4.98	137.5	5.13	150.0	6.52	171.0	6.12
127.5	4.94	138.0	5.57	151.0	6.43	172.0	6.08
128.0	4.90	138.5	5.83	152.0	6.36	173.0	6.01
128.5	4.83	139.0	5.72	153.0	6.46	174.0	5.91
129.0	4.75	139.5	5.54	154.0	6.64	175.0	5.85
129.5	4.69	140.0	5.32	155.0	6.85	176.0	5.82
130.0	4.73	140.5	5.23	156.0	7.16	177.0	5.80
130.5	4.65	141.0	5.21	157.0	7.38	178.0	5.68
131.0	4.66	141.5	5.20	158.0	7.47	179.0	5.66
131.5	4.59	142.0	5.28	159.0	7.51	180.0	5.66
132.0	4.55	142.5	5.36	160.0	7.47	181.0	5.56
132.5	4.52	143.0	5.53	161.0	7.38	182.0	5.49
133.0	4.52	143.5	5.91	162.0	7.19	183.0	5.46
133.5	4.47	144.0	6.26	163.0	7.05	184.0	5.40
134.0	4.70	144.5	6.60	164.0	6.92	185.0	5.36
134.5	5.06	145.0	7.03	165.0	6.80	186.0	5.32
135.0	5.28	145.5	7.30	166.0	6.68	187.0	5.30

Table A.8 (continued)

Photon energy (eV)	Differential oscillator strength ( $10^{-2} \text{ eV}^{-1}$ )	Photon energy (eV)	Differential oscillator strength ( $10^{-2} \text{ eV}^{-1}$ )	Photon energy (eV)	Differential oscillator strength ( $10^{-2} \text{ eV}^{-1}$ )	Photon energy (eV)	Differential oscillator strength ( $10^{-2} \text{ eV}^{-1}$ )
188.0	5.31	208.0	4.80	240.0	3.96	272.0	3.21
189.0	5.29	210.0	4.74	242.0	3.92	274.0	3.16
190.0	5.41	212.0	4.77	244.0	3.84	276.0	3.11
191.0	5.63	214.0	4.69	246.0	3.79	278.0	3.06
192.0	5.99	216.0	4.72	248.0	3.75	280.0	3.05
193.0	5.43	218.0	4.59	250.0	3.66	282.0	2.98
194.0	5.22	220.0	4.57	252.0	3.61	284.0	3.00
195.0	5.20	222.0	4.53	254.0	3.57	286.0	2.92
196.0	5.09	224.0	4.48	256.0	3.52	288.0	2.93
197.0	5.09	226.0	4.44	258.0	3.49	290.0	2.89
198.0	5.11	228.0	4.39	260.0	3.45	292.0	2.85
199.0	5.02	230.0	4.33	262.0	3.35	294.0	2.81
200.0	4.91	232.0	4.24	264.0	3.35	296.0	2.79
202.0	4.79	234.0	4.16	266.0	3.29	298.0	2.75
204.0	4.81	236.0	4.12	268.0	3.27	300.0	2.72
206.0	4.87	238.0	4.01	270.0	3.24		

<sup>a</sup> The partial photoabsorption differential oscillator strengths for the P  $2p,2s$  inner-shells can be obtained by substituting the A, B, and C parameters given in table 5.1 into equation (3.1) and then subtracting the resulting valence-shell contributions from the corresponding total photoabsorption values in this table.

Table A.9

Absolute differential oscillator strengths for the total photoabsorption and the dissociative photoionization of  $\text{PCl}_3$  (1 eV fwhm) up to 125 eV

Photon energy (eV)	Differential oscillator strength ( $10^{-2} \text{ eV}^{-1}$ )						Photoionization Efficiency
	Photo-absorption	$\text{PCl}_3^+$	$\text{PCl}_2^+$	$\text{PCl}^+$	$\text{Cl}^+$	$\text{P}^+$	$\eta_i$
4.5	1.21						
5.0	0.01						
5.5	9.40						
6.0	11.92						
6.5	12.52						
7.0	15.00						
7.5	17.08						
8.0	29.24						
8.5	40.38						
9.0	53.72						
9.5	61.32						
10.0	80.66	4.76	0.05				0.06
10.5	95.26	9.00	0.17				0.10
11.0	97.71	13.59	2.03				0.16
11.5	104.39	19.66	11.14		0.09		0.30
12.0	117.71	24.21	24.85		0.19		0.42
12.5	136.36	26.92	37.38		0.32		0.47
13.0	148.85	29.34	47.16		0.34		0.52
13.5	156.51	30.46	52.60		0.50		0.53
14.0	151.73	30.73	56.16	0.20	0.56		0.58
14.5	144.77	30.21	59.50	0.29	0.61		0.63
15.0	138.24	30.22	63.16	0.35	0.67		0.68
15.5	134.95	30.21	66.91	0.35	0.78		0.73
16.0	133.20	30.64	68.89	0.81	0.83	0.22	0.76
16.5	132.05	30.65	70.29	1.41	0.75	0.15	0.78
17.0	128.60	30.02	70.49	2.26	1.00	0.18	0.81
17.5	125.56	29.00	70.15	3.51	0.91	0.27	0.83
18.0	121.86	28.07	69.35	4.70	0.97	0.24	0.85
18.5	118.04	27.75	68.12	6.15	1.15	0.25	0.88
19.0	113.97	26.55	66.80	7.45	1.24	0.16	0.90
19.5	110.19	25.20	64.63	8.30	1.25	0.27	0.90
20.0	104.54	24.14	63.86	8.89	1.34	0.29	0.94
20.5	101.28	22.84	62.34	9.35	1.57	0.35	0.95
21.0	94.90	20.71	59.72	9.35	1.43	0.45	0.97
21.5	90.47	19.35	57.19	9.69	1.33	0.88	0.98
22.0	85.36	17.75	54.22	9.46	1.44	1.32	0.99
22.5	81.48	16.32	51.06	9.10	1.40	1.92	0.98
23.0	77.60	15.16	48.95	8.92	1.52	2.65	0.99

Table A.9 (continued)

Photon energy (eV)	Differential oscillator strength ( $10^{-2} \text{ eV}^{-1}$ )						Photoionization Efficiency $\eta_i$
	Photo-absorption	$\text{PCl}_3^+$	$\text{PCl}_2^+$	$\text{PCl}^+$	$\text{Cl}^+$	$\text{P}^+$	
23.5	73.81	14.26	46.01	8.35	1.64	3.37	1.00 <sup>a</sup>
24.0	71.13	13.42	44.19	7.99	1.59	3.94	
24.5	67.53	12.28	41.59	7.58	1.69	4.39	
25.0	64.15	11.53	39.18	7.09	1.80	4.55	
25.5	59.94	10.44	36.25	6.62	2.06	4.56	
26.0	55.24	9.51	32.92	6.11	2.17	4.53	
26.5	52.74	8.95	31.14	5.77	2.41	4.47	
27.0	48.71	8.06	28.64	5.31	2.58	4.11	
27.5	44.89	7.30	26.21	4.88	2.63	3.86	
28.0	41.86	6.71	24.27	4.47	2.77	3.65	
28.5	37.50	5.85	21.52	3.97	2.79	3.38	
29.0	35.20	5.47	20.02	3.64	2.88	3.20	
29.5	31.97	4.83	18.01	3.30	2.87	2.97	
30.0	28.52	4.28	16.01	2.90	2.69	2.64	
32.0	19.58	2.66	10.32	1.91	2.76	1.93	
34.0	13.19	1.65	6.69	1.35	2.13	1.37	
36.0	8.47	1.00	4.14	0.85	1.63	0.86	
38.0	5.62	0.65	2.54	0.63	1.20	0.60	
40.0	4.17	0.50	1.68	0.50	1.02	0.47	
42.0	3.50	0.40	1.30	0.46	0.90	0.43	
44.0	3.29	0.38	1.14	0.45	0.88	0.44	
46.0	3.24	0.37	1.06	0.43	0.89	0.49	
48.0	3.22	0.38	1.03	0.42	0.93	0.48	
50.0	3.33	0.39	1.07	0.45	0.94	0.49	
55.0	3.45						
60.0	3.49						
65.0	3.48	0.23	0.75	0.44	1.35	0.71	
70.0	3.42						
74.0	3.34						
78.0	3.23						
82.0	3.12						
86.0	3.02						
90.0	2.86						
95.0	2.74	0.18	0.64	0.31	1.08	0.54	
100.0	2.62						
108.0	2.35						
116.0	2.17						
120.0	2.02						
125.0	1.90	0.11	0.45	0.22	0.73	0.38	

<sup>a</sup> The photoionization efficiency is normalized to unity above 23.5 eV.

Table A.10

Absolute differential oscillator strengths for the total photoabsorption<sup>a</sup> of PCl<sub>3</sub> in the P 2*p*,2*s* and Cl 2*p*,2*s* inner-shell regions from 124 to 350 eV

Photon energy (eV)	Differential oscillator strength (10 <sup>-2</sup> eV <sup>-1</sup> )	Photon energy (eV)	Differential oscillator strength (10 <sup>-2</sup> eV <sup>-1</sup> )	Photon energy (eV)	Differential oscillator strength (10 <sup>-2</sup> eV <sup>-1</sup> )	Photon energy (eV)	Differential oscillator strength (10 <sup>-2</sup> eV <sup>-1</sup> )
124.0	1.93	138.0	2.62	154.0	4.42	182.0	3.61
124.5	1.91	138.5	3.21	155.0	4.47	183.0	3.59
125.0	1.90	139.0	3.96	156.0	4.45	184.0	3.55
125.5	1.91	139.5	4.42	157.0	4.46	185.0	3.59
126.0	1.87	140.0	4.45	158.0	4.41	186.0	3.57
126.5	1.88	140.5	4.03	159.0	4.38	187.0	3.57
127.0	1.87	141.0	3.66	160.0	4.36	187.5	3.57
127.5	1.83	141.5	3.47	161.0	4.35	188.0	3.62
128.0	1.86	142.0	3.37	162.0	4.30	188.5	3.68
128.5	1.84	142.5	3.31	163.0	4.25	189.0	3.73
129.0	1.84	143.0	3.30	164.0	4.24	189.5	3.82
129.5	1.83	143.5	3.33	165.0	4.18	190.0	4.01
130.0	1.83	144.0	3.36	166.0	4.10	190.5	4.36
130.5	1.80	144.5	3.41	167.0	4.09	191.0	4.54
131.0	1.81	145.0	3.46	168.0	4.01	191.5	4.31
131.5	1.81	145.5	3.56	169.0	3.96	192.0	3.89
132.0	1.93	146.0	3.65	170.0	3.93	192.5	3.65
132.5	2.46	146.5	3.78	171.0	3.87	193.0	3.45
133.0	3.19	147.0	3.90	172.0	3.85	193.5	3.42
133.5	3.51	147.5	4.03	173.0	3.84	194.0	3.37
134.0	3.30	148.0	4.11	174.0	3.79	194.5	3.39
134.5	2.62	148.5	4.22	175.0	3.77	195.0	3.40
135.0	2.14	149.0	4.31	176.0	3.74	195.5	3.40
135.5	1.96	149.5	4.39	177.0	3.70	196.0	3.41
136.0	1.87	150.0	4.43	178.0	3.66	196.5	3.48
136.5	1.94	151.0	4.43	179.0	3.66	197.0	3.48
137.0	2.07	152.0	4.43	180.0	3.63	197.5	3.51
137.5	2.32	153.0	4.45	181.0	3.62	198.0	3.48

Table A.10 (continued)

Photon energy (eV)	Differential oscillator strength ( $10^{-2} \text{ eV}^{-1}$ )	Photon energy (eV)	Differential oscillator strength ( $10^{-2} \text{ eV}^{-1}$ )	Photon energy (eV)	Differential oscillator strength ( $10^{-2} \text{ eV}^{-1}$ )	Photon energy (eV)	Differential oscillator strength ( $10^{-2} \text{ eV}^{-1}$ )
198.5	3.49	214.0	10.14	265.0	8.35	304.0	7.30
199.0	3.55	215.0	10.41	266.0	8.40	306.0	7.20
199.5	3.77	216.0	10.59	267.0	8.38	308.0	7.13
200.0	4.20	218.0	10.34	268.0	8.38	310.0	7.06
200.5	4.39	220.0	10.25	269.0	8.44	312.0	7.00
201.0	4.45	222.0	10.19	270.0	8.62	314.0	6.90
201.5	4.62	224.0	10.01	271.0	8.83	316.0	6.80
202.0	4.53	226.0	9.80	272.0	8.78	318.0	6.79
202.5	4.32	228.0	9.69	273.0	8.56	320.0	6.71
203.0	4.33	230.0	9.54	274.0	8.46	322.0	6.63
203.5	4.48	232.0	9.43	275.0	8.40	324.0	6.62
204.0	4.39	234.0	9.25	276.0	8.47	326.0	6.57
204.5	4.56	236.0	9.10	277.0	8.53	328.0	6.53
205.0	5.18	238.0	9.02	278.0	8.52	330.0	6.49
205.5	5.79	240.0	8.87	279.0	8.47	332.0	6.45
206.0	6.49	242.0	8.83	280.0	8.40	334.0	6.42
206.5	7.27	244.0	8.77	282.0	8.32	336.0	6.33
207.0	7.56	246.0	8.71	284.0	8.25	338.0	6.32
207.5	7.65	248.0	8.71	286.0	8.17	340.0	6.24
208.0	7.90	250.0	8.67	288.0	8.11	342.0	6.23
208.5	7.99	252.0	8.57	290.0	8.00	344.0	6.19
209.0	8.14	254.0	8.58	292.0	7.88	346.0	6.12
209.5	8.30	256.0	8.53	294.0	7.79	348.0	6.04
210.0	8.54	258.0	8.47	296.0	7.72	350.0	6.01
211.0	8.96	260.0	8.43	298.0	7.57		
212.0	9.37	262.0	8.42	300.0	7.51		
213.0	9.72	264.0	8.36	302.0	7.37		

<sup>a</sup> The partial photoabsorption oscillator strengths for the inner shells (P 2p,2s; Cl 2p,2s) can be estimated by substituting the A, B, and C parameters in table 5.1 into equation (3.1) and then subtracting the resulting valence-shell contributions from the corresponding total photoabsorption values in this table.

Table A.11

Absolute differential oscillator strengths for the total photoabsorption and the dissociative photoionization of PF<sub>5</sub> up to 130 eV

Photon energy (eV)	Differential oscillator strength ( $10^{-2} \text{ eV}^{-1}$ )												Photoionization Efficiency
	Photo-absorption	PF <sub>4</sub> <sup>+</sup>	PF <sub>3</sub> <sup>+</sup>	PF <sub>2</sub> <sup>+</sup>	PF <sub>4</sub> <sup>2+</sup>	PF <sup>+</sup>	PF <sub>3</sub> <sup>2+</sup>	PF <sub>2</sub> <sup>2+</sup>	P <sup>+</sup>	PF <sup>2+</sup>	F <sup>+</sup>	P <sup>2+</sup>	$\eta_i$
10.0	0.26												
10.5	0.84												
11.0	2.61												
11.5	7.84												
12.0	18.53												
12.5	19.56												
13.0	17.33												
13.5	29.36												
14.0	38.66												
14.5	34.31												
15.0	35.24	1.29											0.04
15.5	35.69	4.75											0.13
16.0	40.96	11.78											0.29
16.5	52.83	23.94		0.23									0.46
17.0	54.92	34.75		0.22									0.64
17.5	49.40	37.51		0.34									0.77
18.0	50.41	41.57		0.32									0.83
18.5	55.26	48.04		0.37									0.88
19.0	60.03	54.45		0.38									0.91
19.5	63.87	61.20		0.43									0.96
20.0	66.55	64.62	0.48	0.52									0.99
20.5	68.63	66.81	0.57	0.49									0.99
21.0	70.60	67.71	2.28	0.62									1.00 <sup>a</sup>
21.5	73.35	66.91	5.83	0.61									
22.0	76.38	67.56	8.33	0.49									

Table A.11 (continued)

Photon energy (eV)	Differential oscillator strength ( $10^{-2} \text{ eV}^{-1}$ )												Photoion- ization Efficiency
	Photo- absorp- tion	PF <sub>4</sub> <sup>+</sup>	PF <sub>3</sub> <sup>+</sup>	PF <sub>2</sub> <sup>+</sup>	PF <sub>4</sub> <sup>2+</sup>	PF <sup>+</sup>	PF <sub>3</sub> <sup>2+</sup>	PF <sub>2</sub> <sup>2+</sup>	P <sup>+</sup>	PF <sup>2+</sup>	F <sup>+</sup>	P <sup>2+</sup>	$\eta_i$
22.0	76.38	67.56	8.33	0.49									
22.5	79.52	70.65	8.48	0.40									
23.0	82.21	72.96	8.84	0.41									
23.5	83.78	74.45	8.87	0.46									
24.0	85.25	75.85	8.88	0.52									
24.5	85.51	75.60	9.37	0.53									
25.0	85.01	75.15	9.51	0.35									
25.5	83.59	74.09	9.19	0.31									
26.0	81.10	71.16	9.35	0.59									
26.5	78.09	68.62	9.04	0.44									
27.0	75.42	65.76	9.05	0.61									
27.5	72.71	63.28	8.67	0.76									
28.0	70.44	61.22	8.25	0.98									
28.5	68.28	59.45	7.81	1.02									
29.0	66.44	57.67	7.37	1.40									
29.5	64.35	55.87	6.81	1.68									
30.0	62.47	53.80	6.37	2.01		0.24					0.05		
31.0	59.88	50.25	6.07	2.70		0.56					0.30		
32.0	57.31	48.03	5.51	2.76		0.87					0.14		
33.0	55.53	44.92	5.77	2.97		1.41					0.45		
34.0	54.18	43.04	5.64	2.88		2.28					0.34		
35.0	54.21	41.73	5.78	2.89		3.38					0.44		
36.0	53.39	40.22	5.85	2.57		4.20			0.17		0.39		
37.0	52.96	38.48	5.91	2.45		5.15			0.36		0.61		
38.0	52.27	36.50	5.98	2.45		6.00			0.48		0.85		
39.0	50.01	34.29	5.93	1.89	0.07	6.16			0.75		0.92		

Table A.11 (continued)

Photon energy (eV)	Differential oscillator strength ( $10^{-2} \text{ eV}^{-1}$ )												Photoionization Efficiency
	Photo-absorption	PF <sub>4</sub> <sup>+</sup>	PF <sub>3</sub> <sup>+</sup>	PF <sub>2</sub> <sup>+</sup>	PF <sub>4</sub> <sup>2+</sup>	PF <sup>+</sup>	PF <sub>3</sub> <sup>2+</sup>	PF <sub>2</sub> <sup>2+</sup>	P <sup>+</sup>	PF <sup>2+</sup>	F <sup>+</sup>	P <sup>2+</sup>	$\eta_i$
40.0	47.60	32.69	5.58	1.51	0.16	5.47	0.17		0.97		1.04		
41.0	44.80	30.15	5.68	1.54	0.18	4.83	0.27		1.12		1.03		
42.0	42.71	28.47	5.75	1.20	0.15	4.28	0.40		1.33		1.13		
43.0	40.70	26.66	5.77	1.15	0.21	3.85	0.61		1.36		1.10		
44.0	39.35	25.91	5.56	0.97	0.15	3.56	0.73		1.38		1.08		
45.0	37.76	24.63	5.44	0.97	0.19	3.37	0.81		1.29		1.07		
46.0	36.86	23.60	5.39	0.99	0.17	3.26	0.82		1.40		1.23		
47.0	35.68	22.92	5.03	0.93	0.16	2.97	0.93		1.44	0.08	1.22		
48.0	34.54	21.89	4.96	0.91	0.16	2.82	0.89		1.43	0.13	1.35		
49.0	33.53	21.02	4.71	0.90	0.18	2.73	1.00		1.48	0.08	1.33	0.10	
50.0	32.77	20.33	4.61	0.92	0.13	2.63	1.05		1.40	0.11	1.50	0.08	
55.0	29.72	18.64	3.98	0.78	0.12	2.22	0.84		1.35	0.12	1.60	0.06	
60.0	27.21	16.57	3.51	0.66	0.10	2.03	0.90	0.12	1.31	0.22	1.70	0.09	
65.0	25.23	15.19	3.02	0.70	0.14	1.83	0.86	0.13	1.22	0.32	1.75	0.08	
70.0	22.84	13.69	2.68	0.69	0.09	1.63	0.76	0.13	1.08	0.34	1.67	0.08	
75.0	20.91	12.10	2.46	0.60	0.08	1.54	0.80	0.13	0.99	0.40	1.70	0.11	
80.0	18.68	10.53	2.11	0.56	0.08	1.43	0.71	0.12	0.95	0.37	1.71	0.09	
90.0	15.41	8.36	1.63	0.48	0.06	1.29	0.63	0.08	0.86	0.32	1.64	0.05	
100.0	12.83	6.65	1.23	0.43	0.06	1.07	0.52	0.11	0.75	0.29	1.64	0.08	
110.0	10.92	5.47	1.03	0.34	0.05	0.93	0.44	0.11	0.67	0.29	1.52	0.07	
120.0	9.10	4.54	0.83	0.28	0.07	0.74	0.36	0.09	0.59	0.24	1.28	0.07	
130.0	7.67	3.78	0.74	0.24	0.04	0.65	0.31	0.05	0.51	0.22	1.08	0.05	

<sup>a</sup> The photoionization efficiency is normalized to unity above 21.0 eV.

Table A.12

Absolute differential oscillator strengths for the total photoabsorption<sup>a</sup>  
of PF<sub>5</sub> in the P 2p,2s inner-shell region from 126 to 300 eV.

Photon energy (eV)	Differential oscillator strength (10 <sup>-2</sup> eV <sup>-1</sup> )	Photon energy (eV)	Differential oscillator strength (10 <sup>-2</sup> eV <sup>-1</sup> )	Photon energy (eV)	Differential oscillator strength (10 <sup>-2</sup> eV <sup>-1</sup> )	Photon energy (eV)	Differential oscillator strength (10 <sup>-2</sup> eV <sup>-1</sup> )
126.0	8.23	136.5	6.89	147.0	7.37	159.5	9.29
126.5	8.20	137.0	6.97	147.5	7.98	160.5	9.63
127.0	8.11	137.5	7.62	148.0	8.72	161.5	10.04
127.5	8.02	138.0	8.93	148.5	9.46	162.5	10.18
128.0	7.99	138.5	10.08	149.0	10.00	163.5	10.01
128.5	7.96	139.0	10.54	149.5	10.10	164.5	9.54
129.0	7.81	139.5	9.61	150.0	9.89	165.5	9.16
129.5	7.79	140.0	8.95	150.5	9.40	166.5	8.73
130.0	7.67	140.5	8.98	151.0	8.87	167.5	8.37
130.5	7.63	141.0	8.76	151.5	8.56	168.5	8.05
131.0	7.60	141.5	8.73	152.0	8.25	169.5	7.79
131.5	7.51	142.0	8.54	152.5	8.05	170.5	7.65
132.0	7.50	142.5	8.18	153.0	7.87	172.5	7.32
132.5	7.39	143.0	7.81	153.5	7.83	174.5	7.25
133.0	7.35	143.5	7.38	154.0	7.85	176.5	7.03
133.5	7.27	144.0	7.08	154.5	7.85	178.5	6.93
134.0	7.18	144.5	6.89	155.0	8.04	180.5	6.78
134.5	7.16	145.0	6.84	155.5	8.24	182.5	6.69
135.0	7.06	145.5	6.75	156.5	8.53	184.5	6.49
135.5	7.04	146.0	6.83	157.5	8.81	186.5	6.46
136.0	6.94	146.5	6.98	158.5	9.03	188.5	6.34

Table A.12 (continued)

Photon energy (eV)	Differential oscillator strength ( $10^{-2} \text{ eV}^{-1}$ )	Photon energy (eV)	Differential oscillator strength ( $10^{-2} \text{ eV}^{-1}$ )	Photon energy (eV)	Differential oscillator strength ( $10^{-2} \text{ eV}^{-1}$ )	Photon energy (eV)	Differential oscillator strength ( $10^{-2} \text{ eV}^{-1}$ )
190.5	6.25	210.5	5.39	242.5	4.50	274.5	3.55
192.5	6.12	212.5	5.32	244.5	4.48	276.5	3.46
193.5	6.15	214.5	5.31	246.5	4.40	278.5	3.43
194.5	6.14	216.5	5.21	248.5	4.25	280.5	3.38
195.5	6.20	218.5	5.20	250.5	4.20	282.5	3.30
196.5	6.39	220.5	5.17	252.5	4.15	284.5	3.33
197.5	6.57	222.5	5.17	254.5	4.06	286.5	3.29
198.5	6.47	224.5	5.10	256.5	3.97	288.5	3.23
199.5	6.25	226.5	5.09	258.5	3.93	290.5	3.24
200.5	6.09	228.5	5.02	260.5	3.89	292.5	3.20
201.5	6.03	230.5	5.00	262.5	3.83	294.5	3.14
202.5	6.02	232.5	4.96	264.5	3.75	296.5	3.14
203.5	5.72	234.5	4.86	266.5	3.72	298.5	3.04
204.5	5.67	236.5	4.79	268.5	3.71	300.5	3.03
206.5	5.48	238.5	4.74	270.5	3.59		
208.5	5.38	240.5	4.63	272.5	3.57		

<sup>a</sup> The partial photoabsorption differential oscillator strengths for the P  $2p,2s$  inner-shells can be obtained by substituting the A, B, and C parameters given in table 5.1 into equation (3.1) and then subtracting the resulting valence-shell contributions from the corresponding total photoabsorption values in this table.

**Table A.13**

Absolute differential oscillator strengths for the total photoabsorption and the molecular and dissociative photoionization<sup>a</sup> in the valence and the P 2*p*,2*s* inner shell regions of PF<sub>3</sub> from 130 to 192.5 eV

Photon energy (eV)	Partial oscillator strength (10 <sup>-2</sup> eV <sup>-1</sup> )									
	Photo-absorption	PF <sub>3</sub> <sup>+</sup>	PF <sub>2</sub> <sup>+</sup>	PF <sup>+</sup>	PF <sub>3</sub> <sup>2+</sup>	PF <sub>2</sub> <sup>2+</sup>	P <sup>+</sup>	PF <sup>2+</sup>	F <sup>+</sup>	P <sup>2+</sup>
130.0	4.73	0.19	2.33	0.29	0.03	0.05	0.63	0.17	0.90	0.15
135.0	5.28	0.18	1.93	0.48	0.03	0.06	0.97	0.20	1.22	0.21
136.5	5.63	0.27	2.26	0.47	0.05	0.06	0.89	0.22	1.23	0.19
138.0	5.57	0.20	1.77	0.48	0.02	0.09	1.15	0.21	1.41	0.23
138.5	5.83	0.16	1.88	0.47	0.04	0.08	1.15	0.24	1.58	0.23
139.5	5.54	0.18	1.81	0.39	0.03	0.10	1.11	0.21	1.48	0.22
141.0	5.21	0.19	1.74	0.28	0.05	0.06	1.00	0.20	1.49	0.20
144.0	6.26	0.13	1.48	0.33	0.08	0.07	0.97	0.57	2.13	0.51
145.0	7.03	0.13	1.41	0.40	0.11	0.10	1.11	0.71	2.51	0.56
146.0	7.51	0.11	1.42	0.40	0.10	0.08	1.20	0.75	2.85	0.61
147.0	7.48	0.13	1.54	0.37	0.11	0.12	1.22	0.76	2.67	0.57
148.0	7.24	0.15	1.57	0.33	0.09	0.09	1.16	0.68	2.61	0.56
152.0	6.36	0.09	1.35	0.31	0.10	0.10	1.05	0.64	2.20	0.53
157.0	7.38	0.11	1.23	0.34	0.13	0.08	1.20	0.72	2.85	0.70
162.0	7.19	0.06	1.15	0.32	0.11	0.11	1.14	0.74	2.90	0.68
175.0	5.85	0.07	1.00	0.25	0.07	0.09	0.91	0.54	2.35	0.56
192.5	5.71	0.08	0.76	0.21	0.05	0.08	0.91	0.45	2.54	0.63

<sup>a</sup> Assuming a photoionization efficiency of unity. Note that these values include the contribution from the underlying valence shell.

Table A.14

Absolute differential oscillator strengths for the total photoabsorption and the dissociative photoionization<sup>a</sup> of PCl<sub>3</sub> in the P 2*p*,2*s* and Cl 2*p*,2*s* inner-shell regions from 125 to 271 eV

Photon energy (eV)	Differential oscillator strength (10 <sup>-2</sup> eV <sup>-1</sup> )								
	Photo-absorption	PCl <sub>3</sub> <sup>+</sup>	PCl <sub>2</sub> <sup>+</sup>	PCl <sup>+</sup>	PCl <sub>2</sub> <sup>2+</sup>	Cl <sup>+</sup>	P <sup>+</sup>	Cl <sup>2+</sup>	P <sup>2+</sup>
125.0	1.90	0.11	0.46	0.22		0.75	0.37		
133.5	3.51	0.11	0.50	0.47	0.03	1.56	0.83		
136.5	1.94	0.09	0.33	0.22		0.86	0.43		
139.5	4.42	0.09	0.41	0.47	0.03	2.26	1.13		0.03
142.5	3.31	0.04	0.28	0.34	0.03	1.75	0.84		0.02
150.0	4.43	0.09	0.33	0.46	0.05	2.34	1.07	0.05	0.05
162.0	4.30	0.04	0.24	0.37	0.04	2.33	1.07	0.10	0.09
174.0	3.79	0.05	0.21	0.31	0.04	2.08	0.97	0.07	0.07
191.0	4.54	0.04	0.19	0.29	0.03	2.52	1.26	0.08	0.14
198.0	3.48		0.11	0.21	0.01	2.04	0.94	0.08	0.09
201.5	4.62	0.04	0.18	0.39	0.04	2.42	1.30	0.12	0.13
207.0	7.56		0.19	0.61	0.04	4.42	1.99	0.18	0.13
216.0	10.59		0.35	1.08	0.06	6.29	2.49	0.17	0.16
250.0	8.67		0.14	0.69	0.04	5.27	2.17	0.21	0.14
271.0	8.83		0.16	0.58	0.05	5.38	2.25	0.23	0.18

<sup>a</sup> Assuming a photoionization efficiency of unity.

**Table A.15**

Absolute differential oscillator strengths for the total photoabsorption and the dissociative photoionization<sup>a</sup> of PF<sub>5</sub> in the P 2*p*,2*s* inner-shell region

Photon energy (eV)	Differential oscillator strength (10 <sup>-2</sup> eV <sup>-1</sup> )											
	Photoabsorption	PF <sub>4</sub> <sup>+</sup>	PF <sub>3</sub> <sup>+</sup>	PF <sub>2</sub> <sup>+</sup>	PF <sub>4</sub> <sup>2+</sup>	PF <sup>+</sup>	PF <sub>3</sub> <sup>2+</sup>	PF <sub>2</sub> <sup>2+</sup>	P <sup>+</sup>	PF <sub>2</sub> <sup>2+</sup>	F <sup>+</sup>	P <sup>2+</sup>
130.0	7.67	3.76	0.74	0.24	0.04	0.64	0.31	0.05	0.51	0.22	1.11	0.05
139.0	10.54	2.84	0.75	0.58	0.02	1.38	0.31	0.15	1.10	0.42	2.76	0.22
141.0	8.76	2.89	0.69	0.31	0.03	1.03	0.32	0.09	0.86	0.32	2.10	0.12
143.0	7.81	2.81	0.61	0.27	0.04	0.68	0.36	0.07	0.77	0.25	1.85	0.09
145.0	6.84	2.55	0.53	0.21	0.04	0.58	0.37	0.07	0.61	0.27	1.54	0.07
149.0	10.00	2.00	0.48	0.44	0.05	0.65	0.31	0.18	0.94	0.74	3.97	0.25
153.5	7.83	1.98	0.40	0.30	0.02	0.57	0.24	0.13	0.73	0.51	2.78	0.16
158.0	8.92	1.78	0.40	0.37	0.06	0.60	0.22	0.13	0.87	0.60	3.66	0.24
162.5	10.18	1.73	0.39	0.42	0.03	0.70	0.25	0.17	0.90	0.78	4.49	0.31
167.0	8.55	1.51	0.34	0.32	0.03	0.61	0.22	0.14	0.87	0.61	3.61	0.28
181.0	6.78	1.20	0.29	0.27	0.01	0.46	0.18	0.12	0.64	0.45	2.91	0.23
197.5	6.57	0.91	0.25	0.21	0.01	0.44	0.16	0.09	0.64	0.44	3.16	0.27

<sup>a</sup> Assuming a photoionization efficiency of unity.

Table A.16

Absolute differential oscillator strengths for the total photoabsorption and the molecular and dissociative photoionization of nitrogen dioxide up to 80 eV

Photon energy (eV)	Differential oscillator strength ( $10^{-2} \text{ eV}^{-1}$ )					Photoionization efficiency $\eta_i$
	Photoabsorption	$\text{NO}_2^+$	$\text{O}_2^+$	$\text{NO}^+$	$\text{O}^+$	
1.5	0.00					
2.0	0.03					
2.5	0.31					
3.0	0.72					
3.5	0.56					
4.0	0.23					
4.5	0.06					
5.0	0.04					
5.5	0.47					
6.0	0.31					
6.5	1.64					
7.0	6.20					
7.5	10.59					
8.0	11.39					
8.5	11.45					
9.0	10.91					
9.5	14.46					
10.0	14.72					
10.5	10.33	0.13		0.05		0.02
11.0	11.43	0.53		0.09		0.05
11.5	13.40	1.19		0.17		0.10
12.0	15.00	1.75		0.27		0.13
12.5	16.31	2.17		0.38		0.16
13.0	16.53	2.70		0.95		0.22
13.5	17.31	3.13		2.52		0.33
14.0	19.74	3.54		4.17		0.39
14.5	22.76	3.94		5.57		0.42
15.0	23.67	4.37		6.88		0.48
15.5	22.39	4.67		7.75		0.55
16.0	22.48	4.92		8.70		0.61
16.5	23.60	4.95		9.64	0.05	0.62
17.0	27.40	5.18		11.61	0.08	0.62
17.5	30.13	5.26		13.85	0.12	0.64
18.0	31.27	5.09	0.00	15.71	0.32	0.68
18.5	33.14	4.75	0.04	17.56	0.67	0.69
19.0	33.16	4.35	0.11	18.67	1.86	0.75
19.5	34.74	4.11	0.19	20.03	3.40	0.80
20.0	36.49	3.87	0.27	21.31	4.44	0.82
20.5	37.24	3.85	0.38	22.29	4.96	0.85
21.0	37.84	3.73	0.43	23.07	5.55	0.87
21.5	38.21	3.69	0.50	23.65	5.81	0.88
22.0	38.06	3.68	0.51	24.23	5.91	0.91
22.5	37.51	3.69	0.53	24.54	6.00	0.93

Table A.16 (continued)

Photon energy (eV)	Differential oscillator strength ( $10^{-2} \text{ eV}^{-1}$ )						Photoionization efficiency $\eta_i$
	Photoabsorption	$\text{NO}_2^+$	$\text{O}_2^+$	$\text{NO}^+$	$\text{O}^+$	$\text{N}^+$	
23.0	36.43	3.65	0.57	24.69	5.89	0.15	0.96
23.5	35.46	3.63	0.52	24.40	5.67	0.19	0.97
24.0	34.21	3.48	0.51	23.83	5.51	0.18	0.98
24.5	32.81	3.50	0.45	23.40	5.25	0.20	1.00 <sup>a</sup>
25.0	31.73	3.35	0.47	22.63	5.08	0.20	
25.5	31.00	3.24	0.43	22.17	4.92	0.24	
26.0	30.18	3.15	0.42	21.51	4.76	0.35	
26.5	29.47	3.11	0.41	20.94	4.62	0.39	
27.0	28.95	3.04	0.39	20.54	4.52	0.46	
27.5	28.68	3.01	0.41	20.23	4.48	0.56	
28.0	28.04	2.93	0.37	19.71	4.37	0.66	
28.5	27.66	2.94	0.35	19.20	4.35	0.82	
29.0	27.51	2.95	0.37	18.92	4.37	0.90	
29.5	27.11	2.92	0.37	18.56	4.24	1.03	
30.0	26.82	2.91	0.31	18.22	4.20	1.19	
31.0	25.98	2.70	0.31	17.43	4.25	1.28	
32.0	25.45	2.67	0.30	16.63	4.25	1.59	
33.0	24.57	2.63	0.26	15.67	4.15	1.86	
34.0	24.09	2.57	0.25	14.94	4.22	2.10	
35.0	23.47	2.49	0.24	14.16	4.27	2.32	
36.0	23.06	2.44	0.24	13.52	4.37	2.48	
37.0	22.58	2.34	0.23	12.93	4.48	2.61	
38.0	21.87	2.27	0.21	12.31	4.49	2.59	
39.0	21.09	2.17	0.21	11.68	4.51	2.52	
40.0	20.23	2.06	0.17	11.11	4.44	2.44	
41.0	19.59	2.02	0.17	10.64	4.44	2.32	
42.0	19.13	1.92	0.17	10.31	4.45	2.27	
43.0	18.67	1.88	0.16	10.00	4.46	2.18	
44.0	18.44	1.84	0.16	9.75	4.57	2.13	
45.0	18.02	1.82	0.16	9.40	4.58	2.05	
46.0	17.81	1.77	0.16	9.22	4.61	2.04	
47.0	17.26	1.65	0.14	8.87	4.59	2.00	
48.0	16.79	1.65	0.15	8.57	4.49	1.94	
49.0	16.14	1.58	0.14	8.22	4.35	1.85	
50.0	15.51	1.51	0.12	7.87	4.25	1.77	
55.0	13.02	1.19	0.16	6.40	3.70	1.57	
60.0	11.13	0.93	0.11	5.33	3.33	1.43	
65.0	9.69	0.75	0.10	4.50	3.00	1.34	
70.0	8.45	0.60	0.09	3.84	2.69	1.23	
75.0	7.52	0.50	0.08	3.27	2.51	1.17	
80.0	6.58	0.41	0.07	2.82	2.26	1.02	

<sup>a</sup> The photoionization efficiency is normalized to unity above 24.5 eV.

Table A.17

Absolute differential oscillator strengths for the valence-shell photoabsorption of nitrogen dioxide from 80 to 200 eV

Photon energy (eV)	Differential oscillator strength ( $10^{-2} \text{ eV}^{-1}$ )	Photon energy (eV)	Differential oscillator strength ( $10^{-2} \text{ eV}^{-1}$ )	Photon energy (eV)	Differential oscillator strength ( $10^{-2} \text{ eV}^{-1}$ )	Photon energy (eV)	Differential oscillator strength ( $10^{-2} \text{ eV}^{-1}$ )
80.0	6.58	102.0	3.91	136.0	1.96	170.0	1.18
81.0	6.54	104.0	3.75	138.0	1.90	172.0	1.17
82.0	6.22	106.0	3.58	140.0	1.82	174.0	1.14
83.0	6.09	108.0	3.44	142.0	1.76	176.0	1.16
84.0	5.96	110.0	3.29	144.0	1.71	178.0	1.08
85.0	5.76	112.0	3.16	146.0	1.68	180.0	1.05
86.0	5.65	114.0	3.01	148.0	1.60	182.0	1.06
87.0	5.52	116.0	2.90	150.0	1.57	184.0	0.99
88.0	5.39	118.0	2.78	152.0	1.51	186.0	0.95
89.0	5.26	120.0	2.64	154.0	1.49	188.0	0.97
90.0	5.14	122.0	2.54	156.0	1.42	190.0	0.93
91.0	5.03	124.0	2.46	158.0	1.41	192.0	0.93
92.0	4.92	126.0	2.36	160.0	1.38	194.0	0.91
94.0	4.70	128.0	2.28	162.0	1.33	196.0	0.88
96.0	4.48	130.0	2.17	164.0	1.29	198.0	0.86
98.0	4.28	132.0	2.12	166.0	1.24	200.0	0.88
100.0	4.09	134.0	2.02	168.0	1.23		

**Table A.18**

Absolute differential oscillator strengths for the valence-shell photoabsorption of  $\text{CFCl}_3$  from 5.5 to 200 eV

Photon energy (eV)	Differential oscillator strength ( $10^{-2} \text{ eV}^{-1}$ )	Photon energy (eV)	Differential oscillator strength ( $10^{-2} \text{ eV}^{-1}$ )	Photon energy (eV)	Differential oscillator strength ( $10^{-2} \text{ eV}^{-1}$ )	Photon energy (eV)	Differential oscillator strength ( $10^{-2} \text{ eV}^{-1}$ )
5.5	0.00	16.5	119.55	27.5	57.37	38.5	15.63
6.0	1.51	17.0	120.68	28.0	53.80	39.0	15.09
6.5	2.42	17.5	119.51	28.5	50.65	39.5	14.73
7.0	3.42	18.0	117.85	29.0	47.32	40.0	14.52
7.5	4.17	18.5	115.53	29.5	44.72	40.5	14.25
8.0	5.08	19.0	112.19	30.0	40.88	41.0	13.87
8.5	10.74	19.5	110.11	30.5	38.07	41.5	13.61
9.0	27.67	20.0	109.04	31.0	35.20	42.0	13.42
9.5	64.25	20.5	107.91	31.5	32.76	42.5	13.23
10.0	74.71	21.0	105.51	32.0	30.70	43.0	13.04
10.5	69.79	21.5	103.75	32.5	28.72	44.0	12.73
11.0	67.42	22.0	101.15	33.0	26.85	45.0	12.46
11.5	70.47	22.5	97.82	33.5	24.78	46.0	12.15
12.0	72.65	23.0	93.39	34.0	23.13	47.0	11.93
12.5	78.54	23.5	89.35	34.5	22.18	48.0	11.66
13.0	86.93	24.0	84.94	35.0	20.75	49.0	11.32
13.5	100.80	24.5	80.32	35.5	19.84	50.0	11.10
14.0	113.62	25.0	77.27	36.0	18.74	51.0	10.82
14.5	125.16	25.5	72.98	36.5	17.94	52.0	10.65
15.0	128.89	26.0	69.06	37.0	17.34	53.0	10.44
15.5	122.88	26.5	65.22	37.5	16.66	54.0	10.31
16.0	118.31	27.0	61.22	38.0	16.18	55.0	10.12

Table A.18 (continued)

Photon energy (eV)	Differential oscillator strength ( $10^{-2} \text{ eV}^{-1}$ )	Photon energy (eV)	Differential oscillator strength ( $10^{-2} \text{ eV}^{-1}$ )	Photon energy (eV)	Differential oscillator strength ( $10^{-2} \text{ eV}^{-1}$ )	Photon energy (eV)	Differential oscillator strength ( $10^{-2} \text{ eV}^{-1}$ )
56.0	9.86	79.0	7.12	116.0	4.22	162.0	2.36
57.0	9.73	80.0	7.01	118.0	4.10	164.0	2.34
58.0	9.56	81.0	6.88	120.0	4.00	166.0	2.28
59.0	9.43	82.0	6.79	122.0	3.91	168.0	2.24
60.0	9.32	83.0	6.66	124.0	3.80	170.0	2.17
61.0	9.20	84.0	6.52	126.0	3.72	172.0	2.16
62.0	9.04	85.0	6.41	128.0	3.61	174.0	2.14
63.0	8.89	86.0	6.31	130.0	3.46	176.0	2.05
64.0	8.84	87.0	6.17	132.0	3.42	178.0	2.00
65.0	8.73	88.0	6.12	134.0	3.33	180.0	2.00
66.0	8.63	90.0	5.93	136.0	3.18	182.0	1.95
67.0	8.49	92.0	5.74	138.0	3.16	184.0	1.95
68.0	8.41	94.0	5.57	140.0	3.05	186.0	1.88
69.0	8.29	96.0	5.42	142.0	2.99	188.0	1.85
70.0	8.18	98.0	5.28	144.0	2.92	190.0	1.83
71.0	8.06	100.0	5.16	146.0	2.81	192.0	1.76
72.0	7.89	102.0	5.02	148.0	2.73	194.0	1.75
73.0	7.82	104.0	4.91	150.0	2.71	196.0	1.72
74.0	7.67	106.0	4.75	152.0	2.63	198.0	1.66
75.0	7.58	108.0	4.66	154.0	2.57	200.0	1.83
76.0	7.44	110.0	4.53	156.0	2.55		
77.0	7.33	112.0	4.45	158.0	2.46		
78.0	7.25	114.0	4.32	160.0	2.43		

**Table A.19**

Absolute differential oscillator strengths for the valence-shell photoabsorption of  $\text{CF}_2\text{Cl}_2$  from 6 to 200 eV

Photon energy (eV)	Differential oscillator strength ( $10^{-2} \text{ eV}^{-1}$ )	Photon energy (eV)	Differential oscillator strength ( $10^{-2} \text{ eV}^{-1}$ )	Photon energy (eV)	Differential oscillator strength ( $10^{-2} \text{ eV}^{-1}$ )	Photon energy (eV)	Differential oscillator strength ( $10^{-2} \text{ eV}^{-1}$ )
6.0	0.00	17.0	92.18	28.0	54.77	39.0	24.42
6.5	0.53	17.5	93.16	28.5	52.49	39.5	23.94
7.0	1.07	18.0	95.83	29.0	49.42	40.0	23.67
7.5	0.80	18.5	98.09	29.5	47.06	40.5	22.96
8.0	0.86	19.0	99.47	30.0	45.02	41.0	22.81
8.5	3.23	19.5	100.48	30.5	42.60	41.5	22.54
9.0	13.49	20.0	99.80	31.0	40.23	42.0	21.99
9.5	32.55	20.5	96.22	31.5	38.02	42.5	21.43
10.0	38.52	21.0	93.43	32.0	36.36	43.0	21.38
10.5	44.53	21.5	90.28	32.5	35.07	43.5	20.85
11.0	54.30	22.0	87.19	33.0	33.56	44.0	20.66
11.5	60.00	22.5	84.00	33.5	31.93	44.5	20.32
12.0	64.54	23.0	81.81	34.0	30.47	45.0	20.06
12.5	70.65	23.5	79.62	34.5	29.70	46.0	19.39
13.0	74.92	24.0	77.13	35.0	28.32	47.0	18.78
13.5	71.38	24.5	74.19	35.5	27.80	48.0	18.21
14.0	70.75	25.0	72.17	36.0	27.40	49.0	17.62
14.5	81.51	25.5	69.44	36.5	26.05	50.0	17.08
15.0	87.26	26.0	66.35	37.0	26.09	51.0	16.51
15.5	87.97	26.5	63.60	37.5	25.53	52.0	16.17
16.0	91.11	27.0	60.80	38.0	25.30	53.0	15.70
16.5	93.06	27.5	57.62	38.5	25.15	54.0	15.42

Table A.19 (continued)

Photon energy (eV)	Differential oscillator strength ( $10^{-2} \text{ eV}^{-1}$ )	Photon energy (eV)	Differential oscillator strength ( $10^{-2} \text{ eV}^{-1}$ )	Photon energy (eV)	Differential oscillator strength ( $10^{-2} \text{ eV}^{-1}$ )	Photon energy (eV)	Differential oscillator strength ( $10^{-2} \text{ eV}^{-1}$ )
55.0	15.01	78.0	10.20	120.0	5.31	166.0	2.78
56.0	14.81	79.0	10.04	122.0	5.17	168.0	2.69
57.0	14.52	80.0	9.83	124.0	5.03	170.0	2.66
58.0	14.24	81.0	9.71	126.0	4.85	172.0	2.62
59.0	14.05	82.0	9.48	128.0	4.72	174.0	2.54
60.0	13.74	84.0	9.12	130.0	4.60	176.0	2.48
61.0	13.63	86.0	8.82	132.0	4.46	178.0	2.40
62.0	13.35	88.0	8.52	134.0	4.35	180.0	2.38
63.0	13.20	90.0	8.24	136.0	4.21	182.0	2.28
64.0	13.06	92.0	7.98	138.0	4.08	184.0	2.36
65.0	12.76	94.0	7.71	140.0	3.94	186.0	2.20
66.0	12.67	96.0	7.52	142.0	3.84	188.0	2.11
67.0	12.32	98.0	7.29	144.0	3.73	190.0	2.08
68.0	12.26	100.0	7.10	146.0	3.63	192.0	2.14
69.0	12.09	102.0	6.91	148.0	3.56	194.0	2.04
70.0	11.81	104.0	6.68	150.0	3.38	196.0	1.95
71.0	11.61	106.0	6.51	152.0	3.35	198.0	1.93
72.0	11.41	108.0	6.38	154.0	3.29	200.0	2.29
73.0	11.32	110.0	6.13	156.0	3.16		
74.0	11.05	112.0	5.97	158.0	3.05		
75.0	10.86	114.0	5.81	160.0	2.98		
76.0	10.64	116.0	5.68	162.0	2.99		
77.0	10.52	118.0	5.45	164.0	2.88		

**Table A.20**

Absolute differential oscillator strengths for the valence-shell photoabsorption of CF<sub>3</sub>Cl from 9 to 200 eV

Photon energy (eV)	Differential oscillator strength (10 <sup>-2</sup> eV <sup>-1</sup> )	Photon energy (eV)	Differential oscillator strength (10 <sup>-2</sup> eV <sup>-1</sup> )	Photon energy (eV)	Differential oscillator strength (10 <sup>-2</sup> eV <sup>-1</sup> )	Photon energy (eV)	Differential oscillator strength (10 <sup>-2</sup> eV <sup>-1</sup> )
7.0	0.10	18.0	75.07	29.0	49.68	40.0	34.73
7.5	0.14	18.5	76.82	29.5	48.32	40.5	33.89
8.0	0.14	19.0	77.11	30.0	46.43	41.0	33.50
8.5	0.28	19.5	75.78	30.5	45.64	41.5	32.98
9.0	3.59	20.0	75.28	31.0	44.67	42.0	32.46
9.5	14.69	20.5	75.44	31.5	43.15	42.5	31.79
10.0	14.85	21.0	75.82	32.0	41.81	43.0	30.67
10.5	13.67	21.5	74.97	32.5	40.90	44.0	29.29
11.0	23.52	22.0	74.86	33.0	39.96	45.0	28.07
11.5	42.33	22.5	75.37	33.5	39.06	46.0	26.93
12.0	44.62	23.0	73.74	34.0	38.26	47.0	26.12
12.5	48.39	23.5	72.37	34.5	37.59	48.0	25.19
13.0	59.88	24.0	69.75	35.0	37.51	49.0	24.38
13.5	63.18	24.5	66.83	35.5	36.69	50.0	23.53
14.0	56.86	25.0	64.31	36.0	36.65	51.0	22.88
14.5	51.80	25.5	62.43	36.5	35.80	52.0	22.30
15.0	49.53	26.0	60.70	37.0	35.69	53.0	21.72
15.5	52.15	26.5	58.70	37.5	35.95	54.0	21.37
16.0	62.18	27.0	57.18	38.0	35.74	55.0	20.85
16.5	68.56	27.5	54.86	38.5	35.35	56.0	20.32
17.0	71.70	28.0	53.36	39.0	35.45	57.0	19.96
17.5	73.73	28.5	51.73	39.5	34.99	58.0	19.61

Table A.20 (continued)

Photon energy (eV)	Differential oscillator strength ( $10^{-2} \text{ eV}^{-1}$ )	Photon energy (eV)	Differential oscillator strength ( $10^{-2} \text{ eV}^{-1}$ )	Photon energy (eV)	Differential oscillator strength ( $10^{-2} \text{ eV}^{-1}$ )	Photon energy (eV)	Differential oscillator strength ( $10^{-2} \text{ eV}^{-1}$ )
59.0	19.26	82.0	12.92	120.0	6.73	166.0	3.16
60.0	19.02	83.0	12.63	122.0	6.50	168.0	3.10
61.0	18.84	84.0	12.31	124.0	6.31	170.0	3.00
62.0	18.47	85.0	12.12	126.0	6.12	172.0	2.94
63.0	18.21	86.0	11.88	128.0	5.92	174.0	2.76
64.0	17.89	87.0	11.65	130.0	5.72	176.0	2.75
65.0	17.57	88.0	11.45	132.0	5.52	178.0	2.65
66.0	17.33	89.0	11.24	134.0	5.28	180.0	2.58
67.0	16.97	90.0	11.07	136.0	5.19	182.0	2.46
68.0	16.83	92.0	10.67	138.0	5.02	184.0	2.49
69.0	16.33	94.0	10.27	140.0	4.87	186.0	2.24
70.0	15.99	96.0	9.95	142.0	4.70	188.0	2.30
71.0	15.83	98.0	9.58	144.0	4.50	190.0	2.16
72.0	15.55	100.0	9.30	146.0	4.40	192.0	2.06
73.0	15.37	102.0	9.03	148.0	4.30	194.0	2.02
74.0	15.09	104.0	8.68	150.0	4.14	196.0	1.93
75.0	14.70	106.0	8.38	152.0	3.98	198.0	1.99
76.0	14.48	108.0	8.15	154.0	3.86	200.0	1.84
77.0	14.10	110.0	7.93	156.0	3.70		
78.0	13.93	112.0	7.65	158.0	3.66		
79.0	13.62	114.0	7.38	160.0	3.50		
80.0	13.27	116.0	7.23	162.0	3.47		
81.0	13.08	118.0	6.96	164.0	3.26		

**Table A.21**

Absolute differential oscillator strengths for the valence-shell photoabsorption of  $\text{CF}_4$  from 10 to 200 eV

Photon energy (eV)	Differential oscillator strength ( $10^{-2} \text{ eV}^{-1}$ )	Photon energy (eV)	Differential oscillator strength ( $10^{-2} \text{ eV}^{-1}$ )	Photon energy (eV)	Differential oscillator strength ( $10^{-2} \text{ eV}^{-1}$ )	Photon energy (eV)	Differential oscillator strength ( $10^{-2} \text{ eV}^{-1}$ )
10.0	0.05	21.0	58.65	32.0	44.56	43.0	37.73
10.5	0.06	21.5	60.84	32.5	44.15	43.5	36.62
11.0	0.10	22.0	62.47	33.0	44.20	44.0	35.71
11.5	0.27	22.5	62.01	33.5	44.42	44.5	35.18
12.0	1.32	23.0	60.63	34.0	44.23	45.0	34.05
12.5	3.51	23.5	59.36	34.5	43.65	45.5	33.21
13.0	11.97	24.0	57.26	35.0	43.44	46.0	32.14
13.5	29.62	24.5	54.58	35.5	43.23	47.0	30.72
14.0	31.67	25.0	52.55	36.0	42.79	48.0	29.45
14.5	19.92	25.5	50.40	36.5	42.69	49.0	28.25
15.0	16.82	26.0	48.52	37.0	42.52	50.0	27.56
15.5	28.76	26.5	47.15	37.5	42.77	51.0	26.71
16.0	35.24	27.0	45.89	38.0	42.65	52.0	26.11
16.5	35.92	27.5	45.11	38.5	42.56	53.0	25.50
17.0	39.14	28.0	44.67	39.0	42.98	54.0	24.91
17.5	41.84	28.5	44.49	39.5	42.57	55.0	24.40
18.0	44.86	29.0	44.27	40.0	42.33	56.0	23.91
18.5	46.84	29.5	44.27	40.5	41.93	57.0	23.60
19.0	48.48	30.0	44.35	41.0	41.10	58.0	23.14
19.5	49.98	30.5	44.61	41.5	40.51	59.0	22.60
20.0	51.66	31.0	44.67	42.0	39.84	60.0	22.35
20.5	55.96	31.5	44.30	42.5	38.82	61.0	21.92

Table A.21 (continued)

Photon energy (eV)	Differential oscillator strength ( $10^{-2} \text{ eV}^{-1}$ )	Photon energy (eV)	Differential oscillator strength ( $10^{-2} \text{ eV}^{-1}$ )	Photon energy (eV)	Differential oscillator strength ( $10^{-2} \text{ eV}^{-1}$ )	Photon energy (eV)	Differential oscillator strength ( $10^{-2} \text{ eV}^{-1}$ )
62.0	21.40	85.0	13.62	120.0	7.35	166.0	3.75
63.0	21.06	86.0	13.51	122.0	7.15	168.0	3.58
64.0	20.52	87.0	13.24	124.0	6.94	170.0	3.46
65.0	20.17	88.0	12.74	126.0	6.71	172.0	3.35
66.0	19.92	89.0	12.66	128.0	6.45	174.0	3.26
67.0	19.55	90.0	12.47	130.0	6.27	176.0	3.17
68.0	19.00	91.0	12.18	132.0	6.09	178.0	3.10
69.0	18.84	92.0	11.84	134.0	5.91	180.0	3.13
70.0	18.39	93.0	11.73	136.0	5.69	182.0	2.99
71.0	18.05	94.0	11.50	138.0	5.56	184.0	2.91
72.0	17.81	95.0	11.23	140.0	5.30	186.0	2.79
73.0	17.31	96.0	11.01	142.0	5.18	188.0	2.67
74.0	17.06	98.0	10.61	144.0	5.03	190.0	2.68
75.0	16.62	100.0	10.33	146.0	4.87	192.0	2.72
76.0	16.43	102.0	9.98	148.0	4.74	194.0	2.55
77.0	16.02	104.0	9.65	150.0	4.52	196.0	2.52
78.0	15.74	106.0	9.31	152.0	4.42	198.0	2.45
79.0	15.43	108.0	9.02	154.0	4.27	200.0	2.42
80.0	15.12	110.0	8.65	156.0	4.15		
81.0	14.64	112.0	8.43	158.0	4.13		
82.0	14.57	114.0	8.13	160.0	3.94		
83.0	14.05	116.0	7.86	162.0	3.89		
84.0	13.87	118.0	7.64	164.0	3.80		